Modelos Relativistas Tridimensionales de Chorros Astrofísicos.

Chorros extragalácticos y Erupciones de Rayos Gamma.

UNIVERSITAT DE VALÈNCIA

UNIVERSIDAD DE VALENCIA

DEPARTAMENTO DE ASTRONOMIA Y ASTROFISICA

TESIS DOCTORAL

PRESENTADA POR

MIGUEL ANGEL ALOY TORAS

NOVIEMBRE 1999

D. José María Ibáñez Cabanell, Catedrático de Universidad del Departamento de Astronomía y Astrofísica de la Universidad de Valencia y D. José María Martí Puig, Profesor Titular de Escuela Universitaria del Departamento de Astronomía y Astrofísica de la Universidad de Valencia,

CERTIFICAN:

Que esta memoria: **Modelos Relativistas Tridimensionales de Chorros Astrofísicos. Chorros extragalácticos y Erupciones de Rayos Gamma**, ha sido realizada bajo su dirección en el Departamento de Astronomía y Astrofísica de la Universidad de Valencia por D. **Miguel Angel Aloy Torás**, y que es su Tesis Doctoral para optar al grado de Doctor en Física.

Y para que así conste, en cumplimiento de la legislación vigente, firman este certificado.

Burjasot, 10 de Noviembre de 1999

José María Ibáñez Cabanell　　José María Martí Puig

A mis padres. A Irene.

Nunca hice nada ni me salió ningún invento por accidente; siempre mediante el trabajo.

Thomas A. Edison

Hay que desplegar más energía en los asuntos administrativos que en la guerra.

Napoleón Bonaparte

Cultivad asiduamente la ciencia de los números, porque nuestros crímenes no son más que errores de cálculo.

Pitágoras de Samos

He comprendido que hay dos verdades, una de las cuales jamás debe ser dicha.

Marcel Camus

El ordenador ha sido hasta ahora el producto más genial de la vagancia humana.

IBM

No es bueno que el hombre esté solo.

Génesis, II – 18

Agradecimientos

El trabajo presentado en esta memoria ha sido el resultado de mi interacción (tanto científica como humana) con una serie bastante numerosa de personas a quienes estoy enormemente agradecido.

En primer lugar tengo que agradecer a mis directores de tesis José María y Chema su acertada guía a lo largo de estos cuatro años durante los cuales no sólo me han instruido convenientemente sino también me han aconsejado personal y profesionalmente. Las múltiples revisiones de esta Memoria, fruto de su paciente y crítica lectura, han mejorado ostensiblemente la calidad de la misma. Gracias a tí José María por *enseñarme a sumar* y posibilitar las múltiples colaboraciones internacionales en las que he participado y que, posiblemente, me permitan encauzar mi futuro postdoctoral. Gracias a tí Chema por enseñarme que el rigor y la estricta aplicación del método científico suelen conducir a las respuestas acertadas (aunque cueste mucho más tiempo...).

Quiero agradecer a Juan Antonio Miralles sus clarificadoras discusiones científicas sin las cuales la sección referente a la ecuación de estado no hubiera sido tan clara. En esta línea, también me gustaría dar las gracias a José Pons, con quien, además de colaborar científicamente (el Apéndice B es el resultado de nuestro trabajo de investigación en el ámbito numérico), he compartido un lugar de trabajo *calentito*.

Gracias en general a todos los que han sido o son miembros del grupo de José María, especialmente a Toni Font (por su colaboración y hospitalidad durante mis estancias en el AEI de Potsdam y por sus comentarios de los capítulos 3 y 4), a Vicent Quilis (con quien he compartido los sinsabores de nuestra situación de becarios de Consellería y experiencias computacionales en el CEPBA y en Centro de Cálculo de la Universidad de Valencia), a Armando Pérez (que ha sido mi tutor a efectos legales y con quien he compartido agradables veladas a orillas del Sena durante el *Texas Symposium on Relativisitic Astrophysics*), y a Vicent Romero (por sus esfuerzos para ayudarnos en la administración del parque de ordenadores del grupo).

No puedo olvidar en esta lista la gratitud que siento hacia mis colaboradores científicos ajenos al departamento de Astronomía: Ewald Müller, José Luís Gómez, Silvano Massaglia, Gianluigi Bodo, Paula Rossi y Andrew MacFadyen. Particularmente agradezco a José Luís su incansable labor científica (sin él no hubieran sido posibles los cálculos sobre emisión de chorros relativistas) como personal (las estancias en el IAA de Granada han resultado francamente agradables y acogedoras). *I would like to outline the collaboration with Ewald whose experienced hints and the valuable comments on the original manuscript have allowed me to improve the chapter on GRBs (sorry Ewald, I don't know enough German to write these lines in your mother tongue!).*

Me gustaría agrader a la fundación Max-Planck la ayuda económica para realizar las diversas estancias de investigación en Alemania, particularmente en el *Max-Planck-Institut für Astrophysik* y al *Max-Planck-Institut für Gravitationsphysik*.

Es de justicia agradecer a la Consellería de Educación su soporte económico en forma de beca FPI durante toda mi formación doctoral. Así mismo, quiero dar las gracias al Depto. de Astronomía y Astrofísica donde he trabajado desde que me licencié. No quisiera olvidar el buen hacer que a nivel administrativo y personal ha desarrollado el PAS del departamento (tanto los miembros permanentes como los sustitutos).

Por imperativo legal, y sobre todo moral, es necesario reconocer que: *esta investigación ha sido realizada utilizando los recursos del Centre de Computació i Comunicacions de Catalunya*. Gracias a Oriol Riu y a Judit Giménez por su buen hacer al frente del grupo de soporte a usuarios del CEPBA. Este agradecimiento lo hago extensivo al CEPBA como institución, que nos ha apoyado con recursos tecnológicos y humanos cuando más necesarios han sido. Sin ellos no se hubieran podido hacer los cálculos del capítulo 3 y parte de los del 4. También quiero agradecer a Fernando Durá su inestimable colaboración para desarrollar mis cálculos en el Servei d'Informàtica de esta Universidad (a pesar de encontrarse, por lo general, atrapado entre la gestión óptima de una máquina de la dimensión de *tiberio* y las presiones de los poderes fácticos de esta institución universitaria).

Debo volver a agradecer a Irene su paciencia en los momentos difíciles (en especial durante los meses anteriores a la deposición del manuscrito) y haberse mantenido fiel a un compromiso que la ha vinculado tanto conmigo como con la Astrofísica (muy a su pesar...). A ella también le dedico este trabajo como señal de afecto y estima. Por supuesto, el agradecimiento lo hago extensivo a su familia cuya hospitalidad (y

gastronomía) he disfrutado.

Finalmente, aunque no menos importante, es absolutamente indispensable dar las gracias a mi familia, por su apoyo y paciencia. No tengo palabras para agradecer a mi madre su humilde y callada contribución. Gracias a mi padre por hacer arraigar en mí los principios de la honradez, el esfuerzo y la tenacidad (el fruto de estos dos últimos ha sido esta memoria). A ellos dos dedico de nuevo estas páginas.

Contents

Chapter 1

Introducción

La presente memoria está dedicada al estudio, por medio de simulaciones numéricas, de dos escenarios astrofísicos: los *chorros extragalácticos* y las *erupciones de rayos gamma* (ERG). Ambos fenómenos tienen en común la presencia de material moviéndose a velocidades cercanas a las de propagación de la luz en el vacío y, por tanto, su evolución dinámica puede tratarse convenientemente utilizando las ecuaciones de la Hidrodinámica Relativista.

Los chorros extragalácticos son canales de plasma magnetizado que se propagan (sin perder apreciablemente su colimación) desde los núcleos de algunas galáxias (galáxias activas) hasta adentrarse en el medio intergaláctico (pudiendo alcanzar longitudes de varios megaparsecs) y son detectados fundamentalmente por su emisión en radio frecuencia.

Las ERG son fenómenos esporádicos de alta energía cuyo espectro presenta una enorme variabilidad temporal y energética. Están constituidos por fotones muy duros de energías comprendidas entre varios centenares de keV y algunos MeV y son observados fundamentalmente en la región gamma del espectro, aunque también emiten parte de su energía en las bandas X, radio y óptico.

Ambos fenómenos están formalmente relacionados, dado que existe un mecanismo común de formación, a saber, el acrecimiento de material sobre un agujero negro (AN, en adelante) central en rotación que, por procesos púramente hidrodinámicos o magneto-hidrodinámicos da lugar a la transformación de enegía gravitacional en energía cinética. El resultado de esta conversión energética es la eyección de material en la dirección del eje de rotación del sistema formado por el AN y el disco de acrecimiento que le rodea. Tales eyeciones de material son colimadas por mecanismos magneto-hidrodinámicos (en el caso de chorros extragalácticos) o por confinamiento inercial (en el caso de ERGs), y pueden llegar a alcanzar velocidades relativistas.

A pesar de las similitudes entre ambos escenários, también los separan múltiples diferencias. Por ejemplo, el "motor central" del los chorros extragalácticos es un AN supermasivo (de $10^7 M_\odot - 10^9 M_\odot$), mientras que las ERG se supone que están vinculadas a AH estelares (es decir, de unas pocas masas solares). El mecanismo de aceleración es también distinto. Los chorros son acelerados por mecanismos magneto-hidrodinámicos; las ERG por la deposición de energía y momento (cerca de las regiones axiales) debida a procesos de aniquilación de neutrinos conducentes a la creación de pares electrón-positrón (que a su vez se aniquilan para formar fotones de alta energía). Así mismo, el medio que rodea al lugar de formación es muy diferente en ambos casos. Los chorros extragalácticos se forman en los núcleos de galáxias activas en regiones con tamaños típicos de $\sim 10^{11}$ cm y con densidades muy pequeñas. Las EGR se originan en regiones típicas de $\sim 10^6$ cm y las densidades son muy elevadas (corresponden a las existentes en los núcleos de estrellas masivas). Por supuesto, el medio a través del que se propagan es también muy distinto, sobre todo, en las etapas iniciales: las ERG están originadas, presumiblemente, en el seno de estrellas masivas o en las regiones de coalescencia de sistemas binarios compactos; los chorros extragalácticos se propagan inicialmente a través de regiones de mucho menor densidad y presión en el interior de los cúmulos estelares que existen en los núcleos galácticos.

Es notable, sin embargo, que ambos fenómenos pueden estudiarse empleando una aproximación *tipo fluido*. Ello permite estudiar su evolución mediante las ecuaciones de la Hidrodinámica Relativista. No obstante, dadas las peculiaridades de cada fenómeno, además de estas ecuaciones son necesarios otros ingredientes para su simulación numérica. Uno de esos ingredientes, es el adecuado tratamiento del campo gravitatorio. En el caso de los chorros extragalácticos, si pretendemos estudiar su evolución a distancias suficientemente grandes del AN central, el campo gravitatorio no es importante y puede abordarse su estudio en el marco de la Relatividad Especial. La formación de ERGs necesita de la inclusión del campo gravitatorio en los cálculos, puesto que se generan a distancias del AH a las cuales la gravedad sigue siendo importante. Además, ese campo gravitatorio es necesario para mantener la estructura material de la estrella o de la región de mezcla de un sistema binario compacto (esto es, para equilibrar la tendencia disgregadora de la presión del sistema). Otro ingrediente importante es la ecuación de estado empleada. Los chorros extragalácticos están razonablemente bien caracterizados por ecuaciones de estado del tipo gas ideal (aunque, por supuesto, sería muy interesante considerar los efectos dinámicos de ecuaciones de estado más realistas que consideraran la existencia de un plasma formado por pares electrón-positrón). Las ERG necesitan, al menos, incluir los efectos de la radiación y los pares electrón-positrón en equilibrio con la materia, puesto que en las etapas de formación, estas ERG son ópticamente gruesas, lo que significa que los fotones no pueden escapar libremente del sistema, de modo que contribuyen significativamente en la termodinámica del mismo.

La simulación numérica de estos fenómenos requiere como parte esencial la construcción de un código robusto que resuelva numéricamente las ecuaciones de la Hidrodinámica Relativista. Esta parte técnica se complica enormemente cuando se consideran simulaciones multidimensionales y, particularmente en tres dimensiones espaciales (3D). GENESIS es un código hidrodinámico, relativista, multidimensional, de alta resolución en la captura de choques que se ha desarrollado para abordar problemas astrofísicos generales que involucren un tratamiento hidrodinámico y relativista. La pieza clave a partir de la que se construye un código de este tipo (*tipo Godunov*), es el resolvedor de problemas de Riemann[1]. La idea básica de los métodos tipo Godunov es discretizar una solucion física sobre una malla numérica y tomar en cada nodo de esa malla el valor medio de cada variable en un entorno del nodo (este entorno es la celda computacional). El proceso de promediado espacial introduce discontinuidades en las interfases de las celdas computacionales. A su vez, la presencia de discontinuidades da lugar a *flujos* de las variables promediadas hacia (o

[1]Un problema de Riemann es un problema unidimensional de valores iniciales discontínuos que, tiene una solución analítica conocida en el caso de las ecuaciones de la Hidrodinámica.

desde) las celdas adyacentes, cuyo valor puede calcularse resolviendo los problemas de Riemann correspondientes a cada interfase. Tras evaluar los flujos espaciales, la evolucion temporal del sistema hasta un instante de tiempo posterior, puede determinarse mediante un método explícito de alto orden. De esta forma se obtiene la solución numérica en el instante $t^n + 1$ partiendo de los valores en el instante t^n.

GENESIS permite, dada su modularidad, la posibilidad de utilizar cualquiera de los resolvedores linealizados existentes en la literatura. Particularmente, las aplicaciones que se muestran en esta memoria se han realizado utilizando el resolvedor (o fórmula de flujos) de Marquina (Marquina *et al.* 1992). La resolución espacial se incrementa utilizando una interpolación parabólica monótona (PPM; *Piecewise Parabolic Method*) de tercer orden. Las capacidades y rendimiento de GENESIS tanto en ejecuciones secuenciales como en paralelas (para las que ha sido preparado) se han analizado en el capítulo 2 de esta memoria. En concreto, en dicho capítulo, se presentan los resultados de una batería extensa de tests numéricos que demuestran que el código puede capturar y evolucionar con precisión choques fuertes en 3D. El código es multiplataforma, y ha sido probado con éxito en varias arquitecturas computacionales (HP y SGI), aunque en el futuro se pretende utilizar GENESIS en superordenadores masivamente paralelos con memoria distribuida (en la actualidad se está utilizando en arquitecturas multiprocesadoras de superordenadores con memoria central compartida).

En el campo numérico hemos estudiado la implementación eficiente de las fórmulas aproximadas de flujos en varias dimensiones espaciales. Estas fórmulas de flujos son una pieza clave en cualquier código numérico basado en técnicas tipo Godunov y, en problemas hidrodinámicos suelen ser una de las partes que demandan más tiempo de cálculo (dada su complejidad). Las expresiones que se dan en el Apéndice B generalizan (e incluyen) en el ámbito analítico a otras dadas por diferentes autores (además de incluir prescripciones para aumentar el rendimiento computacional).

Se han realizado las primeras simulaciones numéricas de alta resolución en tres dimensiones espaciales de chorros relativistas alcanzando el haz del chorro factores de Lorentz 7 (publicadas en Aloy *et al.* 1999b). El material que compone el chorro (así como también el medio que lo rodea), se describe empleando una ecuación de estado de gas ideal (de tipo politrópico). La resolución espacial de estas simulaciones ha sido de 8 celdas computacionales por cada radio del haz (el radio del haz, R_b, es una escala de longitud característica del sistema). Las simulaciones se han realizado en coordenadas cartesianas y GENESIS se ha modificado levemente para incluir una nueva ecuación de adveción para la variable fracción másica de partículas del haz en cada celda computacional (f). Esta nueva variable conservada no requiere cambio alguno en el resolvedor de problemas de Riemann, dado que las partículas del haz son advectadas con el fluido. La evolución de los chorros se ha seguido hasta alcanzar ~ 75 unidades de tiempo normalizado. Durante ese periodo hemos analizado la morfología y la dinámica de los chorros relativistas tridimensionales (véase capítulo 3).

Con objeto de inducir fenómenos genuinamente tridimensionales se han introducido perturbaciones de tipo helicoidal sobre el campo de velocidades en el punto de injección de un modelo de referencia axisimétrico 3D que, a su vez, nos sirve para calibrar y comparar nuestras simulaciones con las ya existentes en el caso 2D axisimétrico (Martí *et al.* 1997). Las perturbaciones dependen de dos parámetros: amplitud de la perturbación y frecuencia de giro, cuya influencia en la dinámica se ha estudiado considerando varios modelos (con perturbaciones de mayor o menor amplitud y de alta o baja frecuencia).

Nuestras simulaciones muestran multitud de elementos novedosos respecto a otras semejantes en dos dimensiones espaciales (2D) y, por supuesto, respecto a las simulaciones 3D clásicas. Del análisis de los resultados se desprende que en 3D no aparecen contraflujos coherentes extremadamente relativistas que si estaban presentes en los modelos 2D axisimétricos. Así mismo, se ha encontrado que cuando los jets son expuestos a pequeñas perturbaciones no axisimétricas, (i) no muestran las fuertes perturbaciones exitentes en modelos 3D clásicos, tanto hidrodinámicos como magnetohidrodinámicos (al menos durante el periodo de tiempo cubierto por nuestros cálculos), y (ii) los chorros se propagan a velocidades próximas a la estimación unidimensional (1D). Ello se explica como consecuencia, fundamentalmente, de dos hechos: la primera es el tiempo de evolución de nuestros modelos, que está un par de órdenes de magnitud por debajo del de una radio fuente extragaláctica real; la segunda es la resolución con que se han realizado las simulaciones que, pese a ser la mayor las utilizadas hasta la fecha en 3D, puede no ser suficiente para capturar con precisión algunas de las escalas de relevancia en el proceso de interacción chorro-medio externo (el efecto de la resolución se puso de manifiesto en Aloy *et al.* 1999a al comparar la morfodinámica del mismo chorro usando mallas de 4 y 8 celdas/R_b en 3D, y 20 celdas/R_b en el mismo modelo 2D axisimétrico). Otro elemento destacable es que las pequeñas perturbaciones 3D inducen en el haz relativista una distribución de velocidades aparentes de grupo semejeante a la observada en M87.

La parte final capítulo 3, presenta las primeras simulaciones de radioemisión procedentes de modelos relativistas tridimensionales de alta resolución, cuyo principal objetivo es el estudio de las implicaciones observacionales de la interacción entre el chorro y el medio externo (Aloy *et al.* 1999c). Como consecuencia de tal interacción aparece una estratificación natural del chorro, consistente en una "espina" central rápida (parte más interna del haz), rodeada por una capa de fricción caracterizada por una elevada energía interna específica y un campo de velocidades progresivamente decreciente (respecto a la dirección normal al eje del jet). La estratificación y, en particular, la relativamente alta energía interna y la baja velocidad del fluido en la capa de fricción, determinan en gran medida la emisión del chorro. Es de señalar que la estratificación del chorro es el resultado del cálculo y no ha sido impuesta *a priori* (tal como han hecho otros autores para estudiar numéricamente las propiedades de las capas de fricción entre el haz y el medio ambiente).

La inclusión *ad hoc* de diferentes configuraciones de campo magnético en el chorro ha permitido extraer consecuencias observaciones importantes. Si, por ejemplo, el campo magnético en la capa de fricción combina un campo helicoidal (quizás inducido por el efecto de fricción actuando sobre un campo magnético alineado con el eje del jet que se une a un campo magnético toroidal) la emisión se observa que muestra una asimetría en sobre la sección transversal del chorro (respecto a la dirección normal al eje del chorro). Tal asimetría, además del abrillantamiento hacia los bordes o hacia la espina central, se debe al efecto relativista de *aberración de la luz* y es función del ángulo de visión y de la velocidad del fluido, y puede cambiar su sentido si el chorro cambia su dirección con respecto al observador (debido a su interacción con el medio externo), o presenta un cambio en velocidad. La asimetría es más notable en el flujo polarizado, a resultas de la cancelación (o amplificación) del campo a lo largo de la línea de visión. Suponiendo que el modelo es válido, hemos interpretado las observaciones de polarización del *blazar* 1055+018 realizadas por Attridge, Roberts y Wardle (1999), concluyendo que el jet de esta fuente se está decelerando, y que tal deceleración es la responsable del cambio brusco en la polarización (entre las partes superior e inferior del chorro).

El último capítulo lo ocupa el estudio de flujos colimados relativistas propuestos, en el modelo de *collapsar*, como un mecanismo para generar erupciones de rayos gamma. Empleando el modelo de collapsar de MacFadyen y Woosley (1999) como progenitor de una ERG, se ha simulado la propagación de un chorro relativista a través del manto y la envoltura de una estrella masiva en rotación que colapsa. Para estas simulaciones ha sido necesario modificar el código GENESIS para que incluya un campo gravitacional estático de Schwarzschild semejante al producido por el AN central en el modelo de collapsar. Adicionalmente, se ha incluido en GENESIS una ecuación de estado analítica (Witti, Janka y Takahashi 1994) que incluya las contribuciones de la radiación, de los pares electrón-positrón y de nueve gases de Boltzman ideales que se corresponden con los núcleos de siete elementos representativos del sistema, protones y neutrones. Esto es necesario porque con una ecuación de estado de gas ideal con exponente adiabático constante estariamos representando incorrectamente bien el chorro caliente y dominado por la presión de radiación y los pares, bien el resto del manto que es no relativista y está soportado por la presión de los bariones. De este modo, nuestra ecuación de estado es formalmente equivalente a una ecuación de índice adiabático variable. Sin embargo, esta ecuación de estado es sólo aproximada (de hecho, el tratamiento de los pares se realiza haciendo una interpolación entre altas y bajas temperaturas). El modelo inicial de MacFadyen y Woosley se obtiene utilizando la ecuación de estado de Blinnikov, Dunina-Barkovskaya y Nadyozhin (1996), que es más realista (tanto en el tratamiento de los pares como en el de las contribuciones a la presión de los electrones degenerados), aunque las diferencias efectivas entre esta ecuación y la de Witti, Janka y Takahashi (1994) sólo son relevantes en las partes más densas del toro (que se excluyen del modelo inicial al eliminar los 200 km más internos de la estrella sustituyéndolos por una condición de contorno adecuada).

El flujo saliente con forma de chorro se origina como resultado de la deposición de $\sim 10^{50} - 10^{51}$ erg/s en el seno de un cono de 30° alrededor del eje de rotación de la estrella progenitora. El fluido del chorro generado se propaga siguiendo este eje debido a que la rotación del manto crea un canal de baja densidad alrededor de tal eje (debido a la fuerza centrífuga). La distribución de masa del modelo inicial es tal que el fluido del chorro saliente es fuertemente colimado (el chorro presenta un ángulo de apertura menor o del orden de unos pocos grados) por el confinamiento inercial proporcinado por las paredes del canal central y, adicionalmente, mantiene su estructura (altamente colimada) hasta llegar a la superficie de la estrella progenitora ($r \approx 3 \times 10^{10}$ cm).

Para verificar la convergencia de los modelos numéricos se han repetido dos simulaciones (la de $\sim 10^{50}$ erg/s y 10^{51} erg/s) sobre mallas de diferentes tamaños la dirección angular (manteniendo fija la resolución radial), siendo el resultado claramente dependiente de la resolución empleada excepto cuando las mallas son suficientemente finas como para capturar las escalas apropiadas del problema (cosa que sucede para resoluciones efectivas cerca del eje de rotación de medio grado).

Uno de los resultados del presente trabajo es que el máximo factor de Lorentz alcanzado por los modelos justo cuando alcanzan la superficie de la estrella está en el intervalo $20 - 34$. Claramente estos factores de Lorentz están por debajo de los mínimos requeridos desde el punto de vista teórico para explicar las observaciones. Ello ha motivado que se estudiase la propagación del chorro tras haber alcanzado la superficie de la estrella. Naturalmente, dado que nuestro modelo inicial unicamente cubría la estrella progenitora propiamente dicha, ha sido necesario incluir una atmósfera *ad hoc*, cuyas características no se ajustan exactamente a las que cabría esperar en la atmósfera de una estrella Wolf-Rayet (modelo inicial). No obstante, el perfil de la atmósfera (primero gaussiano y enlazando después con una región uniforme) permite estudiar la evolución del chorro tanto en un ambiente progresivamente más diluido y rarificado como en un medio uniforme.

Los principales resultados del análisis de la propagación a través del medio externo son que se produce una mayor acelerción tanto del fluido del haz como de la onda de choque delantera del chorro. Esta aceleración es mayor en la dirección lateral que en la longitudinal (respecto al eje del chorro), tal como se espera teóricamente. Cabe señalar, sin embargo, que nuestras simulaciones sólo cubren una parte pequeña de la evolución de una ERG (de hecho, considerando distancias de propagación, sólo alcanzan entre la décima y la centésima parte de la distancia carácterística a partir de la cual comienzan a ser detectables), por tanto, la extrapolación de nuestros resultados debe ser hecha cuidadosamente. No obstante, es de señalar que la viabilidad del modelo de collapsar como progenitor de erupciones de rayos gamma, depende fuertemente del ritmo de deposición de energía y del perfil del gradiente del medio que rodee a la estrella Wolf-Rayet a través del cual este *proto-ERG* se propaga.

Chapter 2

GENESIS: A high–resolution code for 3D RHD

2.1. Introduction

Numerical relativistic hydrodynamics (RHD) has experienced an important step forward in recent years when modern high–resolution shock–capturing (HRSC) techniques began to be applied to solve the equations of RHD in conservation form. Prior to the advent of HRSC techniques the field was dominated for more than one decade by Wilson (1979)'s approach to relativistic hydrodynamics. This approach relies on the use of artificial viscosity in order to handle the discontinuities (shocks, contact discontinuities, etc.) that may appear in the flow numerically. However, techniques based on artificial viscosity are prone to severe numerical difficulties when simulating ultrarelativistic flows (see, e.g., Centrella & Wilson 1984). Using modern HRSC techniques instead, these difficulties are overcome (see, e.g., Donat *et al.* 1998) allowing one to simulate challenging relativistic astrophysical phenomena like, e.g., relativistic jets or gamma-ray bursts (GRB hereafter).

The need for a relativistic treatment in the framework of astrophysical jets is justified because flow velocities as large as 99.5% of the speed of light (Lorentz factors > 10) are required – according to the nowadays accepted standard model (see 3.1.2) – to explain the apparent superluminal motion observed at parsec scales in many jets of extragalactic radio sources associated to active galactic nuclei. Similar arguments applied to the galactic superluminal sources GRS1915+105 (Mirabel & Rodriguez 1994) and GROJ1655–40 (Tingay et al. 1995) allow one to infer intrinsic velocities of $\approx 0.9c$ in the jets of these sources. Further independent indication of highly relativistic speeds can be inferred from the intraday variability occurring in more than a quarter of all compact extragalactic radio sources (Krichbaum, Quirrenbach & Witzel 1992). If the observed intraday radio variability is intrinsic and results from incoherent synchrotron radiation (according to Begelman, Rees & Sikora 1994), the associated jets must have bulk Lorentz factors in the range $\sim 30 - 100$.

Another astrophysical phenomenon which also involves flows with velocities very close to the speed of light are the GRBs. The standard fireball model (see 4.1.1) assumes that the fireball that originates the GRB is accelerated to reach Lorentz factors $> 10^2$ (Cavallo & Rees 1978; Piran, Shemi & Narayan 1993). In addition to this high velocities, the thermodynamics of the GRB production needs a relativistic treatment (for example, the energies involved in the GRB production are ~ 1 MeV per particle –Rees 1997–), which for practical purposes means that a consistent relativistic equation of state (EOS) must be used. Furthermore, this relativistic thermodynamics is closely linked to the dynamical evolution of any relativistic plasma, governed by the RHD equations, through the value of the enthalpy as was pointed out by Martí *et al.* (1997) in the context of relativistic jets.

In the following we describe the main features of a special relativistic 3D hydrodynamic code, which is based on explicit HRSC methods, and which is a considerably extended version of the special relativistic 2D hydrodynamic code developed by Martí, Müller & Ibáñez (1994) and by Martí *et al.* (1995). The code has been designed modularly which allows one to use different reconstruction algorithms and Riemann solvers. As it is the final goal of our work to simulate relativistic jets and GRBs in three spatial dimensions, the code has successfully been subjected to an intensive testing in the ultrarelativistic regime (see Section (2.4)). In particular, GENESIS has successfully passed the spherical shock reflection test (simulated in 3D Cartesian coordinates) involving flow Lorentz factors larger than 700 (see §(2.4.3)).

The chapter is organized as follows. In Section (2.2), we introduce the 3D equations of RHD in Cartesian coordinates in differential and discretized forms.

The latter have been implemented into our 3D RHD code GENESIS. Detailed information about the structure and the main features of the code is given in Section (2.3). Several 1D, 2D and 3D relativistic test problems computed with GENESIS are described in Section (2.4). The performance of GENESIS on scalar and multiprocessor computers is analyzed in Section (2.5).

A summary of the chapter containing our main conclusions can be found in Section (2.6). In Appendix A, we give the spectral decomposition of the three dimensional system of RHD equations with explicit expressions for the eigenvalues and the right- and left-eigenvectors. Appendix B shows how to get an efficient implementation of flux formulae in multidimensional relativistic hydrodynamical codes paying special attention to the explicit formulae for the numerical viscosity of Marquina's (Donat & Marquina 1996) flux formula. The Appendix C describes the explicit algorithm to recover the primitive variables form the conserved ones.

2.2. Equations of RHD in conservation form

The evolution of a relativistic perfect fluid is described by five conserved quantities: rest mass density, D, momentum density, $\mathbf{S}$, and energy density, τ (all of them measured in the laboratory frame and in natural units, i.e., the speed of light $c = 1$),

$$
\begin{aligned}
D &= \rho W && (2.1)\\
S^j &= \rho h W^2 v^j \quad (j = 1, 2, 3) && (2.2)\\
\tau &= \rho h W^2 - p - \rho W, && (2.3)
\end{aligned}
$$

where the Lorentz factor $W = (1-\mathrm{v}^2)^{-1/2}$ and $\mathrm{v}^2 = \delta_{ij} v^i v^j$ (the Einstein summation convention is used here, and δ_{ij} is the Kronecker symbol). Furthermore, ρ is the rest–mass density, p the pressure and h the specific enthalpy given by $h = 1+\varepsilon+p/\rho$ with ε being the specific internal energy. The components of the vector of variables $\mathbf{w} \equiv (\rho, v^i, \varepsilon)^T$ are called *primitive* or physical variables.

The relativistic Euler equations form a system of conservation laws (see, e.g., Font *et al.* 1994) which can be written in Cartesian coordinates as

$$\frac{\partial D}{\partial t} + \sum_{j=1}^{3} \frac{\partial}{\partial x^j}(Dv^j) = 0 \tag{2.4}$$

$$\frac{\partial S^i}{\partial t} + \sum_{j=1}^{3} \frac{\partial}{\partial x^j}(S^i v^j + \delta^{ij} p) = 0 \qquad \text{(i=1, 2, 3)} \tag{2.5}$$

$$\frac{\partial \tau}{\partial t} + \sum_{j=1}^{3} \frac{\partial}{\partial x^j}(S^j - Dv^j) = 0 \tag{2.6}$$

or, equivalently, as

$$\frac{\partial \mathbf{U}}{\partial t} + \sum_{i=1}^{3} \frac{\partial \mathbf{F}^i}{\partial x^i} = 0\,, \tag{2.7}$$

where the vector of unknowns $\mathbf{U}$ (i.e., the conserved variables) is given by

$$\mathbf{U} = \left(D,\ S^1,\ S^2,\ S^3,\ \tau\right)^T\ , \tag{2.8}$$

and the fluxes are defined by

$$\mathbf{F}^i \ = \ \left(Dv^i, S^1 v^i + p\delta^{1i}, S^2 v^i + p\delta^{2i}, S^3 v^i + p\delta^{3i}, S^i - Dv^i\right)^T\ . \tag{2.9}$$

The system (2.7) of partial differential equations is closed with an equation of state $p = p(\rho, \varepsilon)$. Anile (1989) has shown that system (2.7) is hyperbolic for causal equations of state, i.e., for those where the local sound speed, c_s, defined by

$$hc_s^2 = \frac{\partial p}{\partial \rho} + (p/\rho^2)\frac{\partial p}{\partial \epsilon}, \tag{2.10}$$

satisfies $c_s < 1$.

The structure of the characteristic fields corresponding to the nonlinear system of conservation laws (2.7) has explicitly been derived in Donat *et al.* (1998) and is summarised in Appendix A.

In order to evolve system (2.7) numerically, one has to discretize the state vector $\mathbf{U}$ within computational cells. The temporal evolution of the state vector is determined by the flux balance across the zone interfaces of each cell and the contribution of source terms. Using a method of lines (see, e.g., LeVeque 1991), our discretization reads

$$\begin{aligned}\frac{d\mathbf{U}_{i,j,k}}{dt} &= -\frac{1}{\Delta x}\left(\tilde{\mathbf{F}}^x_{i+\frac{1}{2},j,k} - \tilde{\mathbf{F}}^x_{i-\frac{1}{2},j,k}\right) - \frac{1}{\Delta y}\left(\tilde{\mathbf{F}}^y_{i,j+\frac{1}{2},k} - \tilde{\mathbf{F}}^y_{i,j-\frac{1}{2},k}\right) \\ &\quad -\frac{1}{\Delta z}\left(\tilde{\mathbf{F}}^z_{i,j,k+\frac{1}{2}} - \tilde{\mathbf{F}}^z_{i,j,k-\frac{1}{2}}\right) + \mathbf{S}_{i,j,k} \equiv L(\mathbf{U})\,, \end{aligned} \tag{2.11}$$

where Latin subscripts i, j and k refer to the x, y and z coordinate direction, respectively. $\mathbf{U}_{ijk}$ and $\mathbf{S}_{i,j,k}$ are the mean values of the state and source vector (if non zero) in the corresponding three-dimensional cell, while $\tilde{\mathbf{F}}^x_{i\pm\frac{1}{2},j,k}$, $\tilde{\mathbf{F}}^y_{i,j\pm\frac{1}{2},k}$ and $\tilde{\mathbf{F}}^z_{i,j,k\pm\frac{1}{2}}$ are the numerical fluxes at the respective cell interface. Finally, $L(\mathbf{U})$ is a short hand notation of the spatial operator in our method.

At this stage, our system of conservation laws is a system of ordinary differential equations which can be integrated with a large number of algorithms. We have chosen a multi-step Runge–Kutta (RK) method developed by Shu & Osher (1988) which can provide second (RK2) and third (RK3) order in time. The explicit form of the algorithms is (subindexes (i,j,k) are ommited to clarify the notation):

1. Prediction step (common for both RK2 and RK3):

$$\mathbf{U}^{(1)} = \mathbf{U}^n + \Delta t L(\mathbf{U}^n) \tag{2.12}$$

2. Depending on the order do:

   - RK2:

$$\mathbf{U}^{n+1} = \frac{1}{\alpha}\left(\beta\mathbf{U}^n + \mathbf{U}^{(1)} + \Delta t L(\mathbf{U}^{(1)})\right), \tag{2.13}$$

     being $\alpha = 2$ and $\beta = 1$.

   - RK3:

$$\begin{aligned}\mathbf{U}^{(2)} &= \frac{1}{\alpha}\left(\beta\mathbf{U}^n + \mathbf{U}^{(1)} + \Delta t L(\mathbf{U}^{(1)})\right) \\ \mathbf{U}^{n+1} &= \frac{1}{\beta}\left(\beta\mathbf{U}^n + 2\mathbf{U}^{(2)} + 2\Delta t L(\mathbf{U}^{(2)})\right), \end{aligned} \tag{2.14}$$

$$\tag{2.15}$$

     in this case, $\alpha = 4$ and $\beta = 3$.

2.3. The relativistic hydrodynamic code GENESIS

2.3.1. Code structure

The special relativistic multidimensional hydrodynamic code GENESIS described in detail in the following is a 3D extension of the 2D HRSC hydrodynamic code developed by some of the authors. The 2D code has been successfully used for the simulation of relativistic jets (Martí *et al.* 1994, 1995, 1997; Gómez *et al.* 1995, 1997). The main structural features of Martí *et al.*'s code has been kept, but there are important changes in the computational part. Besides the addition of the third spatial dimension, a large effort has been made to *minimise memory requirements* and to *optimize the performance* of the code as well as to enhance its *portability*.

Like its predecessor, GENESIS evolves the equations of RHD in conservation form using a finite volume approach in Cartesian coordinates. In accordance with the method of lines, we split the discretization process in two parts. First, we only discretize the differential equations in space, i.e. the problem remains continuous in time. This leads to a system of ordinary differential equations (ODEs) in time (2.11). The numerical fluxes between adjacent cells required for the time integration are obtained by solving the appropriate 1D Riemann problems along the coordinate directions (spatial sweeps). High-order spatial accuracy is achieved by applying a high-order interpolation procedure in space, while high-order accuracy in time is obtained by using high-order ODE solvers.

GENESIS integrates the 3D RHD equations on uniform grids in each spatial direction. In order to have a flexible code GENESIS is programmed to allow for different boundary conditions, spatial reconstruction algorithms, Riemann solvers, ODE solvers for the time integration and external forces. The user selects these options at the preprocessor level, which reduces the number of *if*–clauses inside the nested 3D loops to a minimum, and thereby maximizing the code's efficiency.

Making the selection at the preprocessing stage has allowed us to obtain a code, which is independent of a specific (shared memory) machine architecture. Hence, it runs on different types of machines and processors. Up to now, we have tested GENESIS on SGI platforms (INDY workstations, Power Challenge and Cray-Origin 2000 arrays), on HP machines (712 workstations and J280 computers), and on a

CRAY-JEDI multiprocessor system. As a next step we plan to port GENESIS on a CRAY-T3E massively parallel computer.

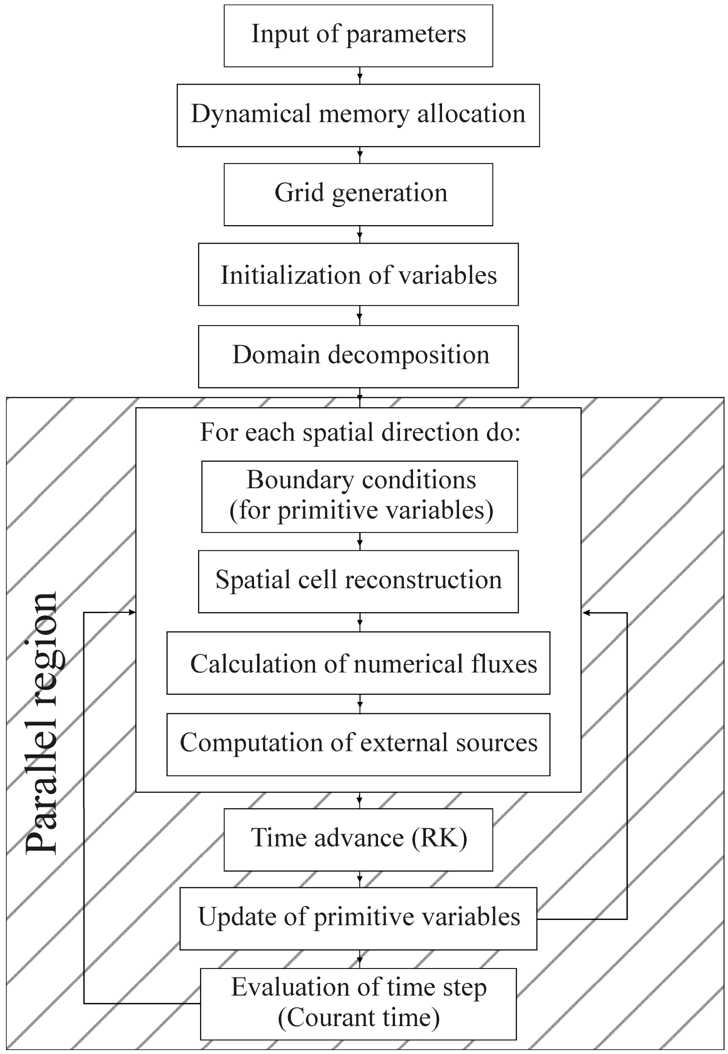

Fig. 2.1.— Flow diagram of GENESIS.

The flow diagram of GENESIS is shown in figure 2.1. Details of the major components of GENESIS are discussed in the following subsections.

2.3.2. Memory requirements

The current version of GENESIS, which is written in FORTRAN 90 has the capability of allocating memory *dynamically*, i.e. the number of computational cells can be chosen at run time. Reducing the RAM requirements of a 3D hydrodynamic code is obviously crucial. In GENESIS multidimensional variables are responsible for about 99% of the code's memory requirement. Thus, the number of these 3D arrays has to be kept at the absolute minimum possible. In its present version, GENESIS only requires three sets of five 3D arrays each, consisting of one set of conserved variables at the beginning of each time level ($\mathbf{U}^n$), another set of primitive variables and a third set of scratch variables ($\tilde{\mathbf{U}}$). The time integration scheme (eqs. 2.12–2.14) which results in the updated values of the conserved variables at the next time level ($\mathbf{U}^{n+1}$) then reads:

1. Prediction step (common for RK2 and RK3):

$$\tilde{\mathbf{U}} = \mathbf{U}^n + \Delta t L(\mathbf{U}^n)$$

2. Depending on the order of accuracy of the time integration scheme do:

RK2:

$$\begin{aligned} \tilde{\mathbf{U}} &= \tilde{\mathbf{U}} + \Delta t L(\tilde{\mathbf{U}}), \\ \mathbf{U}^{n+1} &= \frac{1}{\alpha}\left(\beta \mathbf{U}^n + \tilde{\mathbf{U}}\right), \end{aligned}$$

with $\alpha = 2$ and $\beta = 1$, or

RK3:

$$\begin{aligned} \tilde{\mathbf{U}} &= \tilde{\mathbf{U}} + \Delta t L(\tilde{\mathbf{U}}), \\ \tilde{\mathbf{U}} &= \frac{1}{\alpha}\left(\beta \mathbf{U}^n + \tilde{\mathbf{U}}\right), \\ \tilde{\mathbf{U}} &= \tilde{\mathbf{U}} + \Delta t L(\tilde{\mathbf{U}}), \\ \mathbf{U}^{n+1} &= \frac{1}{\beta}\left(\beta \mathbf{U}^n + 2\tilde{\mathbf{U}}\right), \end{aligned}$$

with $\alpha = 4$ and $\beta = 3$.

Quantities like entropy, internal energy, sound speed or Lorentz factor are implemented as FORTRAN scalars. Consequently, GENESIS needs about 1 Gbyte of RAM memory to handle a grid of $100 \times 100 \times 720$ (in double precision).

2.3.3. Domain decomposition

The technique of domain decomposition is used to optimize the parallelization of the code and to guarantee its performance in real applications, too. It is also the first step towards the development of a parallel version of GENESIS which runs efficiently on parallel computers with distributed memory.

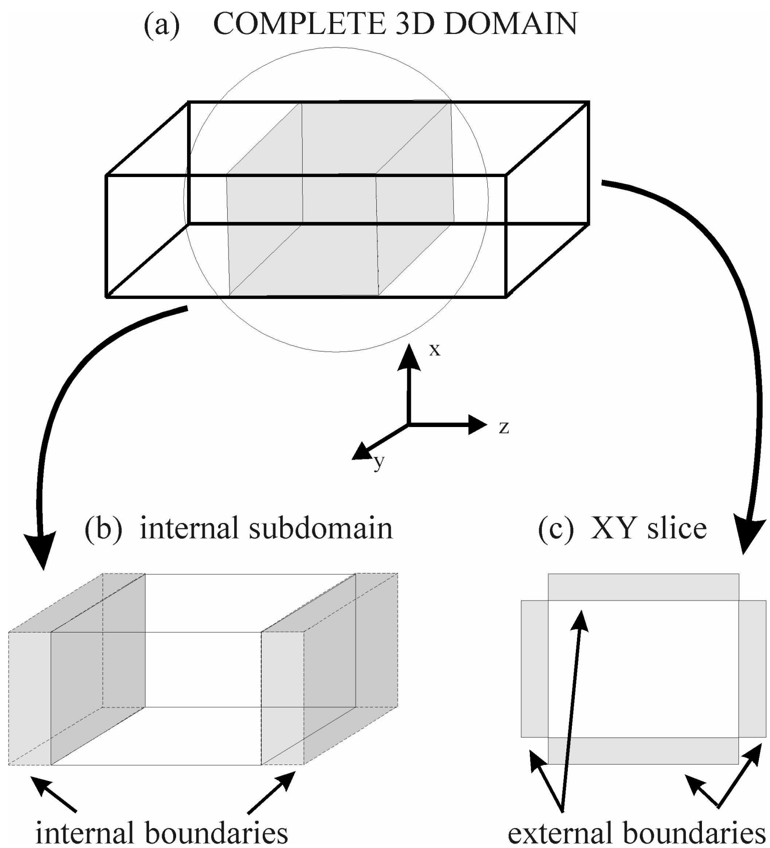

Fig. 2.2.— (a) Complete three dimensional computational domain, showing a typical subdomain (in grey). (b) Zoom of the previous subdomain including its internal boundaries. These regions overlap with contiguous subdomains. (c) Cut through the computational grid along the X-Y plane displaying the external boundaries.

The physical domain is split along *one* arbitrary spatial direction (z, in the present version) in a set of subdomains (i.e. *slices*, see Fig. 2.2a) of similar computational load. The subdomains are then distributed across processors. Numerical fluxes at subdomain boundaries are calculated by providing the appropriate internal and external boundary conditions (see Fig. 2.2b,c, respectively, and § 2.3.4).

2.3.4. Boundary conditions

The computational grid is extended in each coordinate in positive and negative direction by four so-called *ghost* zones, which provide a convenient way to implement different types of boundary conditions. These boundary conditions have to be provided in each spatial sweep for all primitive variables. In GENESIS several types of boundary conditions are available including reflecting, inflow, outflow, time-dependent and analytically prescribed boundary conditions.

Flow conditions at subdomain boundaries must be provided, too, in order to calculate numerical fluxes at subdomain interfaces. Hence, subdomains are also enlarged by four ghost zones in each coordinate direction. Note that these ghost zones do overlap with adjacent subdomains (see Fig. 2.2). The internal boundary conditions in these overlapping regions are defined by copying the corresponding values of the respective adjacent subdomain. For NS subdomains and $NX \times NY \times NZ$ computational zones the number of overlapping cells is $(4+4) \times (NS-1) \times NX \times NY$, i.e. the fraction of overlapping cells is $8 \times (NS-1)/NZ$. Hence, for $NS = 16$ and $NZ = 1000$ (typical of a jet simulation) the fraction of overlapping cells is about 12%.

2.3.5. Spatial reconstruction

In order to improve the spatial accuracy of the code, we interpolate the values of the pressure, the proper rest–mass density and the spatial components of the four–velocity (Wv^i) within computational cells. These reconstructed variables are afterwards used to compute the numerical fluxes. Because of the monotonicity of the reconstruction procedures (see below) used in GENESIS, the occurrence of unphysical (i.e., negative) values in the reconstructed profiles of pressure and density are avoided. In addition, reconstructing the spatial components of the four-velocity with monotonic schemes, also prevents the occurrence of unphysical values of the flow velocity, i.e., the flow velocity always remains smaller than the speed of light even in multidimensional calculations.

GENESIS provides, at the preprocessing level, four different types of reconstruction schemes: piecewise constant, linear using the minmod function of Van Leer (1979), parabolic using the piecewise parabolic method, PPM, of Colella & Woodward (1984; see also Martí & Müller 1996) or hyperbolic using the piecewise hyperbolic method, PHM, of Marquina (1994).

2.3.6. Source terms

Gravity, local radiative processes, etc., are coupled with hydrodynamics through terms on the right hand side of the RHD equations (i.e., via the source terms, $\mathbf{S}_{i,j,k}$, in Eq. (2.11)). GENESIS integrates such terms assuming piecewise constant profiles for the source functions.

2.3.7. Computation of the numerical fluxes

In this paper we use a variant of Marquina's flux formula (see Donat & Marquina 1996) which has already been shown to work properly in the simulation of relativistic jets in 2D (Martí *et al.* 1997).

The approach followed by Donat & Marquina (1996) relies on the extension of the entropy–satisfying scalar numerical flux of Shu & Osher (1989) to hyperbolic systems of conservation laws. Given the spectral decomposition of the RHD equations (see Appendix A), the implementation of Marquina's scheme is straightforward.

The original Marquina's algorithm computes the contribution to the numerical viscosity of each characteristic field in a different way depending on whether the corresponding eigenvalue (characteristic speed) does change its sign between the left and right states or whether it does not. However, instead of using the original algorithm, we only consider that part which corresponds to characteristic speeds changing their signs between the left and right states of every numerical interface. The modified algorithm has a larger numerical viscosity, but it is more stable and does not involve any *if*-clause. Hence, it can easily be vectorized.

In the 2D version used in Martí *et al.* (1997) the left eigenvectors of the Jacobians are calculated numerically by inverting the matrix of right eigenvectors. In GENESIS we use the analytical expressions for the left eigenvectors, which allow one to simplify the computation of the numerical viscosity terms.

The explicit expressions for the numerical fluxes ($\tilde{\mathbf{F}}^i$, $i \in x, y, z$ in Eq. 2.11) as a function of the local (reconstructed) primitive and conserved variables are given in Appendix B. Besides its influence on the efficiency of the code, the use of explicit expressions for the left eigenvectors also leads to analytical cancellations in the computation of the numerical viscosity causing a damping of the growth of round-off errors and an improvement of the overall accuracy of the code. Previous versions of GENESIS, in which numerical fluxes were calculated without the use of analytical expressions, suffered from a growth of round-off errors due to the large number of operations involved and due to the finite precision of floating point arithmetics. This growth of errors manifests itself in a gradual loss of symmetry in initially perfectly symmetric problems. Our experience shows that the analytical manipulation of the expressions of the numerical flux together with their appropriate symmetrization (i.e., using commutating formulas for the components of the velocity parallel to cell interfaces) allows one to achieve a perfect numerical symmetry (see §2.3.10 and §2.4.2).

2.3.8. Time advance and time step computation

Time integration is carried out by two different total variation diminishing RK methods developed in Shu & Osher (1988). The user can choose, at preprocessing level, between the RK2 and RK3 algorithm (see eqs. 2.12–2.14). Results of similar quality can be obtained either with the RK3 algorithm or with RK2 using smaller time steps. Nevertheless, for a given time step, the computational cost of RK3 is about a factor 1.5 larger than that of RK2.

As in any explicit hydrodynamic code, time steps are limited for stability reasons by the Courant-Friedrichs-Levy (CFL) condition, which is computed using the characteristic speeds. At the end of each time step the size of the new time step is determined as the minimum of the time steps of all subdomains. This requires a global operation across all subdomains. Experience has shown that acceptable CFL numbers lie in the interval $[0.1, 0.8]$. CFL numbers larger than 0.8 can lead to post shock oscillations.

2.3.9. Recovering primitive variables

The solution of the Riemann problem requires knowledge of the value of the pressure and its thermodynamic derivatives. Given the functional dependence between conserved and primitive variables (see eq. (2.2)), the recovering procedure can not be formulated in closed form. Instead a kind of iterative method must be used, which is very time consuming. Hence, usage of the recovering procedure should be reduced to the absolute minimum. Therefore, primitive variables are consistently updated from the mean values of the conserved variables after each Runge-Kutta step and their values are stored in a set of 3D arrays.

Our approach is the same as that of Martí, Ibáñez & Miralles (1991) and that of Martí *et al.* (1997). Its explicit form can be found in Appendix C (see also Martí & Müller 1996). The iterative recovering procedure is based on a second order accurate Newton-Raphson method to solve an implicit equation for the pressure.

In zones where the flow conditions change smoothly the typical number of iterations ranges from 1 to 3 when a relative accuracy of 10^{-10} is requested. There exist zones, however, inside shocks or near strong gradients, where the number of iterations required is larger depending on the strength of the shock or the steepness of the gradient. For example, in the shock reflection test in 3D, the shock zone needs about 4 to 8 iterations.

2.3.10. Some notes on code structure

We have taken special care in designing a numerical code that accurately preserves any symmetries present in the initial data. This is an important point for a code aimed to study, for example, the stability and long term evolution of initially axisymmetric jets.

There exist two potential sources of numerical *asymmetries* in our code, both of them are related to the fact that floating point arithmetics is not associative. One cause of asymmetries is due to the computation of numerical fluxes in spatial sweeps, which violates what we call henceforth *sweep–level symmetry* (SLS). In order to guarantee SLS the expressions by which the numerical fluxes are evaluated have been symmetrized (see §2.3.7).

A second source of (numerically caused) asymmetry arises specifically in 3D codes using directional splitting. It can only be avoided, if the code has a property which we call *sweep–coherence symmetry* (SCS). It refers to the symmetry of the integration algorithm with respect to the order in which the 1D-sweeps are performed. This symmetry property of the algorithm becomes crucial if an initially spherically symmetric state is considered. We found that its initial symmetry is lost unless special care is taken in the calculation of the Lorentz factor (in the numerical flux routine), which involves the summation of the squares of the three velocity components. To guarantee a perfect sweep–coherence symmetry of the algorithm the addition of the vector components has to be performed in a cyclic manner, i.e. in the X–sweep the components are summed up in x, y, z order, in the Y–sweep in y, z, x order, and finally in the Z–sweep in z, x, y order. Due to the stochastic nature of round-off errors, a violation of the sweep–coherence symmetry manifests itself only in the last few significant digits of the state variables, if the number of time steps is not too large (less than about 3000; see section §2.4.3).

Given that round–off errors grow sufficiently slow and that they do not interact with the truncation errors due to the finite difference scheme (which can render the scheme *unstable*), GENESIS does keep the symmetry of an initial state at an acceptable level. We have also tried to develop a version of GENESIS with a perfect 3D symmetry (limited by the Cartesian discretization). For this purpose, we applied the *extended partial precision* technique in the computation of expressions in which the associative property should be satisfied. The procedure was successful, but increased the total computational costs by more than 30%. All the results presented in the following have been obtained without making use of such a technique.

2.4. Code Testing

The capabilities of GENESIS to solve problems in special relativistic hydrodynamics are checked by means of three tests calculations that involve strong shocks and a wide range of flow Lorentz factors. In these test runs an ideal gas equation of state with an adiabatic exponent γ has been used. All results presented in this section have been obtained with the PPM reconstruction procedure and the relativistic Riemann solver based on Marquina's flux formula (see previous section for details).

2.4.1. Mildly Relativistic Riemann Problem (MRRP)

In the first test we consider the time evolution of an initial discontinuous state of a fluid at rest. The initial state is given by $\rho_L = 10$, $\epsilon_L = 2$, $v_L = 0$, $\gamma_L = 5/3$, $\rho_R = 1$, $\epsilon_R = 10^{-6}$, $v_R = 0$ and $\gamma_R = 5/3$, where the subscript L (R) denotes the state to the left (right) of the initial discontinuity. This test problem has been considered by several authors in the past (in 1D by Hawley, Smarr & Wilson 1984, Schneider *et al.* 1993, Martí & Müller 1996, Wen, Panaitescu & Laguna 1997; in 2D by Martí *et al.* 1997). It involves the formation of an intermediate state bounded by a shock wave propagating to the right and a transonic rarefaction propagating to the left. The fluid in the intermediate state moves at a mildly relativistic speed ($v = 0.72c$) to the right. Flow particles accumulate in a dense shell behind the shock wave compressing the fluid by a factor of 5 and heating it up to values of the internal energy much larger than the rest-mass energy. Hence, the fluid is extremely relativistic from a thermodynamical point of view, but only mildly relativistic dynamically.

To change this intrinsically one dimensional test problem into a multidimensional one we have rotated the initial discontinuity (normal to the x-axis) by an angle of 45^o around the y-axis, and then again by an angle of 45^o around the z-axis. Gas states L and R are placed within a cube of major diagonal equal to 1 that constitutes the 3D numerical grid.

The analytical solution to this test problem can be found in Martí & Müller (1994). Our analysis is restricted to the flow conditions along the major diagonal of the numerical grid, which is normal to the initial discontinuity. Figure 2.3 shows the solution along the major diagonal at time $t = 0.5$. The shock is captured in two to three zones in accordance with the capabilities of HRSC methods. The transonic rarefaction has a smooth profile across the sonic point located at $x = 0.5$, and exhibits sharp corners. The contact discontinuity is spread out over roughly three zones.

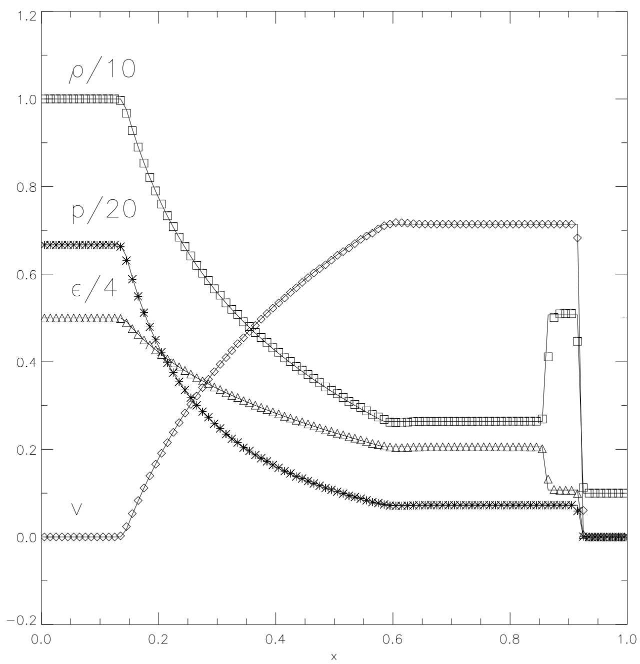

Fig. 2.3.— Numerical and exact solution of the mildly relativistic Riemann test problem (MRRP) described in the text after 0.5 time units. The computed one–dimensional distributions of proper rest–mass density, pressure, specific internal energy and flow velocity are shown, in normalized units, with discrete symbols. Continuous lines depict the corresponding exact solution. The simulation was performed on a grid of 100^3 zones. The CFL number was set equal to 0.6 and a second–order Runge-Kutta was used for time integration.

Cells	Pressure	Density	Velocity
40^3	8.0(2.0)E–2	1.1(0.3)E–1	0.9(0.4)E–2
60^3	5.2(0.4)E–2	9.8(0.8)E–2	1.1(0.3)E–2
80^3	4.5(0.2)E–2	9.2(0.5)E–2	1.1(0.1)E–2
100^3	3.7(0.4)E–2	7.0(0.9)E–2	7.0(2.0)E–3
150^3	2.5(0.2)E–2	4.8(0.7)E–2	5.0(2.0)E–3

Table 2.1: Absolute global errors (L_1 norm) of the primitive variables for the mildly relativistic Riemann test problem (MRRP) for different grids at $t = 0.5$. As the errors are dominated by those zones located inside the shock and as the grid resolution is still poor even on the finest grid, we have repeated every calculation four times varying t within an interval $t \pm \delta t$ (δt being of the order of one Courant time) and calculated the mean errors. In parentheses we give the standard root mean square deviation of the errors ($\sigma_{\text{n-1}}$).

The absolute global errors[1] of pressure, density and velocity are given in Table 2.1 for different grid resolutions at $t = 0.5$. Table 2.1 implies a convergence rate of slightly less than 1 when comparing the errors obtained on the coarsest (40^3) and the largest (150^3) grid. This behavior is expected for multidimensional problems involving discontinuities (see, e.g. LeVeque 1991).

2.4.2. Relativistic Planar Shock Reflection (RPSR)

This 1D test problem involves the propagation of a strong shock wave generated when two cold gases, moving at relativistic speeds in opposite directions, collide. The problem has been considered as a test for almost any new relativistic hydrodynamic code (Centrella & Wilson 1984; Hawley, Smarr & Wilson 1984; Martí & Müller 1994;

[1]in L_1 norm given by $\epsilon_{\text{abs}} = \sum_{i,j,k} \left|\mathbf{w}^n_{i,j,k} - \mathbf{w}(\mathbf{x}_{i,j,k}, t_n)\right| \Delta x_i \Delta y_j \Delta z_k$, where $\mathbf{w}^n_{i,j,k}$ and $\mathbf{w}(\mathbf{x}_{i,j,k}, t_n)$ are the numerical and exact solution, respectively

Eulderink & Mellema 1994; Falle & Komissarov 1996).

After the collision of the two gases, two shock waves are created in the plane of symmetry of the physical domain propagating in opposite directions. The inflowing gas is heated in the shocks and comes to a rest. The exact solution of this Riemann problem was obtained by Blandford & McKee (1976).

The initial data are $\rho_L = 1$, $\epsilon_L = 2.29\,10^{-5}$, $v_L = v_i$, $\rho_R = 1$, $\epsilon_R = 2.29\,10^{-5}$ and $v_R = -v_i$, where v_i is the inflow velocity of the colliding gas.

Figure 2.4 shows the numerical solution at $t = 2.0$ on the left half of a grid having a total of 401 zones. The results obtained in the right half of the grid are strictly symmetric with respect to the collision point ($x = 0$), i.e., the sweep–level symmetry (SLS; see section §2.3.10) is exactly fulfilled. Near $x = 0$, the numerical solution shows small errors (of the same order as the mean error in the post-shock state, 0.3%) which are due to the *wall heating* phenomenon (Noh 1987) characterized by an overshooting of the internal specific energy and an undershooting of the proper rest-mass density.

In Table 2.2 we give the global absolute errors (L_1 norm) of the primitive variables for different grids at $t = 2.0$ and for an inflow velocity $v_i = 0.999c$. We find a convergence rate about equal to one (see columns 5-7) for all variables.

We can use this test problem to check the robustness of GENESIS in the ultra-relativistic regime. To simplify notation, we define the quantity $\nu = 1 - v_i$, which tends to zero when v_i tends to one. Table 2.3 contains the relative global errors of the primitive variables at $t = 2.0$ for a set of calculations performed on a grid of 401 zones, where we have varied ν from 10^{-1} to 10^{-11}. The latter value corresponds to a Lorentz factor $W = 2.24 \times 10^5$. The relative error of the primitive variables shows a weak dependence on the inflow velocity. It never exceeds 3.5% and for $\nu \geq 10^{-9}$ it is smaller than 1%.

The PPM parameters (see Colella & Woodward 1984) have been tuned to minimize the number of zones within the shock without introducing unacceptable numerical post–shock oscillations. Fig. 2.5 demonstrates that there are no numerical post-shock oscillations for $\nu \leq 10^{-5}$ when the shock is captured by 2 to 3 zones.

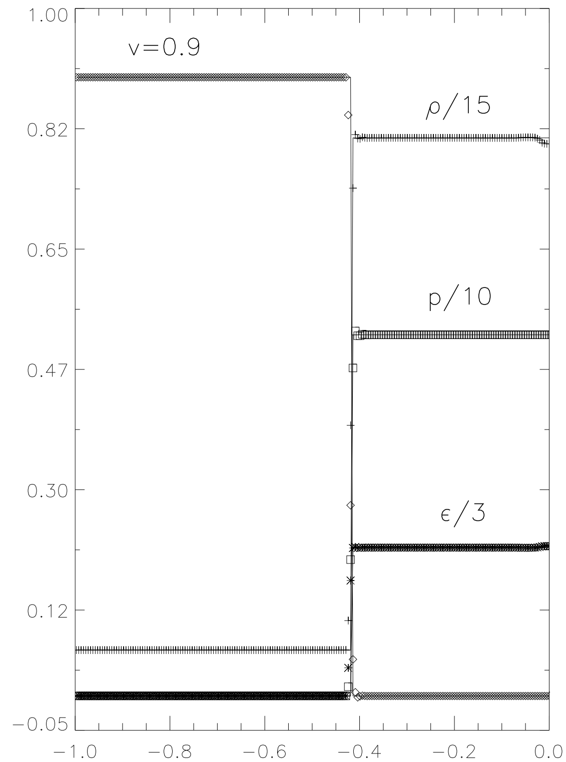

Fig. 2.4.— Numerical and exact solution of the relativistic planar shock reflection problem (RPSR) described in the text after 2.0 time units. The computed distributions of proper rest–mass density, pressure, specific internal energy and flow velocity are shown, in normalized units, with discrete symbols, for an inflow velocity of the colliding gases equal $v_i = 0.9$. Continuous lines depict the corresponding exact solution. The simulation was performed on a grid of 401 zones spanning the interval $[-1, 1]$ with both gases colliding in the middle of the grid at $x = 0$. Only the left half of the grid is shown. The CFL number was set equal to 0.3 and a second–order Runge–Kutta was used for time integration.

2.4.3. Relativistic Spherical Shock Reflection (RSSR)

The initial setup consists of a spherical inflow at speed v_i (which might be ultrarelativistic) colliding at the centre of symmetry of a sphere of radius unity. For a hydrodynamic code in Cartesian coordinates this is a 3D test problem, which allows one to evaluate the directional splitting technique as well as the symmetry

Cells	Pressure	Density	Velocity	r_ρ	r_p	r_v
101	19.3(0.3)E+0	290.8(0.4)E–2	2.4(0.1)E–2			
201	10.8(0.2)E+0	147.2(0.7)E–2	10.1(0.4)E–3	0.99	0.84	1.26
401	49.2(0.7)E–1	85.0(1.0)E–2	92.8(0.8)E–4	0.80	1.14	0.14
801	25.2(0.2)E–1	37.3(0.1)E–2	3.4(0.1)E–3	1.19	0.97	1.44
1601	13.8(0.1)E–1	187.4(0.7)E–3	17.3(0.4)E–4	0.99	0.87	0.98

Table 2.2: Absolute global errors (L_1 norm) of the primitive variables (columns 2-4) and the corresponding convergence rates (columns 5-7) for the relativistic planar shock reflection test problem (RPSR) for different grids at $t = 2.0$. The test runs have been performed with a Courant number equal to 0.1 and the third order accurate Runge-Kutta time integration method (RK3). In parenthesis we give the standard root mean square deviation of the errors (see also Table 2.1).

properties of the algorithm. Figure 2.6 shows the numerical results for $v_i = 0.9c$ on a grid of 101^3 zones at $t = 2.0$. The shock capturing properties of GENESIS, which we have already demonstrated in 1D, are retained in this genuine multidimensional case. Two or three zones are required to handle the shock wave. The pressure and proper rest–mass density have global relative errors of about 12% and 8% respectively.

Ultrarelativistic flows have been explored by increasing the inflow Lorentz factor. Table 2.4 gives the growth of the relative global errors[2] on a fixed grid size of 81^3 zones for v_i in the range $0.9c$ to $0.999999c$ (the latter inflow velocity corresponding to a Lorentz factor $W \approx 707$). The relative global errors are acceptable (considering the inherent difficulty of the test and the resolution of the experiments) and do not grow dramatically with the Lorentz factor. The observed growth can be explained by the fact that the errors are dominated by the shock region and that the shock strength increases with the Lorentz factor.

[2] $\epsilon_{\rm rel} = \epsilon_{\rm abs} / \sum_{i,j,k} |\mathbf{w}(\mathbf{x}_{i,j,k}, t_n)| \; \Delta x_j \Delta y_j \Delta z_k$

ν	Pressure	Density	Velocity
10^{-1}	90.7(0.5)E–4	96.6(0.5)E–4	80.3(0.5)E–4
10^{-3}	58.0(0.8)E–4	72.0(0.8)E–4	12.6(0.1)E–3
10^{-5}	100.3(0.5)E–5	79.3(0.5)E–4	72.0(0.8)E–4
10^{-7}	61.0(0.8)E–4	93.0(0.1)E–4	85.6(0.1)E–4
10^{-9}	65.2(0.1)E–4	103.0(0.1)E–4	81.3(0.5)E–4
10^{-11}	141.0(0.1)E–5	340.1(0.1)E–4	325.7(0.5)E–5

Table 2.3: Relative global errors (L_1 norm) of the primitive variables for the planar shock reflection test problem (RPSR) on a grid of 401 zones at $t = 2.0$. The quantity ν is defined as $\nu = 1 - v_i$. The test runs have been performed with a Courant number equal to 0.1 and the third order accurate Runge-Kutta time integration method (RK3). In parenthesis we give the standard root mean square deviation of the errors (see also Table 2.1).

The CFL factors used in the last two tests of this series are unusually small (0.019 and 0.005) which is due to the strength of the shock and the relatively small grid resolution (compared with the 1D case). It is noticeable that for $v_i = 0.999999c$ the errors are considerably larger (last entry in Table 2.4). This has two reasons. Firstly, the global relative errors decrease with time in the RSSR test problem. Secondly, we could not continue the run with $v_i = 0.999999c$ beyond 1.5 time units, because interaction with the grid boundaries became severe causing the code to crash. Hence, $v_i = 0.999999c$ must be considered as the maximum inflow velocity in the RSSR test problem, which the present code can handle properly (for the resolution used). The symmetry properties of the RSSR solution are very well maintained by GENESIS, even though the number of timesteps was very large ($>$ 30000) in the last two test runs.

The absolute global errors (L_1 norm) and the convergence rates of the primitive variables at $t = 2.0$ are displayed in Table 2.5. Obviously, the errors are much larger in the 3D test than in the corresponding 1D one. This can be explained considering

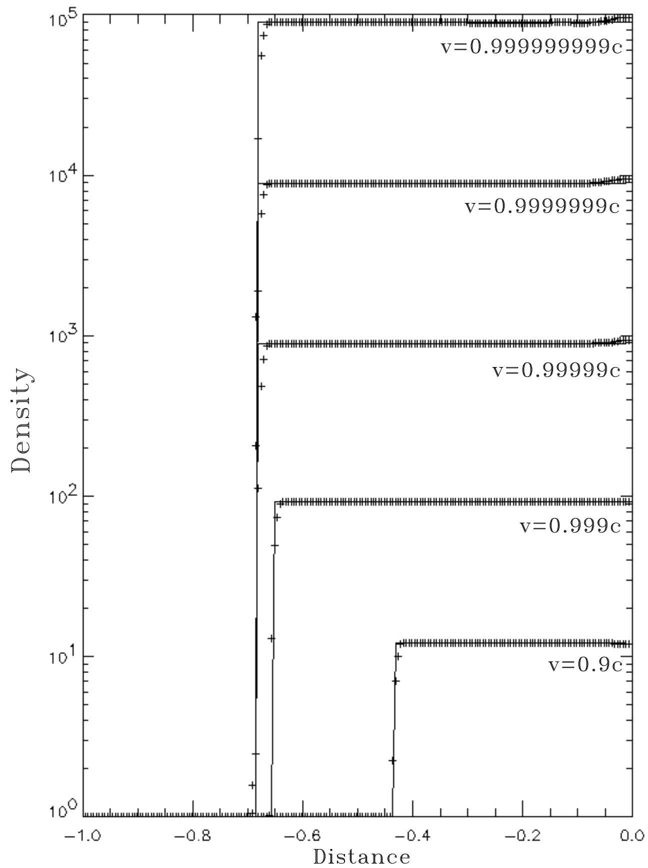

Fig. 2.5.— Density jump (in logarithmic scale) for different inflow velocities in the relativistic planar shock reflection problem (RPSR), over an equally spaced grid of 401 zones at $t = 2.0$. As in the previous Figure, only the left half of the grid is shown. Solid lines represent the exact solution while symbols refer to numerical values. A third–order Runge–Kutta was used for time integration.

that (i) the grids are coarser than in 1D, and that (ii) the jumps in pressure and density across the shock are nearly a factor of 30 larger in the 3D test than in the planar case.

The preservation of the sweep-level symmetry (SLS; see section §2.3.10) is reflected in the symmetry of the one dimensional profiles in Fig. 2.6. Moreover, a comparison of the profiles in X and Y direction in Fig. 2.6 shows the capability of

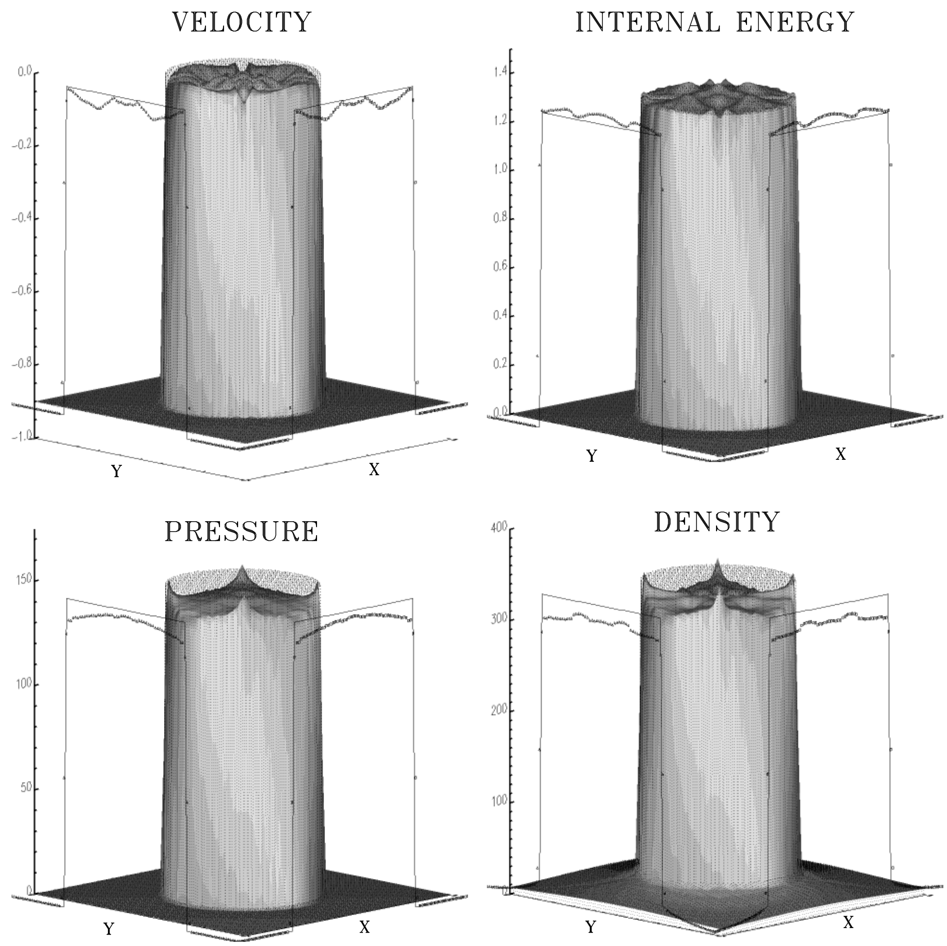

Fig. 2.6.— Intensity plots of proper rest–mass density, pressure, specific internal energy and flow velocity over the plane XY at $z = 0$ in the relativistic spherical shock reflection test problem (RSSR) described in the text, after 2.0 time units. Shaded surfaces represent the numerical results while dotted surfaces are the exact solution. One dimensional plots along X and Y axes are projected on the front sides of the pictures. Symbols inside the one dimensional plots are numerical values; solid lines represent the exact solution on the same axis. The test was ran using a CFL equal to 0.2 and a third–order Runge–Kutta for time integration.

ν	Pressure (%)	Density (%)	Velocity (%)
10^{-1}	15.8	10.5	0.82
10^{-3}	19.9	22.1	3.07
10^{-5}	22.1	27.8	3.89
$10^{-6 (a)}$	32.2	39.1	1.91

Table 2.4: Growth of relative global errors of the primitive variables for the relativistic spherical shock reflection test problem (RSSR) for different inflow velocities at $t = 2.0$. The four test runs have been performed with RK3 and Courant numbers 0.1, 0.1, 0.019 and 0.005, respectively. The quantity ν has the same meaning as in Table 2.3.

[a] The run time for this test is 1.5.

Cells	Pressure	Density	Velocity	r_ρ	r_p	r_v
41^3	11.8(0.2)E+0	30.3(0.4)E+0	80.0(3.0)E–3			
61^3	76.5(0.7)E–1	20.1(0.2)E+0	55.8(0.6)E–3	1.09	1.03	0.91
81^3	57.5(0.8)E–1	15.5(0.2)E+0	41.0(0.8)E–3	1.01	0.92	1.09
101^3	45.2(0.8)E–1	12.5(0.1)E+0	32.4(0.5)E–3	0.99	0.97	1.07

Table 2.5: Absolute global errors (L_1 norm) and convergence rates of the primitive variables for the relativistic spherical shock reflection test problem (RSSR) for different grids at $t = 2.0$. The test runs have been performed with a Courant number equal to 0.1 and the third order accurate Runge-Kutta time integration method (RK3). In parenthesis we give the standard root mean square deviation of the errors (see also Table 2.1).

the code to maintain the sweep-coherence symmetry (SCS), too.

2.5. Code Performance

We have parallelized GENESIS in order to run on multiprocessor computers with shared memory. Apart from the initial setup of variables, the grid generation and the output, the rest of the program is organized in a 4-level nested loop. The outermost loop runs from one to the total number of sub-domains, assigning one sub-domain to each processor. This procedure allows an almost complete parallelization of the code employing the corresponding parallelization directives (see Fig. 2.1).

The MRRP and RSSR tests have been run for different grids on a SGI Cray-Origin 2000 computer. Tables 2.6 and 2.7 show the total execution time for every run as a function of the number of CPUs used. We also give the *speed up* factor, defined as the CPU ratio between a one processor run and one using several processors in parallel. This factor is a measure of the degree of parallelization of the code and should ideally be equal to the number of CPUs used. The tables also contain the execution time per cell and time iteration (TCI). The TCI for a given number of processors is nearly independent of the number of computational cells, and can be used as a time unit to estimate the total execution time needed in a particular simulation.

According to the data shown in Tables 2.6 and 2.7 the TCI is about 7.6 10^{-5}, 2.1 10^{-5} and 1.3 10^{-5} seconds for 1, 4 and 8 processors, respectively. A significant drop of the performance is noticeable for a grid of 64^3 zones due to the phenomenon of *cache trashing*, because in this case the dimensions of the 3D matrices are multiples of the size of cache lines. Hence, different 3D matrices are mapped into the same set of cache lines, and every time the program needs to reference a new 3D matrix all cache lines are updated.

Concerning the speed up factor, it is noticeable from Tables 2.6 and 2.7 that it increases with the number of grid points, because the 3D nested loops consume a larger percentage of the total CPU time when the number of grid zones is larger. The maximum speed up factors are 3.7 and 6.5 for 4 and 8 CPUs, respectively. We also notice a *super linear* behavior, for the largest grid, for the MRRP test problem. As typical 3D simulations are performed with zone numbers larger than the ones used in the test runs, we expect to reach even larger speed up factors in these applications.

# cells	# CPUs	Time	Speed up	# iter	TCI	Mflops
44^3	1	3.91E2		86	5.34E–5	64.73/——
	4	1.13E2	3.48		1.54E–5	59.03/236.11
	8	6.02E1	6.50		8.22E–6	58.58/468.65
64^3	1	3.85E3		118	1.24E–4	30.05/——
	4	1.84E3	2.09		5.94E–5	16.25/65.00
	8	1.49E3	2.59		4.81E–5	10.46/83.70
84^3	1	5.56E3		150	6.26E–5	62.04/——
	4	1.56E3	3.57		1.75E–5	56.77/227.08
	8	8.46E2	6.58		9.52E–6	53.99/431.88
104^3	1	1.31E4		183	6.35E–5	62.72/——
	4	3.66E3	3.57		1.78E–5	57.02/228.08
	8	2.36E3	5.54		1.15E–5	45.47/363.75
154^3	1	8.94E4		265	9.23E–5	45.12/——
	4	1.84E4	4.87		1.90E–5	54.92/219.68
	8	1.15E4	7.80		1.18E–5	44.74/357.91
	16	7.39E3	12.09		7.64E–6	35.90/574.41

Table 2.6: Performance of GENESIS for the mildly relativistic Riemann test problem (MRRP) on different grids. The test runs are stopped at $t = 0.5$, and are performed with a Courant number equal to 0.8 and the second order accurate Runge-Kutta time integration (RK2) method. Times are measured in seconds on a SGI Cray–Origin 2000. The last column displays the number of Mflops per processor and the total number of Mflops. One notices that the efficiency per processor in parallel mode (Speed Up/CPUs) multiplied by the number of Mflops in sequential mode is equal to the number of Mflops in parallel mode. Megaflops are calculated using SGI's *Perfex Tool*.

The number of Mflops (millions of floating point operations per second) achieved by the code is about 60 on one processor (R10000) of a SGI Cray–Origin 2000 computer. The theoretical peak speed of such a processor is 400 Mflops. For com-

# cells	# CPUs	Time	Speed up	# iter	TCI	Mflops
45^3	1	8.73E2		114	8.40E–5	62.53/——
	4	2.53E2	3.45		2.44E–5	56.88/225.67
	8	1.51E2	5.78		1.45E–5	50.15/401.21
65^3	1	4.94E3		198	9.08E–5	62.27/——
	4	1.50E3	3.29		2.76E–5	52.88/211.54
	8	1.10E3	4.49		2.02E–5	37.54/300.28
85^3	1	2.15E4		369	9.49E–5	61.76/——
	4	6.13E3	3.51		2.71E–5	55.40/221.60
	8	3.41E3	6.30		1.51E–5	51.35/410.79
105^3	1	9.92E4		890	9.63E–5	62.09/——
	4	2.78E4	3.57		2.70E–5	56.41/225.65
	8	1.57E3	6.31		1.53E–5	48.97/391.79

Table 2.7: Performance of GENESIS for the relativistic spherical shock reflection test problem (RSSR) on different grids. The test runs are stopped at $t = 2.0$, and are performed with a Courant number varying from 0.8 (45^3 grid) to 0.2 (105^3 grid). The third order accurate Runge-Kutta time integration (RK3) method has been used. Times are measured in seconds on a SGI Cray–Origin 2000. The last column displays the number of Mflops per processor and the total number of Mflops. One notices that the efficiency per processor in parallel mode (Speed Up/CPUs) multiplied by the number of Mflops in sequential mode is equal to the number of Mflops in parallel mode. Megaflops are calculated using SGI's *Perfex Tool*.

parison, Pen (1998) reports a performance of 48 Mflops for his 3D adaptive moving mesh classical hydrodynamic code using a SGI Power Challenge machine with R8000 processors (300 Mflops theoretical peak speed).

Finally, we compare the performance of GENESIS achieved on the PA8000 processor of Hewlett Packard with that obtained on the R10000 processor of Silicon Graphics. For the comparison we used a HP J280 workstation equipped with a

PA8000 processor with a 180 MHz clock and a cache memory of 512 Kbytes and a SGI Cray-Origin 2000 equipped with a R10000 processor with a 195 MHz clock and 4 Mbytes of cache memory. The test problem selected for the comparison was the relativistic spherical shock reflection test (RSSR) with an inflow velocity of $0.9c$. Test runs were done with four different grids. The resulting execution times per zone and time step (TCI) are given in Table 2.8.

# cells	Machine	Time	# iter	TCI
45^3	SGI	8.73E2	114	8.40E-5
	HP	2.11E3	101	2.29E-4
65^3	SGI	4.94E3	198	9.08E-5
	HP	1.33E4	220	2.20E-4
85^3	SGI	2.15E4	369	9.49E-5
	HP	4.76E4	357	2.17E-4
105^3	SGI	9.92E4	890	9.63E-5
	HP	2.16E5	879	2.12E-4

Table 2.8: Performance of GENESIS for the relativistic spherical shock reflection test (RSSR) on different grids and machines.

We find that $\mathrm{TCI}_{HP} \approx 2\times\mathrm{TCI}_{SGI}$. From Table 2.8 we can infer a general trend. The TCIs obtained on both machines tend to become similar when the number of zones increases. Furthermore, the TCI for the HP machine is nearly independent of the number of zones, while the TCI for the SGI machine increases with that number. This behavior may result from the fact that the problem size always leads to an overflow of the cache memory on the HP workstation, while this does not generally happen for the larger cache memory of the SGI machine.

2.6. Conclusions

We have described the main features of a novel three dimensional, high–resolution special relativistic hydrodynamic code GENESIS based on relativistic Riemann solvers. We have discussed several test problems involving strong shocks in three dimensions which GENESIS has passed successfully. The performance of GENESIS on single and multiprocessor machines (HP J280 and SGI Cray–Origin 2000) has been investigated. Typical simulations (in double precission) with up to $7\,10^6$ computational cells can be performed with 1Gbyte of RAM memory with a performance of $\approx 7\,10^{-5}\,$s of CPU time per zone and time step (on a SCI Cray-Origin 2000 with a R10000 processor). Currently we are working on a version of GENESIS suited for massively parallel computers with distributed memory (like, e.g., Cray T3E).

GENESIS has been designed to handle highly relativistic flows. Hence, it is well suited for three dimensional simulations of relativistic jets. First results will be presented in a separate paper (Aloy et al. 1999b). Further applications envisaged are the simulation of relativistic outflows from merging compact objects (see, e.g., Ruffert et.al. 1997), from hypernovae (Paczynski 1998), or collapsars (MacFadyen & Woosley 1998). In all these models ultra-relativistic outflow is thought to occur and to play a crucial role in the generation of gamma-ray bursts.

Chapter 3

High–Resolution 3D Simulations of Relativistic Jets

3.1. Extragalactic jets

The first physical application in which we are interested in is the simulation of the dynamical evolution of extragalactic jets and their emission properties. An astrophysical jet is a collimate flux of plasma that some galaxies, quasars, micro-quasars, X-ray binaries, etc., may produce as a consequence of the accretion of matter onto massive objects. In order to motivate our work, we are going to establish the observational framework in which the jet phenomenon is included (Sect. 3.1.1). Then we will outline the standard model which tries to explain the current observations (Sect. 3.1.2). In the next Section (Sect. 3.1.3) an historical overview of the numerical simulations in this field will be given. Section 3.2 includes the results obtained by Aloy *et al.* (1999b), in which we explore the 3D relativistic regime by means of helically perturbed axisymmetric models. Additionally, we will make a comparative study of a set of perturbed models with the one pesented in Aloy *et al.* (1999b). Finally, the emission properties of 3D relativistic jets are evaluated in section 3.3.

3.1.1. Phenomenology

The first detected jet (Curtis 1918) was the one in the giant elliptic galaxy M87. Although this jet was originally seen at optical wavelengths, typical jets are observed at radio frequencies. This explains why the progress in the discovery of new sources is strongly linked to the technical improvements in the radio observations. The first observed radio jets where those associated to powerful radio sources. More precisely, Jennison & Das Gupta (1953) reported that the radio emission from Cygnus A originated from two lobes straddling the associated optical galaxy rather than the galaxy itself. With the advent of the Cambridge 5 km telescope (in the mid 1970s), the Very Large Array (VLA) and MERLIN telescopes (both in the early 1980s), jets were discovered to be associated with a large number of double radio sources. The development of Very Large Baseline Interpherometry (VLBI) showed that jets were also common among compact radio sources. In addition to extragalactic jets, there are many examples of jets and outflows that have been found within the Milky Way. The galactic jets span a great range of luminosities and collimation factors, from the optically visible jets and *lobes* associated with low-mass young stellar objects (YSOs), which are morphologically very similar to the classical radiogalaxies, to the poorly collimated and much less clearly defined *jets* associated with the Galactic Center and with various supernova remnants (Padman, Lasenby & Green 1991). VLA has allowed to detect in our galaxy the object SS433 (Abell & Margon 1979) and the *micro-quasars* GRS 1915+105 (Mirabel & Rodriguez 1994) and GRO J1655-40 (Tingay *et al.* 1995). In combination with VLBA (Very Large Baseline Array).

In the case of the diverse forms of extragalactic radio sources, the presence of jets is a manifestation of a more general phenomenon which is the nuclear activity in some galaxies. This nuclear activity characterizes the Active Galactic Nuclei (AGNs) which are among the most spectacular objects in the sky. They produce enormous luminosities (in some cases as much as 10^4 times the luminosity of a typical galaxy) in tiny volumes (probably $\gg 1$ pc^3; Krolik 1999). This radiation can emerge over a very broad range of frequencies (from infrared to gamma-rays). Their line spectra show in the optical and UV emission (and occasionally absorption) lines whose total flux is several percent to tens percent of the continuum flux, and whose widths suggest velocities ranging up to $\sim 10^4$ km s^{-1} (see *e.g.*, Krolik 1999).

The interpretation of the diverse forms of observed radio source structures has motivated the introduction of a classification scheme. Such classification scheme has changed as the number of observations has increased. Nowadays, the primary division among radio loud sources is the one that considers which part of the source has a large relative emission. Actually, the observations show that at low frequencies (*i.e.,* a few hundred MHz), in most instances the radio emission comes from a pair of extremely large lobes on opposite sides of the host galaxy. These lobes are often several hundred kpc in length and can be separated from the galaxy by a similar distance. The axis of the two lobes and the center of the galaxy generally lie along a common line. However, there are other radio loud objects in which, especially at higher frequencies (*i.e.,* several GHz), the region responsible for the bulk of emission is essentially unresolved on VLA (*i.e.,* 1 arcsecond scales), so that the source must be smaller than $\sim 20(D_A H_0/c)(h/0.75)^{-1}$ kpc, where D_A is the *angular diameter distance* (*i.e.,* distance at which the length between two objects whose angular separation is ϵ is given by $D_A\epsilon$), H_0 is the Hubble constant ($H_0 = 100h$ km s^{-1}) and h is the scale of the Hubble constant (usually $h = 0.65$). With this criterion, radio sources are divided into *lobe dominated* and *core dominated* (Muxlow & Garrington 1991). Each of these types have in its turn several subclasses. In the lobe dominated radio structures found in luminous spiral and elliptical galaxies are distinguishable three subtypes, associated to different classes of AGNs, *radio Seyfert galaxies*, *lobe-dominated radio galaxies* and *lobe-dominated radio-loud quasars.* Many Seyfert galaxies show S-shaped kpc scale radio structure (perhaps due to the disruption of the jet) and they are often less powerful emitters than elliptical galaxies. Usually, this difference is ascribed to the lower power output of the central nuclear engine and the dense rotating interstellar medium found in spiral discs (which difficults the plasma ejection through it). Some Seyferts however, do not contain any evident jet structure. Typical luminosities at 1 GHz ($P_{\rm 1GHz}$) of this radio structures lie in the range $P_{\rm 1GHz} \sim 10^{21} - 10^{25}$ W Hz^{-1}.

The properties of lobe-dominated radio galaxies are dependent on their luminosity. In fact there exits a critical luminosity ($P_{\rm 178MHz} = 5 \times 10^{25}$ W Hz^{-1}) around which, structures seem to undergo an abrupt transition (Faranoff & Riley 1974) and, therefore they are conveniently classified as Fanaroff-Riley I (FR I) and II (FR II) if their luminosities are, respectively, below or above the former limit. FR I sources tend to have prominent smooth (*i.e.,* not knotty) continuous two-sided jets in antiparallel directions running into large-scale lobe structures (*plumes*) which are *edge-darkened*[1] and whose steepest radio spectra lie in the outermost extended regions furthest from the host galaxy. They exhibit linear polarization with electric vector normal to the jet, *i.e.,* the embedded magnetic field is aligned with the jet. The jets often contribute over 10% of the total power of the extended structure. A typical FR I source is associated to the radio galaxy 3C 449. FR II however, tend to have large-scale structures which are *edge-brightened* with bright outer hot spots and they are usually one-sided with a jet to counter-jet intensity ratio $> 4:1$. These jets are usually not smooth (*i.e.,* formed by a set of bright knots). The steepest radio spectra are found in the inner extended regions of the lobes or *bridges*. They show parallel polarization with a magnetic field perpendicular to the jet axis. The cores and jets in these structures usually contain $< 10\%$ of the total source luminosity which results in the non-detection of some cores. The opening angle of jets in FR II sources are smaller than those for FR I structures. Of course, the transition from FR I to FR II is not abrupt, and there is a special class of sources (*fat doubles*) which are among the weakest FR II sources (near the FR I/FR II luminosity limit), have a steeper spectrum than typical FR II, and are characterized by fatter lobes and almost no evidence for cores, jets or hot spots. The most characteristic example of FR II source is Cygnus A (3C 405).

The overall morphology of lobe-dominated radio sources is believed to be dominated by their interaction with the external medium (*e.g.,* Blandford & Rees 1974 –BR74, hereafter–). Actually, due to this interaction, it is possible that the path of the jet would be changed or even considerably bent. This is the case for *Narrow-Angle-Tail* (NAT) sources, *Wide-Angle-Tail* (WAT) sources, and *Steep spectrum core* sources. NATs are FR I type structures with bent two-sided (and almost symmetrical) jets running into an extended tail. They are usually located in clusters of galaxies where the host galaxy has a large proper motion with respect to the cluster

[1]Edge-darkened (see *e.g.,* Muxlow & Garrington 1991, or, Krolik 1999) means that the ratio of the total separation of the peaks of radio lobe emission to the source size (*i.e.,* the distance between the outermost detected parts of the lobes), is significantly less than unity. For FR I sources this ratio is less than 0.5, while for FR II sources the ratio is close to one.

and the radio structure is bent back by ram pressure from the hot external medium found in clusters (Begelman, Rees & Blandford 1979). The most well-known example of this class is NGC 1265. WATs sources were first classified as a new morphological class by Owen & Rudnick (1976). They are C-shaped structures formed by FR I disrupted plumes or tails with inner hot spots linked to the central components by jets. Jets seem to have physical properties similar to FR II type structures (quite knotty and with jet/counter-jet intensity ratios $> 4:1$). Although there are not too many observed structures of this type, they are often associated to optical dominant galaxies in rich clusters, and have total radio luminosities intermediate between NAT sources and typical FR IIs. An example of this structural type is 3C 465. Steep Spectrum Core sources are dominated by a kpc scale steep spectrum component associated with the nucleus of the parent object, surrounded by a diffuse low surface brightness halo. Objects of this class are also called *Core-Halo* sources, where "Core" states for the complete nuclear component rather than the compact flat spectrum feature within it. The best studied example of this structural type is the radio galaxy M 87.

The *lobe-dominated radio-loud quasars* are mainly found at high redshift and consist of very powerful radio extended structures surrounding some quasars. Their luminosity is above $P_{178\mathrm{MHz}} = 5 \times 10^{25}$ W Hz^{-1}, and display morphological features similar to FR II sources of equivalent luminosity. They have bright one-sided radio jets and cores with higher luminosities than those found in radio galaxies. The jets are knotty, one-sided (jet/counter-jet intensity ratios $> 4:1$) and with small opening angles. An example of this type of sources is 3C 179 (Shone, Porcas & Zensus 1985).

Core-dominated sources have very luminous cores and usually bright one-sided jets. VLBI studies (for which these objects are particularly appropriate because they have a very high core surface brightness) have pointed out that there is a continuity between the small and large-scale structures with a milliarcsecond scale one-sided jet ($i.e., 20(\theta/1\mathrm{mas})(D_A H_0/c)(h/0.75)^{-1}$, being θ the angular size) running into the outer arcsecond scale jet (kpc scale). Significant bending of the jet, specially near the core, is a common feature in these sources; for example 3C 273 bends by $\sim 20^o$ within the first 10 mas before extending continuously for 22 arcseconds (~ 40.7 kpc) from the core to beyond the limit of the optical jet (Whitney *et al.* 1971; Cohen *et* *al.* 1971). Knots in the VLBI jet are often observed to be moving away from the core with apparent *superluminal* speed. 3C 120 was one of the first four sources in which superluminal motion was detected on the scale of pc (Seielstad *et al.* 1979; Walker, Benson & Unwin 1987) to tens of pc (Benson *et al.* 1988; Walker 1997; Muxlow & Wilkinson, 1991; Gómez *et al.* 1998, etc.). The most complete set of epochs and high resolution VLBA observations has been undertaken by Gómez, Marsher & Alberdi (1999). In this work and in Gómez *et al.* (1998), up to ten superluminal components, with velocities between 2.3 and 5.4 $h^{-1}c$, are shown. In addition to the core and jet, VLA images show a low surface brightness extended component that is often found on the opposite side to the jet and, in some cases, this whole triple structure is embedded in a very low surface brightness amorphous halo like in the case of 1642+690 (Browne 1987). The jet properties are broadly similar to those found in lobe-dominated quasars, but are of higher luminosity and show a greater degree of bending.

Finally, there exist a morphological class (which is a remnant of the poor resolved observations with the Cambridge 5 km telescope) named *compact steep-spectrum* sources (Fanty *et al.* 1990). Most of them resembled miniature extended sources. Detailed VLA and VLBI observations conclude that these radio structures are of galactic or subgalactic dimensions (*i.e.,* linear sizes $\sim 1 - 10$ kpc) and have a wide variety of morphologies (some are like doubles, others appear as core-jet structures, and in a number of cases they are so extremely distorted that cannot be easily classified). Fanty *et al.* (1985) have shown that there is a clear division between quasars and radio galaxies in this class: the quasars are generally core-jet or complex while the galaxies are doubles. Furthermore, some authors (*e.g.,* Phillips & Mutel 1980) have claimed that the double structures represent the young progenitors of classical double radio sources. Others have argued that these sources are a separate class of intrinsically small objects where the jets encounter great difficulty in escaping from the inner regions of the host galaxy or quasar (Fanti & Fanti, 1986).

3.1.2. The standard model

We have stated above which is the gross classification of the enormous set of observations of radio sources. Now we focus on the models that allow us to understand such observations. There exists a unifying interpretation consisting in that our view of a radio source is influenced by our relative orientation with respect to the source axis (regardless of its luminosity). In the standard model (BR74; Scheuer 1974) jets are considered as continuous channels of matter highly collimated, supersonic and very stable. Additionally, following Blandford & Königl (1979) the superluminal motions and the jet asymmetries in compact sources are explained by assuming that both the jet and the counter-jet propagate with relativistic speeds at a small angle to the line of sight towards the observer. The relativistic Doppler beaming of the emission in the direction of motion can account for the observed asymmetry in the luminosity of the jets. Additionally, the component of the velocity over the plane of the sky may exceed the light speed due to a pure kinematic relativistic effect giving rise to apparent superluminal velocities[2]. Assuming that this interpretation of the superluminal motion is true and taking into account the relativistic beaming, bulk flow motions with Lorentz factors as large as 20 may be assigned to many compact radio jets.

The mechanism for the jet formation and collimation is still a challenge, mainly because we have not detailed enough observations (*i.e.,* with sufficient resolution) because the most detailed high-frequency VLBI observations of nearby radio sources can resolve at most the compact radio cores with linear resolutions of ≥ 100 mpc (Blandford 1990) [3] while the Schwarzschild radius ($R_s = GM/c^2$) of a $10^9 M_\odot$ galactic BH is ~ 10 μpc. Consistently, our theoretical view of the jet formation must be mainly constrained by the fact that many jets are well collimated by the time they have propagated to a distance $\leq$ 1pc from the nucleus (Blandford 1990; Junor & Biretta 1995). Considering this element, many mechanisms have been proposed, all

[2]The apparent velocity is define as $v_{\rm app} = v \sin\Psi/(1 - v\cos\Psi)$, Ψ and v being the angle that forms the source respect to the line of sight and the velocity, respectively.

[3]Nowadays, within the project VLBI Space Observatory Program (VSOP), the angular resolution is higher allowing for linear resolution of $\sim 0.1 - 1$ pc even in distant sources like S5 0836+710 ($z = 2.17$; Lovanov *et al.* 1998).

of which present some difficulties (Begelman, Blandford & Rees, 1984) and, additionally, there is a wide variety in the observed properties of jets, so there may be a variety of jet collimation mechanisms.

Our common wisdom about AGNs establish the following *anatomy* for the innermost (*i.e.*, ≤ 100 mpc) part of the nuclei:

- **10 mpc scale.** It is usually accepted that the power that feeds the ejection is the matter which is accreted onto a black hole (BH) coming from an accretion disk. The morphology and dynamics of this accretion disk is different depending on the distance to the BH. At this scale, the disk may be *ionized*, being the evidence for this the optical continuum in quasars (if it is true that this continuum is mainly thermal in origin). A relativistic jet is still formed which emits due to synchrotron and inverse Compton. Moreover, a toroidal magnetic field may be the responsible for jet collimation.

- **1 mpc scale.** At this scale, the temperature is higher and may produce UV radiation. The disk would be *radiation pressure* and *Thomson opacity* dominated. The poloidal component of the magnetic field presumably helps to extract matter from the accretion disk and accelerate it at velocities of $\sim 0.1c$.

- **100 μpc scale.** Within ten times of the radius of the BH, the nature of the gas flow is quite controversial, but with complete certainty the effects of *General Relativity* must determinate their characteristics. Observation of highly variable X-ray emission from Seyfert galaxies imply that the X-rays originate from this region (produced by electron–positron (e^-e^+) annihilation into the plasma that forms the relativistic jet).

- **10 μpc scale.** This is the typical BH scale and perhaps also its magnetosphere. The mass of the BH dictates a characteristic length and luminosity scale for nuclear activity.

The collimation of such matter emissions can be due to the combined action of toroidal magnetic fields, radiation pressure, purely thermal pressure and other not yet understood processes. In the following paragraphs we will summarize the main issues that have been pointed out in order to explain the jet collimation up to ~ 1 pc (for more details see *e.g.*, Kembhavi & Narlikar 1999; Krolik 1999; or Blandford 1990).

The first force one might look to in order to drive outflows is ordinary gas pressure gradients. In the original scheme suggested by BR74, two twin antiparallel channels propagate in opposite directions from the nucleus. The jets, assumed to be made up of ultrarelativistic plasma, are subsonic close to the nucleus, but pass through a nozzle (*de Laval nozzle*) where the cross-sectional area is a minimum, and the flow is trans-sonic. Beyond the nozzle the flow is supersonic, and though the cross-sectional area increases, the angle which is subtended at the nucleus decreases, and well-collimated jets could be produced. However, even allowing for the reduced collimation caused by internal dissipation, entrainment, etc., this mechanism does not seem capable of creating well-collimated jets. The reason is that VLBI observations require that the collimation has to be produced on a scale $\lesssim$1 pc, where the gas pressure and density required would have to be very large that the consequent X-ray emission would easily exceed the observed upper limits for powerful sources. This collimation model can therefore work only for jets of low power $\lesssim 10^{43}$erg sec^{-1}.

Another possibility for jet collimation are the radiation forces. Such forces may be important in powerful sources (like quasars) which would be radiating very close to their Eddington limits. Then the pressure of radiation acting on e^-e^+ pairs may be sufficient to overcome gravity along certain directions. This would happen in the funnels formed by a radiation-pressure supported torus orbiting around a BH. The most fundamental problem of this model is that once the flow reaches mildly relativistic speeds[4] (much less than those usually invoked to account for superluminal motion), a medley of effects make further acceleration inefficient, while any isotropic radiation acts as a source of drag[5] (Phinney 1987). This radiative acceleration model may not apply to sources which are observed to radiate at sub-Eddington rates. Moreover, a theoretical complication of the model is that radiation-supported tori could not be dynamically stable, which puts in question their long term existence.

[4]Lorentz factors $\lesssim$3 (for a pair plasma) or smaller (for a plasma of electrons and ions).

[5]This radiation may drag the well collimated fluid from its outflowing direction, thus, loosing directionality and collimation.

A third possibility arises if magnetic forces are an important ingredient. These models are mainly based on thin magnetized accretion disks. Collimation seems to be a generic feature of hydromagnetic winds, the reason for this tendency being that one expects the footpoints of magnetic field lines to be fixed to the matter of the accretion disk. The field lines will then rotate with the orbital frequencies of their footpoints, creating a toroidal magnetic field even if there was none to begin with. This toroidal component has an associated *hoop* stress which can act to collimate the poloidal flow of the plasma. As the flows are centrifugally driven and magnetically confined, the gas pressure is not very important except, perhaps, close to the disk. In this magnetohydrodynamic (MHD) flows, there are three critical points, along a flow line, at which the gas becomes sonic (corresponding to the three types of wave modes which exist in MHD: fast, Alfvén and slow waves). After the field passes through the third point, the magnetic field becomes mostly toroidal, and the magnetic energy and angular momentum fluxes are typically half converted into mechanical energy and angular momentum. In the process the jets become collimated, whether they are relativistic or non-relativistic. In this models there is a correlation between the accretion rate and the speed of jets on the pc scale, so that quasar jets have highly relativistic speeds while jets in FR I galaxies may be non-relativistic (Camenzind 1993). A theoretical difficulty with this explanation for AGN jets is that magnetically collimated plasma is unstable, particularly to non-axisymmetric perturbations.

Having summarized in the previous paragraphs the fundamental theories that try to explain the mechanisms of jet formation and collimation, it is necessary to remark that only a limited progress has been made in understanding jet physics, because of the lack of detailed structural information on the very small spatial scales on which the jets are produced, as well as the complexity of the physical processes involved in the production and collimation. However, on bigger scales (from $\gtrsim 10\,\mathrm{mpc}$ to $\sim 1\,\mathrm{Mpc}$) a very detailed set of observations has been made in a large number of AGNs. This wide sample of observations has allow us to understand that powerful sources are supposed to comprise a core, and two jets which feed a pair of radio-emitting lobes. The radio-emitting electrons are supposed to be convected outward along the jet with relativistic speed so that they beam their emission along their directions of motion (due to the *relativistic beaming*). Most of the compact radio sources are intrinsically weaker and their compactness is mainly a projection effect due to that they are beamed in our direction so that their compact jet emission outshines the unbeamed emission from the lobes. In addition to this, from the observations, it is possible to infer a characteristic *anatomy* of the observable parts of the jets, in which two main regions are distinguishable in terms of the distance to their origin: the *parsec* and *kiloparsec* scales.[6]

a) the *parsec scale (100 mpc – 100 pc)*:

- *Observational facts*: the jet emits at radio frequencies due to synchrotron and inverse Compton processes, and it is observed using VLBI imaging. It displays a high collimation and its morphology is characterized by a bright spot at the jet end and a series of components (usually preceded by outbursts in emission at radio wavelengths) which separate from the core, sometimes at superluminal speeds. Many parsec scale jets show intraday variability of the radio flux, excess in brightness temperatures and one-sidedness. Between 1 and 10 pc the *broad emission lines* seem to be produced. These are observed in about 12% of all quasars (Weymann *et al.* 1991). At about 10 pc the BH's gravity may begin to dominate the stellar distribution. In some galaxies the stellar velocity rises with decreasing radius. The jets may exhibit structure reflecting this change in gravitational potential. The *narrow emission lines* are detected at scales ~ 100 pc.
- *Theoretical interpretation*: the jet material moves at small angles to the line of sight with bulk Lorentz factors $W \simeq 10(H_0 h)^{-1}$ (Ghisellini *et al.* 1993), or maybe larger ($W \simeq 30 - 100$) if the intraday variability is intrinsic and a result of incoherent synchrotron radiation (Begelman, Rees & Sikora 1994). The moving components are interpreted in the shock-in-jet model as traveling shock waves (Marscher & Gear 1985; Hughes, Aller & Aller 1989; Gómez, Alberdi & Marcaide, 1994, Gómez *et al.* 1994). A worthy byproduct of this model is the explanation of the complex

[6] This division follows in distance to the previous scale (the *subparsec scale*) that we have explained previously.

multifrequency brightness and polarization variations in blazars. The width of the emission lines is interpreted in terms of the local velocity of the clouds where the absorption is produced. For the broad lines, a Doppler spreading interpretation ascribes flow velocities up to 60000 km sec^{-1} in the gas which is within the quasar itself, relative to the emission redshift. The narrow emission lines are generated in clouds which are farther from the AGN center.

b) the *kiloparsec scale (1 kp – 1 Mpc)*:

- *Observational facts*: $\sim$ 1 kp and $\sim$ 10 kpc are the typical sizes of the galactic center nucleus, and the host galaxies, respectively. At this scale there exist a dichotomy between FR I and FR II sources whose basis seems to be the source power. Between 100 kpc and 1 Mpc the radio jets are quite common, and extended radio lobes (which eventually may contain bright host spots) can be found. The overall shapes of the jets are sensitive to the galactic and circumgalactic environment (for example, NAT and WAT sources have their characteristic morphology due to the presence of high peculiar velocities in rich clusters of galaxies). Evidences of mildly relativistic jet speeds ($\sim 0.6-0.8$c, for the double–lobed quasar 3C 179; Akujor 1992) well outside the galaxy have been found, like *e.g.,* flux asymmetries between jets and counter-jets (Bridle *et al.* 1994) and superluminal motions at kpc scales (*e.g.,* in 1928+738, Hummel *et al.* 1992, in 1055+201, 1830+285, 2209+080, Hooimeyer *et al.* 1992).
- *Theoretical interpretation*: morphologies of FR I sources are the result of a deceleration from relativistic to non-relativistic speeds (Bicknell 1996; Laing 1996). FR I sources are mostly supposed to be moving with subrelativistic and probably no more than transonic speeds (Bicknell 1984; Begelman, Blandford & Rees, 1984). Their jets are therefore visible from both sides of the central galaxy (because small relativistic velocities imply small relativistic beaming). The transonic speeds on kpc are explained in terms of a slower shear layer that surrounds the inner core of the jet (for example, in M 87, Biretta & Owen, 1990 or Biretta, Zhou & Owen, 1995, have detected a shear layer with Lorentz factor ≤ 2). The existence of this

layer has been pointed out by several authors both theoretically (Laing 1996; Komissarov 1990) and observationally (*e.g.,* Swain, Bridle & Baum 1998; Biretta, Zhou & Owen 1995), and has been buttressed by numerical simulations (like *e.g.,* Aloy *et al.* 1999b –3D RHD–; Hardee & Rosen, 1999 –3D MHD–). In the most powerful sources (FR II and quasars), the jet–counter-jet asymmetries are understood as the result the enhancement of the jet emission due to the relativistic beaming while the counter-jet is outshined. The mechanism by which the relativistic flows inferred from radio jets at pc scales extend to kpc scales is still an unresolved question. However, the named transition and the ulterior propagation of jets needs of an efficient mechanism that stabilizes the possible developing of (magneto-)hydrodynamical instabilities (mainly Kelvin-Helmholtz instabilities).

3.1.3. Numerical simulations

The study of the jet phenomenon using numerical simulations has become an important tool to understand the nature of the jets along with theory and observations. In order to simulate astrophysical jets a *fluid-like* approximation is usually made, considering the intergalactic medium (IGM) and the jets themselves as continuous mediums in which the hydrodynamic (HD) equations hold. The validity of this approximation is justified because of the presence of micro-Gauss magnetic fields which provide the collisional coupling of the plasma (and hence, diminishing the collisional mean free path of the jet plasma) and, moreover, Begelman, Blandford & Rees (1984) stated that in extragalactic jets the Larmor radii and Debye lengths of positrons (or protons) and electrons are several orders of magnitude smaller that the jet widths.

In BR74 was made the first one-dimensional Newtonian study of jets in order to analyze the behavior of a steady flux in pressure equilibrium with the IGM. From this work is concluded that the head of the jet must end into a discontinuity that has a supersonic velocity which, in its turn, produces a *bow shock* behind the contact discontinuity. In addition, the authors suggest that a movement parallel but with opposite sense to the jet ought to appear (the *backflow*) giving rise to the formation of a *cocoon* than surrounds the beam.

The simulations performed by Rayburn (1977) and, remarkably, by Norman *et al.* (1982) allowed for the verification of the jet model of BR74 and Scheuer (1974). Similarly to the observations, the evolution of numerical complexity of the simulations has grown in parallel to the improvement of computers and computational techniques. The main goals of the numerical work in the late 1970s and 1980s have been the simulation of classical (Newtonian) jets in three spatial dimensions and the consideration of dynamically important magnetic fields (in the framework of the ideal MHD). Classical HD simulations provided us a new insight into the structures observed in many VLA radio images (Norman *et al.* 1982) while MHD simulations showed the importance of toroidal magnetic fields for the confinement of jets (Clarke, Norman & Burns 1989; Lind *et al.* 1989; Kössl, Müller & Hillebrandt 1990; Appl & Camenzind 1992). The stability and mixing properties of high Mach number jets have been studied by means of HD numerical simulations in Bodo *et al.* (1995) (2D slab symmetry) or Bodo *et al.* (1998) (3D). The stability of MHD jets using an artificial viscosity scheme (see Chapter 2, §2.1) was explored by Hardee & Norman (1988), Norman & Hardee (1988) or Hardee *et al.* (1992) (2D slab symmetry), and Hardee, Clarke & Howell (1995) or Rosen *et al.* (1999) (3D jets). Numerical simulations have been used to investigate the confinement properties of overpressured cocoons in hypersonic jets (see Begelman & Cioffi, 1989) by Loken *et al.* (1992). In order to explain the observed morphologies in NAT and WAT sources, the interaction with the IGM has been included in some simulations like *e.g.*, Balsara & Norman (1992) –3D simulations of NAT jets with a cross wind–, Norman, Burns & Sulkanen (1988) and Loken *et al.* (1995) –2D and 3D simulations of WAT sources in which the ambient gradients play a crucial rôle in the morphology–.

In the late 1980s and during the 1990s the dynamical and morphological properties of relativistic jets have been investigated by means of relativistic simulations. The classical numerical techniques (*e.g.*, Wilson 1979) failed to describe accurately complex fluids with strong shocks, large Lorentz factors or were impractical in multidimensions (see Norman & Winkler 1986). Such drawback restricted the relativistic simulations to the stationary regime (Wilson 1987; Daly & Marscher 1988; Dubal

& Pantano 1993; Bowman 1994). Thereat, in order to fix these problems and to be able of undertaking relativistic simulations it was necessary to write the equations of RHD as a system of conservation laws, and employ new numerical methods exploiting the hyperbolic and conservative character of RHD equations (see *e.g.,* Martí *et al.* 1991; Marquina *et al.* 1992; Schneider *et al.* 1993; Eulderink & Mellema 1995; Martí & Müller 1996). The new treatment has allowed to produce axisymmetric time-dependent relativistic hydrodynamical simulations (Duncan & Hughes 1994; Eulderink & Mellema 1994; Martí *et al.* 1994, 1995, 1997; Komissarov & Falle 1998; Rosen *et al.* 1999). These simulations allowed to conclude that the main relativistic effect is that both the internal energy and the Lorentz factor increase the effective inertial mass of the beam which directly contributes to enhance the stability of relativistic jets compared to their classical equivalents with *similar* parameterizations.[7]

Relativistic MHD simulations in 2D (van Putten 1993, 1996 –using pseudo-spectral techniques–; Koide, Nishikawa & Muttel 1996; Koide 1997) and 3D (Nishikawa *et al.* 1997, 1998) have been another step forward in the understanding of the jet phenomenon. A remarkable difference between our HRSC methods and the TVD methods used by the Japanese group is that Koide and collaborators code, instead of using fluxes obtained by solving Riemann problems at zone interfaces, rely on the addition of nonlinear dissipation terms to their Lax–Wendroff scheme to stabilize the code across discontinuities. This stabilization method was originally proposed by Davis (1984), who applied it successfully to the equations of classical HD. The method is robust and simple as no detailed characteristic information is needed. Koide and collaborators did simulate the evolution of the jet only for a very brief period of time. This fact and the coarse grid zoning used in their simulations, prevented them from studying genuine 3D effects in relativistic jets in any detail. On the other hand, the relative smallness of the beam flow Lorentz factor (4.56, beam speed ≈ 0.98) assumed in their simulations does not allow for a comparison with Riemann-solver-based HRSC methods in the ultrarelativistic limit.

[7] The direct comparison between classical and relativistic jets is not possible, because the beam velocity is an extra parameter (in the relativistic case) which cannot exceed the light speed. Some issues in the method for this comparison have been outlined by Komissarov (1996), who suggested to establish equivalents considering jets with the same *useful* power (the energy flux) or the same thrust (the momentum flux) at the jet inlet.

Finally, only very recently, within the framework of General Relativity, general relativistic MHD 2D axisymmetric simulations of jet formation near a rotating Kerr BH (assuming a fixed Kerr background metric) have been performed by Koide *et al.* (1999a,b). However, their results are still preliminar, because in Koide *et al.* (1999a) it is said that a jet is formed with a maximum velocity $0.93c$ ($W = 2.7$), and for a non-rotating Schwarzschild black hole, the maximum outflow velocity is less than $0.6c$ for initial magnetospheric conditions similar to those of the Kerr black hole case. In Koide *et al.* (1999b), nevertheless, the maximum velocities obtained are $0.4c$ (counter-rotating disk) and $0.3c$ (co-rotating disk), and the results in the Schwarzschild case are very similar to the co-rotating case.

3.2. 3D Hydrodynamical simulations of large–scale jets

As stated in Chapter 2, one of the applications of GENESIS is the study of large–scale jets. In order to begin such a research in three spatial dimensions we have first considered a 3D axisymmetric reference model consisting of a relativistic jet propagating through an homogeneous atmosphere. Of course, this model could be calculated with a two-dimensional code using cylindrical coordinates. However, it will be taken as a calibration of the results in 3D (compared with the same model in 2D), and additionally it will be used as a reference model in order to compare with other 3D models which result from a slight perturbation of the axisymmetric one.

3.2.1. An axisymmetric jet in 3D

We have considered a 3D model corresponding to model C2 of Martí *et al.* (1997), which is characterized by a beam-to-external proper rest-mass density ratio $\eta = 0.01$, a beam Mach number $\mathcal{M}_b = 6.0$, and a beam flow speed $v_b = 0.99c$ (beam Lorentz factor $W_b \approx 7.09$). An ideal gas equation of state with an adiabatic exponent

$\gamma = 5/3$ is assumed to describe both the jet matter and the ambient gas.[8] The beam is in pressure equilibrium with the ambient medium which fills a Cartesian domain (X,Y,Z) with a size of $15R_b \times 15R_b \times 75R_b$ ($120 \times 120 \times 600$ computational cells), where R_b is the beam radius. The jet is injected at $z = 0$ in the direction of the positive z-axis through a circular nozzle defined by $x^2 + y^2 \leq R_b^2$, and is in pressure equilibrium with the ambient medium. Outflow boundary conditions are imposed everywhere except at the plane $z = 0$, where injection is assumed through the nozzle and the rest of the plane has a reflecting boundary. Two different spatial resolutions with 4 and 8 zones per beam radius were used in our calculations (Figs. 3.1, 3.2). Simulations are typically performed with 16 processors and need about ten thousand time iterations.

Given that our relativistic, highly-supersonic models are dimensionless, we can scale the beam kinetic power, P_j, of the jets according to

$$P_j = 3.5\,10^{46} \left(\frac{R_b}{100\,\mathrm{pc}}\right)^2 \left(\frac{\rho_a}{10^{-26}\,\mathrm{g\,cm^{-3}}}\right) \mathrm{erg\,s^{-1}}\ , \tag{3.1}$$

which for typical values of the beam radius and the ambient density is that of a powerful jet (Rawlings & Saunders 1991, Daly 1995).

In Martí et al. (1997) the simulation was performed in cylindrical coordinates assuming axial symmetry. The spatial resolution was 20 zones per beam radius both in the axial and radial directions. It is well known that the propagation of a supersonic jet is governed by the interaction of jet matter with the ambient medium, which produces a bow shock in the ambient medium and an envelope surrounding the central beam (the *cocoon*, in BR74). The cocoon contains jet material deflected backward at the head of the jet. In the case of highly supersonic jets, discussed in Martí et al. (1997), extensive, overpressured cocoons are formed with large vortices of jet matter propagating down the cocoon/ambient medium interface. The vortices are the result of Kelvin–Helmholtz instabilities at the interface between the jet and the shocked ambient medium. The interaction of these vortices with the central beam causes internal shocks inside the beam. These, in turn, affect the advance

[8] According to Martí *et al.* (1997), high Mach numbers correspond to flows with small specific internal energies and, consistently we have chosen for this model a nonrelativistic value for γ.

speed of the jet making it highly non–stationary. The propagation speed of the jet can be estimated from the momentum transfer between the jet and the external medium assuming a one dimensional flow. For model C2 one obtains an advance speed equal to $0.42c$ (which agrees with the 1D estimate for the head of the jet speed[9]), whereas the 2D hydrodynamic simulation presented in Martí et al. (1997) gives a mean jet advance speed of $0.37c$.

The four panels in Figs. 3.1, 3.2 display, from top to bottom, the logarithm of the proper rest-mass density, pressure and specific internal energy and flow Lorentz factor in the plane $x = 0$ at $t = 160\,R_b/c$, when the jet has propagated about $75\,R_b$. The analysis of cross sections of the grid perpendicular to the the jet's direction of propagation (not shown here) reveals acceptable symmetry of the numerical simulation, *i.e.,* both the SLS and the SCS properties are maintained (see §2.3.10).

The gross morphological and dynamical properties of highly relativistic jets as inferred from our 3D simulations are qualitatively similar to those established in earlier 2D simulations. An extensive, overpressured cocoon with pressure about 20 times that in the beam at the injection point is found surrounding the jet. The pressure and density at the head of the jet in the model with 8 zones/R_b are a factor of 2 larger and 1.3 smaller, respectively, than in the 2D calculation. For the model with 4 zones/R_b these factors are 1 and 1.3, respectively. In contrast with the model with 4 zones/R_b, in which the propagation speed coincides with the 1D estimate, the larger pressure at the head of the jet in the model with 8 zones/R_b causes it to propagate through the ambient medium at a larger speed in the 3D calculation ($0.47c$ instead of $0.42c$ for the 1D estimate and $0.37c$ for the 2D simulation) producing a narrower profile of the bow shock near the head. In all the simulations, the supersonic beam displays rich internal structure with oblique shocks effectively decelerating the flow in the beam from a Lorentz factor equal to 7 at the injection point down to a value of about 4 near the head. Whereas gross morphological properties are qualitatively similar in all three simulations, finer jet details (e.g., number, size, position and development of turbulent vortices in the cocoon) do not agree. However, it has been pointed out before that the fine structure

[9] $v_{1D} = \sqrt{\eta_R^*}/(1+\sqrt{\eta_R^*})v_b$, with $\eta_R^* = (\rho_b h_b)/(\rho_m h_m)W_b^2$, ρ_m and h_m being the density and the enthalpy of the external medium (for more details see, *e.g.,* Martí *et al.* 1997)

is highly dependent on the numerical grid resolution (see, *e.g.*, Kössl & Müller 1988).

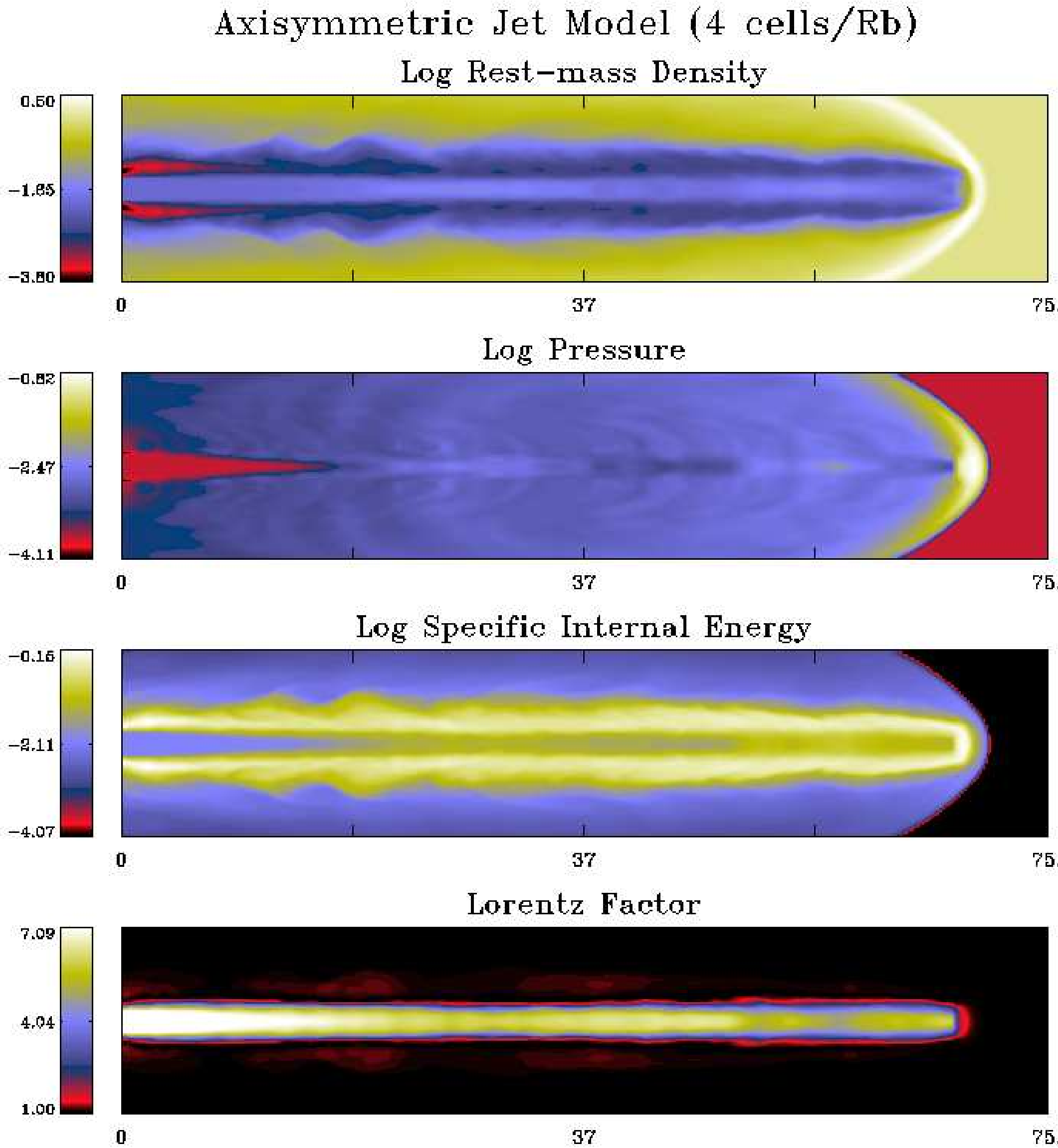

Fig. 3.1.— Snapshots (from top to bottom) of the proper rest–mass density distribution, pressure, specific internal energy (all on a logarithmic scale) and Lorentz factor of the relativistic jet model discussed in the text ($v_b = 0.99c$, $\mathcal{M}_b = 6.0$, $\eta = 0.01$, $\gamma = 5/3$) after 160 units of time. The resolution is 4 zones/R_b.

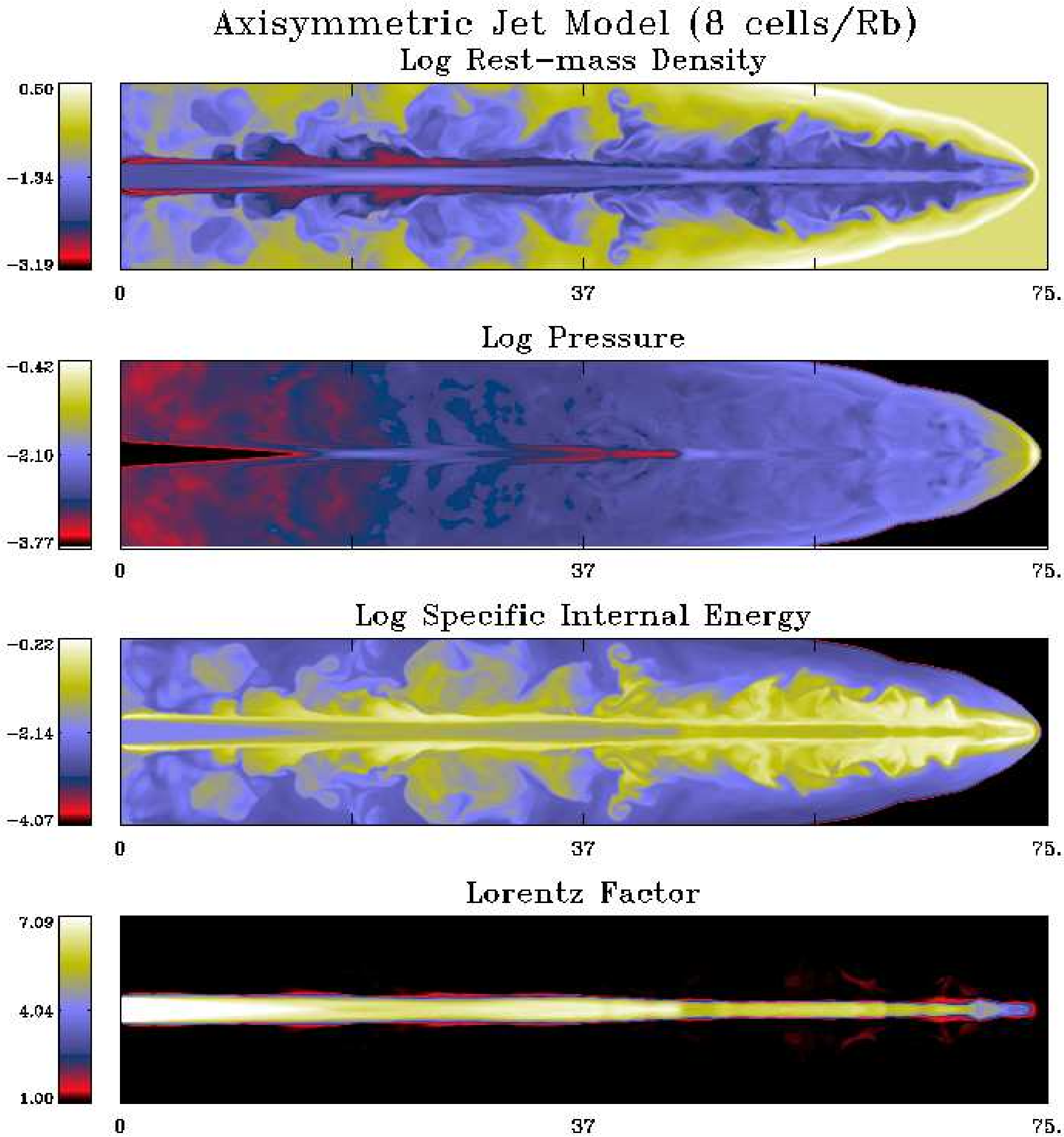

Fig. 3.2.— Same as Fig. 3.1 but with a resolution of 8 zones/R_b.

In the model with 4 zones/R_b (see Fig. 3.1), the material deflected at the head of the jet forms a thick, stable overpressured cocoon surrounding the beam up to the nozzle. Due to the small resolution only large vortices develop in the cocoon/external medium surface which grow slowly. A turbulent cocoon with smaller vortices growing at a faster rate (much more similar to the one got in the 2D cylindrical model) are obtained by doubling the resolution (compare, *e.g.*, the proper rest–mass density panels in Figs. 3.1, 3.2). There exists a layer of high energy around the beam, which is wider an more energetic in the model with the worst resolution. The layer widens from the nozzle to the hot spot.

3.2.2. General considerations

The calculations in the following sections have been performed with an updated version of the code GENESIS (see Chapter 2), which includes an additional conservation equation for the beam-to-external density fraction to distinguish between beam and external medium fluids. The beam material is injected with a beam mass fraction $f = 1$, and the computational domain is initially filled with an external medium ($f = 0$).

First of all, we will discus in detail the simulation showed in Aloy *et al.* (1999b). In this memory such simulation corresponds to the model n50p01 (see Table 3.1). This model is slightly perturbed compared with the axisymmetric case, but it displays all of the specific 3D morphodynamical features that are common to the remaining simulations. After that we will compare with other perturbed 3D models. Aloy *et al.* (1999b) reported on a high-resolution 3D simulation of a relativistic jet with the largest beam flow Lorentz factor performed up to now (7.09), the largest resolution (8 cells per beam radius), and covering the longest time evolution (75 normalized time units; a normalized time unit is defined as the time needed for the jet to cross a unit length; see Massaglia, Bodo & Ferrari 1996). These facts together with the high performance of our hydrodynamic code allowed us to study the morphology and dynamics of 3D relativistic jets for the first time. Here, we consider a wider sample of models to study such features in more detail.

The evolution of the jet was simulated up to $T \approx 150 R_b/c$, when the head of the jet is about to leave the grid. The mean jet propagation speed is $v_h \approx 0.5c$, while $v_{1D} \approx 0.42c$, *i.e.,* our simulations are still within the 1D phase (see Martí, Müller & Ibáñez 1998). The scaled final time $T \approx 4.6\,10^4\,(R_b/100\,\mathrm{pc})$ yr is about two orders of magnitude smaller than the estimated ages of powerful jets. It is expected that in the long term evolution (Martí, Müller & Ibáñez 1998) both the jet advance speed and the jet's head pressure $p_h \approx 2.6\,10^{-7}(\rho_a/10^{-26}\,\mathrm{g\,cm^{-3}})\,\mathrm{dyn\,cm^{-2}}$ decrease until they reach realistic values ($v_h \approx 0.05c$, $p_h \lesssim 10^{-8}\,\mathrm{dyn\,cm^{-2}}$; Daly 1995). Hence, our simulations cannot describe the long term evolution of these sources and conclusions should be extrapolated cautiously.

In order to induce three-dimensional effects, non–axisymmetry was imposed by means of a helical velocity perturbation at the nozzle given by

$$v_b^x = \zeta_p v_b \cos\left(\frac{2\pi t}{\tau_p}\right),\; v_b^y = \zeta_p v_b \sin\left(\frac{2\pi t}{\tau_p}\right),\; v_b^z = v_b\sqrt{1-\zeta_p^2}, \tag{3.2}$$

where ζ_p is the ratio of the toroidal to total velocity and τ_p the perturbation period (*i.e.,* $\tau_p = T/n$, n being the number of cycles completed during the whole simulation). This velocity field causes a differential rotation of the beam, the fluid near the axis rotating faster. The wavelength of the perturbation, λ_p, is obtained from the expression

$$\lambda_p = v_b^z \tau_p \approx \frac{v_b}{v_h}\frac{L}{n}, \tag{3.3}$$

where L is the axial dimension of the grid (in our simulations, 75 R_b). Note that the perturbation is chosen such that it does not change the velocity modulus, *i.e.,* it preserves mass, momentum and energy flux of the beam. Table 3.1 collects the perturbation parameters considered in our study. The chosen parameters try to cover different perturbation types and all their possible combinations. This is the reason to include *high* ($n = 50$) and *low* ($n = 15$) frequency modes and *small* ($\zeta_p = 0.01$) and *medium* ($\zeta_p = 0.05$) amplitude perturbations.

3.2.3. Morphology and dynamics of 3D relativistic jets

Figure 3.3 shows various quantities of the model n50p01 in the plane $y = 0$ at the end of the simulation. Two values of the beam mass fraction are marked with white contour levels. The beam structure is dominated by the imposed helical

Model	n	ζ_p	τ_p	λ_p
n15p01	15	0.01	10	11.8
n15p05	15	0.05	10	11.8
n50p01	50	0.01	3	3.5
n50p05	50	0.05	3	3.5

Table 3.1: Perturbation parameters of the numerical simulations and expected values of the perturbation wavelength.

pattern with a characteristic wavelength of $\approx 3.0R_b$ (to be compared with the value $\lambda = 3.5R_b$ expected from Eq. (3.3)) and an amplitude of $\approx 0.2R_b$.

3.2.3.1. Cocoon

The overall jet's morphology is characterized by the presence of a highly turbulent, subsonic, nearly asymmetric cocoon. The pressure distribution outside the beam is quite homogeneous giving rise to a symmetric bow shock (Figs. 3.3b). As in the classical case (Norman 1996), relativistic 3D simulations show less ordered structures in the cocoon than in the 2D axisymmetric calculations (where strongly structured circular vortices are present). As seen from the beam mass fraction levels, the cocoon remains quite thin ($\sim 2R_b - 3R_b$).

The flow field outside the beam shows that the high velocity backflow is restricted to a small region in the vicinity of the hot spot (Fig. 3.3e), the largest backflow velocities ($\sim 0.5c$) being significantly smaller than in 2D models. The flow annulus with high Lorentz factor found in axisymmetric simulations (see flow patterns in Martí *et al.* 1996) is also present, but it is restricted to a thin layer around the beam and possesses sub-relativistic speeds ($\sim 0.25c$). The smallness of the backflow velocities in the cocoon do not support the possibility of having relativistic beaming of the emitting material moving backwards in the counter-jet. The unrealistically large speed of the hot spot (see Sect. 3.2.3.4) prevents fast backflows because the

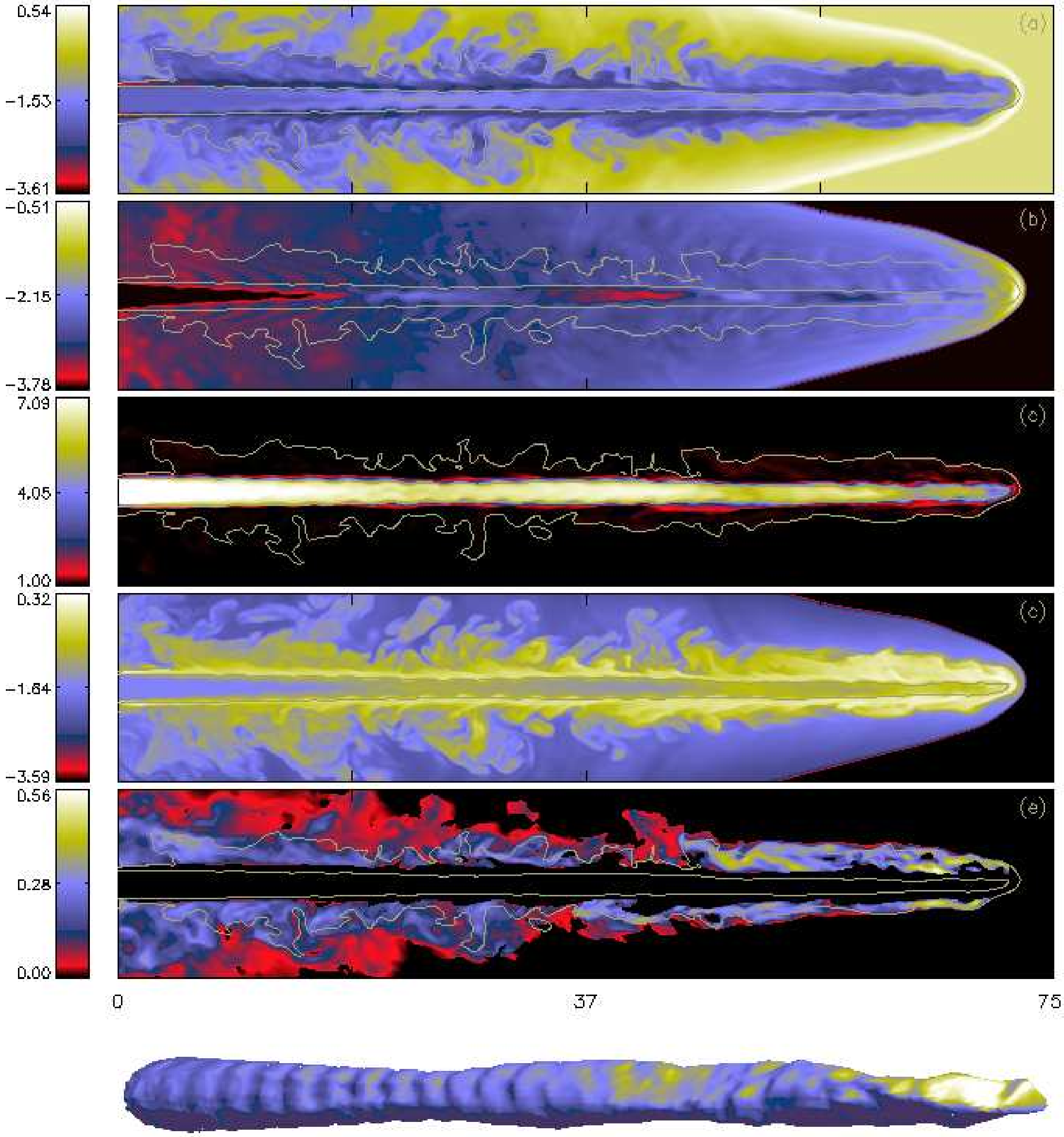

Fig. 3.3.— Rest-mass density, pressure, flow Lorentz factor, specific internal energy and backflow velocity distributions (from top to bottom) of the model n50p01 in the plane $y = 0$ at the end of the simulation. White contour levels appearing in each frame correspond to values 0.95 (inner contour; representative of the beam) and 0.05 (representative of the cocoon/shocked external medium interface) of the beam mass fraction. The bottom panel displays the isosurface of beam mass fraction equal to 0.95.

material efficiently pushes the terminal contact discontinuity and, therefore, only a small fraction of the beam fluid is deflected backwards. However, as the hot spot pressure is larger too, it favors the acceleration of the rear-going beam material.

3.2.3.2. Beam and hot spot

Within the beam the perturbation pattern is superimposed to the conical shocks at about 26 and 50 R_b. The beam does not exhibit the strong perturbations (deflection, twisting, flattening or even filamentation) found by other authors in the classical case (Norman (1996) for 3D HD jets; Hardee (1996) for 3D MHD jets). This can be taken as a sign of stability, although it can be argued that our simulation has not evolved far enough. The beam cross section and the internal conical shock structure are correlated (Fig. 3.3). Before the first recollimation shock the beam cross section shrinks to an effective radius of $0.7R_b$. After this shock and in the rarefaction the beam reexpands and stretches due to an elliptical surface mode (*e.g.*, Hardee 1996). Between $37R_b \lesssim z \lesssim 50R_b$ the beam flow is influenced by the second recollimation shock, which causes a compression of the beam. A triangular mode seems to grow in this region.

The helical pattern propagates along the jet at a velocity which is intermediate between the jet's head speed and the beam speed[10] which could yield to superluminal components when viewed at appropriate angles. Besides this superluminal pattern, the presence of emitting fluid elements moving at different velocities and orientations could lead to local variations of the apparent superluminal motion within the jet. This is shown in Fig. 3.4, where we have computed the mean (along each line of sight, and for a viewing angle of 40 degrees) local apparent speed. The distribution of apparent motions is inhomogeneous and resembles that of the observed individual features within knots in M87 (Biretta, Zhou, & Owen 1995). In this source, whereas a typical apparent speed of 0.5c is measured for knots A, B and D, small regions within the knots show a large range in speeds (up to 2.5c). Besides that, significant motions transverse to the jet axis were found in knots A, B and C with a trend for

[10]see animation at http://scry.uv.es/aloy.html/JETS/videos/n50p01

larger transverse speeds at larger distances from the nucleus, and specially in the regions where the jet appears to bend and oscillate form side to side.

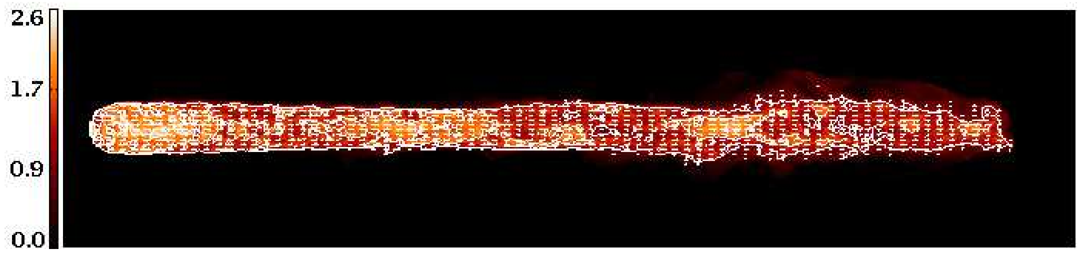

Fig. 3.4.— Mean local apparent speed for the jet of Fig. 3.3 observed at an angle of 40 degrees. Arrows show the projected direction and magnitude of the apparent motion the contours corresponding to values of $1.0\,c$, $1.6\,c$, and $2.2\,c$, respectively. Averages have been computed along each line of sight using the emission coefficient as a weight.

The jet can be traced continuously up to the hot spot which propagates as a strong shock through the ambient medium. Beam material impinges on the hot spot at high Lorentz factors. We could not identify a terminal Mach disk in the flow. We find flow speeds near (and in) the hot spot much larger than those inferred from the one dimensional estimate. This fact was already noticed for 2D models by Komissarov & Falle (1996) and suggested by them as an acceptable explanation for an excess in hot spot beaming.

3.2.3.3. Beam/cocoon shear layer

We find a layer of high specific internal energy (Fig. 3.3d) surrounding the beam like in previous axisymmetric models (Aloy *et al.* 1999a or §3.2.1) although in the specific internal energy is higher in the perturbed models (by more than a factor of 3). A comparison with the backflow velocities (Fig. 3.3e) shows that it is mainly composed of forward moving beam material at a speed smaller than the beam speed. The intermediate speed of the layer material is due to shear in the beam/cocoon interface, which is also responsible for its high specific internal energy. It is possible to characterize the shear layer, in order to have an operative criterion, as the region having a beam mass fraction $0.2 < f < 0.8$.

The existence of such a boundary layer has been invoked as the cause of a smooth deceleration of the material in the jet which offers an admissible explanation for the existence of emission gaps close to the jet basis and the decrease of the jet sidedness ratio with distance from the nucleus (Laing 1996). For appropriate angles to the line of sight, it would be also responsible of the limb brightening of the jets (Komissarov 1990).

De Young (1993) has compared boundary layers in laboratory experiments with the ones in FR Is as inferred from observations to constrain the properties of the ambient medium surrounding these sources. Additionally, De Young has concluded that the very low radio luminosity of the jets in FR IIs and the lack of deceleration may be due to the relatively weak interaction of the jets in these sources with the ambient (*i.e.,* if a boundary layer exists in FR IIs, its relative importance in the dynamics is smaller than in FR Is). However some manifestation of these boundary layers in FR IIs has been reported recently (Swain, Bridle & Baum 1998). Relying on total and polarized radio observations of the jets in the FR II radio galaxy 3C 353 the authors infer that most of the jet emission comes from a thick outer layer where the magnetic field has no component transverse to the jet axis and where the axial and toroidal components are random and approximately in equipartition. The authors suggest as a possible interpretation that the emission layer is a boundary layer where the field is ordered by velocity shear, the apparently lower emissivity near the jet axis being produced by Doppler hidding of emission from fast flowing material in the jet core.

The diffusion of vorticity caused by numerical viscosity is responsible for the formation of the boundary layer. Although being caused by numerical effects (and not by the physical mechanism of turbulent shear) the properties of PPM–based difference schemes are such that they can mimic turbulent flow to a certain degree (Porter & Woodward 1994). Hence, our calculations represent a first approach to study the development of shear layers in relativistic jets and their observable consequences.

The structure of both the shear layer and the beam core are sketched in Fig 3.5. The specific internal energy of the gas in the shear layer is typically more than one order of magnitude larger than that of the gas in the beam core. The shear layer broadens with distance from $0.2R_b$ near the nozzle to $1.1R_b$ near the head of the jet (Fig. 3.6).

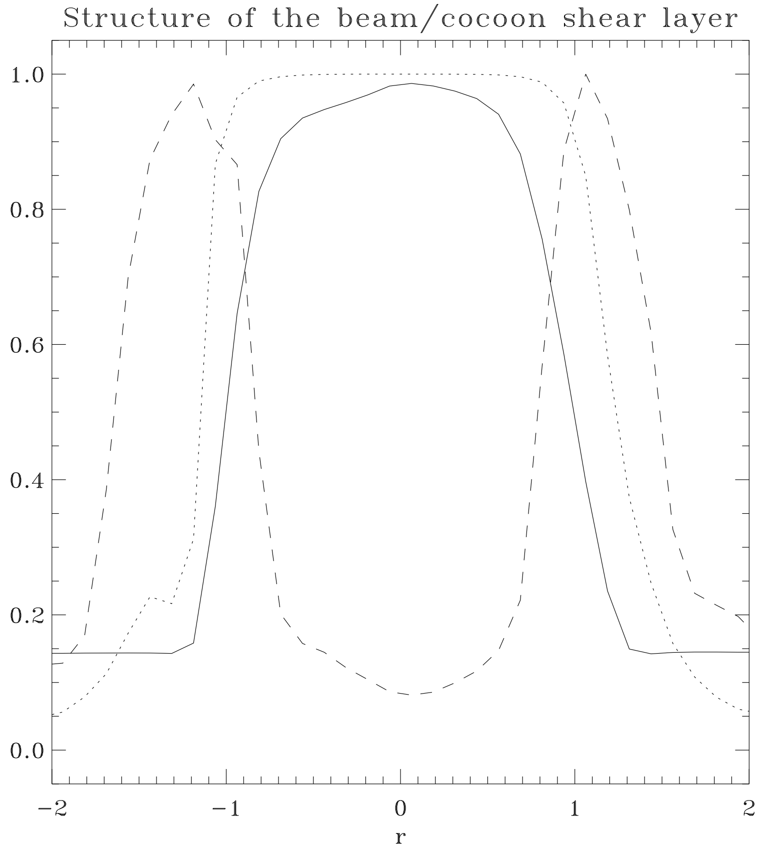

Fig. 3.5.— Beam mass fraction (dotted line), flow Lorentz factor (filled line) and specific internal energy (dashed line), in arbitrary units, accross the beam ($z = 11.7R_b$). Model n50p01.

3.2.3.4. Jet propagation efficiency and disruption

The mean jet advance speed is $0.47c$, but the jet's propagation proceeds in two distinct phases: (i) for $t \lesssim 100$ the jet propagates roughly at the estimated 1D speed ($0.42c$); (ii) for $t \gtrsim 100$ the jet accelerates and propagates faster ($0.55c$). Comparing with the 3D simulation of Norman (1996) we find a similar behaviour: after a short 1D phase and before the deceleration, the jet transiently accelerates to a propagation speed which is $\approx 20\%$ larger than the corresponding 1D estimate. This result contradicts the one obtained by Nishikawa *et al.* (1997, 1998), who found a propagation speed of only 70% of the corresponding 1D estimate in a shorter ($\approx$ 20 normalized time units) simulation of a denser jet. During phase (i) the propagation speed slightly oscillates around the 1D value, a behaviour already found for classical jets (Norman *et al.* 1982) and for axisymmetric relativistic jets (Martí *et al.* 1997). It can be understood in terms of the periodic variations in the terminal shock structure changing from Mach disk to biconical and back. Figure 3.6 shows the axial component of the momentum of the beam particles (integrated across the beam) along the axis, which decreases by 45% within the first $60\,R_b$. Neglecting pressure and viscous effects, and assuming stationarity the axial momentum should be conserved, and hence the beam flow is decelerating. The momentum loss goes along with the growth of the boundary layer whose material is accelerated and heated by viscous stresses. Biconical shocks in the beam are responsible for the break in the axial momentum profiles at $z = 26R_b$ and $z = 50R_b$, because when the beam material passes a conical shock and enters into the adjacent rarefaction fan, it is accelerated by local pressure gradients.

How can the jet accelerate while the beam material is decelerating? Although the beam material decelerates, its terminal Lorentz factor is still large enough to produce a fast jet propagation. On the other hand, in 3D, the beam is prone to strong perturbations which can affect the jet's head structure. In particular, a simple structure like a terminal Mach shock will probably not survive when significant 3D effects develop. It will be substituted by more complex structures in that case, *e.g.,* by a Mach shock which is no longer normal to the beam flow and which wobbles around the instantaneous flow direction. Another possibility is the generation of oblique shocks near the jet head due to off–axis oscillations of the beam. Although difficult to check quantitatively (due to both the lack of an operative definition for Mach disk identification and the present resolution of our simulations[11]) both possibilities will cause a less efficient deceleration of the beam flow at least during some epochs. At longer time scales the growth of 3D perturbations will cause the

[11]In practice, the resolution of our simulations is mainly limited by the available RAM memory of the computer employed

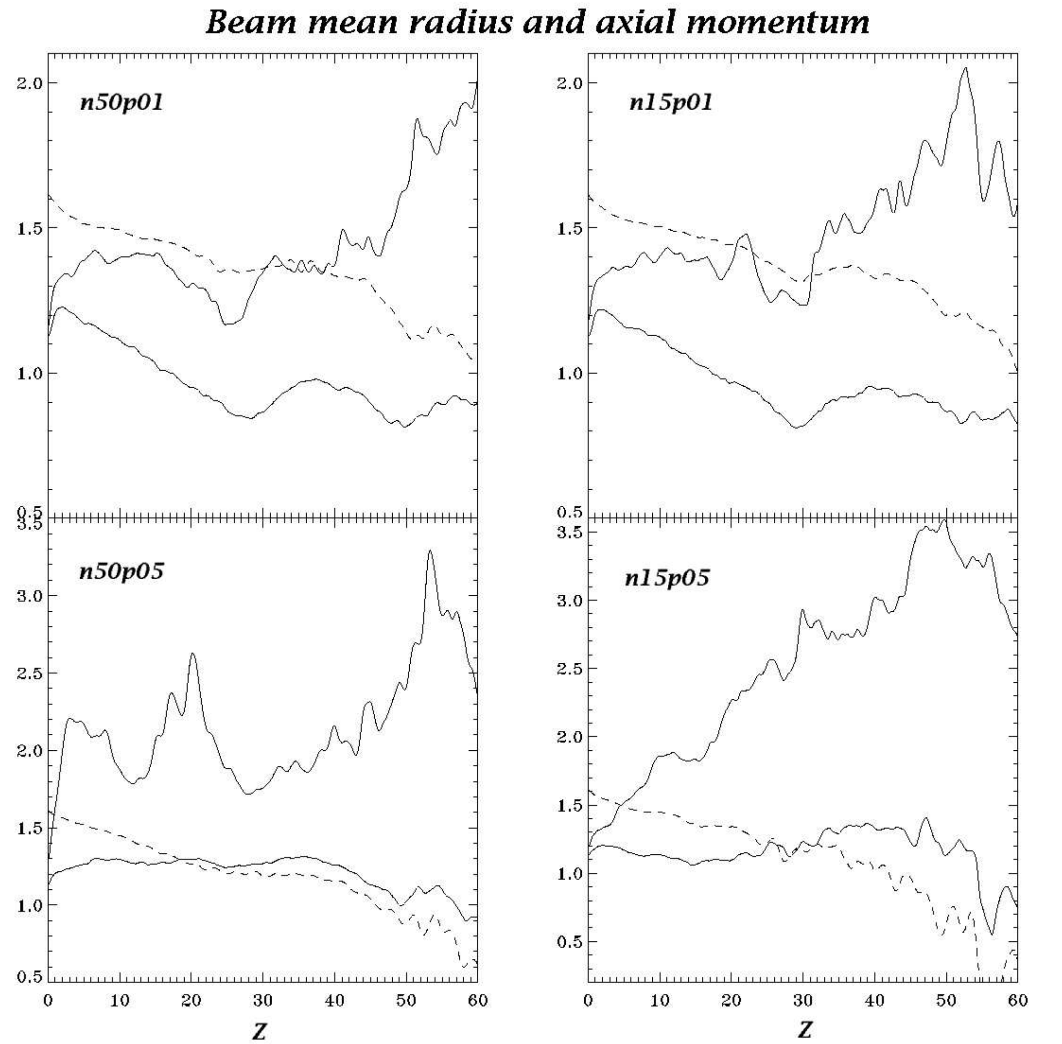

Fig. 3.6.— Into each panel, the dashed line represents the axial component of the momentum of the beam particles (integrated accross the beam) along the jet axis at the end of the simulation. The solid lines mean beam radius as a function of distance for a beam particle fraction $f \geq 0.2$ (top line) and $f \geq 0.8$ (bottom line), respectively. Quantities are in code units.

beam to spread its momentum over a much larger area than that it had initially, which will efficiently reduce the jet advance speed.

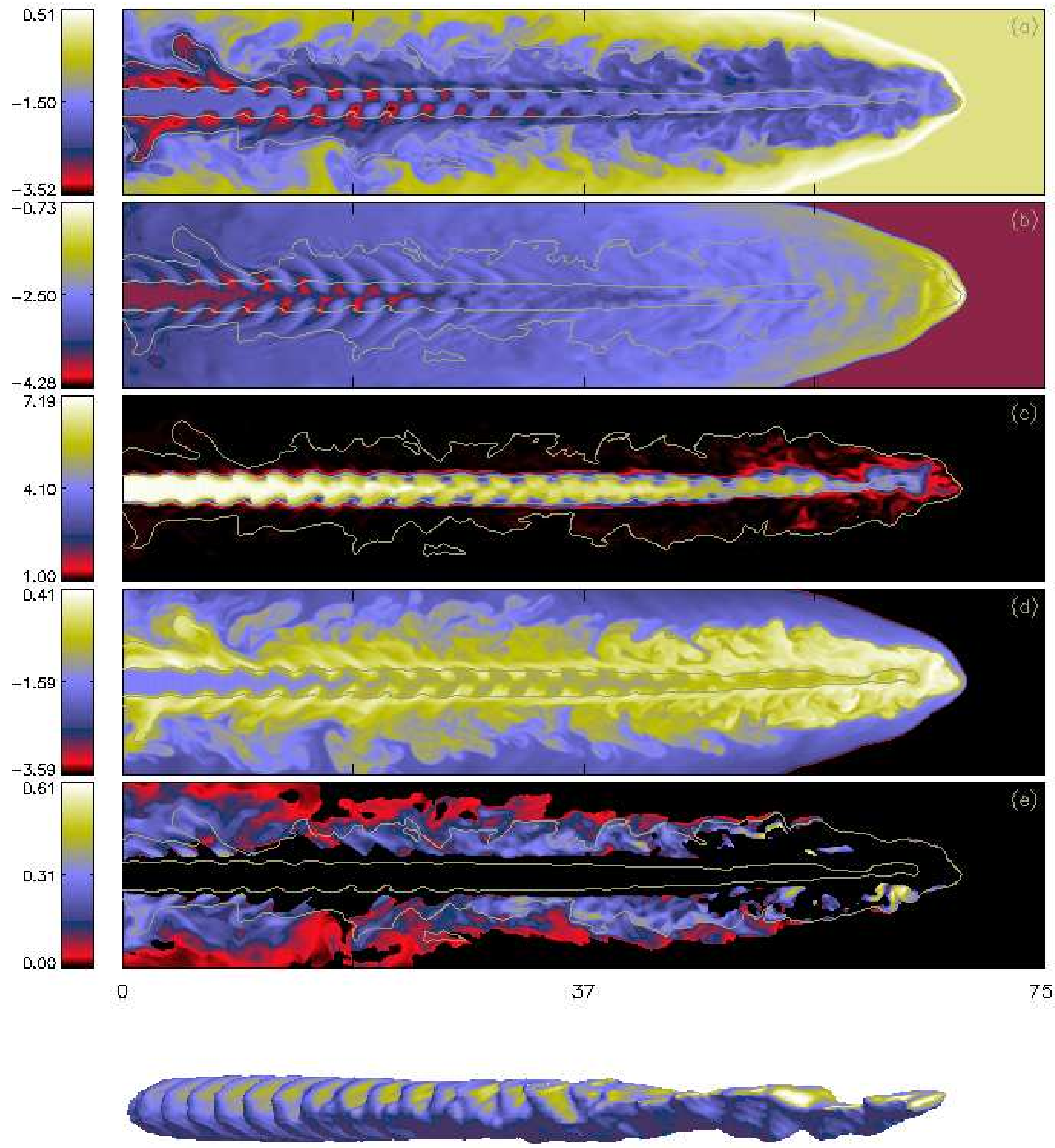

Fig. 3.7.— Same as Fig. 3.3 for model n50p05.

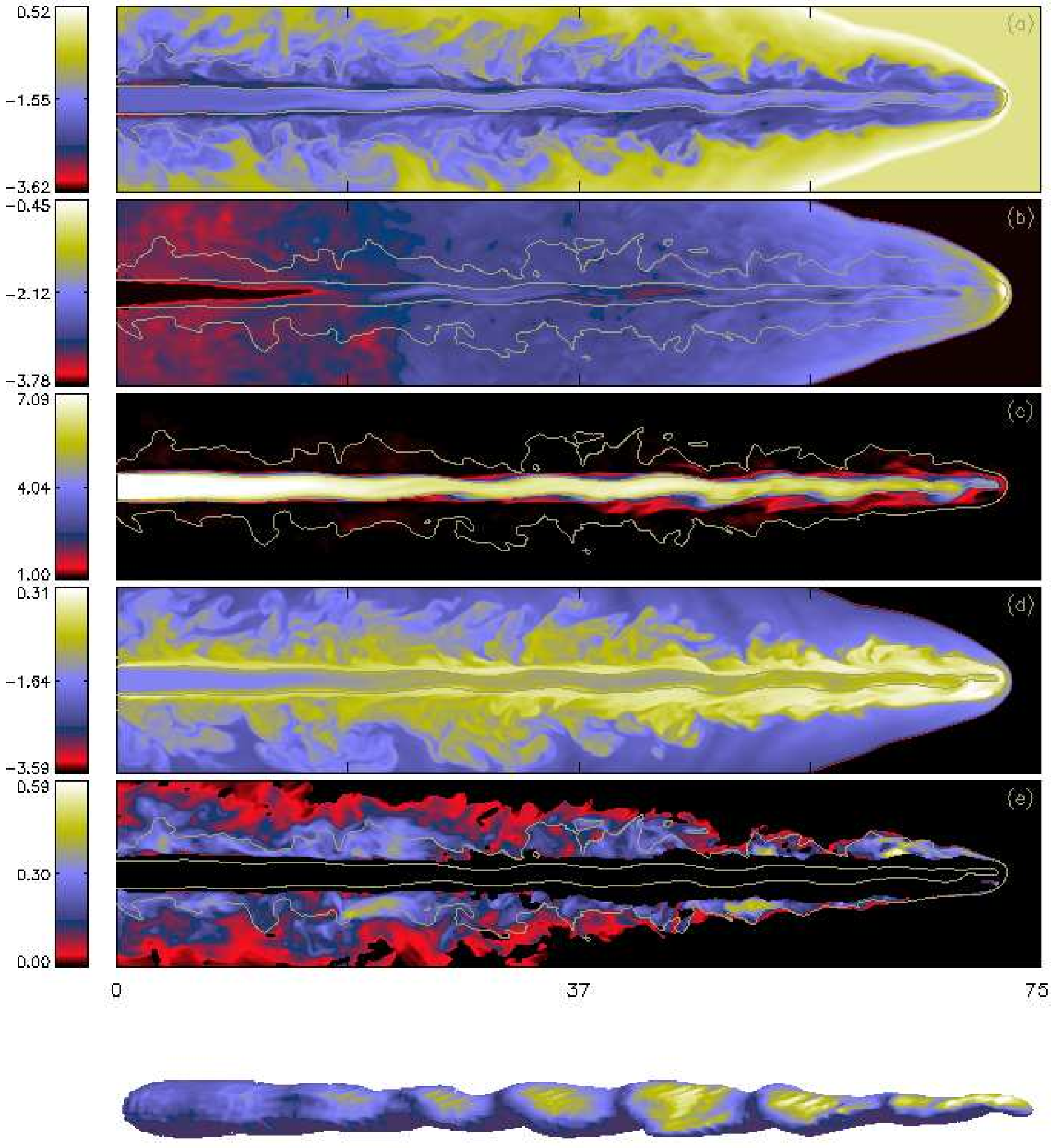

Fig. 3.8.— Same as Fig. 3.3 for model n15p01.

Model	Amplitude (R_b)	λ_p (R_b)	v_h
n15p01	0.2	9.1	0.46
n15p05	1.3	9.0	0.40
n50p01	0.2	3.1	0.48
n50p05	0.4	2.9	0.46

Table 3.2: Approximate numerical values of the perturbation amplitudes, wavelengths and mean jet head propagation speeds of the numerical simulations.

3.2.4. Other models

Next we discuss other models obtained varying the perturbation parameters (Table 3.1). As in the n50p01 case, the evolution of the jets was simulated up to $T \approx 150 R_b/c$. The mean jet propagation speeds (see Table 3.2) lie in the interval $v_h \in [0.4c, 0.5c]$ (compare with $v_{1D} = 0.42c$), so that all of them are still within the 1D phase. Figures 3.7-3.9 show various quantities of the jet in the plane $y = 0$ at the end of the simulation. In every case, the beam structure is dominated by the imposed helical pattern with characteristic wavelengths and amplitudes given in Table 3.2 (to be compared with the values given in Table 3.1 expected from Eq. 3.3).

High frequency modes tend to stabilize the jet despite of the strength of the perturbation, because for $n = 50$, the amplitudes remain below 0.4 R_b, and the morphology is more similar to the non perturbed model (see Fig. 3.2). Low frequency modes seem to be much more perturbed, particularly, the model n15p05 displays the largest off-axis perturbations that, eventually, can made the jet to enter into a disruptive phase on larger time scales. The explanation for this is that for low frequencies of the perturbation, the velocity field at the injection nozzle points into each considered solid angle more time than for high frequencies and, consequently, beam material travels farther in directions normal to the jet axis. Hence, the amplitude of the beam distortion is larger. As expected, the strongest perturbation ($\zeta = 0.05$) induces bigger amplitudes for the same frequency.

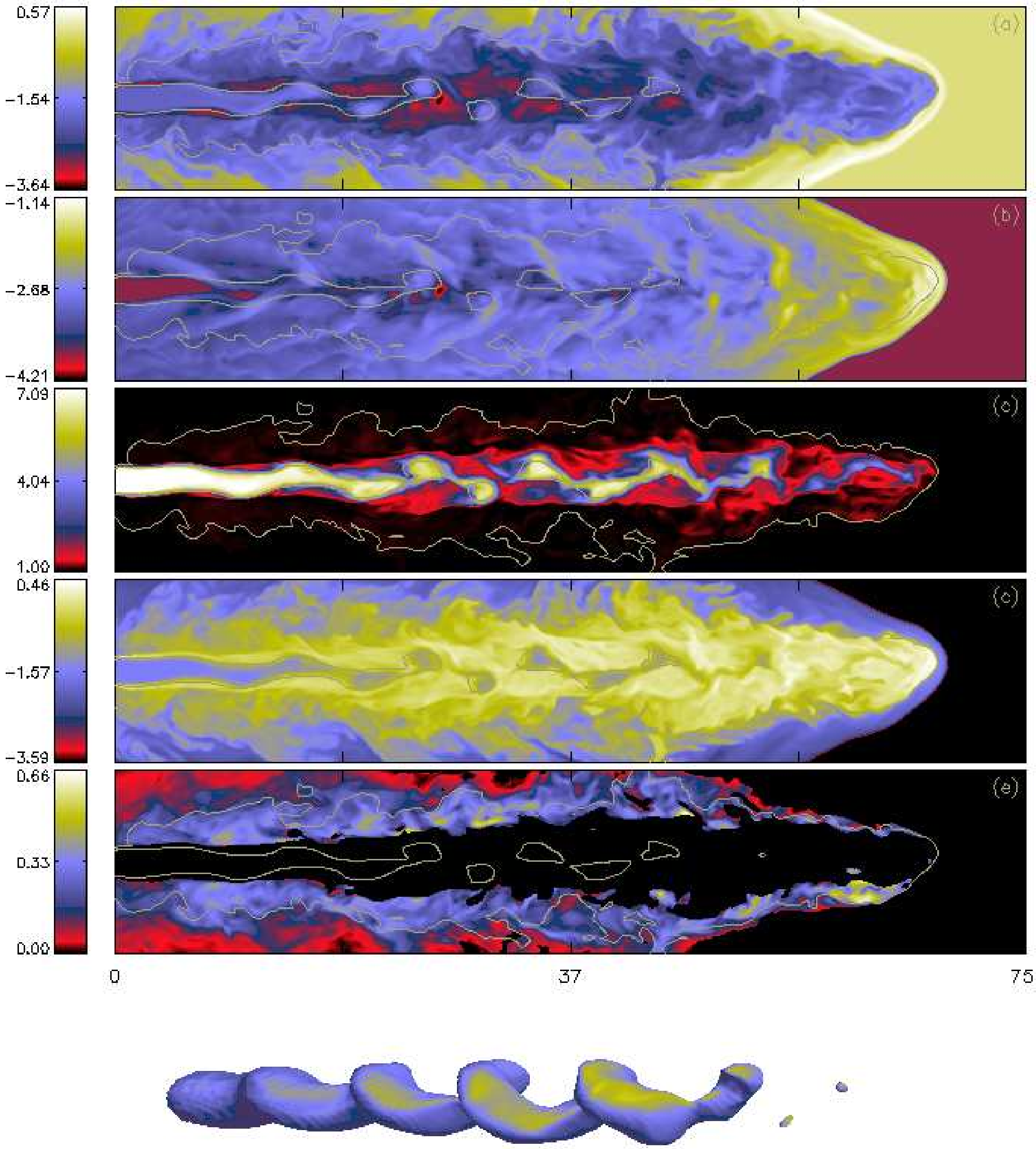

Fig. 3.9.— Same as Fig. 3.3 for model n15p05.

3.2.4.1. Cocoon

Similarly to n50p01, the cocoon is highly turbulent, non-asymmetric and subsonic. It remains quite thin for models with $\zeta_p = 0.01$ but it widens for models with $\zeta_p = 0.05$ ($\sim 3R_b - 5R_b$) as long as the jet propagates efficiently. Nevertheless, the model n15p05 displays a supersonic envelop around the beam formed by material which is dragged by the off-axis perturbed beam material. The beam in this case acts rarefying some regions of a channel (see *e.g.,* the little dark holes at $z = 27R_b$ in panels a and b of figure 3.9) of radius $\sim 1.3R_b$[12]. The dragging effect is due to a mixture of the viscous forces that exist between the beam and the surrounding medium and the Venturi effect that the moving beam material exerts on the surrounding cocooun.

A layer with a relatively high Lorentz factor can be found around the beam (thinner in the models with $\zeta_p = 0.01$ than in those with $\zeta_p = 0.05$), nevertheless, the mean speed of this layer is sub–relativistic ($\sim 0.25c - 0.35c$). The highest backflow velocities ($\sim [0.5c, 0.7c]$) are restricted to a small region in the vicinity of the hot spot (Figs. 3.7-3.9 panels e) and are significantly smaller than in 2D models (consecuently, in no case a relativistic beaming of the counter–jet is feasible). This is due to several factors; the first one is the additional degree of freedom in 3D, which allows the backflow to move in directions different to the one determined by the Z-axis. The second factor is the unrealistically large speeds of the hot spots (see Sect. 3.2.3.4) which prevents fast backflows in models with small perturbations. However, an effect that helps to have larger backflow velocities is the bigger hot spot pressures (see Table 3.3), which favor the acceleration of the deflected beam material, at least for the less perturbed models. For largest perturbation (*e.g.,* model n15p05) the hot spot pressure is smaller than in 2D and, consistently, the propagation speed is the lowest one. Let us remain that $v_h \propto (p_{\rm hs}/\rho_{\rm ext})^{1/2}$, and as can be seen in the second row of Table 3.3 this proportionality is almost confirmed (the constant of proportionality is $\sim 1.42 - 1.93$ for 3D models). Another practical conclusion which may be extracted from Table 3.3 is that the hot spot pressure decreases as the size of the perturbation grows (an explanation for this trend is given below).

---

[12]This is precisely the perturbation amplitude corresponding to this model.

Model	2D	3D	n15p01	n15p05	n50p01	n50p05
$\log p_{\rm hs}$	-0.82	-0.42	-0.45	-1.14	-0.51	-0.73
$\frac{\sqrt{p}_{\rm hs}}{v_h}$	1.79	1.93	1.74	1.42	1.61	1.51

Table 3.3: Values of the hot spot pressure for the unperturbed (2D model C2 of Martí *et al.* 1997, and 3D axisymmetric reference model) and perturbed models at the end of each simulation. The second row shows the constant of proportionality between the hot spot pressure and the mean velocity of the head.

3.2.4.2. Beam and Hot spot

The models with low frequency or high ζ_p value display some twisting, flattening and local deflections of the jet head, although no evident signs of filamentation have been found (see beam mass fraction isosurfaces on Figs. 3.3, 3.7 – 3.9). However, it is remarkable that nor these 3D effects is strong enough to break the beam neither they grow significantly over the linear regime to be disruptive during the simulation run time. Even if this may be a sign of stability, let us remind the reader that in Sect. 3.2.2 we argued that our simulations were still in the 1D phase and, furthermore, our simulations have run for a "physical time" two orders of magnitude smaller that the real sources, and therefore, the perturbations might not have had enough time to grow substantially.

Within the beam the perturbation pattern is superimposed to the shocks. To determinate the location of the shocks we have considered the relative increments of the averaged pressure over each cross section of the beam ($\bar{p}_k^b$[13]). The results are plotted on Fig. 3.10, where the most significative feature is the relative maximum of $\bar{p}_k^b$ in the interval [26, 29] R_b. This fact, together with the increment in density and the jump in velocity, allows us to conclude that the maximum is associated to a recollimation shock. In the 2D axisymmetric case, considering that the evolution

[13]The mathematical definition of this variable is: $\bar{p}_k^b = \frac{\sum_{i,j,f_{ijk}>0.85} p_{ijk} f_{ijk} \Delta x_i \Delta y_j}{\sum_{i,j,f_{ijk}>0.85} f_{ijk} \Delta x_i \Delta y_j}$

of the model C2 has arrived only to 130.23 R_b/c, the first recollimation shock is at 17 R_b(the second shock $\sim 34\,R_b$). The recollimation effect is seen in isosurfaces of f (Figs. 3.3, 3.7 – 3.9) and is presented in Fig. 3.10 as a decrement of $\bar{p}_k^b$ which is inversely proportional to the beam cross section.

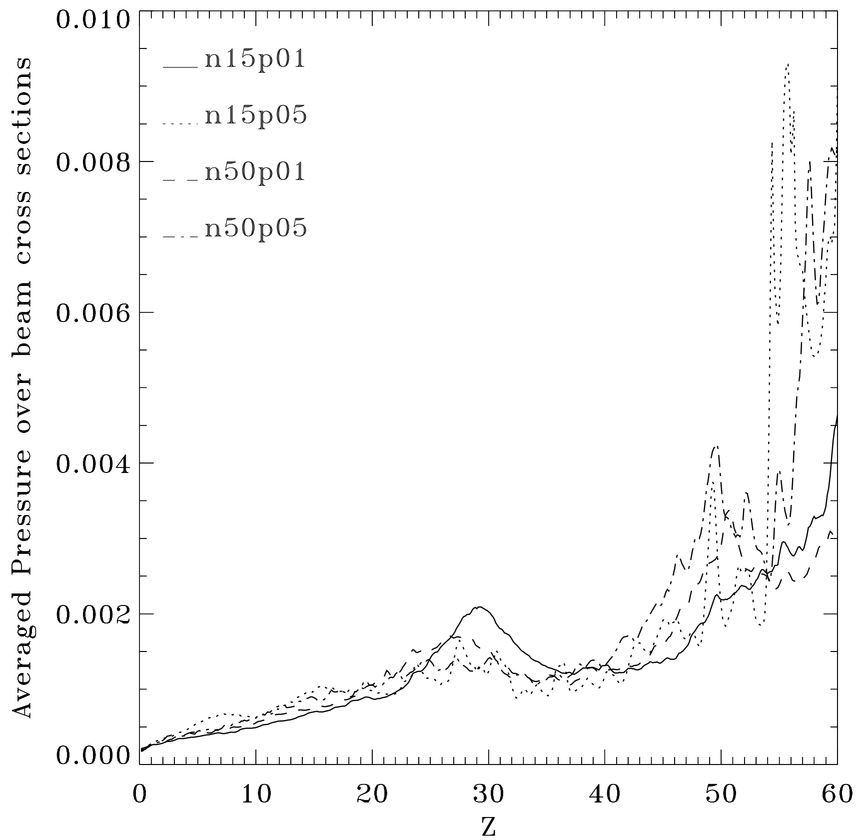

Fig. 3.10.— Averaged beam pressure over each beam cross section.

In the less perturbed models, another recollimation shock is seen at about 50 R_b. This shock seems to disappear in the model n15p05. An acceptable explanation is that all the models are produced as perturbations on a reference axisymmetric one which has the first biconical shock at about 27 R_b, so that it is natural that the structure of the reference model is partially retained by the perturbed ones at least during an initial phase. This justifies the presence and location of the first shock (it is closer to the injection point and the estructure within this region is still dominated by the initial data). However, as the jets evolve the non linearity of the modes excited by the perturbation give rise to a quantitatively different morphology at larger scales. A confirmation of this point is that the beam in the model n15p05 is highly distorted after $50\,R_b$, and the main shock structure is almost lost.

The beam structure is very similar for the models n50p01 (Fig. 3.11) and n15p01 (Fig. 3.13) and, in both cases an effective radius of $0.7R_b$ results from the stretching of the beam cross section (see subsection 3.2.3.2) between the first and the second recollimation shock. Of course, the main difference between both models is that the amplitude of the perturbation is larger for n15p01 than for n50p01 and, consequently, the *beam local axis* oscillates more in n15p01 than in n50p01.

The models n50p05 (Fig. 3.12) and n15p05 (Fig. 3.14) show a smaller contraction of the beam after the first recollimation shock. In the model n50p05, the perturbation symmetrizes the beam shape in such a way that it seems almost circular up to $\sim 33\,R_b$. Then, the cross section shrinks and starts to develop a triangular mode at $\sim 48\,R_b$. Approximately $10\,R_b$ farther this mode is about to break in filaments the beam. The model n15p05 is actually so perturbed that is difficult to evaluate the effect of the shock on the beam structure. Additionally, due to the large off-axis oscillations the shape of the beam is highly distorted by elliptical modes (starting at $\sim 24\,R_b$), triangular modes (at $\sim 37\,R_b$) and other non linear effects. Let us remark that is possible that filaments on the beam are not seen due to the numerical diffusion inherent to the advection of the beam mass fraction.

The helical pattern propagates along the jet at different velocities, depending on the perturbation. While for models less perturbed it is closer to the beam speed, for the more perturbed ones it is nearly equal to the head's velocity (*e.g.,* in n15p01 and n15p05 this velocity is ~ 0.46, while their head's velocities are 0.46 and 0.40 respectively). Given that the presence of emitting fluid elements moving at relativistic speeds in non axial directions can lead to local superluminal motions for favored angles to the line of sight, we have analyzed these possibilities: (i) apparent speeds much larger than the one expected for a Lorentz factor ≈ 7 at a certain viewing angle, (ii) large apparent transverse motions in our models by computing the mean (along each line of sight and for a viewing angle of 40 degrees) local apparent speed of all the fluid elements as if they were emitting flows (Fig. 3.4 with arrows showing the magnitude and projected direction of the apparent motion), and (iii) inhomogeneous distribution of apparent speeds. We find that for model n50p01, the first possibility

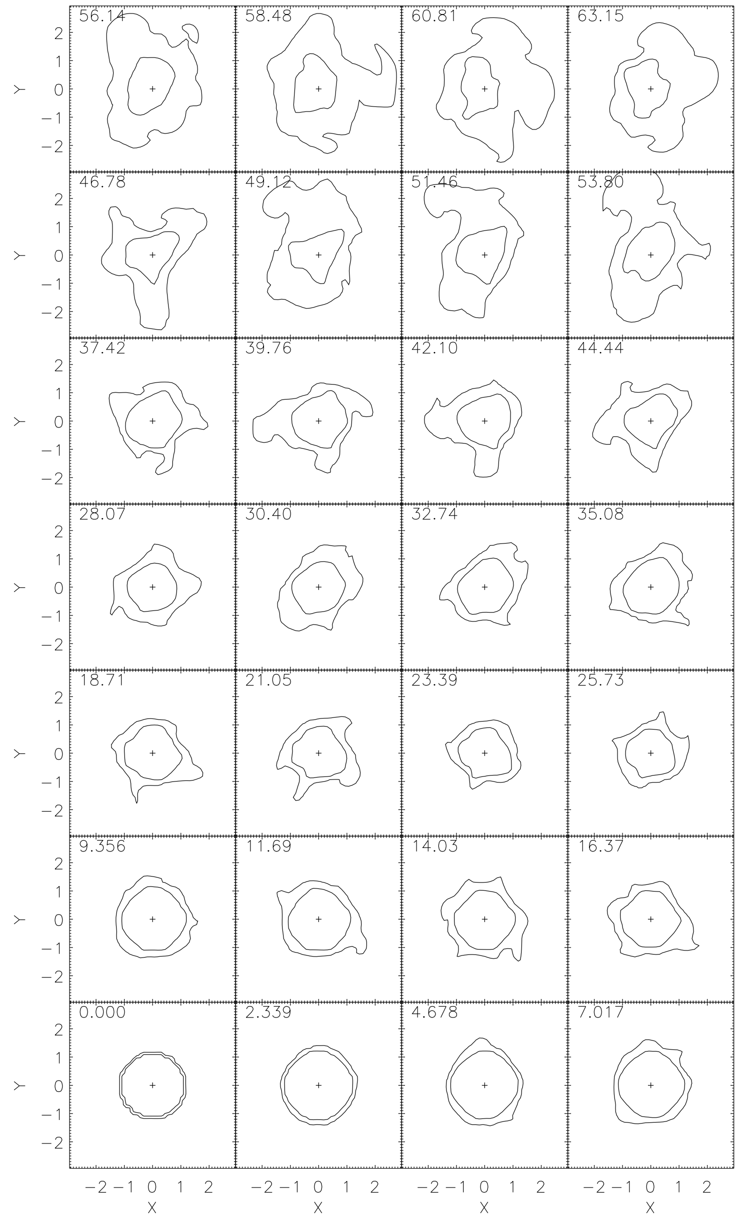

Fig. 3.11.— Shape of the beam mass fraction levels 0.2 and 0.8 for model n50p01 at different distances from the injection point. The central cross represents the $z-$axis.

is rejected because, for the considered viewing angle, the maximum apparent velocity computed is ~ 2.63, which corresponds exactly with the theoretical maximum for the beam speed at the injection point. The second possibility is not completely discarded, although the range of apparent velocities lies in the expected (theoretical)

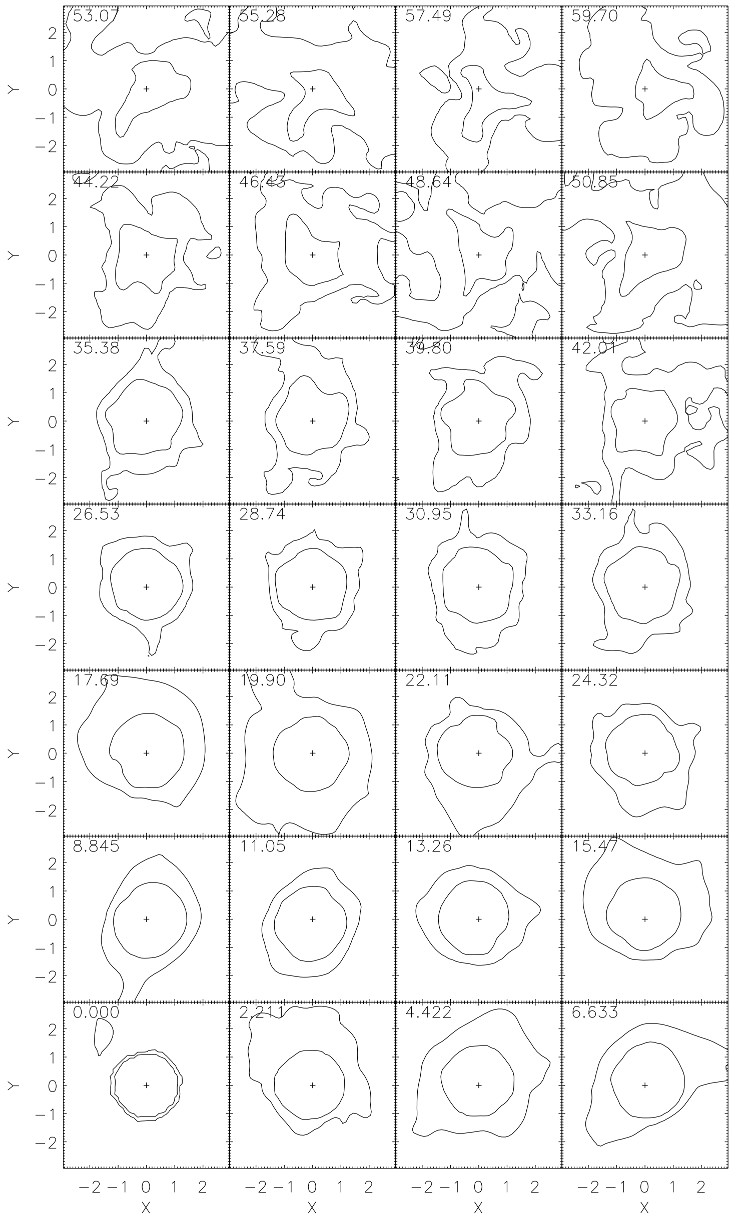

Fig. 3.12.— Same as Fig. 3.11 for model n50p05.

range. However, it is true that we can see a distribution of apparent velocities which is not axisymmetric, and it is the result of the fact that, at the considered time, a number of fluid elements have velocities pointing towards the observer (and this points are enhanced) while other may point in any other direction (having a smaller

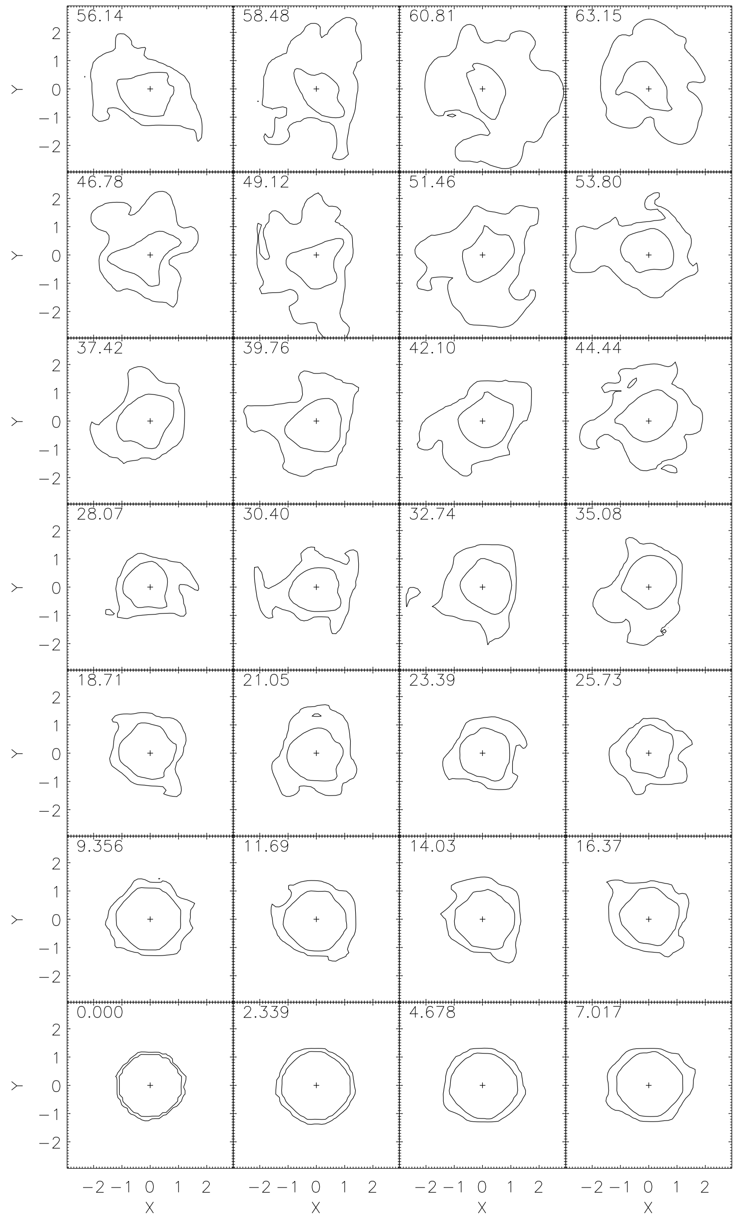

Fig. 3.13.— Same as Fig. 3.11 for model n15p01.

Doppler boosting). Variations of this kind in the apparent velocity field have been found in *e.g.,* M87 (Biretta, Zhou & Owen 1995). The analysis of other models is still not done, however, we expect that all of them satisfy the third possibility. We believe that the model n15p05 is a good candidate to fulfill the second possibility

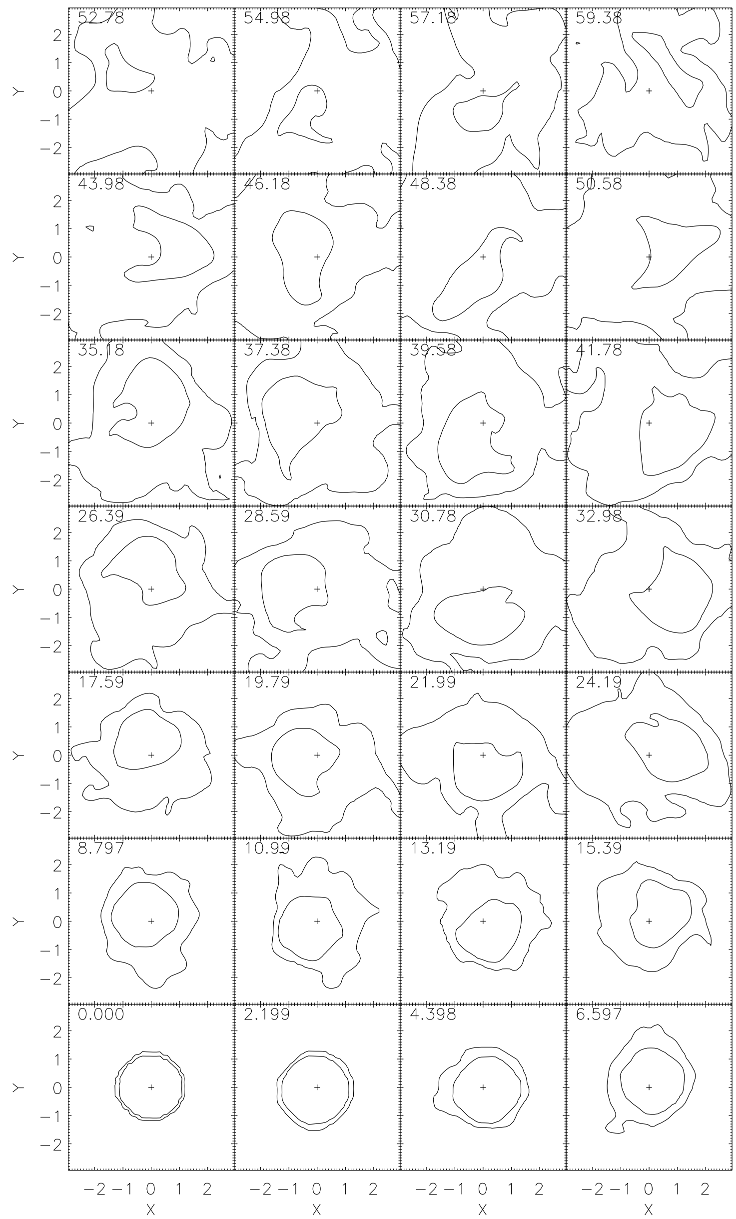

Fig. 3.14.— Same as Fig. 3.11 for model n15p05.

because it displays the largest out of axis motions. In addition, for some angles to the line of sight close to the pitch angle of the helical pattern (roughly 40°; Fig 3.9c) a set of separate components moving with the velocity of the pattern are feasible (although a more detailed analysis is necessary in order to be sure of this assertion).

3.2.4.3. Beam/cocoon shear layer

The layer of high specific internal energy (Figs. 3.3, 3.7 – 3.9 panels d) surrounding the beam and moving forward at a velocity smaller than the beam speed (Figs. 3.3, 3.7 – 3.9 panels e) is present in all the models, but it is more distorted in the more perturbed ones.

The structure of both the shear layer and the beam core are sketched in Figs. 3.5, 3.15 – 3.17 (these figures show one dimensional cuts at a distance of $z = 11.7\,R_b$ from the origin). The specific internal energy of the gas in the shear layer is, in every model, typically more than one order of magnitude larger than that of the gas in the beam core. Table 3.4 shows the approximate range of variation of the width of

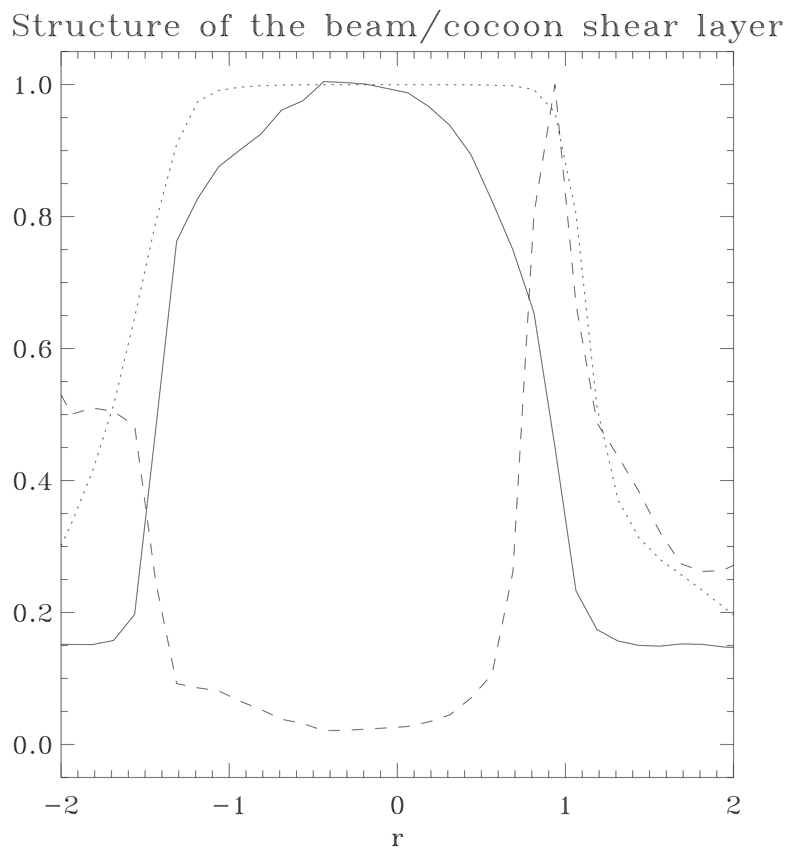

Fig. 3.15.— Same as Fig. 3.5 for the model n50p05.

the core and the shear layer for the models analyzed here. The shear layer broadens with distance from $\sim 0.2\,R_b$ near the nozzle to a value near the head of the jet which is different for every model. Nevertheless, the maximum width of the layer grows with the perturbation size and decreases with the frequency. This trend is shown in Fig. 3.6, where the solid lines display the mean radius as a function of the axial position for the two values of f that determinate the limits of the shear layer.

Model	r_c	Δr_s
n50p01	1.1-0.8	0.2-1.1
n50p05	1.1-0.9	0.2-1.6
n15p01	1.1-0.7	0.2-1.1
n15p05	1.1-0.7	0.2-2.0

Table 3.4: Width of the beam core and shear layer. Values at the left of the variation intervals correspond to values near the injection position whereas values at the right correspond to values near the jet head.

One can realize that the inner part of the shear layer (lower solid lines in the figure) behaves differently for different values of ζ_p. For the models n50p01 and n15p01 the layer grows inwards up to the first recollimation shock ($\sim 26\,R_b$) then it expands and shrinks again reaching a new local minimum at the second recollimation shock ($\sim 48\,R_b$). However, for $\zeta_p = 0.05$ the inner boundary of the shear layer is almost uniform up to $\sim 40\,R_b$ and then it decreases in radius (faster in model n15p05).

A more detailed picture of the shape of the cross section of the shear layer is given by the isocontours $f = 0.2, 0.8$ in Figs. 3.11 – 3.14. Evident signs of disruption of the layer are located from $44\,R_b$ and after, particularly in model n15p05, in which the fixed width selected to display the shear layer (a $3R_b \times 3R_b$ window centered on the initial axis of the simulation) is not enough to capture the full extension of the layer.

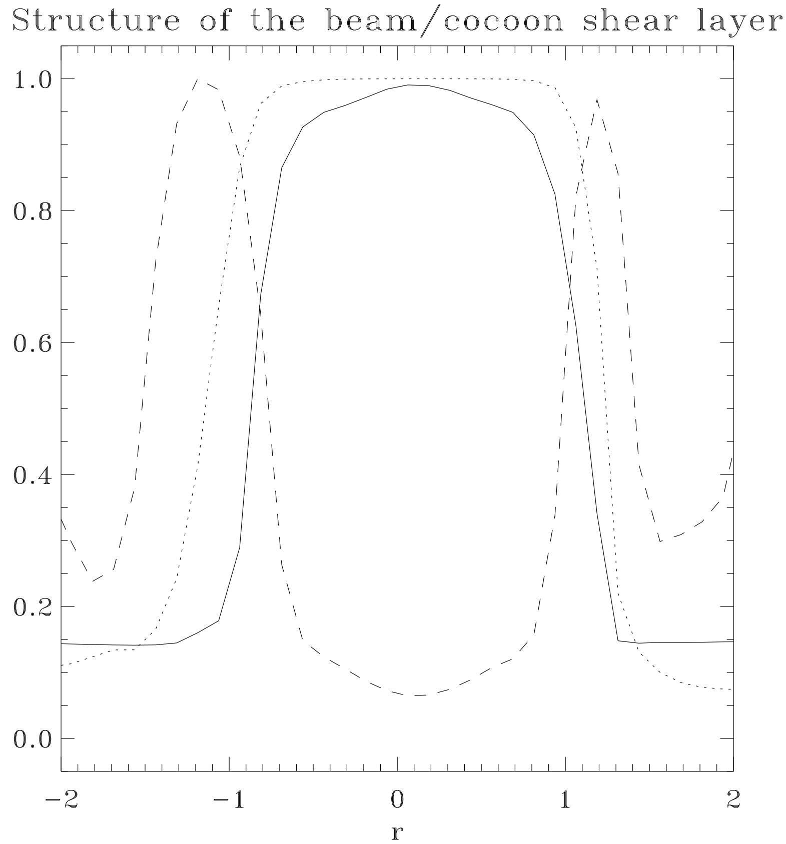

Fig. 3.16.— Same as Fig. 3.5 form the model n15p01.

3.2.4.4. Jet advance and disruption

The evolution of the head's position for every model is displayed in Fig. 3.18. It is noticeable from the head's position at the end of the simulation that the mean jet advance speeds are unrealistically large (the exact values are written in Table 3.2), even larger than the 1D estimated speed of $0.42c$ (except for model n15p05). All the models propagate following two distinct phases which are delimited by a *turning time* (t_{12}) lying in the interval $[85, 110]$, when the head of the jet has propagated along $40\,R_b$. These phases are characterized by different propagation speeds, v_1 (phase 1) and v_2 (phase 2) that are presented in Table 3.5. The general behavior is that the jet starts to propagate with a velocity of $0.43c - 0.45c$, which is close to v_{1D} (but a bit larger). Then, most of the models accelerate at considerably larger speeds (about 9% to 26% larger than the previous v_1 velocities). Contrary to this general

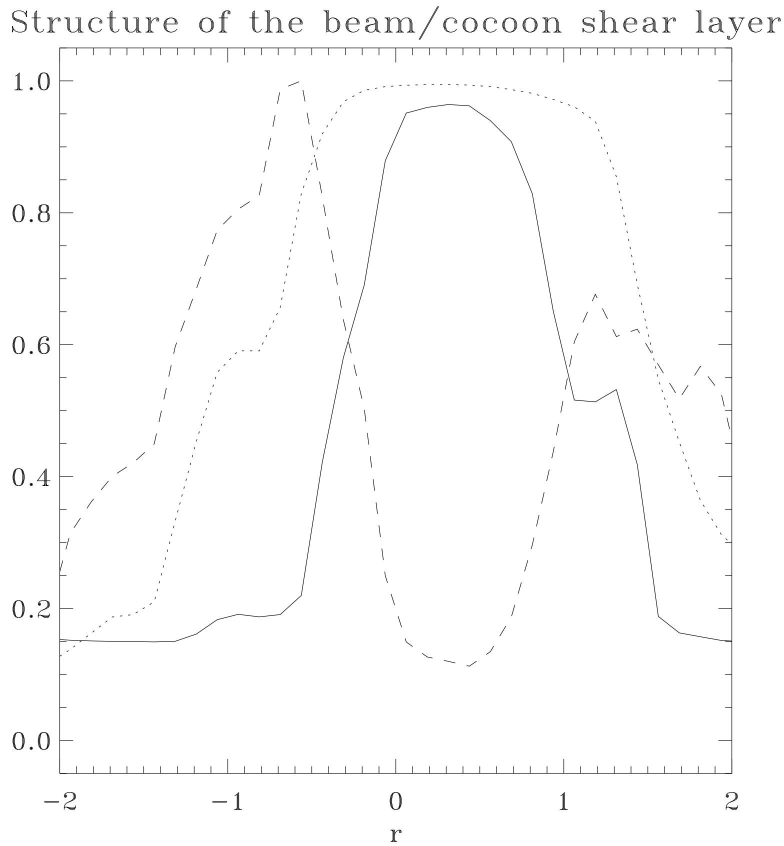

Fig. 3.17.— Same as Fig. 3.5 form the model n15p05.

trend, the model n15p05 decelerates up to $v_2 = 0.37c$. This is again a result of the applied perturbation because as mentioned in previous sections, the cross section of the beam at the jet end is bigger than in the rest of the models. Consequently, the effective advance surface is larger too, and, in addition, the hot spot pressure is the lowest one (see Table 3.3), allowing for a smaller head speed.

From Fig. 3.6 we infer the same qualitative conclusion for all the models than for n50p01 (see 3.2.3.4). The axial component of the momentum of the beam particles decreases and hence the beam flow is decelerating. However, the degree of deceleration is very different for models with $\zeta_p = 0.05$ (the axial momentum at $60\,R_b$ is a factor $\sim 2.7 - 4$ smaller than at injection nozzle) than for those with $\zeta_p = 0.01$ (an smooth momentum loss of $\sim 50\%$ is noticeable in the first $60\,R_b$). This behavior is

Model	v_1	v_2	t_{12}	z_{12}
n50p01	$0.43c$	$0.54c$	85	36
n50p05	$0.45c$	$0.49c$	93	42
n15p01	$0.43c$	$0.52c$	110	46
n15p05	$0.44c$	$0.37c$	80	35

Table 3.5: Velocities of the heads of the jets in each propagation phase. t_{12} and z_{12} are the times and distances that separate the two phases (both quantities in code units).

explained in terms of the growth of the boundary layer (see 3.2.3.4), since this layer is bigger (so that the dissipation of axial momentum due to viscous stresses –which depend on the extension of the contact surface– is bigger) for the strongest perturbation (Figs. 3.12, 3.14) than for the smallest one (Figs. 3.11, 3.13). Furthermore, the strength of the perturbation by itself motivates a change of axial into non-axial momentum, because for $\zeta_p = 0.05$ we are putting in non-axial directions five times more momentum than in the case $\zeta_p = 0.01$. Actually, the perturbation drives the beam along a twisted path instead of along a right one (as in the axisymmetric case), and in order to twist the path, a part of the initial axial momentum is needed. The momentum loss rate is almost constant into the first $40\,R_b$ (of course, it is steeper for $\zeta_p = 0.05$), and then enters into an oscillatory phase which coincides with a region where the cocoon is particularly turbulent and perhaps large external mass entrainment is taking place.

Even if the beam material is decelerating most of the models (except n15p05) accelerate after t_{12}. The suggested mechanism to account for this acceleration has been proposed in subsection 3.2.3.4. However, we expect that at longer time scales the growth of the perturbations will spread the momentum of the beam over a much larger area than that it had initially, reducing the jet advance speed (actually, this is the mechanism that we has started to work for n15p05 –the model having the largest cross sectional area near the head of the jet–).

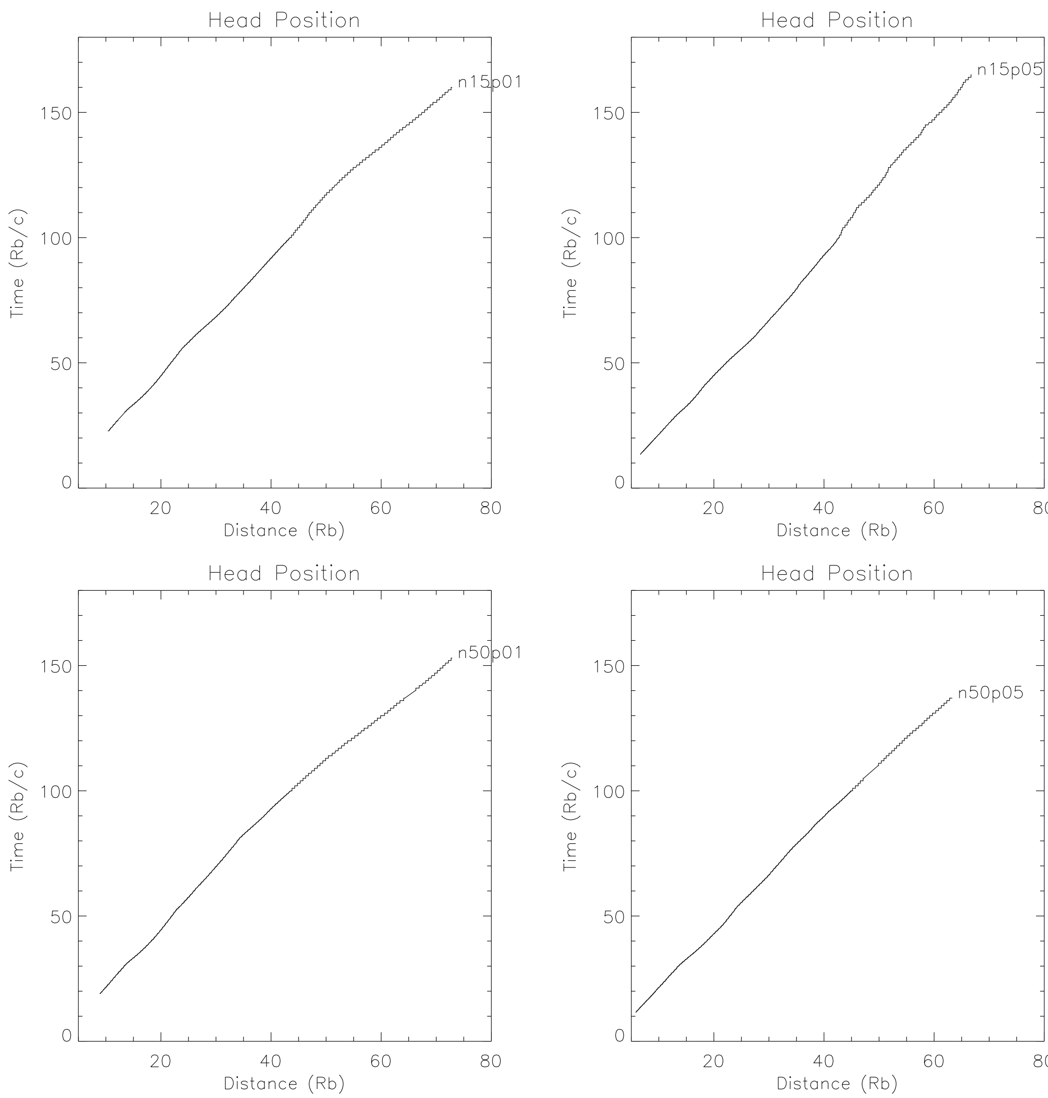

Fig. 3.18.— Evolution of the head's position for every numerical model.

3.3. Emission from 3D relativistic jets

Since the radio-emission is the observable signature of the astrophysical jets, we need to be able to produce radio maps in order to explain totally or partially (*i.e.,* some features) the existent observations. VLBI imaging of some radio-loud AGNs revealed the presence of narrow cones or jets where the radio emission was mainly concentrated, and another smaller regions or components where the emission was more powerful. These components may move at apparent superluminal speeds which is explained in the framework of the standard model (see *e.g.,* Pearson *et al.* 1981, or Sect. 3.1.2) considering a relativistic jet ($W \sim 10$) viewed at small angles to the line of sight.

The analytical models aiming to explain the appearance of radio jets were developed by Jones & O'Dell (1977a,b), Marscher (1980), Marscher & Gear (1985) and Königl (1981). They studied the spectrum of the synchrotron emission produced in different parts of the jet and the perturbations induced on the spectrum of such emission due to the jet inhomogeneities. The inhomogeneities were introduced to mimic the ejection of components in real sources. Such ejections are usually preceded by outbursts in emission at radio wavelengths, whose frequency dependent light curves of both total and polarized flux were successfully interpreted as traveling shock waves (over the underlying steady jet). The three regions in which the jet was divided came from BR74 and, of course, this division relies on a simplified hydrodynamical model (actually, the jet shape is theoretically inferred instead of being the result of a complete numerical calculation).

The standard emission model assumes that the jet (at pc scale) is inertially confined, and it is characterized by its Lorentz factor, the half-opening angle and the distance to a given starting point (the fiducial point). The jet is formed by an ultrarelativistic plasma described as an ideal gas EOS with constant adiabatic index ($\gamma = 4/3$). The plasma is magnetized and the charged particles (electrons, ions or positrons) follow helicoidal paths around the magnetic field lines. Given that the particles are accelerated (due to the helicoidal trajectory), they will emit electromagnetic radiation (the synchrotron radiation). The variations of the magnetic field, the number density per unit of energy, etc., are determined by the adiabatic expansion of the jet. The presence of shocks in the fluid is allowed and they are supposed to comprise two fronts (forward and rear fronts; see Hughes *et al.* 1985) in order to connect the shocked region with the steady jet.

The detected synchrotron emission in the ultraviolet, optic and infrared bands comes from the innermost parts of the jet, which are optically thick to the radioemission. The maximum in the radio band is produced where the Lorentz factor, and hence the Doppler boosting, is maximum. This region is usually identified as the radio-core. The rest of the external part of the jet is optically thin at radio frequencies.

The radiation density in the innermost parts of the jet is a bit larger than the energy density associated to the magnetic field. This makes possible that the relativistic electrons interact with the photons coming from the synchrotron emission increasing their energy (of the photons). This process is known as *synchrotron-self Compton* (SSC). Using this mechanism either X-rays (by first order scattering) or gamma-rays (by second order scattering, being more energetics because the photons have interacted twice with the electrons) are produced. In this region, the internal energy of the relativistic plasma is converted into bulk kinetic energy and the jet accelerates (Marscher 1980; Maraschi *et al.* 1992).

The external part of the jet is characterized by the synchrotron emission in radio and is observed using VLBI. Here the jet does not accelerate any more and expands adiabatically. The conservation of the magnetic flux along with the adiabatic expansion produce a decrease of the magnetic field and the particle density along the jet and, consequently, the synchrotron emission.

The theoretical models gave rise to more detailed numerical models (*e.g.*, Jones 1988; Hughes, Aller & Aller 1989a, b; Marscher, Gear & Travis 1992; Gómez, Alberdi & Marcaide 1993, 1994; Gómez *et al.* 1994) trying to validate the underlying theory and to get the physical jet parameters which were able to match the observations of some sources. However, all these previous works (as the theoretical models) were limited by an oversimplified hydrodynamical evolution (result of the solution of the one-dimensional RHD equations). Such restriction has motivated the combination of RHD in 2D with the calculation of the synchrotron radiation transfer at pc scales. The first numerical simulations of the pc scale synchrotron emission from hydrodynamic relativistic jets were presented in Gómez *et al.* (1995). Since then, other works have followed this idea (Gómez *et al.* 1997; Duncan, Hughes & Opperman 1996; Mioduszewski, Hughes & Duncan 1997; Komissarov & Falle 1997). From their simulations these authors inferred that the observations of such sources can be explained in terms of traveling perturbations (or shocks) in steady relativistic jets. Other important consequence of this description has been the establishment of the rôle played by the external medium in determining the jet opening angle and the presence and positions of standing shocks (actually, the opening angle is a consequence of the external medium pressure gradient).

The present work follows the same algorithm to evaluate the emission from 3D relativistic jets than in Gómez *et al.* (1995). The key points of this method are two: (1) the jet structure is calculated using a relativistic time-dependent hydrodynamical code and (2), the radio emission from the model jets is calculated by integrating the transfer equations of synchrotron radiation, accounting for the appropriate opacity and relativistic effects, such as Doppler boosting and relativistic aberration. The first part is made here by using GENESIS, and we have employed the same hydro-simulations than in the previous sections. The radio emission, has been calculated with the same code than in Gómez *et al.* (1994, 1995 and 1997) and, for the sake of completeness, we explain in the Appendix D the basic ingredients of the calculations involved in what the emission concerns.

Gómez *et al.* (1995) approach relies on several physical hypothesis like, *e.g.,* that the particle and energy density of these non-thermal electrons at the jet inlet are assumed to be proportional to the thermal electrons, which dynamics are computed using our relativistic hydrodynamical simulations, *i.e.,* emissivity of the jet is computed from the high energy relativistic non-thermal electrons. This approach has been followed previously by different authors (Rayburn 1977; Wilson & Scheuer 1983; Mioduszewski, Hughes, & Duncan 1997; Komissarov & Falle 1997) as well as by Jones, Tregillis & Ryu (1999), as the initial assumption before allowing radiative loses or accelerations by shocks to change the energy distribution of the non-thermal electrons.[14] It is therefore a common basic *ansatz* when studying the emission of jets in AGNs using hydrodynamical simulations.

The validity of our assumption can be asserted by considering that the total energy carried by the non-thermal electrons is significantly smaller than for thermal gas, and therefore they are expected to share the same dynamics than the simulated relativistic thermal gas. Any exchange between internal and kinetic energy

[14]In such work, the non-thermal flow is assumed to share the dynamics of their non-relativistic computed flow.

along the jet will maintain the proportionality between thermal and non-thermal electrons. Only gains by particle acceleration in shocks or losses by radiation can modify this proportionality. In the model presented in this memory we are only interested in studying the emission at radio wavelengths, for which the loses can be neglected (specially taking into account that in our model the magnetic field to thermal particle energy ratio is small –see below–). We are only interested in studying the emission from the jet, neglecting the hot spot and the cocoon, where no strong shocks are found (see also Jones, Tregillis & Ryu 1999). Therefore, we do not expect to have strong particle accelerations that could influence the non-thermal spectra, and hence our emission calculations. Furthermore, the emission distribution is not influenced by the particular value chosen for the proportionality between the non-thermal and thermal electrons. It would only change the final quantitative emission values, something that is unimportant in our results.

The magnetic field energy is set to be locally proportional and significantly smaller than the particle energy density. Therefore, although the structure of the magnetic field is set in a certainly arbitrary way, we can be confident that the jet dynamics will not be influenced by the field. Non relativistic MHD simulations of Jones, Tregillis & Ryu (1999) show that even with "weak" magnetic fields there are numerous places in the cocoon where magnetic, Maxwell stresses are significant. Is therefore in the cocoon where the strongest shocks and magnetic influence in the jet dynamics are found, not in the jet itself. We explicitly neglect the emission from the cocoon and hot spot, consistently, our approximation of considering the jet dynamics unaffected by the magnetic field (as well as neglecting the radiative losses in the emission at radio wavelengths) seems completely appropriated. Once the magnetic field has been chosen dynamically unimportant, we are allowed to consider different, certainly *ad hoc*, magnetic field jet geometries.

In this memory we study for the first time the radio emission properties of three-dimensional relativistic hydrodynamical models, focusing on the observational consequences of the interaction between the relativistic jet and the surrounding medium, leading to the development of a shear layer[15]. The presence of such a

[15]The following sections gather and develop the work done in Aloy *et al.* (1999c).

shear layer (with distinct kinematical properties and magnetic field configuration) has been invoked *ad hoc* in the past by several authors (Komissarov 1990, Laing 1996) to account for a number of observational characteristics in FR I radio sources but, its physical nature is still largely unknown. Recently, Swain, Bridle, & Baum (1998) have found evidence of such shear layers in FR II radio galaxies (3C353), and Attridge, Roberts, & Wardle (1999) (ARW99, henceforth) have inferred a two-component structure in the parsec scale jet of the source 1055+018.

3.3.1. Jet Stratification: Beam and Shear Layer

The hydrodynamical model we have used to study the emission properties of relativistic jets is n50p01. The model is characterized by a two-component structure (see Fig. 3.19) with a fast ($W \sim 7$) inner jet and a slower ($W \sim 1.7$) shear layer with high specific internal energy. We define for practical purposes the shear layer as the region with the beam particle fraction between 0.2 and 0.95[16], represented with white contours in Fig. 3.19 (0.95 for the inner contour). Although, as discussed in Sect, 3.2.3.3 the numerical viscosity inherent to our code is the responsible for the formation of the shear layer and not the turbulent shear, it allows us to obtain the first approach to study the physics of shear layers in relativistic jets and their observational consequences. The width of the shear layer, Δr_l, increases with the distance from the nozzle from a value $\Delta r_l \sim 0.2$ near $z = 0$ to $\Delta r_l \sim 0.65 - 1.0$ at $z = 68 R_b$. The broadening of the shear layer is due to the transfer of momentum of the inner jet. As shown in Fig. 3.6, the axial component of the momentum of the beam particles decreases by a 30% within the first 60 R_b. The transfer of momentum conveys a decrease in the Lorentz factor in the inner jet with values $\sim$ 5.8, 5.3, and 4.8 at $z =$ 25, 50, and 68 R_b, respectively.

The computed hydrodynamical structure of the jet agrees with the proposed in two-component jet models (Komissarov 1990, Laing 1996), also revealing a high energy in the shear layer not considered in previous theoretical models. This rela-

[16] Note that in Sect. 3.2.3.3 we defined the *hydrodynamical* shear layer as the fluid having $0.2 < f < 0.8$. Here we have extended inwards (to the axis o the jet) the upper limit of the shear layer because it fits better with some observations (see below).

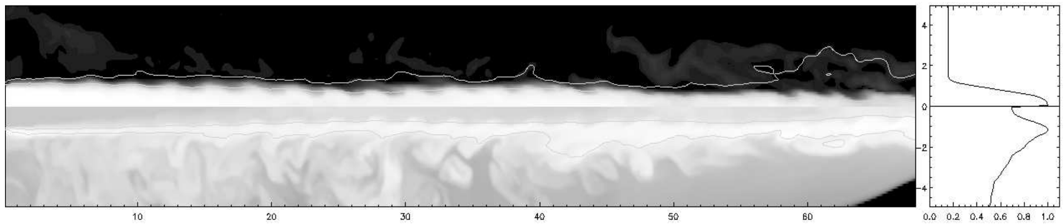

Fig. 3.19.— Cuts of the Lorentz factor (top half panel) and specific internal energy (bottom half panel) distributions of the hydrodynamical model along the plane $y = 0$. White contours representing constant values of the beam particle fraction (0.95 for the inner contours, 0.2 for the outer ones) are used to characterize the shear layer. Rightmost plots show the average, along lines x =constant, of the corresponding distributions across the jet.

tively higher internal energy in the shear layer has specific observational evidence, as shown in the following sections.

3.3.2. Emission properties

In order to study the emission properties of large scale jets in AGN, we need to establish the actual structure of the magnetic field within the jet. For this, the magnetic energy is set to be locally proportional and significantly smaller than the particle energy density, hence being dynamically unimportant. Different *ad hoc* distributions of the magnetic field in the jet spine and shear layer can be considered, allowing us to test different models for the observed jet polarization stratification. In our model we assume that the jet magnetic field compress two components: a toroidal field present in both, the jet spine and shear layer, and a second component (in equipartition with the toroidal field) aligned in the shear layer, and radial in the jet spine. The aligned component in the shear layer may be the result of shear between the jet and external medium, while the radial field in the jet spine can arise from transverse shocks (i.e., ARW99). The resulting magnetic field will be aligned in the shear layer, and perpendicular in the jet spine, as suggested by several observations (Laing 1996; Swain, Bridle, & Baum 1998; ARW99). In order to reproduce the observed relatively low degrees of polarization, an extra randomly oriented magnetic field component is assumed for the shear layer and jet spine. The random field is considered to contain 60% of the total magnetic field energy, obtaining degrees of polarization below $\sim 40\%$. The Stokes parameters that determine the emission are calculated following the prescriptions given in Ap. D.

Since only jet material is expected to radiate, we have multiplied the proper rest–mass density by the beam particle fraction. We are only interested in studying the emission properties of the stratified jet (beam and shear layer), hence we neglect the relatively small emission that can arise from the jet cocoon by limiting the calculations to values of the beam particle fraction above $f = 0.2$. We also ignore the emission from the hot spot, which due to its relatively young evolved state would out shine the rest of the jet. For this, we limit the calculations to the inner $68R_b$.

3.3.2.1. Total and polarized emission stratification as a function of the viewing angle

Because of the highly relativistic speeds in the jet, the emission is mainly determined by the observing viewing angle, Θ, through the Doppler factor and light aberration. The different velocities and magnetic field configurations in the beam and shear layer would then result in substantially different total and polarized emission structure as a function of the viewing angle.

Figures 3.20 and 3.21 show the computed emission from the hydrodynamical model n50p01, corresponding to a viewing angle of 50° and 10°, respectively. The emission is computed for an optically thin observing frequency, an spectral index of the electrons of 2.4. For relatively large viewing angle, as in Fig. 3.20, the jet emission is limb brightened. This is in part due to the higher specific internal energy in the shear layer, resulting in a larger synchrotron emission coefficient. On the other hand, the rôle played by the Doppler factor (see Eq. D13) can either enhance or cancel the limb brightening, as a function of Θ. For $\Theta > 1/W$, the emission is dimmed, while for $\Theta < 1/W$ the emission is boosted in the observer's frame. Because of the jet velocity stratification (see Fig. 3.19), for $\Theta > 1/W$ the fast jet spine suffers a larger amount of dimming than the shear layer, enhancing the limb brightening. For the jet model we study, with a mean $W \sim 7$ in the jet spine, this is maximized for $\theta \sim 50^\circ$, for which the shear layer emission is boosted while the jet spine is

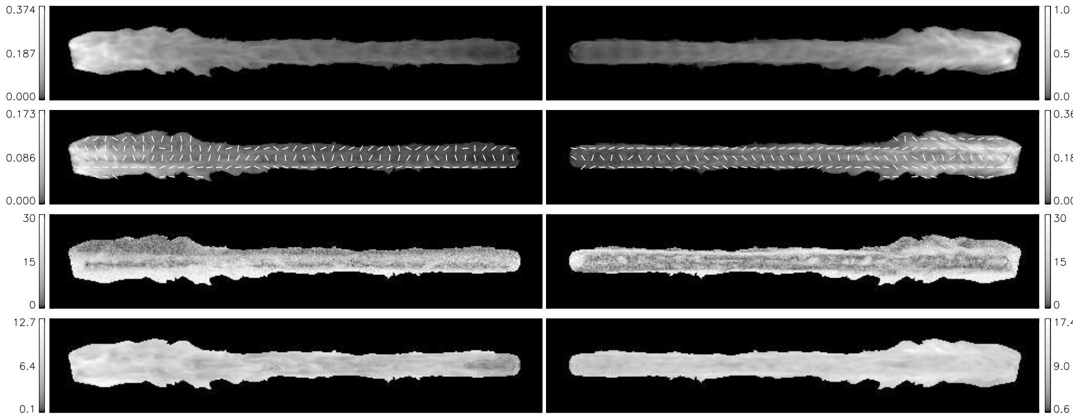

Fig. 3.20.— From top to bottom, panels showing the total intensity, polarized intensity, degree of polarization, and mean Doppler factor for a jet viewed at an angle of 50° (right panels) and its counterjet (left panels). Averages along the line of sight for each pixel, using the emission coefficient as a weight, have been used to plot the Doppler factor. The total and polarized intensities (in units normalized to the maximum in the main jet total intensity) are plotted in a square root scale. The bars in the polarized intensity panels show the direction of the magnetic field.

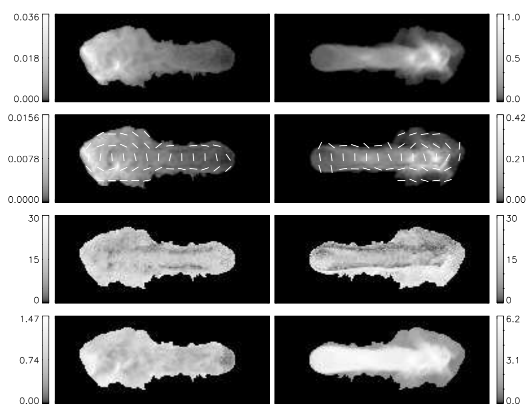

Fig. 3.21.— Same as Fig. 3.20, but for a viewing angle of 10°.

dimmed, as shown in the Doppler factor panel in Fig. 3.20. Cross section profiles of the jet emission at different viewing angles are plotted in Fig. 3.22, where the limb brightening effect can be more easily observed. For smaller viewing angles, as corresponding to Fig. 3.21, the jet spine emission is boosted, while the shear layer emission appears dimmed. Details of the jet spine can then be observed, as for instance two recollimation shocks, situated at $26R_b$ and $50R_b$. The jet emission then becomes spine brightened, instead of limb brightened, as observed in Figs. 3.21 and 3.22.

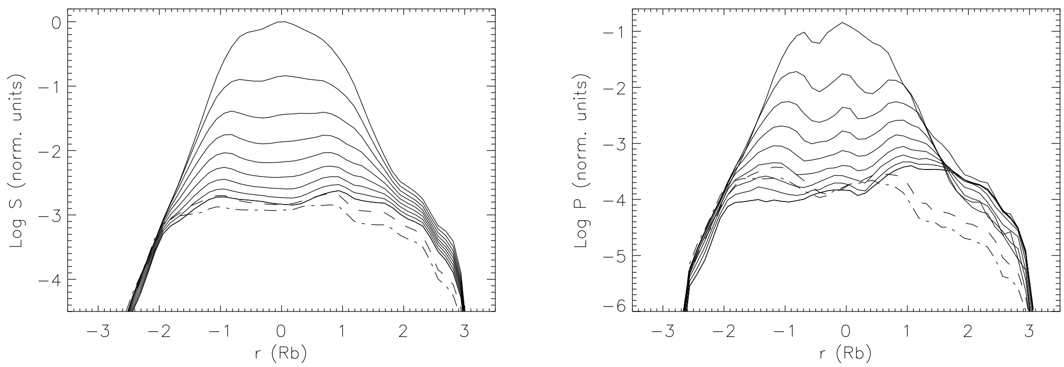

Fig. 3.22.— Logarithm of the integrated total (*left*) and polarized (*right*) intensity across the jet for different viewing angles. Lines are plotted in intervals of 10° from an angle of 10° (top line in both plots), to 90° (showing a progressive decrease in emission). Dashed lines (dot dashed) correspond to an observing angle of -100° (-140°). Positive beam radii correspond to the top in the images of Figs. 3.20 and 3.21. Units are normalized to the maximum in total intensity.

The same arguments apply to the polarized flux and, therefore, we obtain the same limb brightening for large viewing angles, and spine brighting for smaller values. As a result of the helical field in the shear layer, the apparent orientation of the magnetic field at the jet edges is parallel to the jet axis. For the jet spine, the toroidal and radial components of the magnetic field yield a net polarization perpendicular to the jet axis. As observed in Figs. 3.20 and 3.22, for relatively large angles the aligned component of the helical magnetic field in the shear layer projects into the jet spine partially canceling its field, yielding a smaller net polarization, stressing the limb brightening. Rails of low polarization can be observed where the apparent magnetic field rotates between being parallel (in the shear layer) to perpendicular to the jet axis, as observed in 3C353 (Swain, Bridle, Baum 1998).

Some of the kinematical and physical properties of the jet can be deduced by analyzing the jet/counterjet emission ratio, as plotted in Fig. 3.23 corresponding to

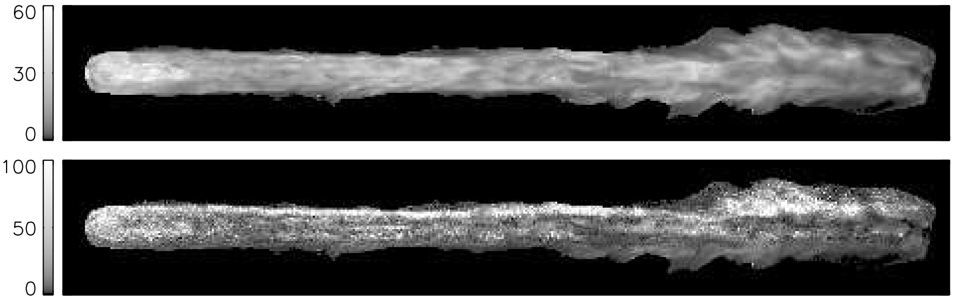

Fig. 3.23.— Total (*top*) and polarized (*bottom*) intensity jet/counterjet ratios for the jet models of Fig. 3.20. Polarized ratio is saturated at 100.

the jet model of Fig. 3.20. Jet deceleration is apparent as a progressively decrease in the total flux ratio along the jet axis. The velocity stratification across the jet is also visible as a decrease of the flux ratio close to the jet edges, that is, in the shear layer. This is visible in the inner jet region, while further down the jet, when the jet spine and shear layer velocities are more similar (due to the jet deceleration), the flux ratio is more uniformly distributed across the jet. The slower velocity in the shear layer and its high emission coefficient result in a smaller global flux ratio between the jet and counterjet than for the case of a “naked” high velocity jet spine (see also Komissarov 1990). This is because the shear layer emission is less affected by the viewing angle, that is, the Doppler factor.

3.3.2.2. Jet cross section emission asymmetry

Because of the helical magnetic field structure in the shear layer, an asymmetry in the emission appears across the jet. This asymmetry is more pronounced in the polarized emission, and is a function of the viewing angle, as shown in Fig. 3.22. In order to understand this effect we need to study the variation across the jet of the angle between the magnetic field and line of sight *in the fluid frame*, ϑ. The synchrotron radiation coefficients are a function of the sinus of this angle (see Eq. D3), and asymmetries in the distribution of ϑ will be translated into the emission maps. In order to compute ϑ we need to Lorentz transform the line of sight from

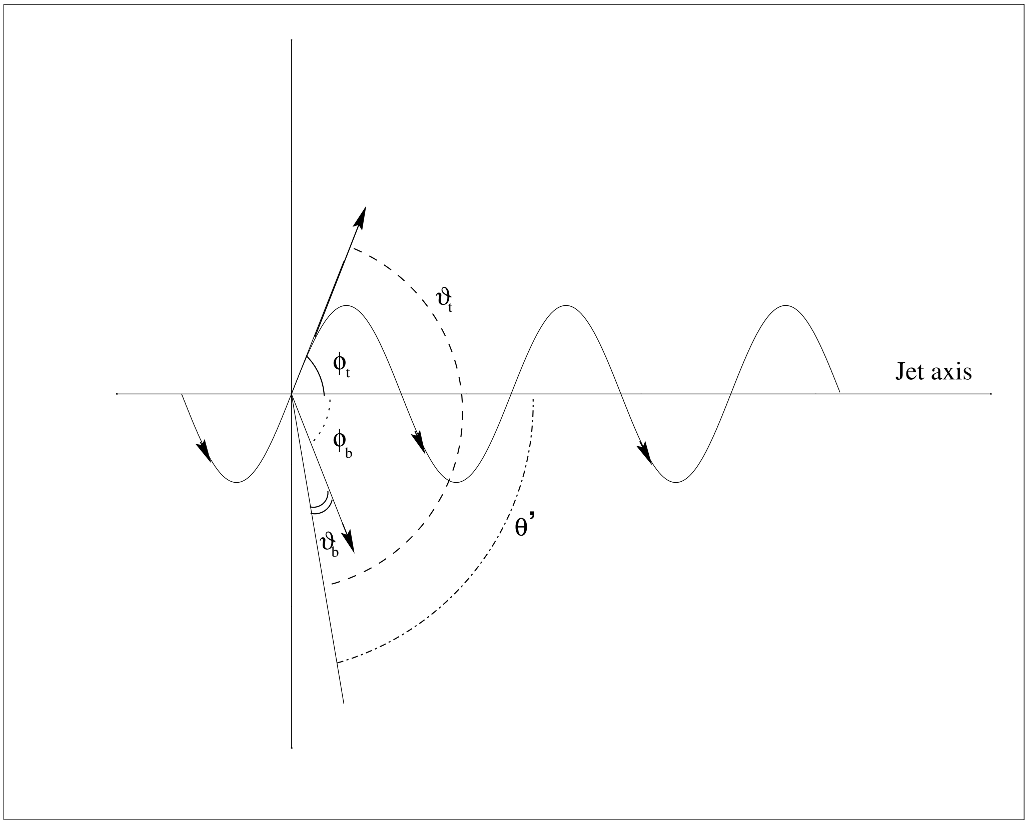

Fig. 3.24.— Relationship between the pitch angles (ϕ_t and ϕ_b) and the angles between the magnetic field and line of sight in the fluid frame (ϑ_t and ϑ_b). θ' is the angle to the line of sight in the fluid frame. The solid line represents the projection over the plane of the sky of the helicoidal magnetic field.

the observer's to the fluid's frame (see e.g., Rybicki & Lightman 1979)

$$\sin\theta' = \frac{\sin\theta}{W(1-\beta\cos\theta)} \quad , \quad \cos\theta' = \frac{\cos\theta-\beta}{(1-\beta\cos\theta)}$$

where θ' is the viewing angle in the fluid frame. Consider an helical magnetic field with a pitch angle ϕ, measured with respect to the jet axis (see Fig. 3.24). The angles ϑ^t and ϑ^b (where upper-script t and b refer to the top and bottom of the jet, respectively) differ by 2ϕ. Therefore, as long as ϕ is not zero or $\pi/2$, that is, the field is not pure aligned or toroidal, the $\sin\vartheta^{t,b}$ in the synchrotron radiation coefficients will introduce an asymmetry in the jet emission. This asymmetry will reach a maximum value for an helical magnetic field with $\phi = \pi/4$, as the one considered here. However, indistinctly of the helix pitch angle, the predominance between $\sin\vartheta^t$ and $\sin\vartheta^b$ will reverse at $\theta' = \pi/2$, which corresponds to a viewing angle in the observer's frame of $\cos\theta_r = \beta$. For an helical field oriented clockwise as seen in the direction of flow motion (i.e., the aligned component of the field is parallel to the jet flow), for $\theta' < \pi/2$ the bottom of the jet will show larger emission, while for $\theta' > \pi/2$ the top of the jet will be brighter (the opposite is true for an helical field oriented counter-clockwise, that is, with $\phi > \pi/2$). The maximum asymmetry will be obtained for $\theta' = \phi$ and $\theta' = \pi - \phi$, and the fastest transition (with changing θ') between top/bottom emission predominance will be obtained for ϕ close to $\pi/2$, that is, when little aligned field is present.

In the model we are considering, the shear layer has a mean $W \sim 1.7$, and therefore $\theta_r \sim 36°$. Smaller angles will show bottom jet dominance in emission, while for larger values the top of the jet will appear brighter. This is more clearly visible in Fig. 3.22. Note also that for the counter jet the helical field rotates opposite to the main jet, and therefore the jet asymmetry emission reverses. This is particularly well observed in the plot of the polarized emission ratio between the jet and counterjet of Fig. 3.23.

Although the $\sin\vartheta$ factor affects to both, total and polarized emission, the asymmetry is more clearly present in the polarized flux (see Figs. 3.20, 3.22, and 3.23). This is due to: i) The presence of randomly oriented magnetic field component, which renders the magnetic field distribution more homogeneous in the jet and diminish the asymmetry. ii) Smaller values of ϑ, indistinctly if present at the top or the bottom of the jet, always represent a larger variation of the magnetic field orientation along the line of sight, which in practice represents a larger degree of randomness in the magnetic field along the integration columns, decreasing the net polarization.

It is interesting to note that for $\theta \sim \theta_r$, small changes in jet velocity or viewing angle will produce a flip in the top/bottom jet emission dominance. For fast jets, θ_r will be accordingly small, and we will be biased towards observing jets with top emission predominance (as long as the helical field rotates clockwise as seen in the direction of flow motion).

An interpretation of the polarization observations of the blazar 1055+018 by

ARW99) can be obtained in terms of the model presented here. For that, we need to assume that 1055+018 is oriented close to θ_r, and contains a shear layer with helical field. If the helical field is oriented clockwise, the polarized emission observed at the top of the jet in inner regions would require that initially $\theta > \theta_r$, or $\theta' > \pi/2$. To obtain the opposite situation further down the jet, θ' has to become smaller than $\pi/2$, and for that either θ decreases, or θ_r increases, which requires that β decreases. Another third possibility, but that we find less plausible, is that the helical field in the shear layer changes orientation, that is, the pitch angles becomes larger that $\pi/2$. Therefore we can successfully explain the flip in the top/bottom orientation of the polarization asymmetry in 1055+018 if the jet bends towards the observer, or if decelerates. ARW99, and references therein) report the existence of bends in the jet of 1055+018. This support our hypothesis, but at the location of the flip in the polarization emission asymmetry, the jet spine emission decreases abruptly, contrary to what it would be expected in the case of a bend towards the observer, which should increase the jet spine emission by differential Doppler boosting. ARW99 obtained significantly larger apparent velocities for components closer to the core, suggesting a deceleration along the jet. Therefore, this points to our hypothesis of jet deceleration as the most plausible for the sudden change in polarization predominance between the top and bottom of the jet in 1055+018, since a jet deceleration will decrease the Doppler boosting, and hence the jet spine emission as observed. A relatively small aligned field (helical pitch angle close to $\pi/2$) will help to obtain such a fast flip in the polarization asymmetry with a relatively small jet deceleration.

Future observations of jet stratification in FRI and FRII sources should provide the necessary information to obtain a more detailed comparison with numerical simulations, helping to understand the nature of the shear layer, which as we have shown, plays an important rôle in the emission of relativistic jets.

3.3.3. Discussion and conclusions

We have analyzed the morpho-dynamical properties of a set of 3D relativistic jets. From our simulations, we can conclude that the coherent fast backflows found in axisymmetric models are not present in 3D models. We have investigated the beam's response to non-axisymmetric perturbations to check its stability. During the period of time studied by us ($t \lesssim 150 R_b/c$), the beam does not display the strong perturbations (particularly the filamentation of the beam) found by other authors in classical jets (Norman 1996, Hardee 1996) and it propagates according to the 1D estimate. Small 3D effects in the relativistic beam give rise to a lumpy distribution of apparent speeds like that observed in M87 (Biretta, Zhou & Owen 1995).

Our study must be extended to a wider range of models and perturbations. In particular, stronger perturbations should be considered to reach the nonlinear regime and to identify the acoustic and mixing phases (Bodo 1998) leading to the jet disruption. Further investigation also requires the dependence of the shear layer properties on the perturbation parameters. Finally, appropriate perturbations can be studied that mimic the wiggles observed in specific sources both at pc (0836+710, Lobanov *et al.* 1998; 0735+178, Gómez *et al.* 1999) and kpc scales (M87; Biretta, Zhou & Owen 1995).

We have also analyzed the properties of the boundary layer present in our models, both considering purely its hydrodynamics and their emission properties. From a dynamical point of view, the shear layer has appeared naturally in our model without being induced initially. The hydrodynamical jet structure agrees with the two-component models of Komissarov (1990) and Laing (1996), although the relatively high energy in the layer is a new element that leads to important observational consequences. Concerning the emission properties, these are closely linked to the *ad hoc* magnetic field configuration, and such fact has allowed us to interpret the ARW99 observations of 1055+018.

Other configurations of the magnetic field should be proven to reproduce particular features of current observations and, of course, the influence of the hydrodynamical model used to calculate the emission has to be investigated. A natural extension of the work would be to study the emission properties of the highly perturbed models in order to see if the characteristics of the shear layer emission persist when the central spine is highly distorted. These results will be reported elsewhere (Aloy *et al.* 2000).

Chapter 4

Relativistic jets from Collapsars.

An astrophysical phenomenon which also involves flows with velocities very close to the speed of light are gamma-ray bursts (GRB). This is the reason why hydrodynamic models (including, in some cases, the appropriate micro-physics) have become a main research tool in order to understand the GRB phenomenon (*e.g.,* Piran, Shemi & Narayan 1993; Mészáros, Laguna & Rees 1993; MacFadyen & Woosley 1999; Ruffert & Janka 1998, 1999a, 1999b; Aloy *et al.* 1999c).

We are going to present the observational framework in which GRBs are included (Sect. 4.1). The standard model trying to explain the current observations will be summarized in Sect. (4.1.1). The next subsection (4.2) gives an historical overview of the numerical simulations in this field. The modifications that we have included in the code GENESIS to treat a background Schwarzschild metric are discussed in Sect. 4.3.2, and the EOS employed in our calculations is described in Sect. 4.3.3. Section 4.3 deals with the relativistic version of the collapsar model introduced, in the Newtonian case, by MacFadyen & Woosley (1999) (MW99 in what follows).

4.1. Phenomenology

Gamma-ray bursts are known observationally since over 30 years. They were discovered by chance by American military satellites of the VELA class, which were developed at Los Alamos in order to detect clandestine nuclear tests in space by their associated gamma-ray emission. The detected radiation consisted of gamma-ray flashes lasting a few seconds. The results of these detections where published five years afterwards (Klebesadal, Strong & Olsen 1973). This paper reported 16 short bursts of photons in the energy range $0.2 - 1.5\,\mathrm{MeV}$ lasting between $0.1 - 30\,\mathrm{s}$ and having a complex time-structure (mainly in the longer bursts).

The phenomenology of these first set of bursts has proven to be the common one of GRBs. These common features, that define a GRB, are described in the following sections (for a longer review see, *e.g.,* Piran 1999 –PI99– or Daigne 1999).

Temporal properties. GRBs are very short events, with a typical duration between several milliseconds and several hundreds of seconds, showing a large variability even at the millisecond scale (suggesting an association between GRB sources with very compact progenitors). They show a bimodal time-distribution, the border between the two groups being at ~ 2 s. The first group is composed of *short* bursts centered around $0.1\,\mathrm{s}$, while the second group consists of *long* bursts (more numerous) centered at about $15\,\mathrm{s}$. The time-structure is very different from burst to burst. There are GRBs which show a simple and regular structure, whereas others have a very complex profile (Norris *et al.* 1996, explain the complex structure as the superposition of several pulses). From the data collected by the BATSE[1] experiment (Kouveliotou *et al.* 1993) and PHEBUS (Dezalay *et al.* 1996) mission it seems that short GRBs are harder than the long ones. Additionally, it is more difficult to detect short bursts, and there exist indications that short GRBs are closer than the longer ones, and that they form a separate subgroup (Mao, Narayan & Piran 1994).

Spectral properties. GRB spectra are non-thermal. The observed energy flux as a function of the energy ($E^2 n(E)$ or νF_ν; where E, $n(E)$, ν and F_ν are the energy, the number of counts per unit of time, area and energy, the frequency and

[1]BATSE (*Burst and Transient Source Experiment*) is an experiment launched in 1990 on board of the satellite CGRO (*Compton Gamma-Ray Observatory*).

the flux per frequency, respectively) can be well described by one or a combination of several power laws. The maximum of the energy distribution corresponds to an energy, E_p (the energy peak), which is characteristic of each GRB and usually is about several hundreds of keV. The spectra can be fitted by the following function (Band *et al.* 1993):

$$n(E) = A \left(\frac{E}{100\mathrm{keV}}\right)^{\alpha} \exp\left(-\frac{E}{E_0}\right) \quad \text{for } E \leq \frac{E}{\alpha - \beta}$$
$$n(E) = A \left(\frac{(\alpha-\beta)E_0}{100\mathrm{keV}}\right)^{\alpha} \exp(\beta - \alpha) \left(\frac{E}{100\mathrm{keV}}\right)^{\beta} \quad \text{for } E \geq \frac{E}{\alpha - \beta}$$

where α and β are the slopes of the power laws at low and high energy, and $E_0 = E_p/(2+\alpha)$. The values of α and β lie in the range $\alpha \in [-3/2, -2/3]$ and $\beta \in [-3, -2]$.

The observed fluence on earth is $10^{-5} - 10^{-7}$ erg/cm^2 the upper limit depending on the duration of the observation, and the lower limit depending on the detector. Redshift measurements of half a dozen of GRBs indicate that, for isotropic emission, the total energy is of the order of $10^{51} - 10^{54}$ erg (PI99). Recent observations (*e.g.,* GRB 990510, Harrison *et al.* 1999) suggest that the radiation is beamed (Sari, Piran & Halpern 1999; Rhoads 1999), reducing this energy by two orders of magnitude.

Spatial distribution. The BATSE experiment has observed more than 2000 events since 1991 (at a rate of $\sim$ 1 per day) in its systematic all-sky coverage. The positional accuracy of this detector is quite low the typical error-boxes being $\sim 1-2$ degrees for the brightest bursts, and more than 5 degrees for the fainter ones. However, there are some bursts whose locations have been pinned down with a precision of minutes of arc or better by triangulation experiments involving deep space probes (*e.g.,* the ULYSSES spacecraft). The technique utilizes the rapid time structure which, when recorded and timed by detectors separated by 10 light-minutes or more, allows for an accurate positioning. The statistical analysis of the BATSE data shows that the bursts are isotropically distributed (BATSE restricts any dipole or quadrupole anisotropy below the few per cent level and shows no evidence for clumping on smaller scales), but not homogeneously (see *e.g.,* Rees 1997). This heterogeneity is found in $\log N - \log P$ diagrams, where $N(P)$ is the number of bursts which have an intensity at maximum larger than a threshold P. These number-versus-intensity diagrams of the events tell us whether they are uniformly distributed in

Euclidean space or not. The reason is that if the events were uniformly distributed, one would expect the number of bursts should be proportional to the volume observed, *i.e.,* $N \sim R^3$. As the luminosity drops with distance as $P \sim R^{-2}$, one should find that $N \sim P^{-3/2}$. Consistently, a homogeneously distributed sample of bursts in Euclidean space must have a slope equal to $-3/2$ in the $\log N - \log P$ plane. The GRB observations are in agreement with such a distribution in the case of short (*i.e.,* powerful) bursts (Katz & Canel 1996; Tavani 1998), but their distribution significantly deviates from this slope for longer (*i.e.,* fainter) bursts (*i.e.,* small values of P).

Interpretation. A key point for the interpretation of the results is the distance at which the bursts occur, because this strongly influences (1) the estimated energetics of the GRB events, (2) the homogeneity of their distribution, and (3) their *production rate*. Concerning the energetics, three different characteristic GRB energies can be derived depending on their distance. Assuming that the energy of each burst is isotropically released these energies are 10^{37} erg, 10^{41} erg, or 10^{51} erg for bursts occurring in the Galactic Disc (at distances of a few hundred of pc), in the Galactic halo (at distances of tens kpc), or at cosmological distances, respectively.

For years a controversial debate has been taken place whether GRBs are local or cosmological (see *e.g.,* Fishman & Meegan 1995; Mèzáros 1995; Piran 1997). However, a galactic origin has to be rejected, because the meanwhile extensive BATSE catalog shows an isotropic distribution of GRBs over the sky, and no source enhancement either towards the plane of the galaxy or towards the galactic center. Moreover, the recent redshift determinations (the first one obtained was $z = 0.695$ for GRB 970228; van Paradijs *et al.* 1997) prove the cosmological origin at least of the majority of GRBs. Observed redshift values are in the range $0.7 \leq z \leq 3.4$ implying emitted gamma-ray energies of $2 \times 10^{51} \leq E \leq 2.3 \times 10^{54}$ erg for an isotropically radiating source. The cosmological origin of the GRBs is consistent with the distribution of bursts in the $\log N - \log P$ plane. Actually, the deviation from the $-3/2$ slope can be interpreted as a consequence of the expansion of the Universe (which is, in addition, consistent with the redshift measurements). In fact, the point at which the deviation from the slope $-3/2$ is observed gives one information about the characteristics and distribution of the GRBs (see *e.g.,* Daigne 1999).

Nonetheless, this picture was challenged by the detection of the Type Ib/c supernova SN 1998bw (Galama *et al.* 1998) within the error box of GRB 980425 (Soffitta *et al.* 1998; Pian *et al.* 1999) whose explosion time is consistent with that of the GRB. BeppoSAX detected two fading X–ray sources within the error box, one being positionally consistent with SN 1998bw (Pian *et al.* 1999)[2].This suggests a relationship between GRBs and SNe Ib/c, *i.e.*, core collapse supernovae of massive stellar progenitors which have lost their hydrogen and helium envelopes (Galama *et al.* 1998; Iwamoto *et al.* 1998; Woosley, Eastman & Schmidt 1998). As the host galaxy of SN 1998bw has a redshift of $z = 0.0085$ (Tinney, Stathakis & Cannon 1998), this has led Castro-Tirado (1999) to estimate the isotropic gamma-ray energy emission of GRB 980425 to be $E_\gamma = 7 \times 10^{47}$ erg (*i.e.*, more than four orders of magnitude fainter than a typical cosmological GRB).

Depending on whether the number of bursts is correlated or not with the stellar formation rate, one can argue:

a) If there is no correlation, the expected redshift for the burst distribution should be $z \sim 1$, the typical energy of an event in gamma-rays should be $E_\gamma \sim 10^{51}(\Omega/4\pi)$ erg (Ω is the solid angle into which the emitted radiation may be beamed), and considering the observed frequency, the burst production rate should be $\sim 10^{-6}(4\pi/\Omega)$ GRB/year/galaxy.

b) If there is a correlation, the effect of the expansion of the Universe would be delayed, and the typical redshift might be $z \gtrsim 3$. The energy per event would be larger than in the previous case, and the production rate smaller ($\sim 10^{-7}(4\pi/\Omega)$ GRB/year/galaxy).

Afterglow observations. The BATSE instrument does not allow for an accurate positioning of the GRB sources and, therefore, it has been very difficult to identify optical counterparts within the instruments error box. Leaving aside the large number of possible candidates for a given burst detection, one of the main problems of this search is that the optical detection starts some time after the burst

[2]However, there exist a debate about the truthfulness of this association, see *e.g.*, Wang & Wheeler 1998, Kippen *et al.* 1998.

has been observed by the gamma-ray satellites and, consequently, possible observations in other wavelengths (X-rays, optical or radio bands) are delayed with respect to the burst itself. Thus, what is actually observed is the "afterglow" of the emission.

The Italian Dutch satellite, BeppoSAX, discovered the first X-ray afterglow for GRB 970228 (Costa *et al.* 1997). Since then, more than two dozen X-ray afterglows have been detected. If an X-ray detection happens, the size of the error box is reduced to 50 arcseconds to 3 arcminutes. With this more accurate position, it is possible to start to look for optical counterparts (using ground based telescopes) with a delay smaller than one hour. However, as BeppoSAX can trigger only long bursts, it is not known whether short bursts also have afterglows. If the optical counterpart is seen, the localization of the object is obtained within an error box of ~ 1 arcsecond size. Moreover, if a radio detection is also successful, the positioning is enhanced up to ~ 1 milliarcseconds. Optical (*e.g.*, van Paradijs 1997) and radio (*e.g.*, Frail *et al.* 1997) afterglows have been discovered in about half of the cases in which X-ray afterglows have been seen. A remarkable feature of the VLBI detection of GRB 970508 has been the observation of a superluminal motion of the emission region (Frail *et al.* 1997) indicating that relativistic expansion of the matter is responsible for the emission.

The main observational properties of the afterglow emission are (PI99):

- The energetics of the process can be estimated from the late phases of the optical afterglows (Galama *et al.* 1998; Granot, Piran & Sari 1999; Wijers & Galama 1998; Vreeswijk *et al.* 1999). The overall energy emitted in the afterglow ($10^{50} - 10^{52}$erg) is a fraction of the one emitted during the GRB. The characteristic energy of the emission decays from the X-ray band to the radio band. Such behavior can be interpreted as the emission of an ultrarelativistic wind braked by its interaction with the ambient medium (Daigne 1999; Daigne & Mochkovitch 1999).

- The afterglow light curves decay in most cases following a single power law in time: $F_\nu = t^{-a}$, with $a \sim 1.2$. Nevertheless, $a \sim 2$ fits much better the bursts GRB 980326 (Grot *et al.* 1998) and GRB 980519 (Halpern *et al.* 1999). In other two cases, GRB 990123 (Kulkarni *et al.* 1999a) and GRB 990510 (PI99) that power-law is broken in two parts ($a \sim 1.1 - 1.2$ to $a \sim 2$), leading to the interpretation of beaming in the GRB emission (Sari, Piran & Halpern 1999). Obviously, such a beaming could reduce the energy release of the GRB by one or two orders of magnitude.

- The GRB 990123 has shown, for first time, a prompt optical emission, *i.e.,* the optical detection was done at the same time than the burst itself, using the ROTSE experiment (Akerlof *et al.* 1999); therefore, this emission is not exactly an *afterglow*, but shows the whole history of the GRB in the optical spectrum. The emission is peaked with a 9th magnitude signal which lagged 70 s after the gamma-ray peak and coincided with the prompt X-ray peak.

4.1.1. The standard model: the relativistic fireball

The observed gamma-rays reveal that GRB spectra are non-thermal. This indicates that the observed emission emerges from an optically thin region. However, the fast variability of the source ($\delta t \leq 1$ s) implies that the emission region is very compact ($\sim c\delta t$). Moreover, gamma-ray energies sometimes exceed 1 MeV, *i.e.,* they are above the pair production threshold in the rest frame. These facts along with the estimate of the number of photons with energies above 500 keV shows that the source should be quite optically thick to pair creation (*e.g.,* Fenimore, Epstein & Ho 1993) and, therefore, the source cannot emit non-thermally. Theoretically, this *compactness problem* has been overcome assuming that the emission region is moving ultrarelativistically towards us (Ruderman 1975; Goodman 1986; Krolik & Pier 1991). This is the basis of the *fireball model*, in which slowing relativistic ejecta produce the GRB and its afterglow. The observed gamma-rays are produced by the synchrotron or synchrotron self-Compton emission of the relativistic electrons that have been efficiently accelerated by shocks.[3] Such shocks can be either internal, *i.e.,* within the plasma (Narayan, Paczyński & Piran 1992; Paczyński & Xu 1994; Rees & Mészáros 1994) or external, *i.e.,* due to the interaction with the ambient medium (Mészáros & Rees 1992).

---

[3]Note the parallelism between this emission mechanism and the one which works in extragalactic jets (see §3.3).

External shocks are collisionless and become effective at $\min(R_{W_s}, R_\Delta)$, where $R_{W_s} \equiv l/W_{s0}^{2/3}$ and $R_\Delta \equiv l^{3/4}\Delta^{1/4}$ (Sari & Piran 1995). W_s and Δ are the Lorentz factor and the width of the shell (in the observer frame), and W_{s_0} is the initial value of the shell Lorentz factor. The radius within which the rest mass energy of the external material, whose density is n_{ism}, equals the initial energy of the ejecta, E_0, is known as the Sedov length, $l \equiv (E_0/[(4\pi/3)n_{ism}m_pc^2])^{1/3}$. Some typical values of the previous quantities are: $l \sim 10^{18}$cm and $R_{W_s} \sim R_\Delta \sim 10^{15} - 10^{16}$cm. However, external shocks may not to be the only cause for the GRB emission, because (1) they cannot produce efficiently the highly variable temporal structure seen in GRBs (Sari & Piran 1997; Fenimore, Madras & Nayakshin 1996), because (2) the lack of any correlation between the width of late sub-pulses (produced when the Lorentz factor is lower and at larger radii, so that they should be longer) and the time of arrival (Fenimore, Ramirez & Summer 1998), and because (3) the invoked mechanism to account for the variability of GRBs in this case (inhomogeneities in the external media –Dermer & Mitman 1999–) is extremely inefficient (Sari & Piran 1997).

The other possibility to explain the emission of GRBs are internal shocks. The non-linear hydrodynamic evolution of the plasma may lead to the growth of internal shocks. It is assumed that faster shells overtake slower ones and collide, converting some of their kinetic energy into internal energy. According to PI99, internal shocks would take place at $R_{int} \sim \delta W_0^2$, where δ is a typical length scale of the problem. Actually, $\delta = c\delta t$ can be inferred from the observed temporal variability $\delta t \leq 1\,\mathrm{s}$ indicating that $R_{int} \sim 10^{13}$cm. If the shocks are formed earlier the radiation does not escape (the fireball is optically thick). The observed GRB time scales reflect the time scales of the "inner engine" (Kobayashi, Piran & Sari 1997), and their duration corresponds to the time of activity of the central engine. Another evidence for the internal shock model is the lack of a direct scaling between the GRB and the afterglow. Nonetheless, internal shocks can extract only a fraction of the total energy (Mochkovitch, Maitia & Marques 1995; Kobayashi, Piran & Sari 1997; Daigne & Mochkovitch 1998). The remaining energy would be extracted later via external shocks giving rise to additional emission at different wavelengths (Sari & Piran 1997).

Let us note that a relativistic expansion reduces the necessary energy budget of the photons because of the relationship between the frequencies in the observers frame (ν) and in the proper frame of the matter moving relativistically (ν'): $\nu = \mathcal{D}\nu'$ (Rybicki & Lightman 1979), where $\mathcal{D}$ is the Doppler factor (defined in Ap. D). In addition, BATSE observations put a constraint on the value of the mean Lorentz factor in the expanding fireball, because they show no indication of high-energy photon-photon collisions (which would enhance the opacity via annihilations $\gamma+\gamma \rightarrow e^{+} + e^{-}$). This means that the interaction cross sections of the photons are pretty small, or would strongly depend on the Lorentz factor. Actually, as matter is moving relativistically with a Lorentz factor W, the emission (*i.e.,* the photons' trajectories) is beamed in a rest frame within a solid angle of $\sim 1/W$. Larger Lorentz factors give more beaming, and the trajectories of the photons tend to become parallel in the ultrarelativistic limit. Hence, the probability of interaction decreases, because the momentum of the photons is directed mainly in radial direction (the opacity due to electrons and pairs is reduced by a factor $\sim W^4$, *e.g.,* Rees 1997). In order to overcome the problem of the photon-photon interactions many authors have arrived to a consensus on the minimum value of the mean Lorentz factor required for the fireball of $W \geq 100$ (*e.g.,* Baring 1995). Such a high Lorentz factor can only be attained if the baryon loading is sufficiently small. If one releases an energy E into a mass M (*initially*), a measure of the baryon loading is the ratio $\frac{1}{\eta} = Mc^2/E$. Assuming that all the energy is converted into kinetic energy, the final Lorentz factor will be $W = E/Mc^2 = \eta$. Thus, a baryon loading $\leq 10^{-2}$ is required in order to obtain $W \geq 100$.

4.1.2. Models for the central engine

The astrophysical scenarios in which the GRBs are produced are still unknown. The main reason is the lack of observations which are detailed enough to resolve the host galaxy or the "burster engine". As GRBs are most probably born at cosmological distances, I will only give a brief review of the theoretical models that consider such cosmological scenarios (the reader interested in a more extensive overview is addressed to the reviews by Blaes 1994, Fishman & Meegan 1995 or Hartmann 1996).

The cosmological origin of GRBs was first proposed by Prilutskii & Usov (1975) and Paczyński (1986). In these early models, bursts were thought to originate in classical extragalactic sources (galaxies, quasars) or in other more exotic objects, like super-conducting cosmic strings or through a random pattern of gravitational radiation which is focused by a distant and steady source. More modern theories involve the coalescence and merging of neutron star binary systems, or the accretion onto a BH in a "failed" supernova.

If GRBs are cosmological, the typical energy of a burst should be $\sim 10^{51} - 10^{54}$ erg. Moreover, the temporal profiles of these events show a fast variability indicating that the size of the GRB's progenitors should not be larger than a few light-milliseconds. Thus, promising astrophysical sources of GRBs involve one or more compact objects of stellar size (*i.e.,* with a mass of a few solar masses). In principle, such compact objects can provide the required energy (after all, whenever a supernova goes off, the binding energy of a neutron star is released in a fraction of a second, and this amounts to 10^{53} erg).

In order to explain the amount of energy released in a GRB ($\sim 10^{51} - 10^{54}$ erg), the necessary Lorentz factors ($\sim 10^2 - 10^3$), the observed rapid variability of the emission (to occur at radii in the range $\sim 10^{14} - 10^{16}$ cm) and the necessary low baryon loading ($\sim 10^{-3} - 10^{-5}$ or $\lesssim 10^{-6} M_\odot$), various catastrophic collapse events have been proposed. These can be categorized as follows:

1) Coalescence of compact binary systems. This group includes NS/NS mergers (Pacyński 1986; Goodman 1986; Eichler *et al.* 1989; Narayan, Pacyński & Piran 1992) and NS/BH mergers (Narayan, Pacyński & Piran 1992; Mochkovitch *et al.* 1993). Recently, the coalescence of a NS or BH with a white dwarf (Fryer *et al.* 1999) or with the Helium core of a red giant has been proposed, too (Fryer & Woosley 1998). A binary NS/NS system, that may survive for $\sim 10^9$ years, will eventually coalesce when gravitational radiation drives both objects together. The final merger, leading probably to the production of a Kerr BH, happens in a fraction of second, and the energy released during the merging process is $\sim 10^{54}$ erg. It is also possible that a $\sim 0.1\, M_\odot$ accretion disk forms around the BH and is accreted within a few seconds, then producing internal shocks leading to the GRB (Katz 1997). The calculated event rates for such phenomena are 100 per year at a distance

smaller than 200 Mpc (Fryer *et al.* 1999). This rate is a tenfold larger if one considers NS/BH mergers. Both rates are compatible (if the beaming factor $\Omega/4\pi$ is not very small and almost every merger produces a GRB) with the hypothesis that the GRBs are not correlated with the stellar formation rate (see previous subsection), in which case a burst frequency of $\sim 10^{-6}(4\pi/\Omega)$ GRB/year/galaxy is expected.

2) *Hyper-accretion* onto compact objects resulting from the gravitational collapse of massive stellar cores. This category includes two families of models: the *hypernovae* (Pacyński 1998) and the *collapsars* (Woosley 1993). The hypernova model assumes that a core of a massive rapidly spinning star collapses directly to a BH without producing a supernova. A collapsar is the result of a failed Type Ib/c supernova which is produced by the gravitational non-spherical collapse of the rotating iron core of a Wolf-Rayet star. The likely result of both models is the formation of a Kerr BH with a $0.1-1\ M_\odot$ dense viscous torus around it. The matter is accreted at a very high rate ($\sim 1\,\mathrm{M_\odot s^{-1}}$; Popham, Woosley & Fryer 1998). Both scenarios are quite similar but they differ in the energy extraction mechanism: while a hypernova releases $\sim 10^{54}\,\mathrm{erg\,s^{-1}}$ of kinetic energy by tapping the rotational energy of the Kerr BH using the Blandford & Znajek (1977) mechanism, a collapsar converts the gravitational binding energy released by accretion into neutrino and anti-neutrino pairs (via viscous dissipation of energy in the accretion torus), which in turn annihilate into electron-positron pairs. It is hard to determine the minimum mass required for a progenitor star to produce any of these collapses but most probably it should be a main sequence star of several dozens of solar masses (which are necessary in order to produce, by evolution, a stellar core of $10-15M_\odot$). In any case, a "fireball", which will also contain the baryons present in the neighbourhood of the BH, will be produced reaching a luminosity ~ 300 times larger than that of a normal SN. For the collapsar model, provided the baryon load of the fireball is not too large, the baryons are accelerated together with the $\mathrm{e^+\,e^-}$ pairs to ultrarelativistic speeds with Lorentz factors $> 10^2$ (Cavallo & Rees 1978; Piran, Shemi & Narayan 1993). The bulk kinetic energy of the fireball then is thought to be converted into gamma-rays via cyclotron radiation and/or inverse Compton processes (see, e.g., Mészáros 1995). The event rate for these models ($\sim 10^{-3}$ per year and galaxy) is larger than that of the coalescing binary systems. However, strong effects due to stellar evolution are expected (a typical $30M_\odot$ star that forms a Wolf-Rayet and then collapses lives for

10^6 years only). As the event rate is correlated with the star formation rate (see 4.1) the number of events expected is $< (4\pi/\Omega)10^{-7}$ per year and galaxy. Consequently, to be consistent with this rate, the beaming should be quite large, or only a fraction of core collapses do produce GRBs.

The two main differences between both families of models are their locations and environment. A typical binary system formed by two NS needs $\sim 10^9$ years to merge. During this time the system can travel tens of kpc due to the large kick velocity acquired during the two supernovae explosions (Tutukov & Yungelson 1994). A massive star on the other side only lives for a few million years and hence cannot move far during its lifetime, *i.e.,* it explodes within the star forming region where it was born. The environment around a Wolf-Rayet star is more complex and dense than that around a binary system because the star has lost an important part of its mass due to the ejection of the outer shells. However, current observations have been unable to give any insight on this issue (the position of the bursts in the host galaxies has not been accurately established yet), although some authors claim that GRBs are produced in star formation regions (Fruchter *et al.* 1999) and possibly, the optical afterglow might be heavily obscured by dust commonly present in such regions (Jenkins 1997). In MW99 is said that the hypernova/collapsar model can explain better long and very energetic bursts than the coalescence of binary systems. The reason being that the dynamical time to accrete the matter of the torus formed due to the merger of the two NS is very small (depending on the viscosity of the model –which is still uncertain– it can be, at most, 0.5 s), and according the standard model, the duration of a burst depends on the life-time of the engine.

All the models just discussed can be subdivided into two groups according to the energy extraction mechanism, namely those which invoke hydromagnetic energy extraction, and others that rely on the dissipation of energy in the accretion disk via neutrino emission. Within the first group of models one considers two different possibilities: (1) extremely intense magnetic fields ($\sim 10^{15} - 10^{16}$ G) extract matter and energy from the disk and the BH itself via the Blandford-Znajek mechanism (Usov 1994; Mészáros & Rees 1997), or (2) reconnection of the magnetic field lines in the corona of the disk (which is much less dense than the disk) liberates enough thermal energy to power a relativistic wind (Narayan, Paczyński, & Piran 1992). The second group of models was proposed by Mészáros & Rees (1992) and Mochkovitch *et al.* (1993), (1995). In this case neutrinos preferentially deposit their energy in a region near the rotation axis, because the inner boundary of the accretion torus is almost parallel to the axis thus favoring "head-on" collisions of the neutrinos.

4.1.3. An afterglow model

The afterglow is the emission that follows a GRB at frequencies gradually declining from X-rays to visible and radio wavelengths. Soon after the first BeppoSAX observations it was suggested by Paczyński & Rhoads (1993) (for the radio afterglow) and independently by Katz (1994) (for the optical afterglow) that the long term interaction of the relativistic ejecta with the external medium will produce a low frequency afterglow. Mészáros & Rees (1997) and Vietri (1997) pointed out that afterglows are produced by the external blast wave moving ahead of the fireball (sweeping the interstellar matter). This afterglow is the long time continuation of the GRB and should have properties similar to the GRB itself, if the emission of the GRB is produced by external shocks. However, as we have noted above, the external shock model for GRBs has several problems. This leads one to the assumption that GRBs themselves emit due to the presence of internal shocks. In the currently accepted "Internal-External" model the GRB and the afterglow are produced by two different processes, i.e. no direct scaling between both is expected.

The radio afterglow of GRB 970508 has provided a direct confirmation of the fireball model, because it has shown an evident flickering (decreasing with time) for about a month. The transition from the flickering to the non-flickering regime has allowed Frail *et al.* (1997), using the theoretical analysis of Goodman (1997) for the determination of angular sizes from *refractive radio scintillation*, to estimate that the afterglow had a size of $\sim 10^{17}$cm one month after the burst. Katz & Piran (1997) estimated a similar size independly, suggesting that the source could become optically thick, if the synchrotron self-absorption rises the spectrum in radio frequencies. Using the observed flux and an estimate of the temperature of the emitting regions they were able to obtain the size of the emitting region. Both observations provide evidence (for first time) that the fireball is expanding relativistically.

4.1.3.1. Emission properties

The generic emission process for both the GRB and the afterglow is synchrotron. The energy distribution of the emitting electrons has the same power law distribution than in the case of relativistic jets (Eq. D4), but the spectral index of the distribution that fits better the observations is $p \sim 2.5$. For this value of p the distribution diverges at low energies. Thus, like for extragalactic jets, this produces a low energy cutoff (Eq. D6).

The emission that originates the afterglow comes from the external shock surrounding the fireball. Actually, such a shock has a more complex structure that fits better with that of a blast wave. The properties of this blast wave can be derived from the synchrotron spectrum (Pacholczyk 1970) of a population of electrons with the addition of self absorption at low frequencies and cooling break, according to Sari, Piran & Narayan (1998). The spectrum depends on four parameters:

- The synchrotron frequency, ν_m, which corresponds to $W_{e,min}$ (or E_{min}; see Eq. D6).

- The cooling frequency, ν_c. This is the synchrotron frequency of an electron that cools during the local hydrodynamic time scale: $E_c/P_{\nu_c}(E_c) = t_{hyd}$ (P_{ν_c} is the power emitted by a single electron due to synchrotron radiation; E_c is the energy corresponding to ν_c). Fast cooling (*i.e.,* typical electrons are cooled within times smaller than t_{hyd}) implies that high energy electrons will cool rapidly for $\nu_c < \nu_m$. Slow cooling leads to a reduced cooling of low energy electrons for $\nu_m < \nu_c$.

- The self-absorption synchrotron frequency, ν_{sa}. The same electrons that produce the synchrotron radiation can also scatter with low energy photons via inverse Compton. Self-absorption may appear at late time typically in radio emission (*e.g.,* Paczyński & Rhoads 1993). It is defined (*e.g.,* Rybicki & Lightman 1979) as the frequency for which the optical depth along the line of sight is equal to one ($\tau(\nu_{sa}) = 1$).

- The maximum flux $F_{\nu,max}$.

The combination of all these effects (fast or slow cooling, presence or not presence of self-absorption) leads to a spectrum which is a combination of four power laws, where three of the four slopes are fixed and one is depending on whether or not the electrons are rapidly cooled. The corresponding flux can be written (at a fixed time) as $F_\nu \propto \nu^\beta$ with:

$$\beta = \begin{cases} 2 & \text{for } \nu < \nu_{sa} \text{ - self absorption;} \\ 1/3 & \text{for } \nu_{sa} < \nu < \min(\nu_m, \nu_c); \\ -1/2 & \text{for } \nu_c < \nu < \nu_m \text{ - fast cooling;} \\ -(p-1)/2 & \text{for } \nu_m < \nu < \nu_c \text{ - slow cooling;} \\ -p/2 & \text{for } \max(\nu_m, \nu_c) < \nu. \end{cases} \tag{4.1}$$

This instantaneous spectrum is valid for the GRB and the afterglow phases. However, as the GRB stage involves simultaneous emission from multiple shocks, the resulting spectrum may be more complicated PI99. To determine the light curve one needs ν_{sa}, ν_m, ν_c, and $F(\nu_m)$ as a function of time (all other fluxes are determined by these quantities). Moreover, for comparison with the observations it is necessary to express the instantaneous size of the fireball (R) and its Lorentz factor as a function of the detector time. The appropriate relations are given by the adiabatic energy equation (if the expansion is ultrarelativistic, the fireball cannot exchange energy with the ISM) and the photon arrival time:

$$E_0 = M(R)c^2W^2, \tag{4.2}$$

and

$$t_{obs} = \frac{R}{2cW^2}, \tag{4.3}$$

$M(R)$ and E_0 are the accumulated mass at a radius R and the value of the initial energy, respectively. With these equations in mind, and if the flux is parameterized in terms of its dependence on frequency and the time as $F_\nu \propto t^{-\alpha}\nu^\beta$ (Sari, Piran & Narayan 1998), a relation between α, β and p can be obtained. For the spherical adiabatic case this relation reads:

$$\alpha = \begin{cases} 3\beta/2 = 3(p-1)/4 & \text{for } \nu < \nu_c, \\ (3\beta - 1)/2 = (3p-2)/4 & \text{for } \nu > \nu_c. \end{cases} \tag{4.4}$$

4.1.4. Are GRBs Jet–like structures?

The aim of this section is to review the observational and theoretical evidence for a non-isotropic evolution of the GRBs or their afterglows. Actually, the present work tries to provide some answers to this question (see §4.3) in case of a particular astrophysical scenario (the collapsar model).

The possibility of non-isotropic emission is important for two reasons: the energetics and the event rate of the bursts. Clearly, beamed emission relaxes the energetic requirements to explain the observations. If the energy happens to be emitted into a solid angle Ω, the overall energy would be lower by a factor $\Omega/4\pi$ (if the angle is small, one can write $\Omega/4\pi = (1-\cos\theta)/2 \simeq \theta^2/4$). On the other hand, if the emission is beamed, we would not see all events (only those which point in our direction), *i.e.,* the actual event rate will be larger by $4\pi/\Omega$.

Beamed emission results both from an anisotropy of the emitting region and from relativistic beaming due to relativistic motion (see §3.3). The second effect produces an enhancement of the emission into a cone with an opening angle W^{-1} (if the source is moving towards us with a Lorentz factor W) independent of the shape of the emitting region. While beaming due relativistic motion is of the same strength in afterglows and in extragalactic jets (in both cases $W \sim 2-10$ implying $\theta_r \sim 0.1$–0.5 rad, θ_r being the angle of beaming of the radiation field, *i.e.,* $\theta_r \sim W^{-1}$), beaming of GRBs is much larger ($W \sim 200 \Rightarrow \theta_r \sim 10^{-2}$ rad). However, the beaming is determined by θ and not by θ_r, because a source will only be seen by those observers with a viewing angle up to θ from the center. Nevertheless, an observer can only see a fraction of the whole region of angular size W^{-1}, because the radiation is beamed at most into such an angle in his direction of observation. Furthermore, each of these fractions are causally disconnected (*e.g.,* Christiansen, Scott & Vestrand 1978; Shapiro 1979). The number of non-causally connected regions for a burst is $\sim (\theta W)^2$.[4] This number decreases with W, hence, during the afterglow there are fewer regions present than during the GRB, and when $\theta_r \sim \theta$ the external shock is coherent (*i.e.,* causally connected).

[4]Such number is calculated as $\dfrac{\Omega}{\Omega_r} = \dfrac{1-\cos\theta}{1-\cos\theta_r} \simeq \dfrac{\theta^2}{\theta_r^2} = (\theta W)^2$.

Can we, by any means, infer from observations the shape of the emitting region?. In particular, can we distinguish a spherical ejecta from a non-isotropic one?. Different authors have answered differently to these questions. Let us examine the alternatives in more detail. In the comoving reference frame of an expanding relativistic flow, the proper time required to reach a radial distance R (measured in the rest frame of the source) is R/cW (due to the contraction of the length in the direction of motion seen by the comoving observer). The maximum sideways expansion is not affected by the length contraction and, therefore it is R/W. As long as the Lorentz factor of the flow is sufficiently high ($W^{-1} < \theta$), the sideways expansion (R/W) is rather small, and according to PI99 matter does not have enough time to expand sideways and to realize that it is not part of a spherical shell.[5] Of course, as W decreases and $W^{-1} \approx \theta$ the communication between all points in the shell becomes causal and matter begins to expand sideways. The transversal expansion velocity is a matter of debate, because Sari, Piran & Halpern (1999) argue that as the matter at the front is constantly shocked to relativistic energies it should expand with the speed of light (*i.e.*, $\theta \sim W^{-1}$). Rhoads (1999) assumes that the sideways expansion occurs at the maximum allowed sound speed, $c/\sqrt{3}$ (*i.e.*, $\theta \sim W^{-1}/\sqrt{3}$). In any case, the sideways motion is so rapid that it dominates completely the fluid expansion. Narayan & Piran (1999) have found for an expansion into a homogeneous medium that[6]

$$W \propto R^{-3/2} \exp\left[-\frac{3}{2}\frac{c}{W_0\theta_0}\left(\frac{R^{3/2}}{R_0^{3/2}} - 1\right)\right] \tag{4.5}$$

where R_0, W_0 and θ_0 are the initial values of the radius, the Lorentz factor and the beaming angle respectively. The reduction of W, and the fact that the radiation is beamed into a larger cone ($W^{-1} > \theta_0$) reduces the observed emission and causes a break in the light curve[7]. After the break the emission decays faster (roughly by an additional factor t^{-1}). As the light curve changes, different relations between the

[5]This assertion can be formulated in hydrodynamical terms as follows: If one has an expanding jet with proper Mach number M_j then the opening angle of the beam is just $\sin\theta = \frac{1}{M_j}$. If the movement is highly relativistic, *i.e.*, $v_j \sim 1$, (even with the maximum allowed sound speed, $c_{s_j} = 1/\sqrt{3}$), it results that $M_j = \frac{W_j v_j}{W_{c_{s_j}} c_{s_j}} \sim W_j$ implying that $\theta \sim \frac{1}{W_j}$.

[6]Changing c in the exponential by c_s one gets Rhoads' (1999) solution.

[7]Panaitescu & Mészáros (1998) claim that two successive breaks will take place, one at $W \approx$

spectral indexes α, β and p arise compared to the spherical adiabatic case (Eq. 4.4) (see Halpern *et al.* 1999):

$$\alpha_{jet} = \begin{cases} 2\beta + 1 = p & \text{for } \nu < \nu_c, \\ 2\beta = p & \text{for } \nu > \nu_c. \end{cases} \tag{4.6}$$

There are many bursts (GRB 970228, 970508 and 980519) which do not show such a break in the light curve. However, Sari, Piran & Narayan (1999) interpret that this is because the sideways spreading must have started before the first optical observations. If this is true, using Eq. (4.3) PI99 finds an upper limit for the opening angle of $\theta < 0.05$ for GRB 980519.

The first direct evidence for a beaming break has been found in GRB 990123 (Kulkarni *et al.* 1999a) by a prompt optical detection. The optical afterglow exhibits three stages: (1) a prompt optical decay that Sari, Piran & Narayan (1999) interpret as coming from a reverse shock decaying like t^{-2} and disappearing quickly, (2) a subsequent afterglow decay proportional to $t^{-1.1\pm0.03}$, and (3) a late fast decline. The most likely explanation of this behavior is that we have observed the transition from a spherical like phase to a sideways expansion phase (Shari, Piran & Narayan 1999). From the transition time (~ 2 days) a beaming angle of $\theta_0 \sim 0.1$ is inferred. Additionally, the lack of a significant radio afterglow in GRB 990123 provides independent evidence for jet–like geometry (Kulkarni *et al.* 1999b). Most recently, Harrison *et al.* (1999) have seen such a transition 1.2 ± 0.08 days after the rising of GRB 990510 going from $t^{-0.82\pm0.02}$ to $t^{-2.18\pm0.05}$.

From all this evidence, it seems that GRBs most probably involve non-isotropic emission. However, the exact shape of the emission is far from being clear. Depending on the apparent geometry several more or less exotic terminologies are in use to describe the shape of GRBs: "jets", "bullets" or "pancakes". PI99 assumes that probably because of the analogy with AGNs jets the terminology "jets" has become the most widely used. However, typical extragalactic jets are long and narrow, and usually they show a continuous activity during $\sim 10^7 - 10^8$ years. Such time scales are much longer than the typical ones of the BHs that power them. A bullet shape,

---

θ_0^{-1}, and a second one induced by the hydrodynamic time scale related with the sound speed at $W \approx (\sqrt{3}\theta_0)^{-1}$.

however, would be more self-consistent, because a bullet has a shorter length (in the direction of motion) and it clearly represents a transient phenomenon. Nevertheless, their angular sizes are $R\theta$ and their "lengths" are $L \sim cT$. Thus, if a burst of 30 s duration typically may have $L \sim 10^{12}$ cm, a radial size $R \sim 10^{13} - 10^{14}$ cm (see §4.1.1) and $\theta \sim 0.1$, one finds $R\theta > L$. To PI99 such a source resembles a "pancake" moving relativistically in a direction perpendicular to its flat part. Moreover, if we look at its shape in the comoving frame it is longer by a factor W, *i.e.,* initially it is actually a bullet. However, even at this early phase the ejecta expands sideways proportionally to R (unless it is continuously collimated) and, consequently, even in the comoving frame it looks like a pancake.

4.2. Numerical simulations

The dynamics of spherically symmetric relativistic fireballs has been studied by several authors by means of 1D Lagrangian hydrodynamic simulations. Piran, Shemi & Narayan (1993) and Mészáros, Laguna & Rees (1993) have examined the expansion of a mass–loaded fireball, initially at rest, from the acceleration stage through the coasting phase. Panaitescu *et al.* (1997) have simulated the interaction between an expanding fireball and a stationary external medium with a uniform or power law density stratification, and Panaitescu & Mészáros (1998) computed the interaction between relativistically expanding shells. Kobayashi, Piran & Sari (1999) have studied the evolution of an adiabatic fireball expanding into a cold uniform medium. Using a 1D relativistic Lagrangian PPM code, Daigne & Mochkovitch (1999) and Daigne (1999) have studied the evolution of a relativistic wind with a very inhomogeneous distribution of the Lorentz factor. Such inhomogeneity produces internal shocks which may radiate reproducing the temporal variability of the observed bursts.

Other authors have studied the generation and transport of energy in potential astrophysical sources which might produce a relativistic fireball. In a sequence of papers Ruffert and coworkers (Ruffert, Janka & Schäfer, 1996, Ruffert *et al.* 1997; Ruffert & Janka 1998, 1999a) have used a Newtonian 3D Eulerian PPM hydrodynamic code (which includes self-gravity, the effects of gravitational wave emission and their back-reaction on the hydrodynamics, a neutrino leakage scheme and a realistic equation of state) in order to show that the neutrino emission associated with the dynamic phase of the merging or collision of two neutron stars, although being powerful, is too short to provide the necessary energy for GRBs by neutrino–antineutrino annihilation (mainly because the accretion torus that forms due to the merger rapidly falls into the hole). Nevertheless, such a mechanism could explain the short GRBs (*i.e.,* those lasting less than 2 s; see Sect. 4.1). Ruffert and collaborators simulate the gravity of the BH by means of an effective Paczyński–Wiita potential and, in a post-processing stage, they evaluate the energy deposition by $\nu\bar{\nu}$ annihilation around the accretion torus.

MW99 have explored the evolution of rotating helium stars ($M_\alpha \gtrsim 10\, M_\odot$), whose iron core collapse does not produce a successful outgoing shock. Instead a BH is formed. For values of the specific angular momentum reasonable for such stars ($j \approx (0.3 \ldots 2) \times 10^{17}\, \mathrm{cm}^2/\mathrm{s}$) a compact accretion disk forms at a radius where the gravitational binding energy of the accreting stellar matter can be efficiently radiated as neutrinos. Assuming that the efficiency of neutrino energy deposition by $\nu\bar{\nu}$–annihilation is higher in the polar regions (because the $\nu\bar{\nu}$ cross-section is $\sigma_{\nu\bar{\nu}} \sim (1 - \cos\theta_{\nu\bar{\nu}})^2$, $\theta_{\nu\bar{\nu}}$ being the angle between the trajectories of the interacting neutrinos) MW99 obtained "relativistic" jets, along the rotation axis, which remain highly focused and seem to be able of penetrating the star. However, as they performed their simulations with a Newtonian hydrodynamic code, they got speeds in the jet flow which were appreciably superluminal, and they had to stop their simulations.

4.3. Relativistic jets from collapsars

The collapsar model of GRBs relies on the presence (or formation) of a fast rotating BH (of a few solar masses) surrounded by a thick accretion disk (torus) formed by the debris of a massive star which is not "instantaneously" accreted onto the BH essentially due the fast rotation of the progenitor star. This fast rotation also causes the formation of a "clean" axial funnel (*i.e.,* of relatively low density) centered around the rotation axis. The funnel favors the escape of the fireball, because it collimates and confines the fireball due to the much larger density of the walls of the funnel, and because it has a smaller baryon content. The expected result is the formation and evolution of a relativistic jet.

In the following we investigate some aspects of the collapsar model of MW99. Using appropriate hydrodynamics (relativistic instead of Newtonian), a better description of the BH gravity (background Schwarzschild metric) and a variable gamma equation of state (which is less realistic than the one of Blinnikov, Dunina-Barkovskaya & Nadyozhin (1996) used by MW99; see §4.3.3) we have studied the question, whether it is possible to produce an ultrarelativistic jet releasing energy (at different deposition rates) near the center of the star in a region restricted to the neighborhood of the rotation axis.

4.3.1. Initial model and the numerical setup

Our axisymmetric relativistic simulations of jets from collapsars are based on Model 14A of MW99, which is obtained by MW99 in several steps. First, they evolve a $35\,M_{\odot}$ from the main sequence, without mass loss and rotation, to the presupernova stage (collapse velocity equal 1000 km/s) using a stellar evolution code. Then, they extract the helium core of the star which has a mass of $14.13\,M_{\odot}$, and remove its inner $2.03\,M_{\odot}$ which correspond to the iron core by introducing an inner boundary at a radius $r = 200$ km. In a third step, MW99 map the helium core model onto a 2D Eulerian grid and add some angular momentum to the spherical model, which is distributed so as to provide a constant ratio of 0.04 of centrifugal force to the component of gravity perpendicular to the rotation axis everywhere. Finally, MW99 evolve the model with a 2D hydrocode taking into account the effects of viscosity in the thick accretion disk (torus), which forms due to the action of rotation, by implementing the alpha viscosity prescription of Shakura & Sunyaev (1973) with $\alpha = 0.1$. At $t = 18.96$ s, when the central black hole, which forms in the center of the star, has acquired a mass of $3.762\,M_{\odot}$, we map the model to our computational grid.

In a consistent collapsar model the jet should be launched due to neutrino energy deposition by $\nu\bar{\nu}$–annihilation. Similar to MW99 we mimic this process by depositing energy at a prescribed (constant or variable) rate within a 30° cone around the rotation axis of the star[8]. In radial direction, the deposition region is bounded by the inner boundary and an outer radius of $r = 6 \times 10^7$ cm. Numerically, the internal energy of the corresponding zones of the computational grid is raised to a certain value. Note that we thereby neglect any momentum deposition by $\nu\bar{\nu}$–annihilation.

We have investigated three different cases (Table 4.1): (i) a constant energy deposition rate of 10^{50} erg/s, (ii) a constant rate of 10^{51} erg/s, and (iii) a strongly (by a factor of ten) and rapidly (on milliseconds) varying energy deposition rate with a mean of value of 10^{50} erg/s. The first two cases roughly bracket the expected energy deposition rates of collapsar models, while the latter case mimics time–dependent mass accretion rates, *i.e.,* time–dependent $\nu\bar{\nu}$–annihilation, and hence a fluctuating energy deposition rate as found by MW99.

The simulations have been performed with GENESIS (see Chapter 2; and Aloy *et al.* 1999a) using 2D spherical coordinates (r, θ). In r–direction, the computational grid consists of 200 zones spaced logarithmically between the inner boundary at $r = 200$ km and the surface of the helium star at $r = 2.98 \times 10^{10}$ cm. Assuming equatorial symmetry we used four different zonings in angular direction: 43, 90 and 180 uniform zones (*i.e.,* $2°, 1°$ and $0.5°$ angular resolution), and 100 nonuniform zones covering the polar region $0° \leq \theta \leq 30°$ with 60 equidistant zones (0.5° resolution) and the remaining 40 zones being logarithmically distributed between $30° \leq \theta \leq 90°$. The latter mesh provides the same resolution than the 180 uniform zone run (Sect. 4.3.4).

As the equatorial region evolves slower than the polar one, the loss of resolution due to the logarithmic spacing in θ does not affect the main conclusions derived below. As the number of angular zones is reduced by almost one half compared to the model with 180 θ-cells, the computational costs are approximately reduced by one half, too. The typical size of a time step for this angular resolution is between tens of microsecond to some microseconds. Several million time step are required to

[8]Let us remind the reader that the numerical energy deposition may, in fact, be produced by any other physical mechanism like, *e.g.,* magneto-hydrodynamic processes. In this sense, our simulations may be representative of either a hypernova or a collapsar.

Name	# zones ($r \times \theta$)	$\dot{E}$ (erg/s)	Deposition rate	M (g)	η^{-1}
e50c043	200×43	10^{50}	constant	$(9 \pm 4) \cdot 10^{29}$	2.1 ± 1.9
e50c090	200×90	10^{50}	“	$(7 \pm 4) \cdot 10^{29}$	1.9 ± 1.7
e50c100	200×100	10^{50}	“	$(5 \pm 2) \cdot 10^{29}$	1.3 ± 0.9
e50v100	200×100	10^{50}	variable	$(7 \pm 2) \cdot 10^{29}$	1.9 ± 0.9
e50c180	200×180	10^{50}	constant	$(5 \pm 4) \cdot 10^{29}$	1.3 ± 2.0
e51c090	200×90	10^{51}	“	$(6 \pm 4) \cdot 10^{30}$	3.2 ± 3.1
e51c100	200×100	10^{51}	“	$(9 \pm 5) \cdot 10^{30}$	3.4 ± 3.4

Table 4.1: Overview of the simulated models at the end of the *pre–breakout* phase. Note that model names involving letters “c” or “v” refer to a constant or variable energy deposition rate $\dot{E}$, respectively. M is the jet rest-mass and η^{-1} is the baryon loading. The errors assigned to the mass are due to uncertainties in determining the material belonging to the jet (we consider that the jet is formed by the material whose velocity is larger than $0.1-0.3\,$c, and whose specific internal energy density is larger than $5 \times 10^{19}\,\mathrm{erg\,g^{-1}}$). The errors in the baryon loading are also caused by this uncertainty.

follow the evolution of the system for several seconds.[9].

4.3.2. Equations of Special RHD in a spherical gravitational background

In order to take into account the BH's gravity, it has been necessary to include a spherical gravitational background field into GENESIS. Effects due to the self-gravity of the star on the dynamical evolution are neglected, *i.e.,* we consider only the potential generated by the BH (as if it were a point mass). The validity of such assumption relies on several facts:

- Deviations from spherical symmetry induced by the non-sphericity of the in-

[9]Working with 8 processors on a SGI ORIGIN 2000 a typical simulation needs 1 to 2 weeks.

ner (and denser) matter distribution (the torus) are small, *i.e.,* a spherically symmetric potential provides a reasonably good approximation.

- The Newtonian gravitational potential of the system (BH + surrounding stellar matter assuming a spherical matter distribution) differs by less than 20% from the potential produced by the central BH mass alone (see Fig. 4.1). The contribution of the stellar matter is negligible, even if the BH mass is smaller than the torus mass, which is distributed over a large volume).

The inner boundary of the computational domain (see §4.3.1) is at more than 35 Schwarzschild radii ($R_s = GM/c^2 \sim 5.6 \times 10^5$cm). General relativistic effects are small at such distances. Hence, although the star and the BH are rotating, it also does not make a large difference to represent the gravitational field of the BH by a static Schwarzschild metric instead of a more appropriate but also more complicated external Kerr metric. A more accurate treatment of General Relativistic effects becomes only necessary, if one comes closer to the event horizon.

The line element of the static Schwarzschild space–time can be written as (*e.g.,* Schutz 1985)

$$ds^2 = -e^{2\phi}dt^2 + e^{-2\phi}dr^2 + r^2 d\theta^2 + r^2 \sin^2\theta d\varphi^2, \tag{4.7}$$

where ϕ is a function only of r given by $e^{2\phi} = 1 - 2GM/rc^2$, or using natural units ($G = c = 1$) by $e^{2\phi} = 1 - 2M/r$. The evolution of a relativistic perfect fluid in this background is described by the following hyperbolic system of conservation laws:

$$\frac{1}{\alpha}\frac{\partial D}{\partial t} + \frac{1}{r^2}\frac{\partial}{\partial r}(r^2 e^{\phi} D v^r) + \frac{1}{r\sin\theta}\frac{\partial}{\partial\theta}(\sin\theta D v^\theta) + \frac{1}{r\sin\theta}\frac{\partial}{\partial\varphi}(D v^\varphi) = 0 \tag{4.8}$$

$$\frac{1}{\alpha}\frac{\partial S^r}{\partial t} + \frac{1}{r^2}\frac{\partial}{\partial r}(r^2 e^{\phi}(S^r v^r + p)) + \frac{1}{r\sin\theta}\frac{\partial}{\partial\theta}(\sin\theta S^r v^\theta) + \frac{1}{r\sin\theta}\frac{\partial}{\partial\varphi}(S^r v^\varphi) = e^{\phi}(-\frac{\partial\phi}{\partial r}(\tau + D) + \frac{1}{r}(2p + v^\theta v^\theta + v^\varphi v^\varphi)) \tag{4.9}$$

$$\frac{1}{\alpha}\frac{\partial S^\theta}{\partial t} + \frac{1}{r^2}\frac{\partial}{\partial r}(r^2 e^{\phi} S^\theta v^r) + \frac{1}{r\sin\theta}\frac{\partial}{\partial\theta}(\sin\theta(S^\theta v^\theta + p)) + \frac{1}{r\sin\theta}\frac{\partial}{\partial\varphi}(S^\theta v^\varphi) = \frac{1}{r}(\frac{\cos\theta}{\sin\theta}(p + S^\varphi v^\theta) - e^{\phi} S^\theta v^\varphi)) \tag{4.10}$$

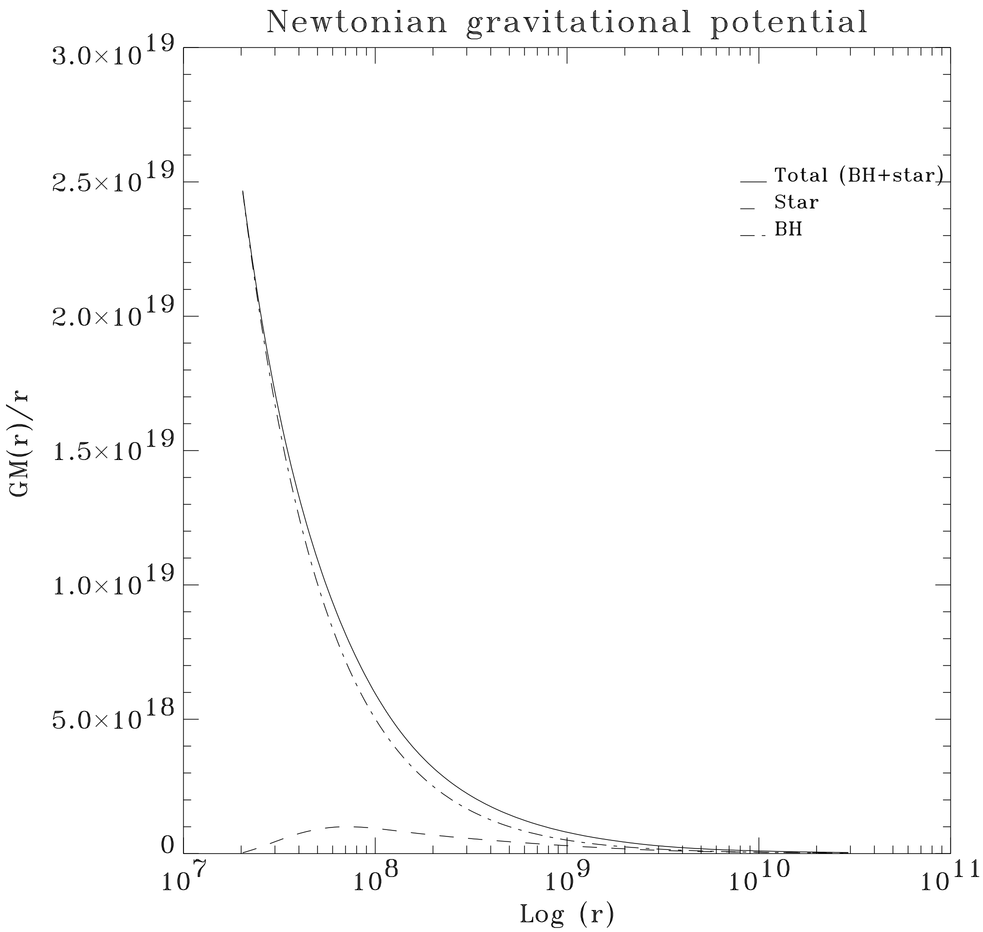

Fig. 4.1.— Newtonian gravitational potential of BH plus star (solid line), of the BH alone ($M(r) = M_{bh} = 3.763 M_{\odot}$; dotted-dashed line), and of the star alone (dashed line). The potential has been calculated assuming that the mass distribution is spherically symmetric (*i.e.*, $M(r)$ is the mass enclosed by an sphere of radius r), which is a good approximation to the real distribution.

$$\frac{1}{\alpha}\frac{\partial S^{\varphi}}{\partial t} + \frac{1}{r^2}\frac{\partial}{\partial r}(r^2 e^{\phi} S^{\varphi} v^r) + \frac{1}{r\sin\theta}\frac{\partial}{\partial\theta}(\sin\theta S^{\varphi} v^{\theta}) + \frac{1}{r\sin\theta}\frac{\partial}{\partial\varphi}(S^{\varphi} v^{\varphi} + p) = -\frac{S^{\varphi}}{r}(e^{\phi} v^r + \frac{\cos\theta}{\sin\theta} v^{\theta}) \quad (4.11)$$

$$\frac{1}{\alpha}\frac{\partial \tau}{\partial t} + \frac{1}{r^2}\frac{\partial}{\partial r}(r^2 e^{\phi} \mathcal{A}^r) + \frac{1}{r\sin\theta}\frac{\partial}{\partial\theta}(\sin\theta \mathcal{A}^{\theta}) + \frac{1}{r\sin\theta}\frac{\partial}{\partial\varphi}\mathcal{A}^{\varphi} = -e^{\phi} S^r \frac{\partial \phi}{\partial r}, \quad (4.12)$$

with $\mathcal{A}^i = S^i - Dv^i$.

In order to derive these equations, we have redefined the 3-velocity (and consistently the momentum) according to

$$
\begin{aligned}
v^j &= \tilde{v}^j \sqrt{g_{jj}} \\
S^j &= \tilde{S}^j \sqrt{g_{jj}},
\end{aligned}
\tag{4.13}
$$

where $\tilde{v}^j$ and $\tilde{S}^j$ are the velocities and momenta defined in §2.2 (note the change of notation). By this change the metric dependence is "hidden" in the contravariant components of the vectors. One has the relation

$$
\mathbf{v} \cdot \mathbf{v} = \sum_{i=1}^{3} g_{ii} \tilde{v}^i \tilde{v}^i = \sum_{i=1}^{3} v^i v^i,
\tag{4.14}
$$

because the metric is diagonal. As all velocities are transformed into locally Minkowskian velocities, one can use Riemann solvers developed for Special Relativity without modification in General Relativity. Our approach only works for diagonal metrics. For a general metric the method Pons *et al.* (1998) must be applied, where a similar variable transformation is performed before calling the Riemann solver (and a corresponding back-transformation afterwards). We simply use the redefined variables.

Energy deposition by neutrinos is incorporated by an additional source term in the energy equation (4.13) of the form $\dot{e}dt$, where $\dot{e}$ is the deposition rate per unit volume, *i.e.*, $\dot{e} = \dot{E}/V_{\mathrm{dep}}$ (here V_{dep} is the volume of the deposition region). The energy is deposited uniformly within the deposition region. Both a constant and a variable deposition rate was considered (see Table 4.1).

4.3.3. Equation of State

The EOS is an approximation to the one used in Witti, Janka & Takahashi (1994) –they used a more accurate treatement of the pairs e^+e^-–. It includes the contribution of non-relativistic nucleons which behave as an arbitrary mixture of Boltzman gases, and the contribution of radiation together with an approximate correction due to pairs e^+e^-, *i.e.,* relativistic particles (photons, e^+ and e^-).[10] Complete ionization is assumed and the effects due to degeneracy are not included.

In order to calculate pressure, temperature (T), specific enthalpy, sound speed and $\frac{\partial P}{\partial \varepsilon}\Big|_\rho$ the local (baryonic) rest-mass density (ρ) and the energy density ($e = \rho\varepsilon$) have to be given. The expression for the pressure then reads:

$$p(\rho, T) = \frac{\mathcal{R}}{\mu}\rho T + \frac{1}{3}aT^4 + \frac{7}{12}aT^4 - \frac{7}{6}ab(T^2 - b\ln(1 + T^2/b)), \tag{4.15}$$

where $\mathcal{R}$ is the universal gas constant, a is the radiation constant, b is a combination of fundamental constants ($b = 5.3 \times 10^{18}\,\mathrm{K}^2$), and μ is the mean molecular weight per free particle (Cox & Giuli 1968)

$$\frac{1}{\mu} = \sum_i \frac{X_i(Z_i + 1)}{A_i}. \tag{4.16}$$

Here X_i are the mass fractions, Z_i the atomic numbers, and A_i the atomic masses of the ideal Boltzmann gases. The pair correction term accounts for the fact that electrons become non–relativistic (at sufficiently small densities) below $T \sim 5 \times 10^9\,\mathrm{K}$, and do not contribute much to the pressure ($\frac{7}{12}aT^4 - \frac{7}{6}ab(T^2 - b\ln(1 + T^2/b)) \rightarrow 0$ if $T^2 \rightarrow 0$ hence explicitly canceling the other correction term).

We have not considered nuclear reactions, *i.e.,* the initial composition at each point is only advected using the same technique as in Sect. 3.2.2 for the beam particle fraction. We advect nine nuclear species which are present in the initial model: C^{12}, O^{16}, Ne^{20}, Mg^{24}, Si^{28}, Ni^{56}, He^4, neutrons and protons.

Expression (4.15) gives the pressure as a function of ρ and T, while the hydrocode advances ρ and e. Hence, it is necessary to solve for the temperature iteratively (using a Newton–Raphson procedure) starting from an initial guess value for T:

$$e_g + e_r - e = 0, \tag{4.17}$$

e_g and e_r being the energy densities of the gas and the radiation (including pair correction), respectively. Both values are computed using the iterated value of the

[10] The approximate expressions for the pressure and energy density of the pairs was derived by Janka & Takahashi (private communication). The corresponding entropy equation is given in Witti, Janka & Takahashi (1994).

temperature, T_*:

$$
\begin{aligned}
e_g &= \frac{3}{2}\frac{R}{\mu}\rho T_*\,, \\
e_r &= aT_*^4\left(1+\frac{7}{12}(\frac{4T_*^2}{b+T_*^2}-1)+\frac{7}{6}ab(T_*^2-b\ln(1+T_*^2/b))\right).
\end{aligned}
$$

Once equation (4.17) has been solved for T up to a prescribed tolerance, the value of p can be computed from (4.15) using the density. Next the specific enthalpy ($h = 1 + \varepsilon + p/\rho$) is calculated, and finally the sound speed is obtained by

$$
c_s = \sqrt{\frac{p\gamma}{\rho h}},
$$

$$
\gamma = \left.\frac{d\ln p}{d\ln\rho}\right|_s = \frac{\frac{p^2}{e}+p_g}{p},
$$

where p_g is the pressure contribution of the nucleons ($p_g = (\mathcal{R}/\mu)\rho T$), and s is the specific entropy.

Finally, for the Riemann solver one needs the value of the derivative $\left.\frac{\partial p}{\partial\varepsilon}\right|_\rho$, which is obtained from

$$
\begin{aligned}
\left.\frac{\partial p}{\partial\varepsilon}\right|_\rho &= \rho\left.\frac{\partial p}{\partial T}\right|_\rho\left(\left.\frac{\partial e}{\partial T}\right|_\rho\right)^{-1}, \\
\left.\frac{\partial p}{\partial T}\right|_\rho &= \frac{R}{\mu}\rho+\frac{1}{3}aT^3\left(11-\frac{7b}{b+T^2}\right), \\
\left.\frac{\partial e}{\partial T}\right|_\rho &= \frac{3}{2}\frac{R}{\mu}\rho+4aT^3\left(\frac{17}{12}+\frac{7}{2}\frac{T^2}{b+T^2}\left(1-\frac{1}{3}\frac{T^2}{b+T^2}\right)-1\right)+\frac{7}{3}ab\frac{T^3}{b+T^2}.
\end{aligned}
$$

4.3.4. Constant and moderate energy deposition rate

The first case we have considered has a constant energy deposition rate of 10^{50} erg/s. Although this rate is only moderate, concerning collapsar models, a relativistic jet forms within a fraction of a second and starts to propagate along the rotation axis. In Figs. 4.2 and 4.5 the evolution of the rest-mass density and the Lorentz factor are plotted in eight snapshots from the initial state (panel (a)) to the last computed model (panel (h)). From these figures one can notice that all the morphological elements of the BR74 jet model are present: the terminal bow shock, a narrow cocoon, a contact discontinuity between the star and the jet itself, a faint hot spot (noticeable in Fig. 4.3), etc. The propagation of the jet is unsteady, because of density inhomogeneities in the star, particularly along the axis. For example, Fig. 4.2c shows the combined effect of matter being piled up (in front of the jet) and of a locally increasing stellar density. This gives rise to a "split" of the head of the jet along with a head deceleration and a cleaning of the central channel. The density inside the jet flow drops considerably with time reaching values as low as $\sim 10^{-6}\,\mathrm{g/cm^3}$ (Fig. 4.4). The density profile within the jet (Fig. 4.4) shows large variations (up to a factor of 100) due to internal shock waves, which can be identified when comparing density and pressure distributions at the same time (Figs. 4.2 and 4.3). Some of the internal shocks are of biconical nature recollimating the beam. These shocks develop during the jets propagation through the star. Additional shocks may appear in the subsequent jet evolution playing the rôle theoretically assigned to the "internal shocks" in the emission processes (see Sect. 4.1.1).

Fig. 4.2 shows that the density structure of the star does not change noticeably during the whole evolution. This statement also holds for other variables (Figs. 4.2 – 4.6), and hence proves that the evolution time scale of the jet is short compared to the (dynamical) time scale required to change the mass distribution within the star. This result, a posteriori, justifies our treatment of the gravity of the star (see Sect. 4.3.2).

The Lorentz factor of the jet continuously increases with time, but it grows non-monotonically (Fig. 4.7). The maximum Lorentz factor is not reached in the head of the jet (which propagates at a mean speed of $7.8 \times 10^9\,\mathrm{cm/s}$, or $W \sim 1.04$), but in the rarefaction waves that form behind the biconical shocks. A particularly strong recollimation shock wave forms during the early stages of the evolution (after the initial transient state). This shock moves outwards, and reaches a distance of $\sim 10^{10}\,\mathrm{cm}$ in the final model (Fig. 4.2h). A very strong rarefaction wave behind this recollimation shock causes the largest local acceleration of the beam material.

Due to the energy deposition and the dropping density, the specific internal energy becomes extremely large within certain parts of the jet, reaching $10^{28}\,\mathrm{erg/g}$ in some small regions near the rotation axis at radii less than $10^8\,\mathrm{cm}$. The mean

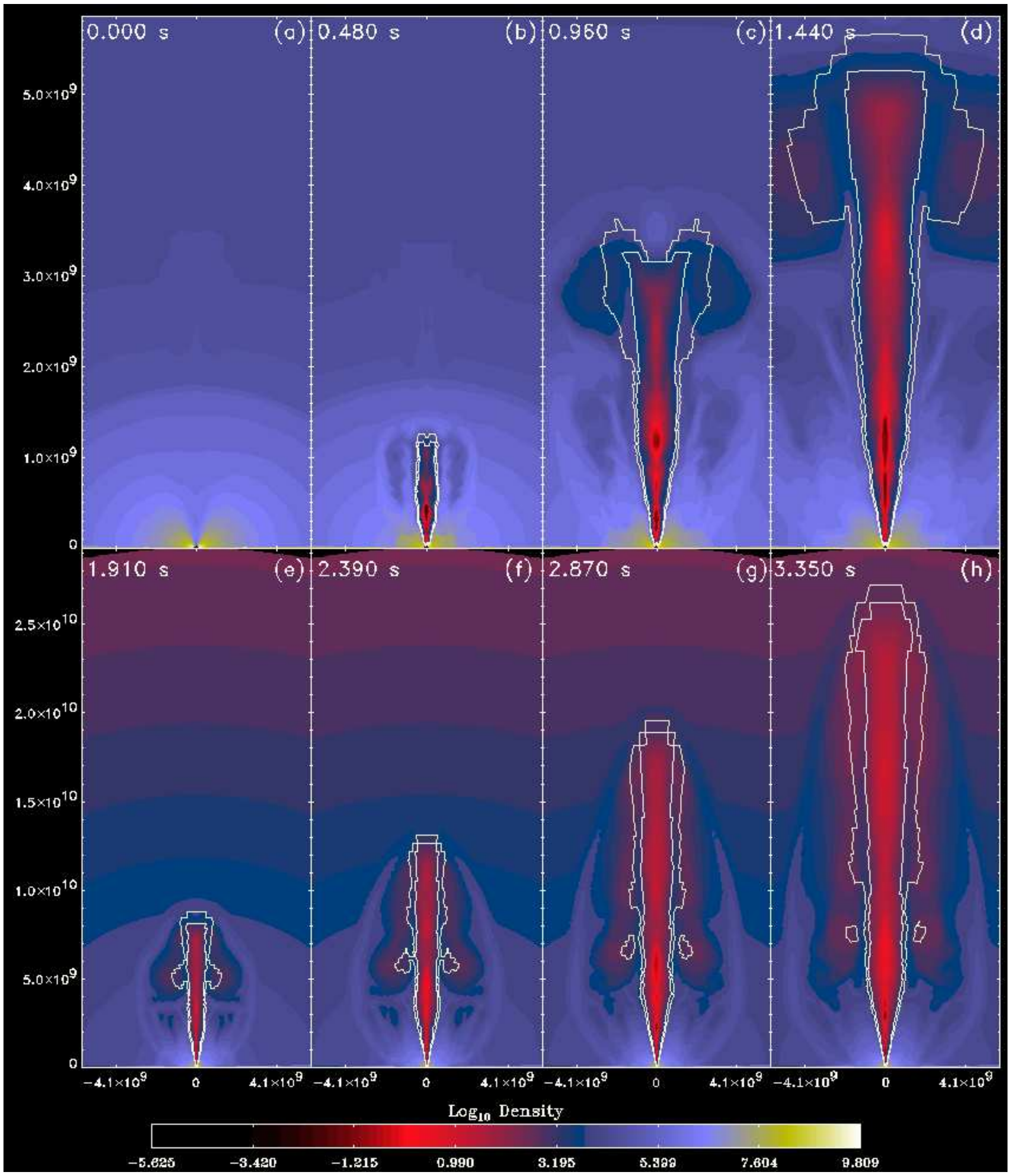

Fig. 4.2.— Color contour maps of the logarithm of the rest–mass density distribution at different evolution times (model e50c100). All the units are given in CGS system. Snapshots are arranged by rows and from left to right corresponding to different evolutionary times (marked in the top left corner of each panel). The panels in the top row have been zoomed by a factor five compared to those in the bottom row to exhibit more details. The two white isocontours correspond to the "limits" of the jet considering two different criteria: the inner contour assumes that the jet is formed by material with $\varepsilon \geq 5 \times 10^{19}$ erg/g and $v_r \geq 0.3c$; the outer contour represents the part of the system with $\varepsilon \geq 5 \times 10^{19}$ erg/g and $v_r \geq 0.1c$.

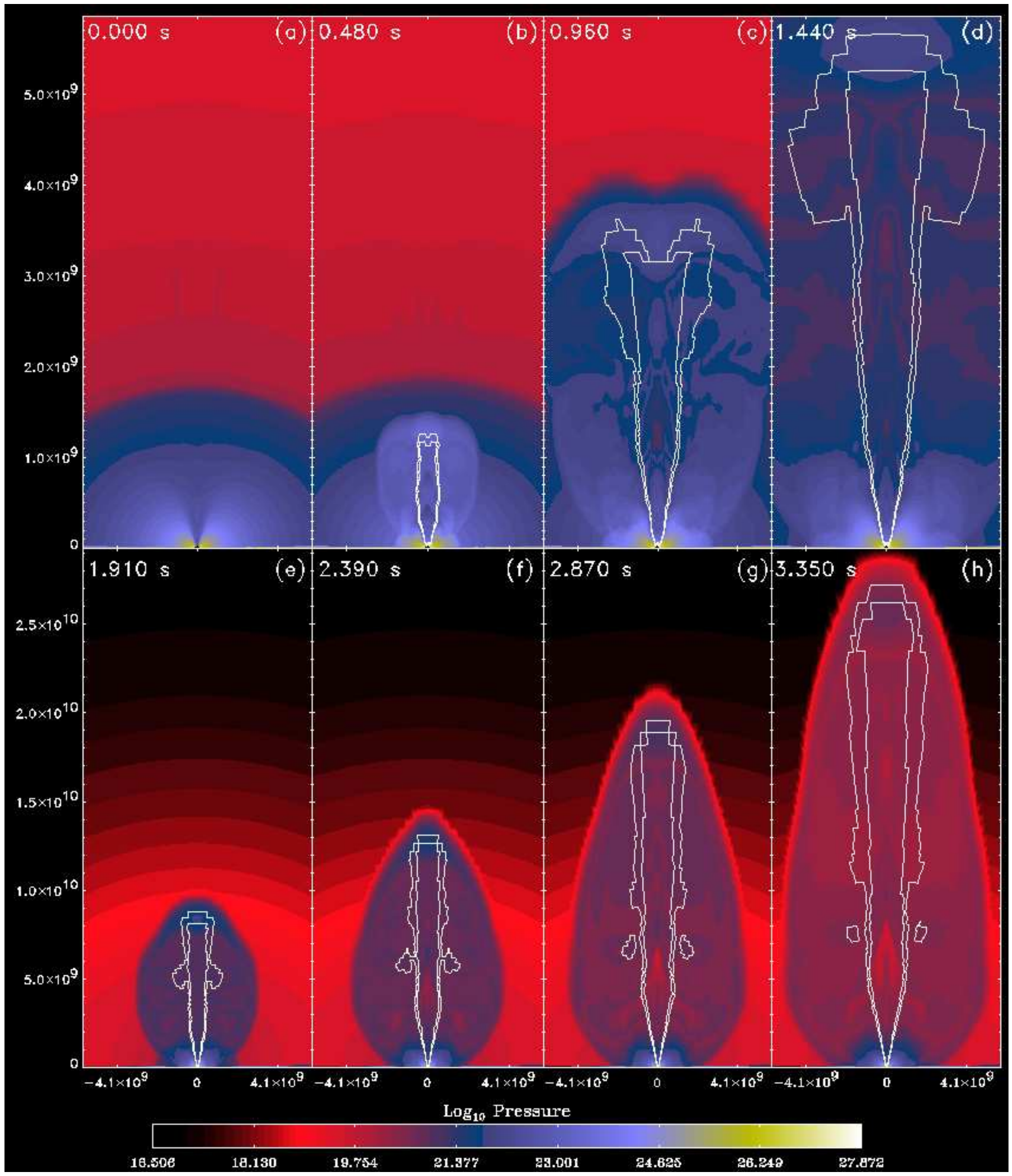

Fig. 4.3.— Same as Fig. 4.2, but showing the logarithm of the pressure distribution.

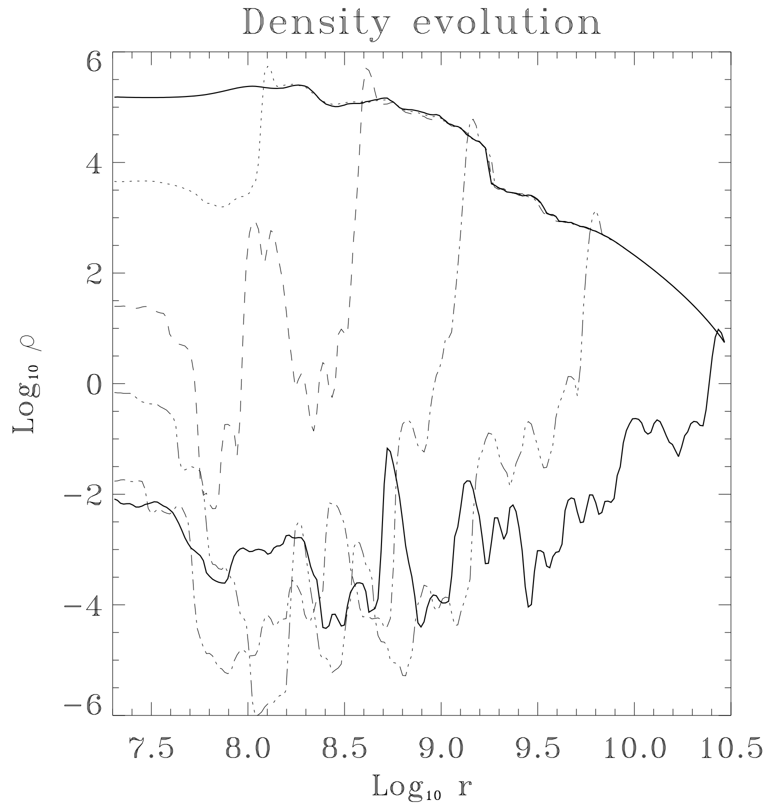

Fig. 4.4.— Evolution of the rest–mass density along the polar axis for several epochs of model e50c100. From top to bottom the different line styles are associated to the times: 0.00, 0.03, 0.13, 0.50, 1.5, and 3.35 s, respectively.

value of ε is $\sim 10^{20} - 10^{21}$ erg/g, or $\sim O(c^2)$ (Fig. 4.8), *i.e.,* the jet is very hot. A mean temperature of $\sim 5 \times 10^8$ K can be estimated from Fig 4.6 implying that its pressure is radiation dominated, in accordance with the simplified EOS used in our simulations. Clearly, the EOS used in MW99 is more realistic, particularly in the denser regions of the torus. But as the jet does not propagate through such regions and as the torus does not evolve significantly from its initial state, the usage of a simplified EOS should not be problematic.

The relativistic treatment of the hydrodynamics leads to a overall qualitatively quite similar (formation of a jet), but quantitatively very different evolution than in MW99, although the energy deposition rate of MW99 is the same than ours. As one can read off from their Fig. 27, the jet has propagated 7,000 km within the first 0.824 s. Using the jet's energy density, MW99 infer from this fact a Lorentz factor

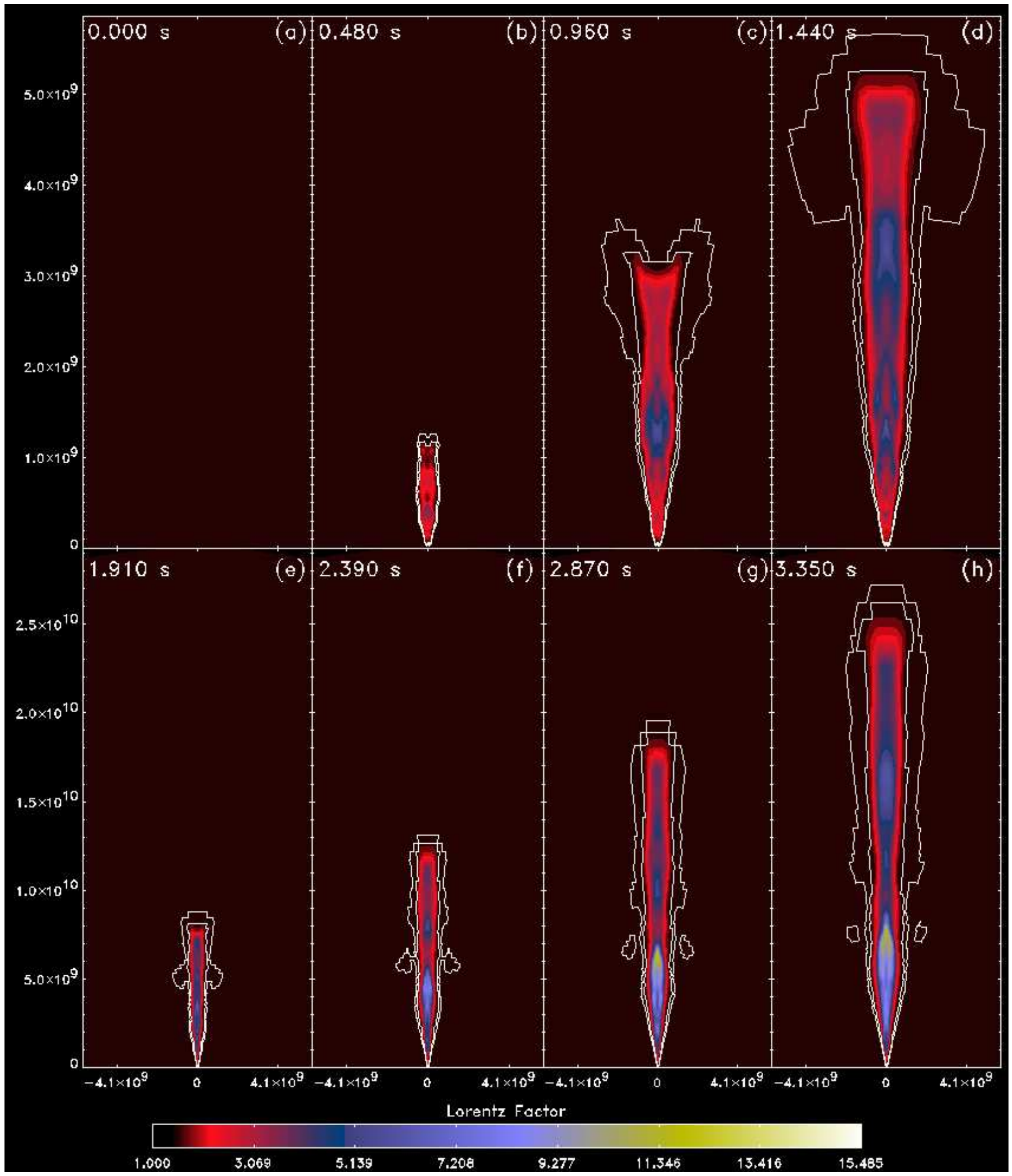

Fig. 4.5.— Same as Fig. 4.2, but showing the distribution of the Lorentz factor.

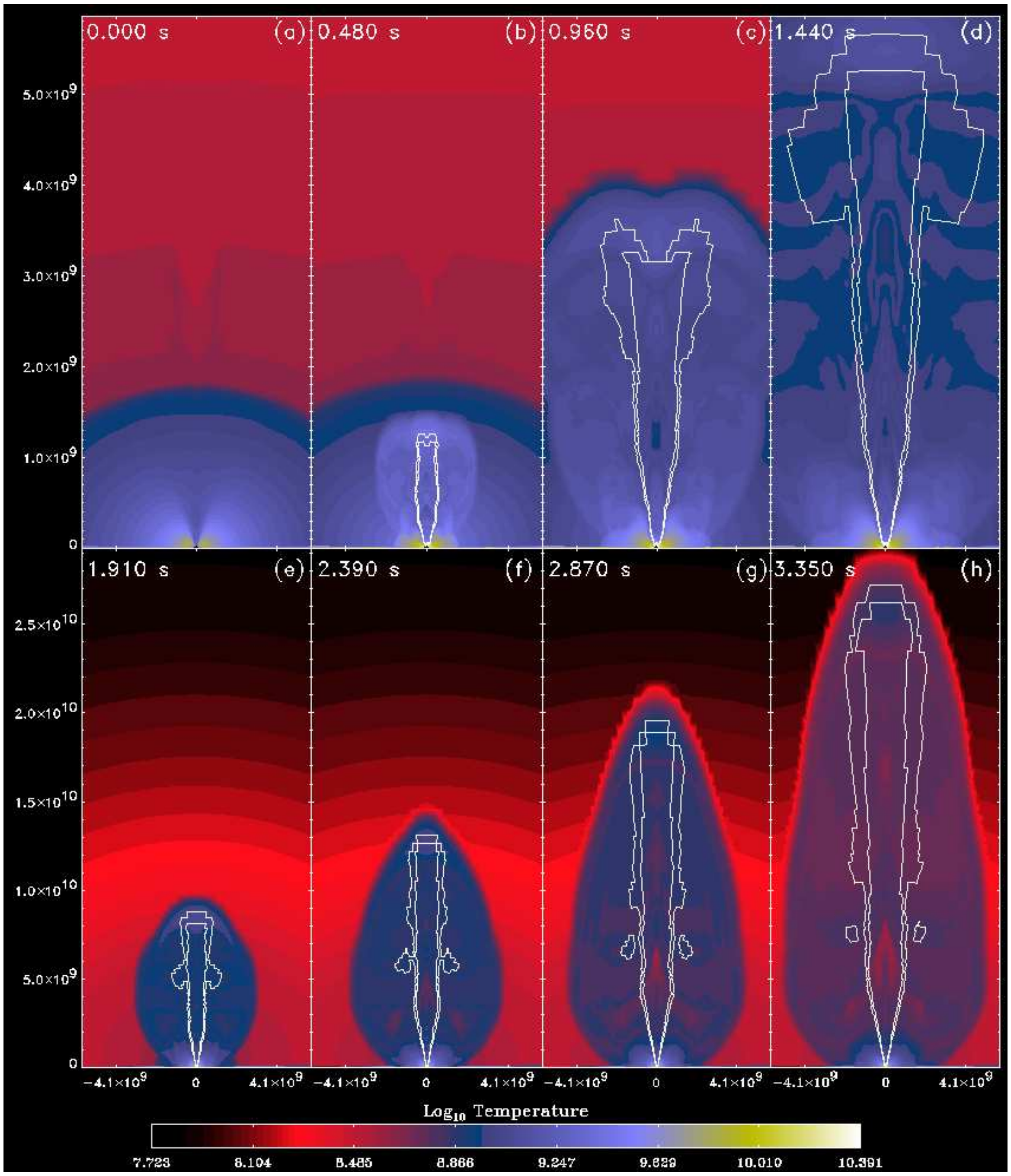

Fig. 4.6.— Same as Fig. 4.2, but showing the logarithm of the temperature distribution.

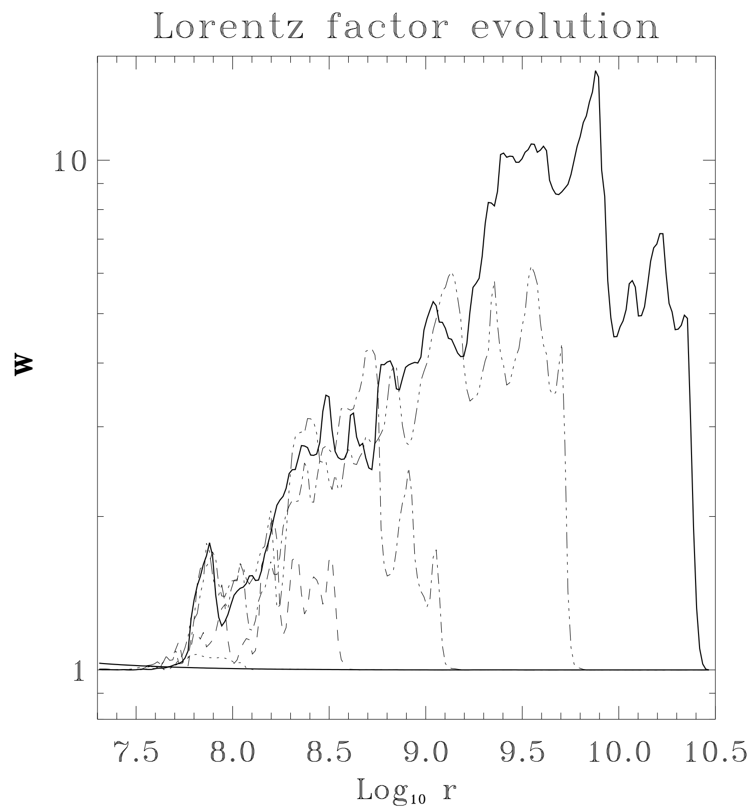

Fig. 4.7.— Evolution of the Lorentz Factor along the polar axis for several epochs of model e50c100. From top to bottom the different line styles are associated to the times: 0.00, 0.03, 0.13, 0.50, 1.50 and 3.35 s.

of the matter of ~ 10. Furthermore, they find a half opening angle for their jet of $10°$. In our simulation, at the same time for the same angular resolution ($\sim 2°$) and the same energy deposition rate (10^{50} erg/s) the head has reached a radius of 30,000 km (4.3 times farther out than in MW99), but its maximum Lorentz factor is only 4.62 (less than half than in MW99) located in a blob at $\sim 12,200$ km. Moreover, in our model another blob of matter moves with a speed of $W \simeq 3$ at a radius of $\simeq 20,000$ km. Our half opening angle is $6°$, *i.e.,* it is roughly half of that of MW99.

Another important issue, that was not analyzed by MW99, is the dependence of the results on the grid resolution. We have investigated the dependence of the results on the angular resolution (for a fixed radial grid). Table 4.2 shows that we find significant changes with resolution. For instance, the radius reached by the

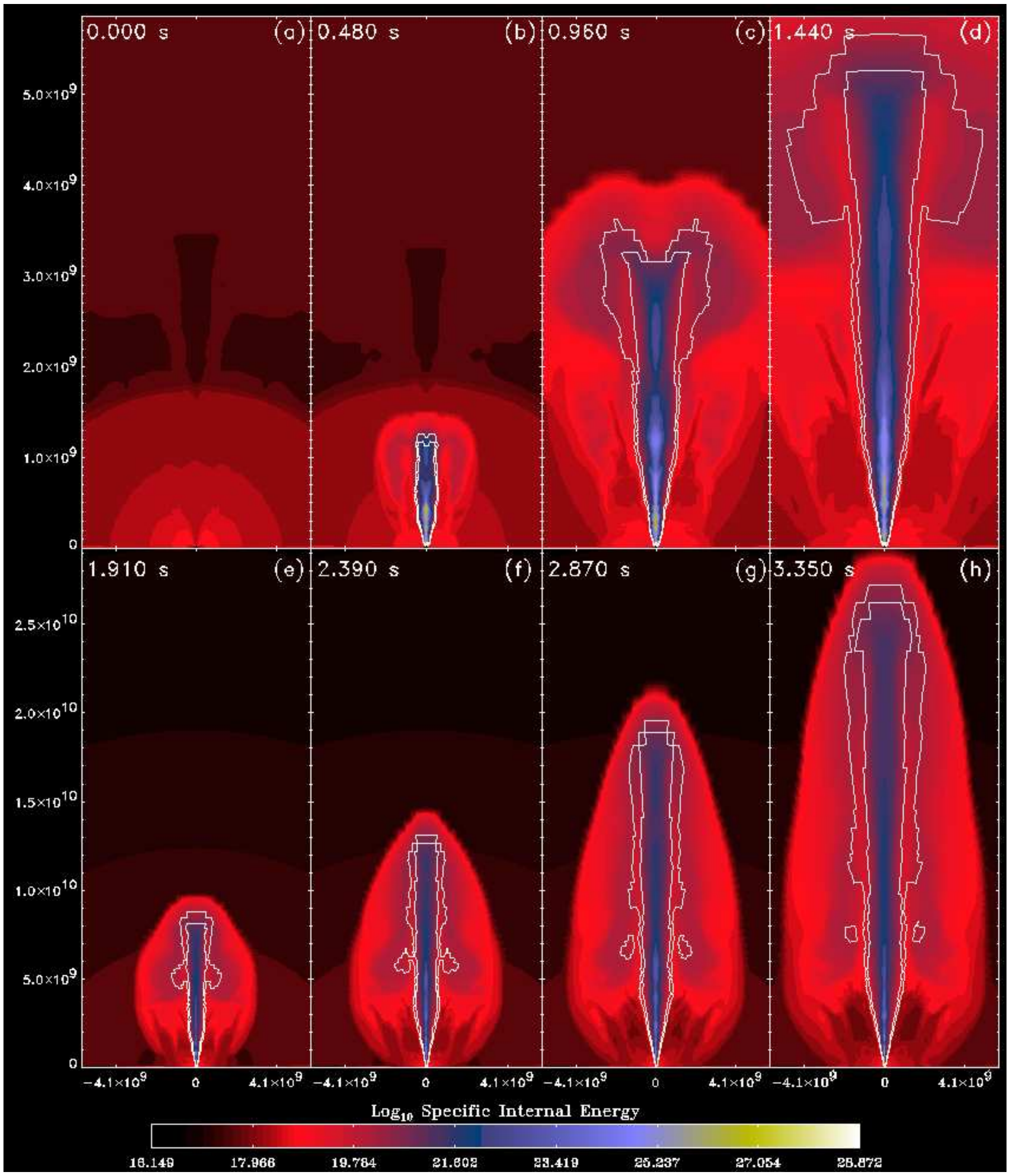

Fig. 4.8.— Same as Fig. 4.2, but showing the distribution of the logarithm of the specific internal energy density.

head of the jet after 0.82 s varies by about 30% when increasing the angular resolution by roughly a factor of four. The propagation speed tends (non-monotonically) towards a value $W_{\max} \approx 4.4$ as the angular grid resolution is increased. A similar comment holds for all hydrodynamic variables. Generally speaking, models e50c100 and e50c180 are very similar globally, even though the local values of the maximum specific internal energy or the minimum density are quite different. This result is not unexpected, because the resolution of both models is the same near the axis (along which the jet is propagating).

Thus, we need an angular resolution four times larger than that of MW99 to reach acceptable numerical convergence. When comparing our results with those of MW99 the question arises to what extent are their results dominated by numerical resolution and to what extent by their different input physics (realistic EOS, Newtonian self-gravity of stellar matter, etc). This problem should be kept in mind in the following discussion.

We are going to discuss now some general trends that can be inferred from the dependence of the results on the resolution (considering the simulations up to 3.35 s).

Model	Distance (km)	$W_{\max}$	θ (deg)	$\rho_{\min}$ (g/cm^3)	$\varepsilon_{\max}$ (erg/g)
e50c043	30,000	6.03	8	2.35×10^{0}	3.38×10^{23}
e50c090	27,000	3.92	8	2.37×10^{-3}	1.53×10^{27}
e50c100	26,000	4.62	6	4.33×10^{-4}	1.36×10^{27}
e50c180	22,000	4.40	7	1.38×10^{-4}	6.14×10^{27}

Table 4.2: Some characteristic quantities obtained for models with an energy deposition rate of $\dot{E} = 10^{50}$ erg/s for different grid resolution at time 0.820 s. Distance gives the radius of the head of the jet, and $W_{\max}$ and $\varepsilon_{\max}$ are the maximum Lorentz factor and specific internal energy at this time. $\rho_{\min}$ is the absolute minimum value of the density. The values of θ are measured with an accuracy of 1°.

The highest specific internal energy is concentrated in small blobs at radii less than 5×10^8 cm. These blobs are connected by a narrow central channel (which gets narrower when the resolution is increased). The average specific internal energy within the jet is $\sim 10^{21}$ erg/g in almost all models. The presence of the central channel could be a numerical artifact (*e.g.,* a *wall heating* effect like that mentioned in Chapter 2, Sect. 2.4.2) related to the reflecting boundary condition along the axis.

At the beginning of the simulations the half opening angle lies in the range $6° - 8°$ which is smaller than $10°$ (MW99 value). Moreover, the opening angle shrinks from $8°$ to $6° - 7°$ when the resolution is increased. Later in the evolution (at ~ 1.5s) a strong recollimation shock reduces the opening angle to less than $1°$. This effect is most remarkable in those models having the best resolution. Consequently, the strong collimation found by us cannot be definitely ascribed to relativistic effects alone, because insufficient grid resolution might play some rôle.

During the late stages of the jet propagation the distance reached by the head of the jet tends to differ slightly (Fig. 4.9), while during the initial stages of the evolution, all models follow very similar evolutionary tracks. This can be explained by the non-linearity of the hydrodynamic equations, which may amplify differences present in the initial models (produced by the interpolation of the initial model of MW99 onto our different computational grids).

When the resolution is increased and becomes sufficiently good, $W_{\max}$ approaches a value of $\sim 15 - 20$ (at shock break out), the maximum value being reached at a radius $\sim 8 \times 10^9$ cm. The value of $\rho_{\min}$ is quite sensitive to the resolution. It drops to a value of about 5×10^{-6} g/cm^3 in the highest resolution run. However, as the density minima are located near the axis (in the first θ-zone), they may be affected by numerical errors. Another much better indicator of the convergence behavior of the code is the mean density in the jet[11] which always lies in the range $10^{-2} - 1$ g/cm^3. In addition, the final maximum density ($\sim 5 \times 10^8$ g/cm^3) is always obtained at a radius of $\sim 3 \times 10^7$ cm within the torus. Hence, even if the point values are not exactly the same, the global maximums and minimums can be found in the same regions. This result also confirms that outside the axial cone resolution does not play an important rôle. Nevertheless, if one wants to include

[11]This indicator is better because it refers to a global property.

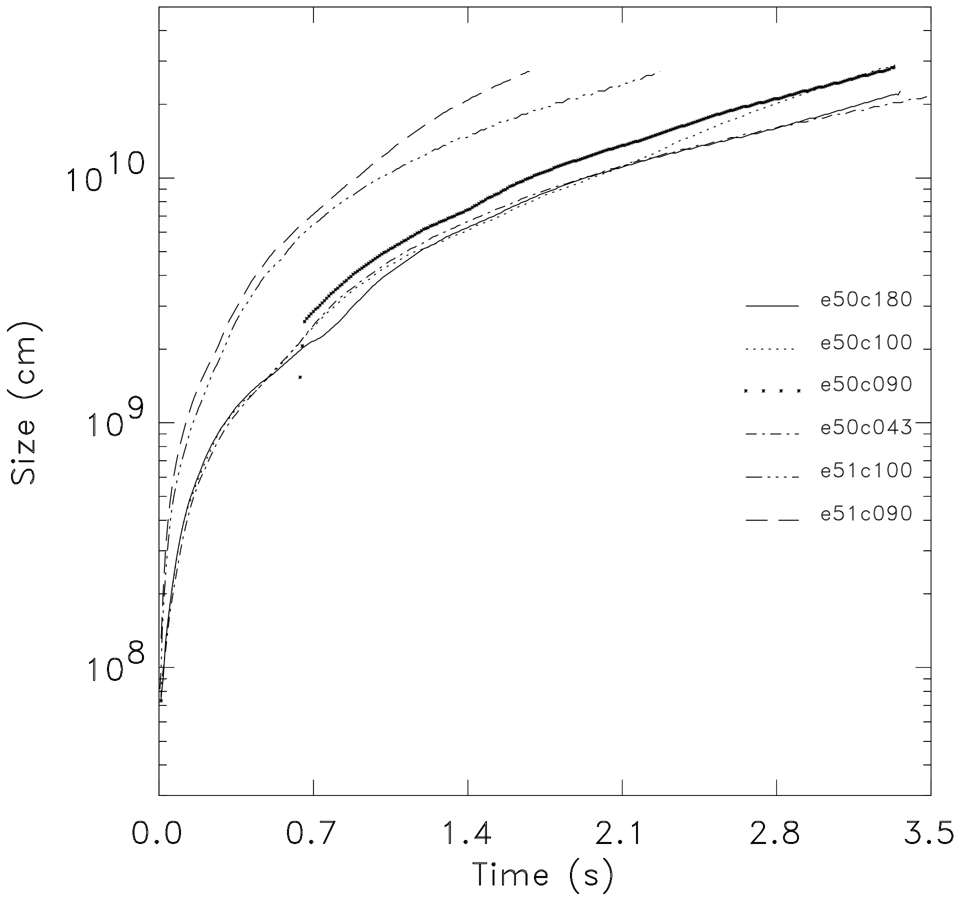

Fig. 4.9.— Evolution of the head position for models with a constant energy deposition rate equal to 10^{50} erg/g. For model e50c090 the available data only cover the interval [0.7, 3.35] s.

neutrino generation and transport processes from the torus into the simulations, and wants to model the accretion from the torus, a better resolution near the equator is crucial (because this region has the highest accretion rate, see below).

The structure of the jet is characterized by shocks and knots with a varying number of blobs of high W and low density. As one expects, the morphology of the jet is richer at better resolution. It shows a narrow spine of low density connecting the various blobs.

The mean temperature in the jet, $\bar{T}$, is (in all models) $\sim 5 \times 10^{8}\,\mathrm{K}$. The maximum temperature in the computational domain, $T_{\max} \sim 2.3 \times 10^{10}\,\mathrm{K}$, is always attained at the central part of the torus. This temperature value implies that our calculations are self-consistent, because even when we deposit energy to heat up the matter, its temperature does never exceed the temperature of the emission region (*i.e.,* the walls of the torus). Moreover, the temperature is well below the pair creation threshold and is compatible with the assumed temperature of the GRB emitting region (a few keV, see Sect. 4.1.1).

The baryon mass enclosed by the jet and its cocoon is about $10^{-4}M_\odot$. This value is large compared with the expected mass of the ejecta in a typical GRB ($\sim 10^{-6}M_\odot$; Rees 1997). It does prevent the formation of a GRB, mainly because in later stages of the evolution new mass will be piled up in front of the expanding jet. Our results show an alternative to the standard model, which is that instead of having a thin shell of matter expanding ultrarelativistically (what requires a low enclosed mass), one has an expanding bubble with an inner jet-like ultrarelativistic core that would be the responsible of the gamma-ray emission (once the bubble becomes optically thin). Such a picture is similar to what is assumed valid for extragalactic jets, in the sense that the head propagation speed (and the sideways expansion) is subrelativistic or mildly relativistic, while the beam itself is relativistic (even at kpc scale) and the main responsible for the synchrotron emission. Actually that situation might even allow for interesting observational implications; for instance, one can imagine that the dense slow matter is iron group matter irradiated by gammas from the beam behind it. This may produce iron lines as indicative in some jet sources (which do not make a GRB because of the orientation of the source relative to an Earth observer.

Mass accretion is slowed down or even stopped by the deposition of energy. The flow of stellar matter across the inner boundary (*i.e.,* the flow of mass that eventually ends up in the black hole) is almost stopped after $\sim 0.15\,\mathrm{s}$ when $\sim 1M_\odot$ has been passed the inner boundary (see Fig. 4.10). The accretion rate is highly variable on time and depends on latitude too. The largest accretion rate is observed in the equatorial layers of the star (between 60° and 90°), because they are the most dense ones (due to the presence of the torus with densities above $10^8\,\mathrm{g/cm^3}$). The accretion rate decreases with angle, and reaches a minimum in a cone of $\sim 10^\circ$ around the axis, because the polar regions initially have the smallest density and the energy deposition promptly stops the accretion there. One can notice from Fig. 4.10 that there is a change in the slope of the accreted mass around $\sim 1.2\,\mathrm{ms}$, which must be a result of (1) the numerical relaxation of the initial model and (2) the energy deposition itself. The effect (1) is due to the interpolation necessary to produce our initial model from data which have been produced by a different code using other EOS and that includes effects such as α-viscosity of the accretion disk. The effect (2) is produced because, initially, the energy deposited is used to heat up the innermost region of the star increasing its pressure, and thereby preventing fast accretion. This effect is smaller and delayed in equatorial regions (see the dotted line in Fig. 4.10 up to a latitude of $63.8^\circ - 90.0^\circ$), which contributes to the accreted mass up to $\sim 0.15\,\mathrm{s}$ because it is farther from the deposition volume. The outermost shells of

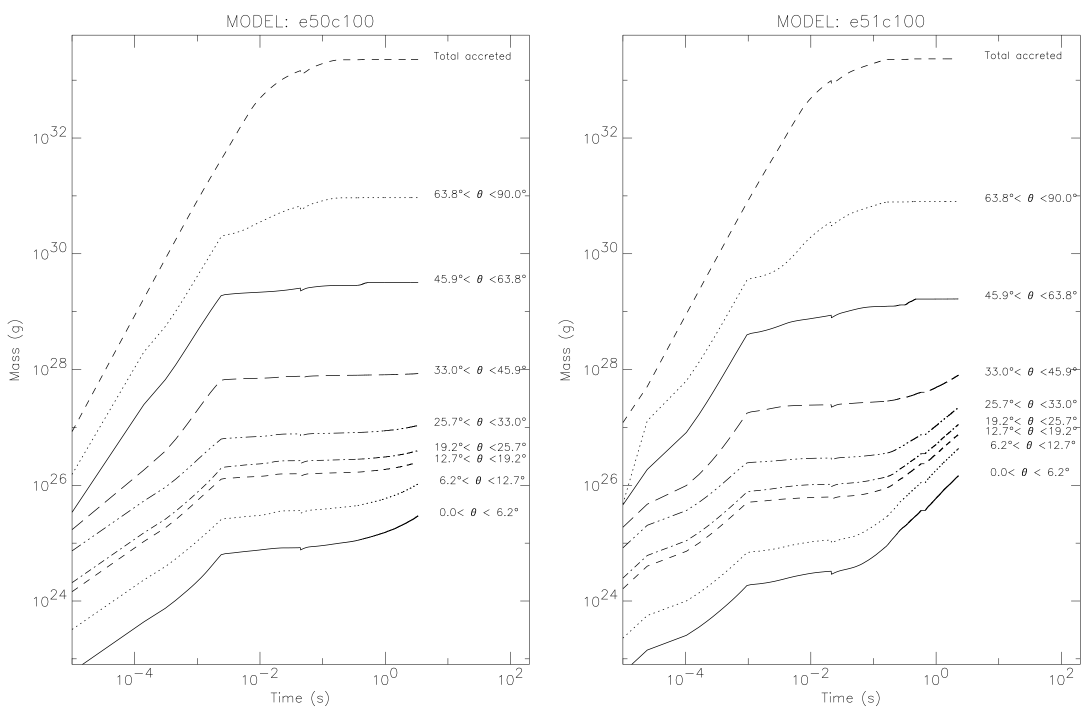

Fig. 4.10.— Time evolution of the cumulative mass that is lost across the inner boundary at different latitudes for models e50c100 (left) and e51c100 (right), respectively.

the star are falling with velocities as small as 10^{-6}c, *i.e.,* a negligible amount of mass

($1.7\times10^{-4} M_{\odot}$) is entering the computational grid through the outer boundary. From an analysis of the radial velocity field at the end of the simulations (see Fig. 4.11 which corresponds to model e50c180, but it is representative of the other models, too) we have found that there exists an extended torus-like region centered around the equator having a velocity ≈ 0. In Fig. 4.11 this region is surrounded by the isocontour where the velocity is equal to zero. Note that the region is not connected to the central torus, because in between (and around the jet cavity –like in MW99–) a layer of infalling material is present. The maximum infall velocity depends on resolution, and lies, in the best resolution run, in the interval $0.357c$ - $0.398c$, while for the lowest resolution the value is $0.097c$. These maximum velocities are found around the central torus.

The baryon load of the jet has been calculated for each model (see Table 4.1) as the ratio of (the approximate value of) the jet mass to the energy deposited. The extraction of the values involves some uncertainty, because there exists some arbitrariness in measuring the jet mass accurately.[12] The baryon load is very similar for the four cases we have studied. It seems to decrease with increasing resolution, although the uncertainties are so large that all models with a deposition rate of 10^{50} erg/s show a baryon load consistent with that of the highest resolution run of $\eta^{-1} \simeq 1.3$. The explanation is simple. Models with the a worse resolution have larger computational cells. Hence, the determination of the jet shape is less accurate, *i.e.,* some cells may include material that does not belong to the jet. This happens for those cells located at the jet boundary.

The value of the baryon contamination found in the simulations is not compatible with that assumed in the standard model (see Sect. 4.1.1). However, such a model considers an isotropic relativistic expansion into a uniform external medium. In our case, neither the expansion is isotropic nor the external medium is uniform. In fact, depending on the criteria employed to *define* the jet, there are regions inside the beam where $\eta^{-1} \lesssim 10^{-3} - 10^{-5}$ (precisely where the Lorentz factor is larger). Additionally, the mass entrained into the jet increases slower with time than the

[12]The jet is not well defined, because we do not have a conserved variable that unanimously identifies jet matter. This situation is different in the case of extragalactic jets, where the beam mass fraction allows us to properly locate the jet boundary (neglecting effects of numerical diffusion).

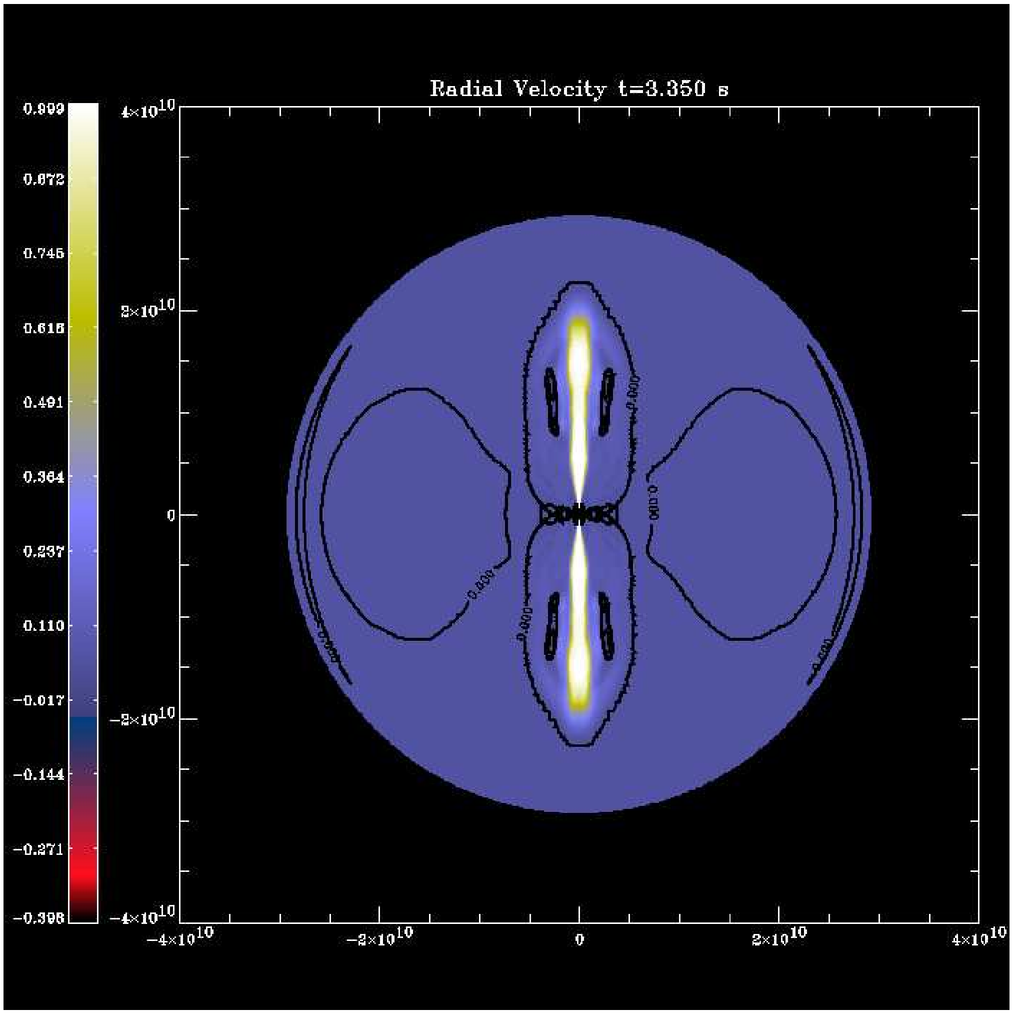

Fig. 4.11.— Snapshot of the radial velocity of model e50c18 at the end of the simulation (at t=3.35 s). Isocontours correspond to velocity values -0.05c, -0.01c and 0, respectively. Numbers at the X and Y axes give the distance in centimeters.

energy released, because once the funnel is evacuated mass entrainment across the jet boundary almost seizes (of course this argument depend on resolving the KH instabilities on the jet funnel). In fact, considering the evolution of η^{-1} for model e50c100 after jet breakout (Sect. 4.3.7), we find a decrease of the baryon load by a factor of four in less than 1.8 s. If this decrease continues in time, a value of $\eta^{-1} \sim 10^{-3}$ is reached in less than 9 s.

4.3.5. Constant large energy deposition rate

In order to investigate the effect of the deposition rate on the overall evolution two runs have been made with a tenfold increased energy deposition rate, e51c090 and e51c100, which differ in grid resolution (Table 4.1). We find that a resolution of 90 θ-zones is insufficient to capture accurately all relevant features. In addition, some numerical problems were encountered in model e51c100. The main reason for these problems is the artificial way in which the energy is released in the computational domain. In reality, the energy deposition of the neutrinos is smoothly distributed over the whole star, but it is strongly peaked near the axis and close to the star's core. In the previous simulations the region where the energy was deposited had a sharp boundary (see Sect. 4.3.1) generating an extremely large jump (in energy) that made the code crash after several ten milliseconds. This initial jump is ten times smaller for the models with an energy deposition rate of 10^{50} erg/s. Therefore, the effect of the artificial deposition had not caused numerical problems in those cases. For model e51c090, the situation was not as critical as for model e51c100. The former one has been computed with a two times smaller angular resolution, and its increased numerical diffusion obviously helped to avoid the problem. However, in order to get model e51c100 to run, we had to include a time dependent deposition rate of the form:

$$\dot{E} = \begin{cases} 10^{51} \exp(-\frac{(t-t_0)}{t_0}) & \text{for } t < t_0; \\ 10^{51} & \text{for } t \geq t_0. \end{cases} \tag{4.18}$$

where $t_0 = 200\,\mathrm{ms}$. Hence, the deposition of energy proceeds in two stages: (1) exponential growth from $10^{51}/e$ erg/s to 10^{51} erg/s up to 200 ms, and (2) constant rate of 10^{51} erg/s afterwards. In addition, the edge of the deposition region was linearly smoothed over 3 cells in radial and angular direction (to decrease the jump between adjacent zones).

Model e51c090

The jet propagates faster than in any model with a deposition rate of 10^{50} erg/s. The time needed to reach the star surface is about 1.68 s (to be compared to 3.35 s for the previous models). $W_{\max} = 20.686$, which is almost equal to the value obtained for model e50c180 (but almost twice the value found for model e50c090, which has the same resolution). As before, $W_{\max}$ is located behind the largest (in size) recollimation shock. This shock is similar to the one in the previous models (Sect. 4.3.4). The half opening angle (in front of the shock) is $\sim 10°$, a bit larger than before, but the recollimation in the strongest shock is larger too. Behind the shock the half opening angle is $\sim 16°$, which then decreases about $6°$. The maximum specific internal energy is 3×10^{28} erg/g, which is about the same as in model e50c180. The central spine of high specific energy connecting blobs with high energy is also present. The baryon load is more than twice as large as that of models with a smaller deposition rate (see Table 4.1). A plausible explanation is that as the deposition rate is ten times larger much more material from the torus is pushed into the jet and, therefore, as this matter is very dense, the ejected mass is higher.

Model e51c100

With this better resolution we get larger Lorentz factors than those obtained with a deposition rate of 10^{50}erg/s. The maximum Lorentz factor is highly time dependent, and there are transients in which it can reach a value of 40, although after 1.2 s some kind of monotonic evolution is obtained, and the Lorentz factor increases non–uniformly from 22 to 33.3 (Fig. 4.12). The morphology is reacher than in the worst resolved model e51c090. It propagates faster than the corresponding 10^{50}erg/s model (see Fig. 4.9), but it is slower than model e51c090, because the time to reach the surface is 2.27 s. As mentioned in the previous section, this is a problem of resolution which was detected in the simulations of extragalactic jets too. In the present case, the lack of resolution near the axis has induced a ballistic propagation of model e51c090, which leads to a very high speed of the head ($0.6c$), preventing very high Lorentz factors within the beam (most of the material impinges against the terminal shock producing an efficient head propagation). The opening angle ($\sim 10°$) almost duplicates that of model e50c100 and it is much wider, roughly a factor of two, than the former (compare, *e.g.,* Fig. 4.7g with Fig. 4.12h), *i.e.,* the jet is less collimated.

The strong recollimation shock present in model e50c100 is not so evident here. Instead, several biconical shocks are observed within a very knotty beam. In addition, the Lorentz factor near the head of the jet is higher and, in the last model (Fig. 4.12h), a beam Lorentz factor as higher as 22 is reached very near the head. The high values of the Lorentz factor are produced by the fact that with this de-

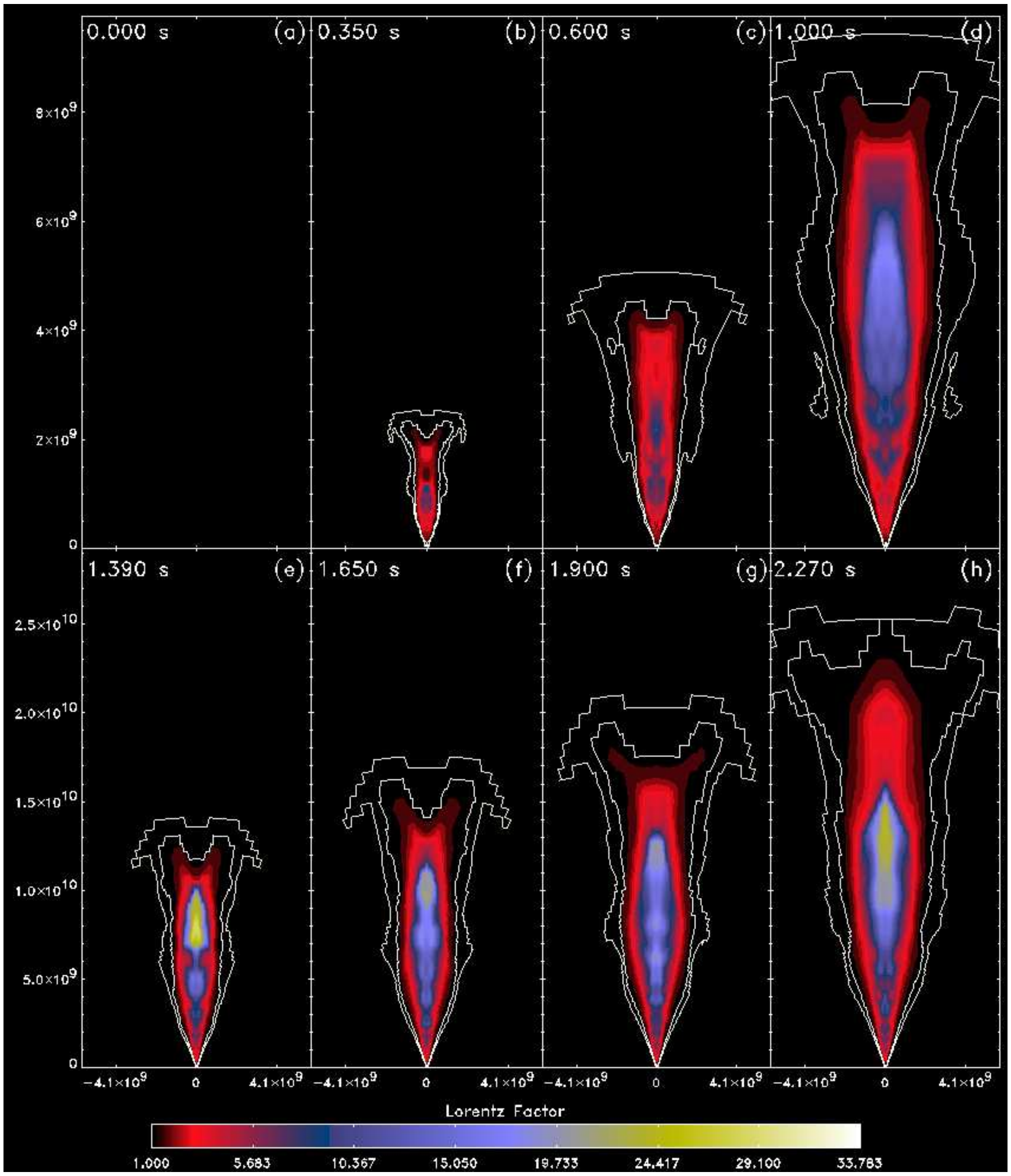

Fig. 4.12.— Same as Fig. 4.2, but for model e51c100 and showing the distribution of the Lorentz factor.

position rate, the central funnel is evacuated faster, and the mean density within the jet is about a factor 5 smaller than in model e50c100 (Fig. 4.13). Moreover, the largest deposition rate explains why, around the axial innermost region (near the limit of the deposition area), the density is as small as $3.5 \times 10^{-13}\,\mathrm{gr/cm^3}$, because

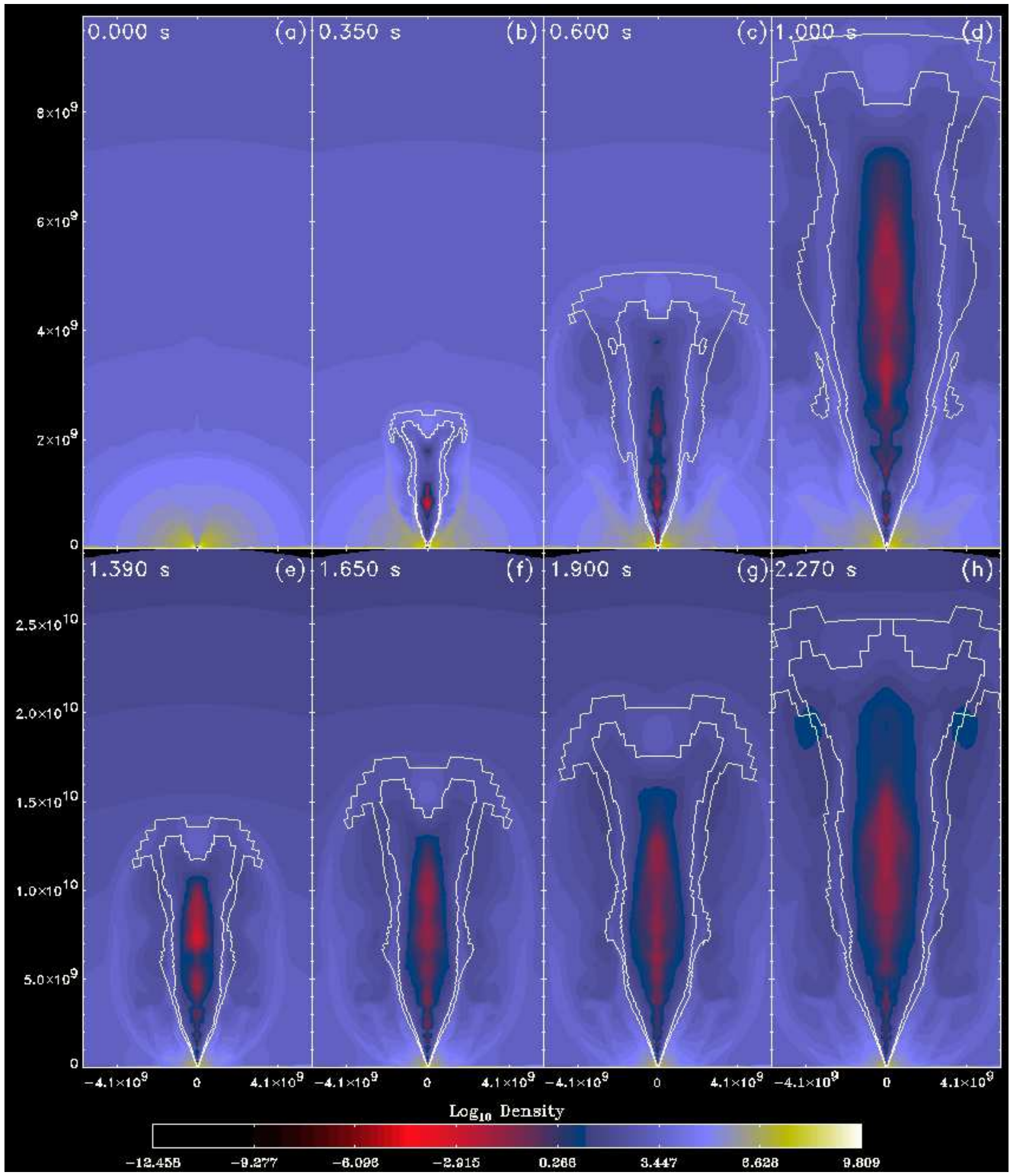

Fig. 4.13.— Same as Fig. 4.12, but showing the distribution of the rest–mass density.

the system has no time to feed the funnel with material coming from the lateral boundaries of the jet.

Models e51c090 and e51c100 have baryon loads (Table 4.1) that are twice larger than in models with a 10^{50} erg/s deposition rate. This is due to the fact that models with a deposition rate of 10^{51} erg/s develop an extended cocoon of mildly relativistic velocities (see the extension of such layer comparing the white contours in Figs. 4.2 and 4.13) and relatively high mean density ($\sim 1\,\mathrm{g/cm^3}$), which increases considerably the jet mass. However, looking at the whole evolution of the model e51c100 (including the post-breakout), the mass entrained into the jet increases slower with time than the energy released (similarly to model e50c100; see Sect. 4.3.4), so that η^{-1} decreases by a factor of two in less than 1.8 s.

In Fig. 4.10, the mass that crosses the innermost boundary as a function of time for different adjacent angular regions is presented for model e51c100. Comparing with the same figure for model e50c100 (left panel), one can notice that the behavior is similar, *i.e.*, , the total accreted mass is roughly the same. However, the largest energy deposition affects to the time at which the largest change of the slope of the curves happens: for model e50c100 it is ~ 1.2 ms, while for e51c100 is ~ 1 ms. Moreover, due to the fact that for e51c100 the deposition rate is not constant (and larger than that of model e50c100) at the beginning the slope of the curves is steeper. Additionally, the behavior of the curves up to $\sim 45°$, from 0.1 s to the end, is different in both models (steeper in e51c100). Another remarkable feature is that the the equatorial region contribute approximately the same to the total mass accreted because they are farther from the deposition volume (*i.e.,* it is less influenced by the details of the energy deposition).

4.3.6. Rapidly varying energy deposition rate

The model e50v100 includes a random varying energy deposition rate with average equal to 10^{50}erg/s. It has been produced in order to check if temporal variations make any significant difference for focusing, propagation or internal jet structure with respect to models with the same deposition rate but constant. Let us remain that the process of energy deposition by the neutrinos is dynamically variable because the region that produces them (the innermost part of the torus), may change with dynamical times of the order of several milliseconds. Consistently, we have imposed a varying energy deposition rate with the same time-variability (of the order of some milliseconds) and energy-variability (the energy deposition rate may change by more than one order of magnitude around the average rate) than that of a collapsar scenario (see MW99). Hence, the varying deposition rate mimics much better the phenomenon that is expected to happen in nature. Concerning the time variation of the deposition rate, we have to consider that 1 ms corresponds to a typical size of $1\,\mathrm{ms}\times c = 3\times10^{7}\,\mathrm{cm}$. Nevertheless, our smaller cells (near the inner boundary) have sizes larger than $2\times10^{7}\,\mathrm{cm}$, what means that we cannot capture properly the smallest time variations. However, as we are not interested right now in producing a realistic spectrum, and we are imposing a random pattern energy deposition (instead of being the result of a calculation involving energy transport and detailed microphysics), such detail is not relevant for the conclusions of the present work.

Fig. 4.14 shows the Lorentz factor evolution for this model. Compared with model e50c100 (Fig. 4.5), the structure is more knotty and rich in shocks, particularly in the firsts 10^9cm. Behind the largest recollimation shock (which is also present at roughly the same distance as in model e50c100) a noticeable blob-like structure is evident. Another remarkable difference is the maximum Lorentz factor reached, which is *almost twice* than the previous model ($W_{\mathrm{max}} = 26.81$), in spite of the fact that the energy deposited is, in average, the same. This means that a variable deposition rate is more efficient to convert internal energy into kinetic energy. We explain the highest efficiency in terms of the internal shocks, which are stronger and more numerous in model e50v100. As an example of this line of reasoning, let us consider the panels (f), (g) and (h) of Figs. 4.5 and 4.14. In Fig. 4.5g, at a distance $\sim 10^9$cm, a biconical shock is present (which is not in the previous panel, but has been generated between these two epochs). This shock is stronger in Fig. 4.14g, and when it collides with the precedent shock (the second shock is faster because it is moving into a channel of minor density than the medium that the first shock finds in its way) and evolves up to $\sim 7\times10^9$cm, accelerates much more the fluid than in the model e50c100 (the resulting Lorentz factor is more than twice).

The mean propagation speed is very similar in both cases (both models reach the surface in ~ 3.3s), although the instantaneous velocity of the jet's head is clearly different (comparing panel to panel in Figs. 4.5 and 4.14, the head is not at the same position, and the differences are even larger in other intermediate evolutionary

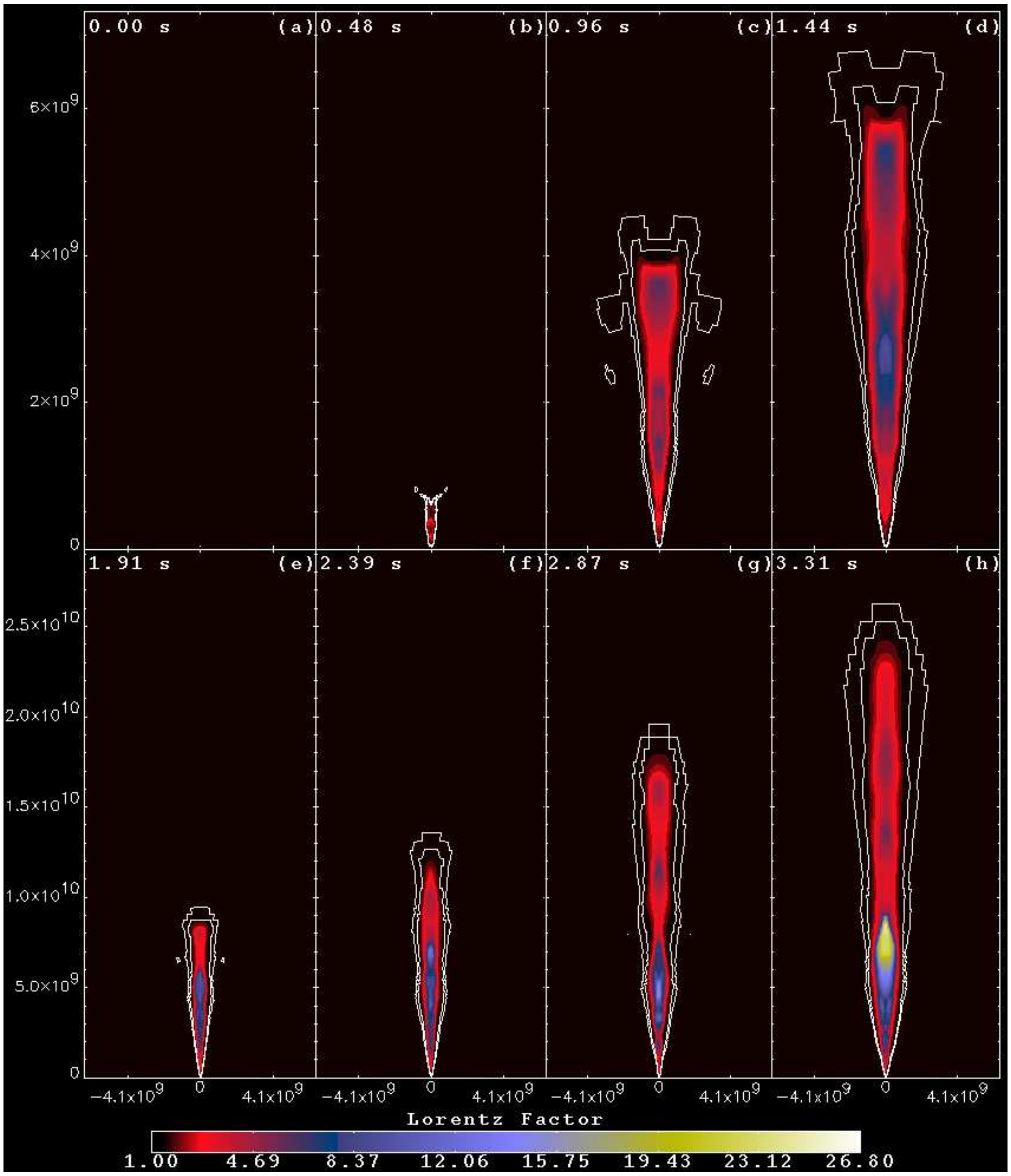

Fig. 4.14.— Same as Fig. 4.2 but for model e50v100 and showing the Lorentz factor distribution.

states). Logically, this happens because the energy input varies in one case and not in the other, but since the mean deposition rate is the same, the mean velocity of the head is the same too. Moreover, the logarithmic grid in radial direction produces a decrement in resolution that tends to average the variations of model e50v100 and, therefore, this numerical effect makes more similar the latest stages of the evolution of both models.

The jet width is usually a bit larger in e50v100 than in e50c100 and the opening angle behind the largest recollimation shock is pretty small in both cases, although in Fig. 4.14h the model e50v100 seems to refocus after 1.7×10^{10}cm. However, this could be a transient effect.

4.3.7. Evolution after shock breakout

After reaching the star's surface, the relativistic jet should continue its propagation through a decreasing atmosphere. The situation then is such that an almost continuous release of energy (that of the jet) is put into a medium whose pressure is negligible compared with the one into the jet cavity, and whose density is of the same order (although as the jet will eventually move outwards in the ISM, density will decrease). This picture corresponds roughly to the propagation of a strong shock wave resulting from a strong explosion, that is, the instantaneous release of a large amount of energy in a relatively small volume. This problem has been studied, analytically by many authors, both in the Newtonian case (*e.g.,* Sedov 1959; Zel'dovich & Raizer 1966) and in the relativistic case (*e.g.,* Colgate & Johnson 1960; Johnson & McKee 1971; Elgroth 1971, 1972; Vitello & Salvati 1976; Blandford & McKee 1976; Shapiro 1979, 1980; Königl 1980). The main results of such works are: (i) the propagation of a planar explosion through a uniform medium follows a self-similar solution both in the classical (Zel'dovich & Raizer 1966) and in the relativistic case (Vitello & Salvati 1976), (ii) it leads to an increasing Lorentz factor with time, and (iii) a rapid decreasing of the post-shock density.

The finite light speed in RHD introduces a characteristic length scale, ct, into all initial value problems which, unlike the Newtonian case, precludes –in general– self-similar solutions. Colgate & Johnson (1960) calculated the relativistic Riemann invariants for the ultrarelativistic limit of a radiation dominated EOS, allowing to Johnson & McKee (1971) to obtain the solution of a planar, strong, ultrarelativistic shock into a cold gas of decreasing density. The method of characteristics used in the one-dimensional planar case could not be directly applied to spherical or cylindrical shocks. In these cases, only approximate solutions for strong, ultrarelativistic (spherical or cylindrical) expanding shocks were found by Elgroth (1972) assuming density gradients proportional to the radius. Blandford & McKee (1976) found an approximate similarity variable for the problem of spherically symmetric relativistic shocks (generated by a point explosion, or by a power supply varying as a power of time) moving into a uniform or decreasing atmosphere, which enabled them to find approximate similarity solutions (accurate to the lowest order in W^{-2}) and to conclude that the scale height of the shocked fluid in the extreme relativistic limit is of the of the order of R_s/W_s^2, where R_s is the radius of the shock and W_s its Lorentz factor.

The external density gradient determines whether the shock will accelerate or decelerate with time, both in the case of adiabatic shocks (Shapiro 1979) or radiative ones (Shapiro 1980). According to Shapiro (1979), the spherically symmetric solutions for relativistic shocks are inherently non-accelerating. The fact that they are self-similar solutions precludes the treatment of density profiles steep enough to produce shock acceleration. Only power laws $\rho \sim r^{-k}$, $k < 3$, are allowed, while the numerical two-dimensional simulations of Shapiro (1979), established that adiabatic point explosion requires $k > 3$. However, power laws as steep as $k > 3$ are unphysical, since they imply an infinite mass enclosed by the shock[13]. Actually, any physically meaningful density profile which is steep enough to accelerate the shock must contain a characteristic radius within which the profile is less steep than r^{-3}. Consistently, at early times, and up to such characteristic radius, the accelerating shock must be a decelerating shock, which prevents self-similar solutions.

The practical conclusion that we can extract for the collapsar model that we are proving is that the structure of the external medium surrounding the central engine will finally determinate the characteristics of the GRB shape (and those of the subsequent afterglow). As no exact analytic solution has been found in the arbitrary relativistic two-dimensional case, numerical simulations are crucial to clarify the outcome of the *proto-GRB*[14] after the breakout.

---

[13]If $k > 3$, $M \propto \int_{R_0}^{R} r^{-k} dV \propto 1/(3-k)(R^{3-k} - R_0^{3-k})$, and when $R_0 \to 0 \Rightarrow M \to \infty$.

[14]We call proto-GRB to our relativistic jet because, actually, the Lorentz factor of the relativistic

Along the previous sections we have analyzed the possibility of formation of a GRB in a collapsar model. The values of the Lorentz factor at the end of the simulation are still far from the ones requested in the fireball model (Sect. 4.1.1). However, according to PI99, internal shocks would be efficient at $R_{int} \sim 10^{13}$cm, because if the shocks arise earlier the radiation does not escape (the fireball is optically thick). In our case, the relativistic jet has reached at most 3×10^{10} cm, 100 times smaller than the distance for the system to be optically thin. This means that if we want to produce a real GRB, a longer evolution should be considered. With this aim, we have extended our computations to a larger domain including an atmosphere for the Wolf-Rayet star.

In order to satisfy the conditions to get an accelerating shock, we have generated a Gaussian atmosphere matching an external uniform medium of the form:

$$\rho(r) = \begin{cases} \rho(R) \exp[-b(r - R_a)^2] & \text{with } b = -\ln\left(\dfrac{\rho(R)}{\rho_e}\right) \text{ for } R < r < R_a; \\ \rho_e & \text{for } R_a < r < R_t. \end{cases} \tag{4.19}$$

ρ_e is the value of the external density outside the atmosphere. The atmosphere extends from $r = R$ (the star's surface) to $r = R_a$. For the pressure, the same profile is used to join the star's surface ($p = p(R)\,\text{dyn/cm}^2$) with the ISM ($p = 10^{-8} p(R)\,\text{dyn/cm}^2$). The rest of thermodynamical variables are got from the EOS. The velocities outside the star have been taken to match that of the surface and decaying radially with $r^{1/2}$, so they are very close to zero in the whole external domain.

The values of the parameters of the atmosphere are: $R_a = 1.8R$, $R_t = 2.54R$, $\rho_e = 10^{-5}\text{g/cm}^3$. Such a election of $p(R)$ and ρ_e is somewhat arbitrary and, therefore, it does not emulate exactly the expected values for the medium surrounding a Wolf-Rayet star (which most probably show a decay of the thermodynamical variables as r^{-2}). However, with a structure like this we can explore the effects of the proto-GRB propagation on a uniform and non-uniform medium. Additionally, the

---

jet is between a factor of 3 to 5 bellow the assumed theoretical values, the baryon load is still larger than the expected in a GRB, etc. In addition, we are considering the formation phase in which the *proto-fireball* is still optically thick, hence, we cannot observe directly such stage of evolution but a later one (if, at the end, the proto-GRB becomes a GRB).

Gaussian profile of the innermost part of the atmosphere is steepest than any radial power-law gradient, thus, satisfying qualitatively the requests of Shapiro (1979) concerning the ambient stratification (see above), in order to produce relativistic expanding shocks that accelerate.

The evolution after the surface breakout has been followed for the models e50c100 and e51c100 (however, the analysis of e51c100 is still under progress, and is not going to be presented here). The numerical domain has been extended with 70 additional radial cells. A picture of the whole evolution (after the jet breakout) is shown in Fig. 4.15. The time needed for the jet to reach R_t, from the star's surface, is $\sim 1.8s$. Hence, the mean propagation velocity of the frontal bow shock in this period is $\sim 0.85c$, which is almost three times faster than the velocity of the head into the star ($0.3c$). Furthermore, after the breakout it is possible to distinguish several epochs characterized by different axial propagation speeds and sideways expansion velocities[15]:

1. The first phase lasts 0.25 s during which both, the lateral expansion and the axial distance grow proportionally to $t^{1.6}$ (lateral expansion) and $t^{1.7}$ (axial distance) (see Fig. 4.16). This epoch is dominated by the inertia of the jet (that remains highly collimated) coming from the star interior Fig. 4.15a). The head's velocity during this phase is $0.48c$. The *ram pressure* near the terminal contact discontinuity ($\bar{F}_{\rm S}$)[16] increases as $\sim t^{0.7}$, while the mean pressure grows as $\sim t^{0.4}$. Moreover $\bar{F}_{\rm S}$ is larger than the mean pressure, which supports the jet-shaped expansion.

2. The second phase (of $\sim 0.56\,$s) is characterized by a large acceleration of the head of the jet up to a velocity of $0.91c$. The reason of such acceleration is

[15]The sideways expansion velocity is calculated as the maximum of the lateral displacements of the pressure bubble for each time. Hence, such velocity does not correspond to a physical point because, for different times, the maximal expansion can take place at different points.

[16]The precise definition of this quantity is $\bar{F}_{\rm S} = (\int_M S_z v_z dV)/(\int_M dV)$, where M is a volume around the terminal contact discontinuity. The quantity is an indicator of how important is the axial momentum, in the morphology of the bubble, compared with the mean pressure within the bubble. If this flux is larger than the mean pressure a "cylindrical" or "jet-shaped" morphology is expected. If pressure dominates the bubble expansion will be spherical.

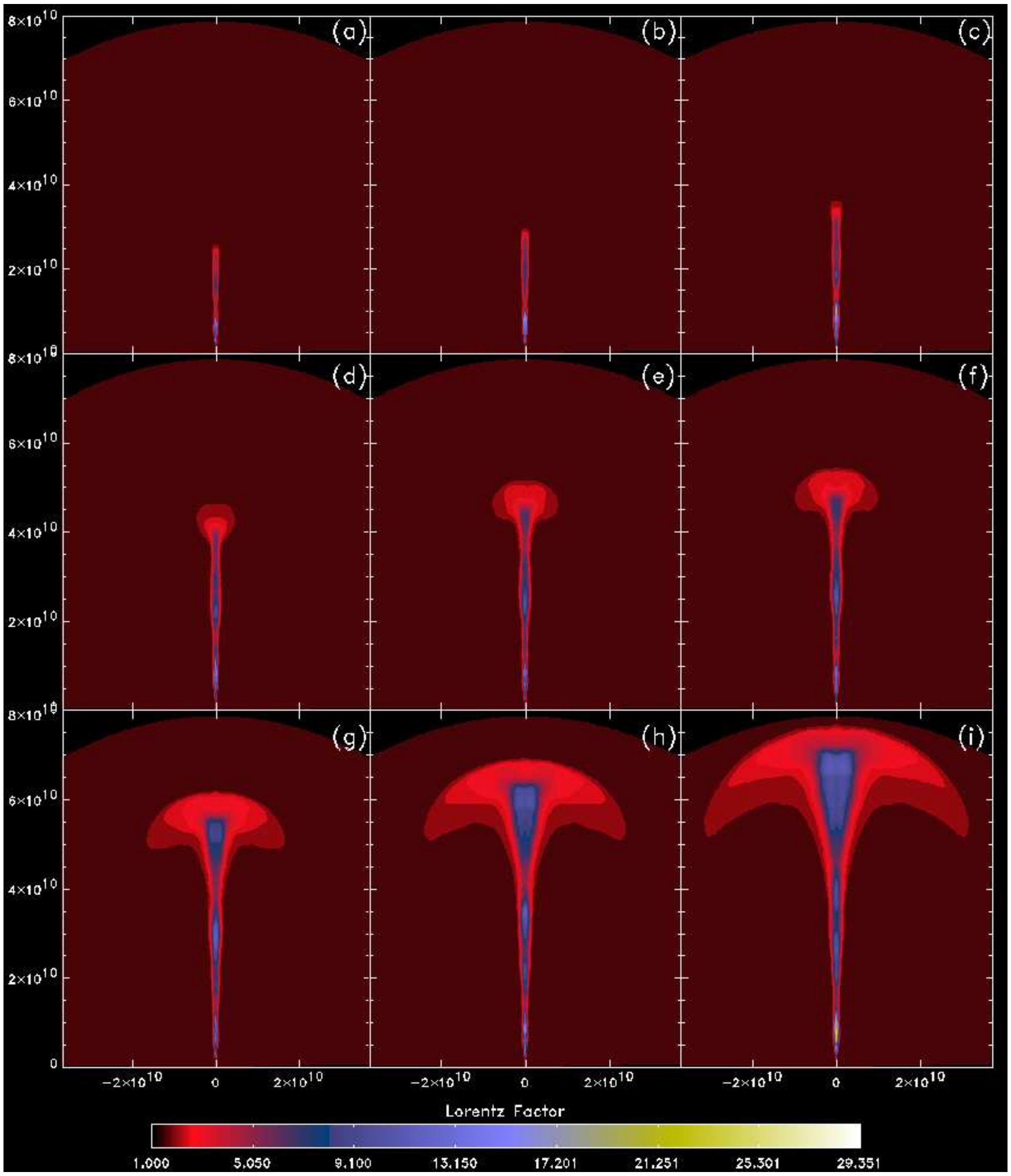

Fig. 4.15.— Nine colored-contour maps of the Lorentz Factor at different evolution times for the model e50c100 after the breakout. X and Y axis measure distance in centimeters. From top to bottom and left to right the corresponding snapshot times are: 3.39, 3.65, 3.91, 4.17, 4.34, 4.43, 4.69, 4.95 and 5.21 s.

the steepest external density gradient along with the $\bar{F}_{\rm S}$ dominance (over the pressure). The sideways expansion is subrelativistic (the expansion velocity being $\sim 0.19c$) and during this stage it grows slower than in the previous phase ($\sim t^{1.0}$). The opening angle increases up to roughly $10°$. In this stage the sideways growth is due to the finite radius of the jet which penetrates the atmosphere (not to a lateral expansion of the beam).

3. The last part of the evolution is marked by the moment in which the bow-shock reaches the homogeneous part of the atmosphere. Here the resistance to the axial advance does not decrease any more while it still does it sideways, leading to a rapid lateral spreading. In fact, one can notice from Fig. 4.16 that the axial growth rate slightly decreases (now it only increases as $t^{1.3}$). The lateral expansion rate changes drastically (see the slope change in dashed line of Fig. 4.16), and the velocity of expansion arrives to be $(1.4 \pm 0.42)c$, *i.e.*, , it grows faster than the axial expansion (solid line). The error that we have assigned to this measure comes from the uncertainty in the determination of the position of the bubble boundary associated to the numerical diffusion of the algorithm (that may spread over 2 or 3 cells the bubble–to–external medium blast wave) and the fact that the radial mesh is logarithmic and some of the external cells may have a relatively large size (the maximum mesh spacing is 1.07×10^9 cm). This behavior in the lateral direction is due to the external density gradient, because the point of maximal expansion coincides with the uniform/non-uniform atmosphere interphase, which means that the material expanding sideways is still sensitive the density gradient, while the axial part of the jet is propagating through a uniform medium. The expansion velocity in the last stage tends rapidly to become relativistic, although in most of the evolution it is subrelativistic or mildly relativistic. This effect produces a more symmetric expansion, tending to be spherical instead of jet-like. Furthermore, both the mean pressure and $\bar{F}_{\rm S}$ decay very fast with time as $\sim t^{-4.8}$ and $\sim t^{4.0}$, respectively.

The evolution of the maximum value of the Lorentz factor is similar to that in the pre-breakout epoch. As before, it is reached behind the first large recollimation shock, which in its turn moves from $\sim 10^{10}$ cm (Fig. 4.15a) to $\sim 1.5 \times 10^{10}$ cm

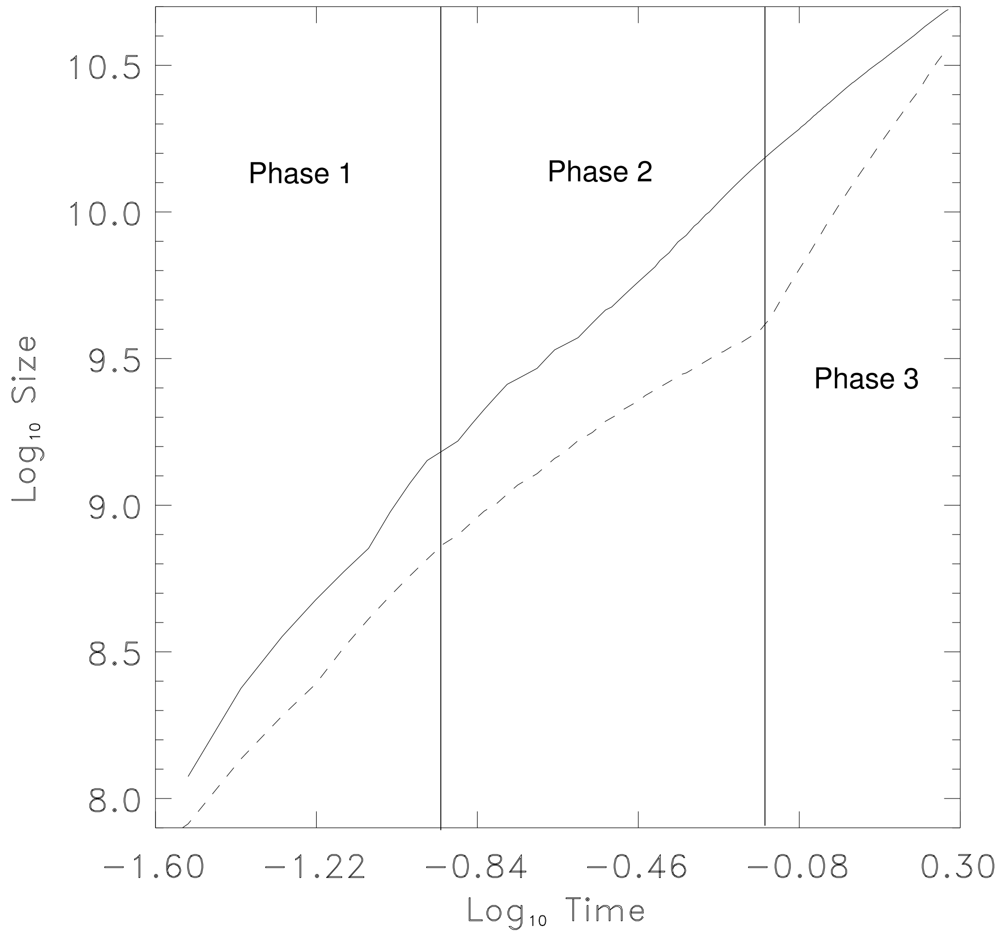

Fig. 4.16.— Evolution of the axial (solid line) and lateral (dashed line) expansions after the jet break out. The axial expansion is calculated detecting the head of the jet and subtracting from it the radius of the star (the breakout point). The lateral expansion is calculated according to footnote 15. Additionally, note that from the sideways expansion distance we subtract the initial radius of the beam.

(Fig. 4.15i) during the post-breakout evolution. At the end of the simulation, the maximum Lorentz factor is 29.35, and the beam material just behind the terminal contact discontinuity (between the head and the external medium) has increased its mean Lorentz factor from ~ 4 (at the breakout) to ~ 9. This values are consistent with an adiabatic expansion because we have checked that along the axis (which is actually a fluid line) the product hW is constant and approximately equal to

15. Around the head the fluid moves mainly along the axis (Fig. 4.17), and near the lateral boundaries of the expanding bubble a strong velocity in the θ direction appears soon after the breakout. The Lorentz factor near the boundaries of the jet cavity grows from ~ 1 (at the beginning of the breakout) to $\sim 2.5 - 5$ (values in the maximal expansion region and in the axis, respectively).

The shape of the expanding bubble is longer than wider (see Fig. 4.18) during the whole post-breakout evolution and, therefore, we can continue referring to it as a "jet" (see Sect. 4.1.4). However, when the jet reaches the uniform part of the atmosphere, as the sideways expansion is faster, the shape is appreciably widen. We have not followed the evolution long enough to see what happens when most of the bubble propagates outside the declining atmosphere. Nevertheless, we can infer from Fig. 4.16 that the trend is to decrease the widening rate in a way similar to what has happened with the axial expansion. The reason is that being most of the bubble inside an homogeneous medium, and considering that at larger distances the bubble will be pressure driven (which would be particularly true if the energy deposition is switched-off), it should tend to expand isotropically.

Over and above all these considerations, it remains true that the evolution has been followed only up to a distance 100 times smaller than R_{int}, and our results are still far to establish whether we can produce a "real" GRB or not. Anyway, the total energy deposited near the inner boundary, is only 5.2×10^{50} erg, and the total evolution time is 5.2 s. Both values are in agreement with the energetics and duration of a generic cosmological GRB (see Sect. 4.1).

Another important remark is that our expansion corresponds to a mildly relativistic bow-shock propagation. However, the fireball model (Sect. 4.1.1) assumes an ultrarelativistic expansion to overcome the compactness problem. Such a problem stems from the assumption that the size of the sources emitting the observed radiation is determined by the observed variability time scale. In addition, the non-thermal spectra of GRBs indicate with certainty that the sources must be optically thin. This has been taken as an indication of the fact that the emission of the GRBs comes from very large distances (compared with the bursters). Thus our breakout simulation corresponds to a previous stage of the GRB evolution: the formation and acceleration of the fireball. Obviously, in order to reach the ultrarelativistic regime,

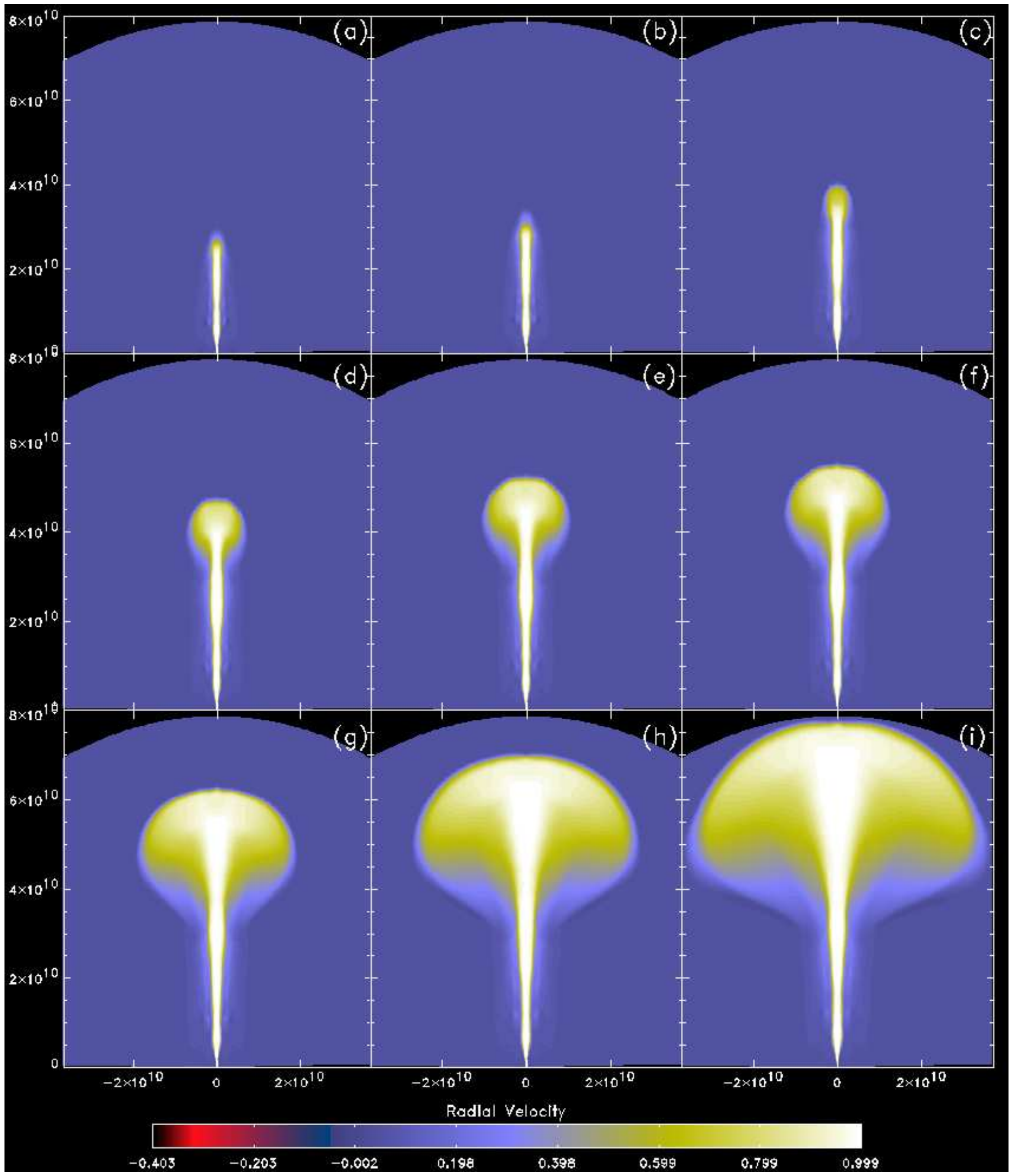

Fig. 4.17.— Same as Fig. 4.15 but for the radial velocity.

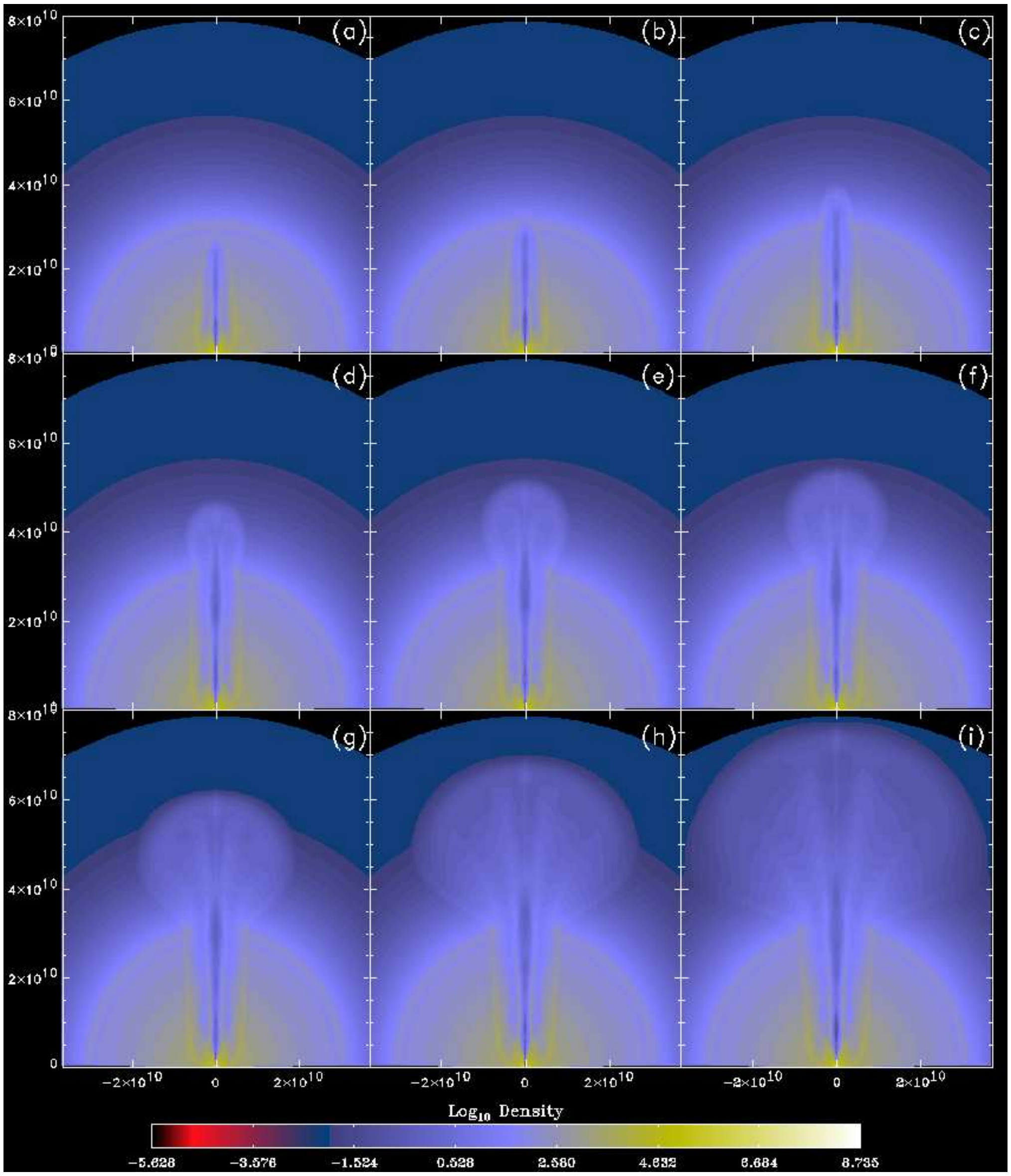

Fig. 4.18.— Same as Fig. 4.15 but for the logarithm of the rest–mass density.

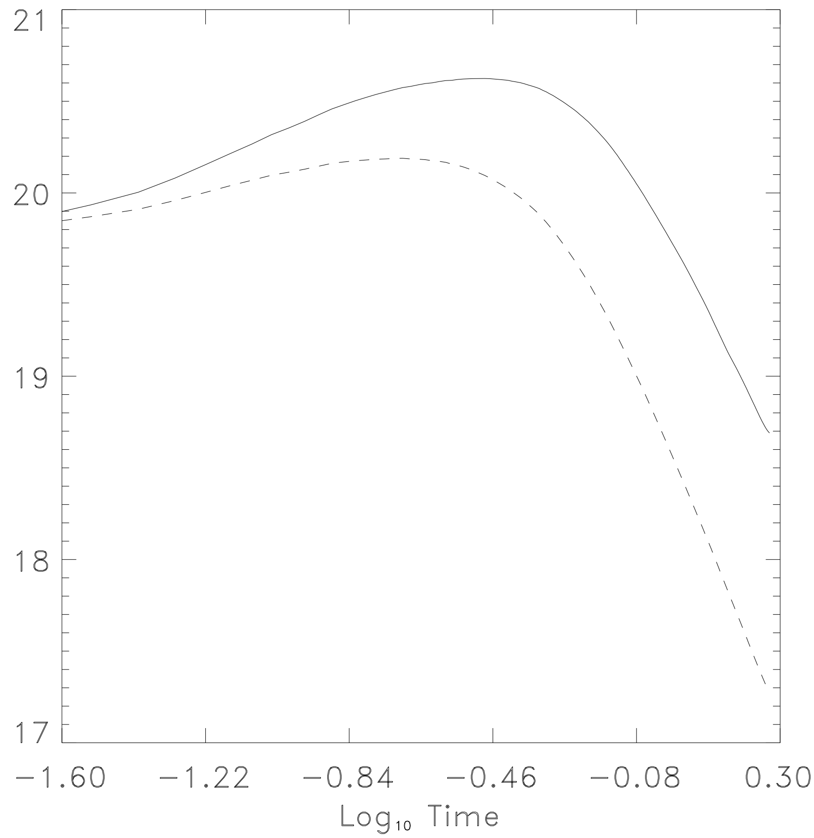

Fig. 4.19.— Evolution of the mean pressure into the jet cavity after the jet breakout (dashed line) and mean axial momentum flux in the neighborhood of the jet's head (solid line) *versus* time.

first the plasma has to be accelerated, and in the initial part of the evolution, the propagation must include a subrelativistic to mildly relativistic regime. Such regime can not be studied analytically and, hence, the numerical simulations become necessary. Our results show that the pre-breakout relativistic jet evolves getting a mildly relativistic propagation speed (the head moves in the final stages at $0.91c$), and it seems that the trend is to accelerate. Additionally, the lateral spreading is present and the expansion velocity tends to the light speed, in agreement with the estimate of Sari, Piran & Halpern (1999), and being less consistent with the estimate of Rhoads (1999) (who assumes a lateral spreading velocity of $c_s = c/\sqrt{3}$ in the comoving fluid frame).

4.4. Conclusions and outlook

Using a collapsar progenitor model of MW99 we have simulated the process of energy deposition that may happen in a realistic Wolf-Rayet star. The result of the deposition has been the formation and propagation of an axisymmetric jet through the mantle and envelope of a collapsing massive star. We have studied two deposition rates (10^{50} and 10^{51} erg/s) which bracket the current estimates for the GRBs energies assuming a cosmological distance. Highly relativistic and collimated outflows have been found. The maximum (final) Lorentz factor reached has happened in the model e51c100 ($W_{\max} = 33$), and it has occurred at the end of the pre-breakout phase (*i.e.,* just before the jet reaches the surface of the star).[17] For the largest energy deposition rate, the jet and in particular the cocoon are less collimated, because when the jet is driven harder it also expands stronger laterally.

The rest-mass density and the internal energy show strong spatial and temporal variations within the jet giving rise to a very inhomogeneous baryon loading. The average baryon load of the jet is $\bar{\eta}^{-1} \sim 1$, but some parts of the jet have a baryon load $\sim 10^{-5}$ or even less. After jet breakout $\bar{\eta}^{-1}$ decreases by a factor of four in less than 1.8 s. If this trend continues $\bar{\eta}^{-1} \sim 10^{-3}$ is reached in less than 9 s.

We have studied the influence of the grid resolution on the results and we have seen that very poor resolutions can underestimate the values of the Lorentz factor and overestimate the mean density inside the jet and the head's velocity. We can conclude that, at least an angular zoning of 0.5° around the axis and covering 3 beam radii is the minimum resolution to obtain a convergent result.

The results of a varying energy deposition (which emulates more accurately the real process) indicate that the formation of a large number of internal shocks helps in the beam fluid acceleration. As the mean energy released in models e50c100 and e50v100 is the same, the mean head speed is roughly the same although the beam

[17] During the post-breakout phase of e51c100 (not shown here) the maximum Lorentz factor in the final model is ~ 46, with some transients in which $W_{\max} \sim 50$.

maximum Lorentz factor is higher (by a factor of two) in the non constant case.

The evolution after the jet breakout is clearly influenced by thermodynamical gradients in the external medium and the final value of the external density ρ_e. Using an atmosphere with a Gaussian profile near the star surface and a constant value afterwards, we have found several evolutionary stages. The different phases are correlated with the times at which the jet reaches the points of change of gradient in the atmosphere and the relative importance of the axial momentum flux compared with the mean pressure in the material surrounded by the bow shock. Anyway, considering the whole evolution, the maximum Lorentz factor grows up to almost 30 in some parts of the beam, and the external shock expands sideways faster than he head advances. However, for this particular election of atmosphere (and ρ_e) the propagation of the bow shock is only mildly relativistic and the main characteristics of our simulations cannot still account for the observational properties of the GRBs or their afterglows.

From the preliminar analysis of the post-breakout evolution of the model e51c100 it comes out that at the end of the simulation, $\sim 2\,M_{\odot}$ have a Lorentz factor of less than three, $3 \times 10^{-4}\,M_{\odot}$ move with $3 \leq W < 10$, and for $2\,10^{-6}\,M_{\odot}$ the Lorentz factor $W \geq 10$ (the latter two masses reduce to $2 \times 10^{-5}\,M_{\odot}$ and $2 \times 10^{-7}\,M_{\odot}$ for model e50c100). Except for the very early evolution ($t < 1\,\mathrm{s}$) the amount of matter moving at moderate ($3 \leq W < 10$) and highly ($W \geq 10$) relativistic velocities increases by a factor ~ 3 every second, *i.e.,* when the central engine is active for another 5 s at the assumed energy deposition rate an amount of matter with mass $\sim 10^{-4}\,M_{\odot}$ will move with $W \geq 10$. As the maximum Lorentz factor is also rapidly increasing, it is not unlikely that maximal Lorentz factors of several hundreds can be reached before the central engine is shut off.

We may regard our set of numerical models as simulations of a proto-GRB, because the scales involved in the problem ($r \lesssim 8 \times 10^{11}\,\mathrm{cm}$) are still far by more than one order of magnitude from the typical distances at which the fireball becomes optically thin ($R_{int} \sim 10^{13}\,\mathrm{cm}$). Consistently, if a GRB would result from some of them, further material acceleration is required.

Concerning the future work, a prompt improvement of the method applied here would include the deposition of momentum along with energy, because, the real process of $\nu\bar{\nu}$–annihilation does not only release energy into the system but also momentum. Taking into account the particular configuration of the torus, this momentum will help in pushing the matter outwards and, hence, in getting larger Lorentz factors for the relativistic proto-fireball.

Another line of work may be to study the influence on the final ejecta of variations in the initial model. For example, following MW99 work, we can try to apply GENESIS to initial models containing an inner boundary closer to the even horizon of the BH. Releasing energy at shorter distances to the BH emulates better the energy deposition by neutrinos because the into the inner parts of the star the temperature is higher and, therefore, the neutrino fluxes are larger (*i.e.,* the number of neutrinos that could interact releasing energy is larger).

In the above mentioned direction we can consider different astrophysical scenarios like, *e.g.,* NS/NS mergers (similar study than that of Ruffert & Janka (1999a) could be done using a relativistic hydro-code like GENESIS) or, NS/BH mergers (like in Ruffert & Janka 1999b). However, such merging scenarios would require a more accurate treatment of the gravitational force. Actually, in order to be fully consistent, a dynamical space-time will be necessary to address properly if these scenarios are suitable to produce GRBs. We have future plans to use the null formulation of the Einstein equations to evolve the space-time metric in the NS/BH merger scenario that the Newtonian studies (Ruffert & Janka 1999b) have pointed out as the most favorable to be GRB progenitor.

More realistic EOS and an feasible transport scheme are necessary to improve the micro-physics. An improved EOS would provide to the code realistic values for the neutrinos' production and will handle more properly with the denser parts of the star (or the merger). In addition, the transport scheme will allow us to include the right energy deposition rate at every point of our domain.

The propagation of the jet into the circumstellar medium depends on its stratification. Thus, further simulations with different environments are planned. It would be interesting and more realistic to consider (outside of the star) stellar winds with a declining density falling as r^{-2}, because this environments are the ones expected around collapsars. We also want to examine progenitors of different size and different internal structure. Larger stars provide longer inertial confinement of the jet probably leading to larger Lorentz factors, if the central engine works at least until the jet reaches the stellar surface. Stars with a less pronounced or even no central torus will provide less initial collimation. As our simulations have not been pushed far enough in time yet, they can (at the present stage) neither account for the observational properties of GRBs nor their afterglows. Hence, we plan to extend them to later times and larger radii ($\sim 10^{13}$ cm) using adaptive mesh refinement (AMR) or multi-resolution techniques.

A. Characteristic fields of the RHD equations

Analytical expressions for the spectral decomposition of the three 5×5 (in 3D) Jacobian matrices $\mathcal{B}^i(\mathbf{U})$ associated to the fluxes $\mathbf{F}^i(\mathbf{U})$ of system (2.7),

$$\mathcal{B}^i(\mathbf{U}) = \frac{\partial \mathbf{F}^i(\mathbf{U})}{\partial \mathbf{U}} \tag{A1}$$

have been given by Donat et al. (1998).

In this Appendix, we explicitly show the eigenvalues and the right and left eigenvectors coresponding to matrix $\mathcal{B}^x$, whereas the cases y and z easily follows from symmetry. The eigenvalues are:

$$\lambda_{\pm} = \frac{1}{1 - \mathrm{v}^2 c_s^2} \left\{ v^x(1 - c_s^2) \pm c_s \sqrt{(1 - \mathrm{v}^2)[1 - v^x v^x - (\mathrm{v}^2 - v^x v^x) c_s^2]} \right\} \tag{A2}$$

$$\lambda_0 = v^x \quad \text{(triple)} \tag{A3}$$

The following expressions define auxiliary quantities:

$$\mathcal{K} \equiv \frac{\tilde{\kappa}}{\tilde{\kappa} - c_s^2}, \quad \tilde{\kappa} = \frac{1}{\rho} \left. \frac{\partial p}{\partial \varepsilon} \right|_{\rho}, \quad \mathcal{A}_{\pm} \equiv \frac{1 - v^x v^x}{1 - v^x \lambda_{\pm}} \tag{A4}$$

A complete set of *right–eigenvectors* is,

$$\mathbf{r}_{0,1} = \left(\frac{\mathcal{K}}{hW}, v^x, v^y, v^z, 1 - \frac{\mathcal{K}}{hW} \right) \tag{A5}$$

$$\mathbf{r}_{0,2} = \left(W v^y, 2hW^2 v^x v^y, h(1 + 2W^2 v^y v^y), 2hW^2 v^y v^z, 2hW^2 v^y - W v^y \right) \tag{A6}$$

$$\mathbf{r}_{0,3} = \left(W v^z, 2hW^2 v^x v^z, 2hW^2 v^y v^z, h(1 + 2W^2 v^z v^z), 2hW^2 v^z - W v^z \right) \tag{A7}$$

$$\mathbf{r}_{\pm} = (1, hW\mathcal{A}_{\pm}\lambda_{\pm}, hWv^y, hWv^z, hW\mathcal{A}_{\pm} - 1) \tag{A8}$$

The corresponding complete set of *left–eigenvectors* is

$$\mathbf{l}_{0,1} = \frac{W}{\mathcal{K} - 1}(h - W, Wv_x, Wv_y, Wv_z, -W)$$

$$\mathbf{l}_{0,2} = \frac{1}{h(1 - v_x v_x)}(-v_y, v_x v_y, 1 - v_x v_x, 0, -v_y)$$

$$\mathbf{l}_{0,3} = \frac{1}{h(1 - v_x v_x)}(-v_z, v_x v_z, 0, 1 - v_x v_x, -v_z)$$

$$\mathbf{l}_{\mp} = (\pm 1)\frac{h^2}{\Delta}\begin{bmatrix} hW\mathcal{A}_{\pm}(v_x - \lambda_{\pm}) + \aleph_{\pm} \\ \\ 1 + W^2(\mathrm{v}^2 - v_x v_x)(2\mathcal{K} - 1)(1 - \mathcal{A}_{\pm}) - \mathcal{K}\mathcal{A}_{\pm} \\ \\ W^2 v_y(2\mathcal{K} - 1)\mathcal{A}_{\pm}(v_x - \lambda_{\pm}) \\ \\ W^2 v_z(2\mathcal{K} - 1)\mathcal{A}_{\pm}(v_x - \lambda_{\pm}) \\ \\ \aleph_{\pm} \end{bmatrix}$$

where Δ is the determinant of the matrix of right-eigenvectors

$$\Delta = h^3 W(\mathcal{K} - 1)(1 - v_x v_x)(\mathcal{A}_+\lambda_+ - \mathcal{A}_-\lambda_-), \tag{A9}$$

and,

$$\aleph_{\pm} = -\left\{-v_x - W^2(\mathrm{v}^2 - v_x v_x)(2\mathcal{K} - 1)(v_x - \mathcal{A}_{\pm}\lambda_{\pm}) + \mathcal{K}\mathcal{A}_{\pm}\lambda_{\pm}\right\} \tag{A10}$$

For an ideal gas equation of state it can be proven that $\mathcal{K}$ is always greater than one (in fact $\mathcal{K} = h$), and Δ is different from zero ($| v^x | < 1$).

B. An Efficient Implementation of Flux Formulae in Multidimensional Relativistic Hydrodynamical Codes

This appendix is an adaptation of Aloy, Pons & Ibáñez (1999) to derive and analyze a simplified formulation of the numerical viscosity terms appearing in the expression of the numerical fluxes associated not only to the modified Marquina's flux formula but also, being more general, to several High-Resolution Shock-Capturing schemes. After some algebraic pre-processing, we give explicit expressions for the numerical viscosity terms of two of the most widely used flux formulae, which implementation saves computational time in multidimensional simulations of relativistic flows. Additionally, such treatment explicitely cancells and factorizes a number of terms helping to amortiguate the growing of round-off errors. We have checked the performance of our formulation running GENESIS to solve a standard test-bed problem and found that the improvement in efficiency is of high practical interest in numerical simulations of relativistic flows in Astrophysics.

The numerical study of the evolution of multidimensional relativistic flows turns out to be a topic of crucial interest in, at least, two different scientific fields: Nuclear Physics (studies of the properties of the equation of state for nuclear matter via comparison of simulations and experiments of heavy ion collisions) and Relativistic Astrophysics. The field of Numerical Relativistic Astrophysics is recently undergoing an extraordinary developement after the important efforts of people working in building up robust codes able to describe many different astrophysical scenarios, such that relativistic jets in quasars and microquasars, accretion onto compact objects, collision of compact objects, stellar core collapse and recent models of Gamma-Ray bursts (see, e.g., the recent review in Ibáñez & Martí, 1998, and references therein). Thus, the improvement in the efficiency of multidimensional hydro-codes becomes a necessity.

It is well known the performance of *modern high-resolution shock-capturing* techniques (HRSC) in simulations of complex classical flows. Most of the HRSC methods are based on the solution of local Riemann problems (i.e., initial value problems with discontiuous initial data) and since 1991 (see Martí, Ibáñez & Miralles 1991) several Riemann Solvers or Flux Formulae have been specifically designed in relativistic fluid dynamics (see, e.g., Martí, 1997, Ibáñez & Martí, 1998, for a review on Riemann solvers in Relativistic Astrophysics). In addition, in Pons et al. (1998) it is showed the way for applying special relativistic Riemann solvers in General Relativistic Hydrodynamics, hence any future new Riemann solver, exhaustively analyzed in Special Relativistic Hydrodynamics (SRH), could be applied to get the numerical solution of local Riemann problems in General Relativistic Hydrodynamics. Consequently, the interest of the results we obtain in this note goes beyond the domain of SRH and can be easily extended to General Relativistic Hydrodynamics.

For consistency, we start by summarizing the basics of the HRSC techniques. A system of *conservation laws* (see LeVeque 1991) is a set of partial differential equations of the form (2.7), where $\mathbf{U} \in \Re^d$ is the *vector of unknowns* and $\mathbf{F}^i(\mathbf{U})$ is the *flux* in the i-direction. In the above system (2.7) we can define a $d \times d$-Jacobian matrix $\mathcal{B}^i(\mathbf{U})$ associated to the flux in the i-direction as:

$$\mathcal{B}^i = \frac{\partial \mathbf{F}^i(\mathbf{U})}{\partial \mathbf{U}}. \tag{B1}$$

The system is said to be hyperbolic if the Jacobian matrices have real eigenvalues.

The main ingredients of a HRSC algorithm are:

i) A finite discretization of the equations in conservation form (2.7). Using a *method of lines*, this discretization reads:

$$\frac{d\mathbf{U}_{i,j,k}(t)}{dt} = -\frac{\hat{\mathbf{F}}_{i+\frac{1}{2},j,k} - \hat{\mathbf{F}}_{i-\frac{1}{2},j,k}}{\Delta x} - \frac{\hat{\mathbf{G}}_{i,j+\frac{1}{2},k} - \hat{\mathbf{G}}_{i,j-\frac{1}{2},k}}{\Delta y} - \frac{\hat{\mathbf{H}}_{i,j,k+\frac{1}{2}} - \hat{\mathbf{H}}_{i,j,k-\frac{1}{2}}}{\Delta z} \tag{B2}$$

where subscripts i, j, k are related, respectively, with x, y and z-discretizations, and refer to cell-centered quantities. The cell width, in the three coordinate directions are, respectively, Δx, Δy and Δz.

ii) Quantities $\hat{\mathbf{F}}_{i+\frac{1}{2},j,k}$, $\hat{\mathbf{G}}_{i,j+\frac{1}{2},k}$ and $\hat{\mathbf{H}}_{i,j,k+\frac{1}{2}}$ are called the *numerical fluxes* at the cell interfaces. These numerical fluxes are, in general, functions of the states of the system at each side of the cell interface. Some HRSC methods derive expressions for the numerical fluxes by giving a consistent flux formulae or solving *local Riemann problems*, with an exact (Martí & E. Müller, 1994) or approximate Riemann solver, after a *cell reconstruction procedure* that gives the state at both sides of the interface, denoted by L (left state) and R (right state). Several monotonic cell reconstruction prescriptions have been given in the scientific literature to achieve different orders of spatial accuracy (van Leer 1979, Woodward & Colella 1984, Marquina 1994).

For clarity, from now on we will omit the indexes relative to the grid and restrict our study to the x_1-splitting of the above system (2.7), assuming that the vector of unknowns satisfies $\mathbf{U} = \mathbf{U}(x_1, t)$.

We have focussed our analysis to some of the most popular HRSC algorithms, and analyzed their expressions for the numerical fluxes. Hence, the sample considered is: HLLE (Harten, Lax, & van Leer 1983, Einfeldt, 1998), Roe (Roe 1981), Marquina (M) (Donat et al. 1998), and a modified Marquina's flux formula (MM) (Aloy et al. 1999). The above selection gathers the most fundamental differences among the large sample of HRSC flux formulae. HLLE is the simplest one, it does not need the full spectral decomposition of the Jacobian matrices. Roe's solver linearizes the information contained in the spectral decomposition into an average state. Marquina's (and its modified version) flux formula considers the information coming from each side of a given interface (it is not a Riemann solver) and, in some astrophysical applications, has produced better results in modelling complex flows.

After some algebraic work, all these flux formulae can be cast into the following general form:

$$\hat{\mathbf{F}}(\mathbf{U}^L, \mathbf{U}^R) = \frac{1}{2}\Big((\mathcal{I} + \widetilde{\mathcal{I}}^L)\mathbf{F}^L + (\mathcal{I} - \widetilde{\mathcal{I}}^R)\mathbf{F}^R + (\mathcal{Q}^L\mathbf{U}^L - \mathcal{Q}^R\mathbf{U}^R)\Big) \tag{B3}$$

where $\mathbf{F}^{L,R}$ stands for the fluxes evaluated at the states $\mathbf{U}^{L,R}$ and $\mathcal{I}$ is the unit matrix. Following Harten (1983), the $\mathcal{Q}^{\mathcal{L},\mathcal{R}}$ terms in the above equation will be referred as the *numerical viscosity matrix*.

Matrices $\widetilde{\mathcal{I}}^{L,R}$ and $\mathcal{Q}^{L,R}$ can be expressed as linear combinations of the projectors onto each eigenspace, i.e., the direct product of the corresponding left and right eigenvectors $\mathbf{l}_p, \mathbf{r}_p$ associated to the p-th characteristic field (p=1,...,d),

$$\widetilde{\mathcal{I}}^{L,R} = \sum_{p=1}^{d} b_p \mathbf{l}_p^{L,R} \mathbf{r}_p^{L,R} \tag{B4}$$

$$\mathcal{Q}^{L,R} = \sum_{p=1}^{d} c_p \mathbf{l}_p^{L,R} \mathbf{r}_p^{L,R} \tag{B5}$$

where superscripts L, R indicate that the eigenvectors are evaluated at the state $\mathbf{U}^{L,R}$. The values of the coefficients b_p and c_p appearing in the above definitions of matrices $\widetilde{\mathcal{I}}^{L,R}$ and $\mathcal{Q}^{L,R}$ depend on the eigenvalues λ_p as shown in Table I, for the four flux formulae analyzed.

TABLE I

Parameters in the numerical fluxes.

Flux Formulae	b_p	c_p
HLLE	$\dfrac{\Psi_+ + \Psi_-}{\Psi_+ - \Psi_-}$	$\dfrac{2\Psi_+\Psi_-}{\Psi_+ - \Psi_-}$
Roe	0	$\mid \lambda_p(\widetilde{\mathbf{U}}) \mid$
M	β_p	$\alpha_p(1-\beta_p^2)$
MM	0	α_p

Table 4.3: In the above table we have introduced the quantities $\Psi_+ = max(0, \lambda_+^R, \lambda_+^L)$ and $\Psi_- = min(0, \lambda_-^R, \lambda_-^L)$, λ_+ and λ_- are, respectively, the maximum and minimum of λ_p, $\alpha_p = max\left(\mid \lambda_p^L \mid, \mid \lambda_p^R \mid\right)$ and $\beta_p = \frac{1}{2}\left(sgn(\lambda_p^L) + sgn(\lambda_p^R)\right)$. We denote by $\widetilde{\mathbf{U}}$ the state of the system according to Roe's average.

Several comments concerning Table I are in order:

i) If we take into account the orthonormality relations between the right and left eigenvectors

$$\sum_{p=1}^{d} \mathbf{l}_p \mathbf{r}_p = \mathcal{I} \tag{B6}$$

and the fact that the coefficients b_p and c_p are, in the case of HLLE, independents of p, then matrices $\widetilde{\mathcal{I}}^{L,R}$ and $\mathcal{Q}^{L,R}$ are, trivially, the unit matrix multiplied by the corresponding factors.

ii) For HLLE's and Roe's flux formulae their corresponding matrices $\widetilde{\mathcal{I}}^{L,R}$ and $\mathcal{Q}^{L,R}$ satisfy the relations: $\widetilde{\mathcal{I}}^L = \widetilde{\mathcal{I}}^R$, $\mathcal{Q}^L = \mathcal{Q}^R$

iii) As it is well known, the knowledge of the spectral decomposition of the Jacobian matrices is a basic ingredient to build up Riemann solvers or many flux formulae. Nevertheless, while HLLE's flux formula only needs the values of the maximum and minimum speeds of propagation of the signals, Roe's and Marquina's flux formulae need explicitly the full knowledge of the spectral decomposition, including right and left eigenvectors.

The system governing the evolution of multidimensional relativistic perfect fluids can be written in Cartesian coordinates in the form (2.7), with $d = 5$, where, in units such that the speed of light $c = 1$, the vector of unknowns $\mathbf{U}$ is given by (2.8), and the fluxes $\mathbf{F}^i$ are defined by (2.9)

A very worthy simplification on the calculation of matrices $\mathcal{Q}$ arises when some eigenvalue is degenerate, i.e., when the system is not strictly hyperbolic. In SRH, like in multidimensional Newtonian hydrodynamics, there is a *linearly degenerate* field, $p = 0$, such that the corresponding eigenvalue λ_0 is triple (the system in the j-direction splitting is not strictly hyperbolic, although the set of eigenvectors is complete). According to equation (B5), and using the orthonormality relations between the right and left eigenvectors

$$\sum_{k=1}^{3} r_{0,k}^m l_{0,k}^n = \delta^{mn} - r_+^m l_+^n - r_-^m l_-^n \tag{B7}$$

where $m, n = 1, \ldots 5$ denote the components of the 5-vector, it is possible to eliminate the three eigenvectors associated to the degenerate field and to write down the following simplified expression (omitting L,R superscripts)

$$\mathcal{Q}^{mn} = c_0 \delta^{mn} + (c_+ - c_0) r_+^m l_+^n + (c_- - c_0) r_-^m l_-^n. \tag{B8}$$

Notice that only $r_\pm$ and $l_\pm$ are needed to evaluate the numerical viscosity. The same procedure can be applied to any system of conservation laws where one of the eigenvectors has multiple degeneracy, because orthogonality relations always allow us to skip the explicit dependence on one of the vector subspaces of the spectral decomposition. In particular, it could be of great interest in the case of the equations of relativistic magnetohydrodynamics where, in the ansatz of a directional splitting, similar degeneracy arises in the structure of the characteristic fields associated to each one of the fluxes.

The explicit formulae for the numerical viscosity term corresponding to the system of equations of special relativistic hydrodynamics are:

HLLE's flux formulae. Since the numerical viscosity matrix is proportional to the identity, the application of the above recipes is obvious.

Roe's flux formulae. The numerical flux across some given interface can be written

$$\hat{\mathbf{F}}(\mathbf{U}^L, \mathbf{U}^R) = \frac{1}{2}[\mathbf{F}^L + \mathbf{F}^R + \mathbf{q}] \tag{B9}$$

$\mathbf{q}$ being the five–vector calculated from the corresponding numerical viscosity matrices of Table I:

$$\mathbf{q} = \mathcal{Q}(\mathbf{U}^L - \mathbf{U}^R) \equiv \mathcal{Q}\Delta\mathbf{U} \tag{B10}$$

In Roe's Riemann solver the quantities relative to the spectral decomposition are evaluated using the corresponding Roe-averages of the left and right states, denoted by $\widetilde{\mathbf{U}}$ (see Roe 1981, for the Newtonian case and Eulderink & Mellema, 1995, for the relativistic case). In practice, other particular averaging (e.g., arithmetic means) have also been used. Note that in the following expressions (B11) all quantities are evaluated using Roe's average, except for Δu_m. After some algebra, the viscosity vector associated to the numerical flux in the j-direction is

$$\begin{aligned}
q_1 &= \mid \lambda_0 \mid \Delta u_1 + \chi_a \\
q_2 &= \mid \lambda_0 \mid \Delta u_2 + hW(v_x\chi_a + \chi_b\delta_{jx}) \\
q_3 &= \mid \lambda_0 \mid \Delta u_3 + hW(v_y\chi_a + \chi_b\delta_{jy}) \\
q_4 &= \mid \lambda_0 \mid \Delta u_4 + hW(v_z\chi_a + \chi_b\delta_{jz}) \\
q_5 &= \mid \lambda_0 \mid \Delta u_5 + hW(\chi_a + v_j\chi_b) - \chi_a
\end{aligned} \tag{B11}$$

where

$$\chi_a = \sum_{m=1}^{5} \left[(\mid \lambda_+ \mid - \mid \lambda_0 \mid) l_+^m + (\mid \lambda_- \mid - \mid \lambda_0 \mid) l_-^m\right] \Delta u_m \tag{B12}$$

$$\chi_b = \sum_{m=1}^{5} \left[(\mid \lambda_+ \mid - \mid \lambda_0 \mid) V_+^j l_+^m + (\mid \lambda_- \mid - \mid \lambda_0 \mid) V_-^j l_-^m\right] \Delta u_m \tag{B13}$$

$$V_\pm^j = \frac{\lambda_\pm - v^j}{1 - v^j \lambda_\pm} \tag{B14}$$

M and MM- flux formulae. The numerical flux across a given interface can be written like equation (B9) with

$$\mathbf{q} = \mathbf{q}^L - \mathbf{q}^R \tag{B15}$$

$$\mathbf{q}^{L,R} = \mathcal{Q}^{L,R}\mathbf{U}^{L,R} \tag{B16}$$

Omitting the superscripts L, R and taken into account the expressions in Table I for MM and the results in Donat el al. (1998), the viscosity vector in the x-splitting is:

$$\begin{aligned}
q_1^{L,R} &= \frac{h^2}{\Delta}\left\{M\left[\mathcal{A}_-\Omega_+ - \mathcal{A}_+\Omega_-\right] + p(c_+\aleph_+ - c_-\aleph_-)\right\} + \\
&\quad c_0 p\frac{W}{h}\left\{\frac{\mathcal{K}}{\mathcal{K}-1} + \frac{v_y^2+v_z^2}{1-v_x^2}\right\} \\
q_2^{L,R} &= \frac{h^3 W}{\Delta}\left\{M\mathcal{A}_+\mathcal{A}_-\left[\Omega_+\lambda_+ - \Omega_-\lambda_-\right] + p(c_+\lambda_+\mathcal{A}_+\aleph_+ - c_-\lambda_-\mathcal{A}_-\aleph_-)\right\} + \\
&\quad c_0 p W^2 v_x\left\{\frac{1}{\mathcal{K}-1} + 2\frac{v_y^2+v_z^2}{1-v_x^2}\right\} \\
q_3^{L,R} &= \frac{h^2 W}{\Delta}v_y\left\{M\left[\Omega_+\mathcal{A}_- - \Omega_-\mathcal{A}_+\right] + p(c_+\aleph_+ - c_-\aleph_-)\right\} + \\
&\quad c_0 p\left\{\frac{W^2}{\mathcal{K}-1} + \frac{1+2W^2(v_y^2+v_z^2)}{1-v_x^2}\right\} \\
q_4^{L,R} &= \frac{h^2 W}{\Delta}v_z\left\{M\left[\Omega_+\mathcal{A}_- - \Omega_-\mathcal{A}_+\right] + p(c_+\aleph_+ - c_-\aleph_-)\right\} + \\
&\quad c_0 p\left\{\frac{W^2}{\mathcal{K}-1} + \frac{1+2W^2(v_y^2+v_z^2)}{1-v_x^2}\right\} \\
q_5^{L,R} &= \frac{h^2}{\Delta}\left\{M\left[\mathcal{A}_-\Omega_+\mathcal{D}_+ - \mathcal{A}_+\Omega_-\mathcal{D}_-\right] + p[c_+\aleph_+\mathcal{D}_+ - c_-\aleph_-\mathcal{D}_-]\right\} + \\
&\quad c_0 p\frac{W}{h}\left\{\frac{hW-\mathcal{K}}{\mathcal{K}-1} + \frac{(2hW-1)(v_y^2+v_z^2)}{1-v_x^2}\right\},
\end{aligned} \tag{B17}$$

with the following auxiliary quantities

$$M = \rho h W^2(\mathcal{K}-1), \quad \Omega_\pm = c_\pm(v_x - \lambda_\mp), \quad \mathcal{D}_\pm = hW\mathcal{A}_\pm - 1, \tag{B18}$$

where quantities $c_{\pm,0}$ are given in Table I and Δ is the determinant of the matrix of right-eigenvectors.

The corresponding viscosity vectors in the other directions are trivially obtained by a cyclic permutation of subindices x, y, z.

We have tested the efficiency of our numerical proposal, for Roe's and MM's flux formulae, running GENESIS, without any optimization at compilation level, in a SGI Origin 2000. A standard initial value problem has been chosen: $\rho_L = 10$, $\epsilon_L = 2$, $v_L = 0$, $\gamma_L = 5/3$, $\rho_R = 1$, $\epsilon_R = 10^{-6}$, $v_R = 0$ and $\gamma_R = 5/3$, where the subscript L (R) denotes the state to the left (right) of the initial discontinuity. This test problem has been considered by several authors in the past (see §2.4 for details in 1D, 2D and 3D).

We have compared the performance of two different implementations of the numerical flux subroutine:

i) *Case A*, stands for the results obtained using our analytical prescription. This means to write down, in the numerical flux routine, just the expressions derived here for the viscosity vector $\mathbf{q}$.

ii) *Case B*, stands for the results obtained running the code with a standard high-efficiency subroutine for inverting matrices (we use a LU decomposition plus an implicit pivoting which is, for general matrices, $O(N^3)$). This subroutine is called to get the left eigenvectors from the matrix of right eigenvectors and is adapted to the particular dimensions of the matrices (3×3, in 1D, 4×4, in 2D and 5×5, in 3D). Hence, unlike case A, now we have to calculate numerically the following quantities: the matrix of left eigenvectors, the characteristic variables and, finally, the components of the viscosity vector $\mathbf{q}$.

TABLE II

CPU time (in microseconds).

		TCI (μs)			
		Roe		MM	
Case	# Zones	Case A	Case B	Case A	Case B
1D	$100 \times 1 \times 1$	12.2	53.8	23.8	118.9
2D	$20 \times 20 \times 1$	25.5	181.8	49.0	373.5
3D	$14 \times 14 \times 14$	39.4	431.9	75.7	879.0

Table 4.4: Time per numerical cell and iteration (TCI) in microseconds employed by the numerical flux routine in our test-bed problem, for three different grids.

Table II summarizes the results: the direct implementation of our numerical viscosity formulae leads to an improvement of the efficiency (in terms of CPU time) of the numerical fluxes subroutine in a factor which, in 3D calculations, ranges between about *eleven* and *twelve* depending on the particular flux formula used. When comparing Roe's and MM's cases a factor two –in favour of Roe– arises due to the fact that MM's flux formulae needs to compute two viscosity vectors (one per each side of a given interface), unlike Roe's flux formula which needs only one viscosity vector evaluated at the average state. As it must be, the efficiency increases with the number of spatial dimensions involved in the problem due to the computationally expensive matrix inverting operations performed at each interface to get the numerical fluxes. Since the numerical flux routine is, typically, one of the most time-consuming, it translates into a speed up factor between *two* and *four* in the total execution time, depending on the specific weight of the flux formulae routine in each particular application.

Our formulation also gives a unified description of the numerical fluxes (B3), permitting a unique implementation with the possibility of switching in cases when the utilisation of a specific flux formula is more appropriate. In addition, due to the fact that we have eliminated, in the generalized MM's flux formula, all the *conditional clauses*, the efficiency is ensured either for scalar or vectorial processors.

Another worthy by-products of our algebraic pre-processing concerns with the significant reduction of round-off errors, as a consequence of the number of operations suppressed and factorization. One of the important issues in designing a multidimensional hydro-code is the accurate preservation of any symmetries present in a physical problem. A numerical violation of these symmetries could arise as a consequence of accumulation of round-off errors in the calculation of the numerical fluxes, as we have explained in §2.3.10. The algebraic simplifications, shown in the present appendix, reduce the number of operations and cure such problem.

Two last additional consequences arise from our work. First is that similar expressions can be worked out for any non-linear hyperbolic system of conservation laws for which the full spectral decomposition is known. In particular, when some of the vectorial subspaces has multiple degeneracy, a similar algebraic preprocessing is very convenient. The other important consequence is that an appropriate combination of a simplified formulation of the numerical viscosity together with the use of special relativistic Riemann solvers in General Relativistic Hydrodynamics (Pons et al. 1998), should allow a very easy and efficient extension to General Relativistic Hydrodynamics.

C. Explicit algorithm to recover primitive variables

In any RHD code evolving the conserved quantities Eq. (2.8) in time, the variables $\{p, v^1, v^2, v^3, \rho, \varepsilon\}$ have to be computed from the conserved quantities at least once per time step. In GENESIS this is achieved using Eqs. (2.1)–(2.3) and the equation of state. For an ideal gas equation of state with constant γ, this implies to find the root of the function

$$f(p) = (\gamma - 1)\rho_* \varepsilon_* - p \tag{C1}$$

with ρ_* and ε_* given by

$$\rho_* = \frac{D}{W_*} \tag{C2}$$

and

$$\varepsilon_* = \frac{\tau + D\,(1 - W_*) + p\,(1 - W_*^2)}{D\,W_*}\,, \tag{C3}$$

where

$$W_* = \frac{1}{\sqrt{1 - \mathbf{v}_* \cdot \mathbf{v}_*}}\,, \tag{C4}$$

and

$$\mathbf{v}_* = \frac{\mathbf{S}}{\tau + D + p}\,. \tag{C5}$$

The zero of $f(p)$ in the physically allowed domain $p \in]p_{\min}, \infty[$ determines the pressure. The monotonicity of $f(p)$ in that domain ensures the uniqueness of the solution. The lower bound of the physically allowed domain, $p_{\min}$, defined by

$$p_{\min} = |\mathbf{S}| - \tau - D, \tag{C6}$$

is obtained from Eq. (C5) taking into account that (in our units) $|\mathbf{v}| \leq 1$. Knowing p, Eq. (C5) then directly gives $\mathbf{v}$, while the remaining state quantities are straightforwardly computed from Eqs. (2.1)–(2.3) and the definition of the Lorentz factor.

In GENESIS, the solution of $f(p) = 0$ is obtained by means of a Newton–Raphson iteration in which the derivative of f, f', is approximated by

$$f' = |\mathbf{v}_*|^2 c_{s*}^2 - 1, \tag{C7}$$

where c_{s*} is the sound speed given by

$$c_{s*} = \sqrt{\frac{(\gamma - 1)\gamma\varepsilon_*}{1 + \gamma\varepsilon_*}}. \tag{C8}$$

This approximation tends to the exact derivative when the solution is approached. On the other hand, it easily allows one to extend the present algorithm to general equations of state.

D. Transfer equations for the synchrotron radiation

The presence of shock waves into the a jet fluid enhance the emission because a shock is usually a very efficient converter of bulk kinetic energy into internal energy of the electrons and energy associated to the magnetic field, and we know that the total emitted power of a charged particle in the form of synchrotron emission is (see *e.g.,* Pacholczyk 1970)

$$\frac{dE}{dt} = \frac{2e^4}{3m^4c^7} B^2 \sin^2 \alpha E^2 \tag{D1}$$

where e and m are the charge and the mass of the particle (electrons or positrons in our case), B is the magnetic field strength, E is the energy of the particle and α is the angle between the velocity and the magnetic field direction.[18]

In order to calculate the synchrotron emission that reaches us coming from a high number of electrons in a relativistic jet, it is necessary (as mentioned before) to solve the transfer equations along the line of sight. To do it we need to know first the emission and absorption coefficients for a set of electrons (expressed in the reference frame of the magnetic field (1,2), see below), which are respectively (see Gómez 1993)

$$\epsilon^{(i)} = \frac{\sqrt{3}e^3}{8\pi mc^2} B \sin\vartheta \int_{E_{min}}^{E_{max}} N(E)[F(x) \pm G(x)]dE \tag{D2}$$

$$\kappa^{(i)} = -\frac{\sqrt{3}e^3}{8\pi m\nu^2} B \sin\vartheta \int_{E_{min}}^{E_{max}} E^2 \frac{d}{dE} \left(\frac{N(E)}{E^2}\right) [F(x) \pm G(x)]dE \tag{D3}$$

where ν is the frequency, $N(E)$ is the electron density with an energy between E and $E + dE$, ϑ being the angle between the magnetic field and the line of sight, the functions F and G are related with the second order Bessel functions as follows

$$F(x) = x \int_x^\infty K_{5/3}(z)dz$$
$$G(x) = xK_{2/3}(x)$$

with $x = \nu/\nu_c$, ν_c being the critical frequency, at which an electron of energy E emits approximately the largest quantity of synchrotron emission, and corresponds

[18]Note that the synchrotron emission grows as the second power of the magnetic field and the energy of the electrons.

to

$$\nu_c = \frac{3e}{4\pi m^3 c^5} B \sin\vartheta E^2.$$

In the equations (D2) and (D3) superindex (i) denotes polarization. The '+' sign corresponds to the polarization $i = 1$ (*i.e.,* in the direction of the axis 1 –normal to the projection of the magnetic field over the plane of the sky–), and the sign '–' to $i = 2$ (*i.e.,* in the direction of the axis 2 –which is the direction of the projection of the magnetic field over the plane of the sky). In general, as E_{min} and E_{max} may have any value in the range $[0, \infty]$, there is no analytical expression of the emission and absorption coefficients and they must be calculated numerically.

Another element that we need to establish is how the internal energy is distributed among the relativistic electrons. Given that observed radio spectra from emission regions which are transparent to radiation are of the power law form $dE/dt \propto \nu^{-\alpha}$, where α is a constant (Kembhavi & Narlikar 1999), and since the electrons receive their random motions through shock-heating, usually it is assumed (following the treatment of non-relativistic shocks) that they develop a power law distribution of energies (see *e.g.,* Blandford 1990):

$$N(E)dE = N_0 E^{-p} dE, \quad E_{min} \leq E \leq E_{max} \tag{D4}$$

where p is the spectral index of the electrons, which usually takes values between one and three. Neglecting radiative energy losses, the ratio C_E between the maximum and minimum energy can be considered constant along all the jet, which allows us to treat this as a parameter of the model.

The power law is fully determined by the equations

$$N_0 = \left[\frac{\mathcal{U}(p-2)}{1 - C_E^{2-p}}\right]^{p-1} \left[\frac{1 - C_E^{1-p}}{\mathcal{N}(p-1)}\right]^{p-1} \tag{D5}$$

and

$$E_{min} = \frac{\mathcal{U}}{\mathcal{N}} \frac{p-2}{p-1} \frac{1 - C_E^{1-p}}{1 - C_E^{2-p}}, \tag{D6}$$

$\mathcal{U}$ and $\mathcal{N}$ being the electron energy density and the number density, respectively; the values of these two parameters as a function of the position in the jet are calculated by the hydrodynamical code. The largest number of electrons is around E_{min} and hence this is also the characteristic electron energy.

The next element that we have to consider in order to evaluate the synchrotron emission is the strength and orientation of the magnetic field. As the hydro-code is not able to calculate the magnetic field evolution we have to establish it in a somewhat arbitrary way. Following Wilson & Scheuer (1983) and Gómez *et al.* (1995, 1997), we assume that the magnetic energy density remains a fixed fraction of the particle energy density, which leads to a field with magnitude proportional to $\mathcal{U}^{1/2}$.

The minimum value E_{min} plays an important role in the *Faraday rotation* and *depolarization* of the polarized flux. The Faraday rotation is the rotation of the polarization plane of a linearly polarized wave which is the result of the superposition of two circularly polarized waves with the same amplitude but rotating in opposite senses and with different initial phases.

The differential change in the polarization angle, $d\chi_F$, (in rad) per unit of length ds (in cm) due to Faraday rotation is determined by

$$\frac{d\chi_F}{ds} = 2.36 \times 10^{-17} N_e B_{||} \lambda^2 \tag{D7}$$

where λ is the wavelength (in cm), $B_{||}$ is the projection of the magnetic field (in Gauss) along the line of sight, and N_e is the electronic density (cm^{-3}) (which is the result of the integration of (D4) in the allowed range of energies).

Of course, different parts of the jet may present different Faraday rotations (due *e.g.,* to differences in the path length followed by the waves), being the global effect of such variations a depolarization (Garrington *et al.* 1988; Laing 1988) or decrease in the polarization degree of the synchrotron emission (hence, the inclusion of this mechanism is necessary to calculate properly the polarization properties of the radiation). The Faraday rotation or depolarization can take place everywhere between the source and the observer, which makes very difficult to determinate exactly the intrinsic polarization of the source.

The last elements that we need to know in order to write the transfer equations are the Stokes parameters. The Stokes parameters are four quantities that express in a convenient form the radiation field. Their definition is (see *e.g.,* Gómez 1993):

$$\begin{aligned} I &= \frac{c}{4\pi}[< (\mathcal{E}_0^a)^2 > + < (\mathcal{E}_0^b)^2 >] \\ Q &= \frac{c}{4\pi}[< (\mathcal{E}_0^a)^2 > - < (\mathcal{E}_0^b)^2 >] \\ U &= \frac{c}{4\pi}2 < \mathcal{E}_0^a\mathcal{E}_0^b \cos\delta > \\ V &= \frac{c}{4\pi}2 < \mathcal{E}_0^a\mathcal{E}_0^b \sin\delta > \end{aligned}$$

where $\delta = \phi_a - \phi_b$ is the phase shift, $\mathcal{E}^{a,b}$ being the electric vector of a monochromatic electromagnetic wave, of frequency ν, which may be written as

$$\begin{aligned} \mathcal{E}^a &= \mathcal{E}_0^a \sin(2\pi\nu - \phi_a) \\ \mathcal{E}^b &= \mathcal{E}_0^b \sin(2\pi\nu - \phi_b) \end{aligned}$$

$\mathcal{E}_0^a$ and $\mathcal{E}_0^b$ being the amplitudes in two perpendicular directions, namely (a, b), which form, together with the wave propagation direction, the *observer frame.*

The physical meaning of the Stokes parameters is the following: I is the total specific intensity, Q and U tell us the type of polarization, and V indicates if the polarization is *left* or *right*, and is zero if the polarization is linear. For the synchrotron radiation, the polarization is always linear, so $V_{syn} = 0$.

Two additional quantities related with the Stokes parameters are the *degree of polarization*, $\Pi = (Q^2 + U^2)^{1/2}$, and the *polarization angle*, $\chi = \frac{1}{2}\arctan(U/Q)$. Finally, the *transfer equations for the synchrotron radiation in the observer frame* are (Gómez 1993)

$$\begin{aligned} \frac{dI^{(a)}}{ds} &= I^{(a)}\left[-\kappa^{(1)}\sin^4\chi_B - \kappa^{(2)}\cos^4\chi_B - \frac{1}{2}\kappa\sin^2 2\chi_B\right] \\ &+U\left[\frac{1}{4}(\kappa^{(1)} - \kappa^{(2)})\sin 2\chi_B + \frac{d\chi_F}{ds}\right] \qquad \text{(D8)} \\ &+\epsilon^{(1)}\sin^2\chi_B + \epsilon^{(2)}\cos^2\chi_B \\ \frac{dI^{(b)}}{ds} &= I^{(b)}\left[-\kappa^{(1)}\cos^4\chi_B - \kappa^{(2)}\sin^4\chi_B - \frac{1}{2}\kappa\sin^2 2\chi_B\right] \\ &+U\left[\frac{1}{4}(\kappa^{(1)} - \kappa^{(2)})\sin 2\chi_B - \frac{d\chi_F}{ds}\right] \qquad \text{(D9)} \\ &+\epsilon^{(1)}\cos^2\chi_B + \epsilon^{(2)}\sin^2\chi_B \end{aligned}$$

$$
\begin{aligned}
\frac{dU}{ds} &= I^{(a)}\left[\frac{1}{2}(\kappa^{(1)}-\kappa^{(2)})\sin 2\chi_B - 2\frac{d\chi_F}{ds}\right] \\
& I^{(b)}\left[\frac{1}{2}(\kappa^{(1)}-\kappa^{(2)})\sin 2\chi_B + 2\frac{d\chi_F}{ds}\right] \\
& -\kappa U - (\epsilon^{(1)}-\epsilon^{(2)})\sin 2\chi_B
\end{aligned}
\tag{D10}
$$

where $\kappa = 1/2(\kappa^{(1)} - \kappa^{(2)})$ is the mean value of the absorption coefficient; the superscripts $(a),(b)$ and $(1),(2)$ refer respectively to the axes (a) and (b) of the observer frame and the frame in which the axis (2) is parallel to the projection of the magnetic vector in the plane perpendicular to the direction of propagation of the electromagnetic field (axis (1) is perpendicular to this direction). χ_B is the angle that the direction (2) (*i.e.,* the projection of the magnetic field over the plane of the sky) forms with the (a) axis. $I^{(a)}$ and $I^{(b)}$ are the specific intensities over the axis (a,b) respectively, and are related with I by $I = I^{(a)} + I^{(b)}$ ($I^{(a),(b)} = (c/4\pi) < (\mathcal{E}_0^{a,b})^2 >$).

The emission is then calculated by integrating equations (D8) to (D10) while accounting for relativistic effects such as Doppler boosting and light aberration. The Doppler boosting affects the transfer equations by changing the emission and absorption coefficients as follows

$$\epsilon(\nu) = \mathcal{D}^2\epsilon^{'}(\nu^{'}) \tag{D11}$$

$$\kappa(\nu) = \mathcal{D}^{-1}\kappa^{'}(\nu^{'}) \tag{D12}$$

where variables without primes are measured in the source rest frame and the primed ones are measured in the comoving frame. $\mathcal{D}$ is the Doppler factor

$$\mathcal{D} = W^{-1}(1 - v\cos\Theta)^{-1}, \tag{D13}$$

Θ being the angle between the fluid direction and the observer.

The light aberration changes the angle of the line of sight when a relative movement between two inertial frames exists. This aberration has two effects in the emission model (Gómez 1993): (1) in the calculus of the emission and absorption coefficients (eqs. D2 and D3) by changing ϑ (the angle between the line of sight and the magnetic field), because both coefficients where expressed in the fluid frame; and (2) changing the polarization properties through the angle χ_B.

Let us remark, that if the magnetic field were completely random in direction, both, ϑ and χ_B would be totally random too, and the light aberration would not cause any effect on the emission. Actually, the randomness degree of the magnetic field determinates, with the Lorentz factor, the corrections due to the effect of light aberration.

Another important effect in the emission time evolution is the light-travel time delays, especially for small viewing angles (*e.g.,* Gómez *et al.* 1997). Such time delays whithin the jet have been ignored assuming that the calculated emission corresponds to that of a stationary jet. This is a plausible approximation for the case of the slow evolving large scale structure in jets. We have not included such effect because it introduces an enormous amount of computational resources and/or complexity. The reason for this is that it involves computation of the emission and absorption coefficients at different (source) times in order to compute a single image in the observer frame. Considering that each 3D RHD model needs $\sim$ 225 Mb and we need to save about 1000 models, about 225 Gb are requested in order to produce a radio image. Although this represents a significant computational effort, it allows the calculation of different emission models (*i.e.,* different viewing angles, observation time and frequency, etc.) with a single hydrodynamical run. A different approach that avoids the storage problems is to calculate the emission at run time. In this alternative it is necessary to pre-select one or several viewing angles before executing the hydrodynamical run. Then, only those data in the appropriate time intervals and predefined directions are saved. The main advantage of the first approach is that after the run it is possible to calculate the radio maps for any desired angle, while in the second case, one needs to infer in advance which are going to be the more interesting viewing angles (and experience shows us that this is usually a *fine tuning* task).

REFERENCES

Abell, G.O. & Margon, B., 1999, *Nature*, 279, 701.

Akerlof, C.W., *et al.* 1999, Nature, 398, 400.

Akujor, C.E. 1992, A&A, 259, L61.

Aloy, M.A., Ibáñez, J.M$^{\underline{a}}$., Martí, J.M$^{\underline{a}}$., & Müller, E. 1999a, ApJS, 122, 151.

Aloy, M.A., Ibáñez, J.M$^{\underline{a}}$., Martí, J.M$^{\underline{a}}$., Gómez, J.L., & Müller, E. 1999b, ApJ, 523, L100.

Aloy, M.A., Ibáñez, J.M$^{\underline{a}}$., Martí, J.M$^{\underline{a}}$., Gómez, J.L., & Müller, E. 1999c, ApJ, submitted.

Aloy, M.A., Ibáñez, J.M$^{\underline{a}}$., Martí, J.M$^{\underline{a}}$., Gómez, J.L., & Müller, E. 2000, in preparation.

Aloy, M.A., Pons, J.A., & Ibáñez, J.M$^{\underline{a}}$. 1999, Comp. Phys. Communications, accepted.

Aloy, M.A., Müller, E., Ibáñez, J.M$^{\underline{a}}$., Martí, J.M$^{\underline{a}}$., MacFadyen, A. 1999c, ApJ, submited.

Andersen, M.I. (1999), *Science* **283**, 2075.

Anile, A.M. 1989, Relativistic Fluids and Magneto-Fluids (Cambridge University Press).

Apple, S.,& Camenzind, M. 1992, A&A, 256, 354.

Attridge, J.M., Roberts, D.H., & Wardle, J.F.C. 1999, ApJ, 518, L87.

Balsara, D.S., & Norman, M.L. 1992, ApJ, 393, 631.

Baring, M.G. 1995, Ap&SS, 231, 169.

Band, D.L., *et al.* 1993, ApJ, 413, 281.

Blandford, R.D., & McKee, C.F. 1976, *Phys. Fluids*, 19, 1130.

Blandford, R.D., & Rees, M.J. 1974, MNRAS, 169, 395.

Blandford, R.D., & Königl, A. 1979, ApJ, 232, 34.

Blandford, R.D., & Znajek, R.L. 1977, MNRAS, 179, 433.

Blandford, R.D. 1990, in *Active Galactic Nuclei*, SSAS Saas-Fee Advanced Course 20, Lectures Notes, eds. T.J.-L. Courvoisier & M. Mayor. (Springer-Verlag), p. 161.

Blaes, O.M. 1994, ApJS, 92, 643.

Begelman, M.C., & Cioffi, D.C. 1989, ApJ, 345, L21.

Begelman, M.C., Blandford, R.D., & Rees, M.J. 1984, Rev. Mod. Phys., 56, 255.

Begelman, M.C., Rees, M.J., & Sikora, M. 1994, ApJ, 429, L57.

Begelman, M.C., Rees, M.J., & Blandford, R.D. 1979, Nature, 279, 770.

Benson, J.M., Walker, R.C., Unwin, S.C., Muxlow, T.W.B., Wilkinson, P.N., Booth, R.S., Pilbratt, G., & Simon, R.S. 1988, ApJ, 334, 560.

Bicknell, G.V. 1984, ApJ, 239, 433.

Bicknell, G.V. 1996, in *Energy Transport in Radio Galaxies and Quasars*, eds. P.E. Hardee, A.H. Bridle, J.A. Zensus. ASP Conference Series, Vol. 100, p. 253.

Biretta, J.A., & Owen, F.N. 1990, in *Parsec-scale Radio Jets*, ed. J.A. Zensus & T.J. Pearson (Cambridge: Cambridge University Press), p. 125.

Biretta, J.A., Zhou, F., & Owen, F.N. 1995, ApJ, 447, 582.

Blinnikov, S.I., Dunina-Barkovskaya N.V., & Nadyozhin D.K. 1996, ApJS, 106, 171.

Bodo, G., Massaglia, S., Rossi, P., Rosner, R., Malagoli, A., & Ferrari, A. 1995, A&A, 303, 281.

Bodo, G., Rossi, P., Massaglia, Ferrari, A., Malagoli, A., & Rosner, R. 1998, A&A, 333, 1117.

Bodo, G., 1998, in *Astrophysical jets: Open problems*, eds. S. Massaglia & G. Bodo, Gordon and Breach, p.161.

Bowman, M., 1994, MNRAS, 269, 137.

Bridle, A.H., Hough, D.H., Lonsdale, C.J., Burns, J.O., & Laing, R.A. 1994, AJ, 108, 766.

Briggs, M.S., Band, D.L., Kippen, R.M., Preece, R.D., Kouveliotou, C., *et al.* (1999), ApJ, submitted; and astro-ph/9903274.

Browne, I.W.A. 1987, in *Superluminal Radio Sources*, eds. J.A. Zensus & T.J. Pearson (Cambridge: Cambridge University Press), p. 111.

Camenzind, M. 1993, in *Jets in Extragalactic Radio Sources*, eds., H.J. Röser & K. Meisenheimer (Springer-Verlag, Berlin), p. 109.

Castro-Tirado, A.J. 1999, A&SS, in press; and astro-ph/9903187.

Cavallo, G. & Rees, M.J., 1978, MNRAS, 183, 359.

Centrella, J. & Wilson, J.R. 1984, ApJS, 54, 229.

Chirstiansen, W.A., Scott, J.S., & Vestrand, W.T., 1978, ApJ, 223, 13.

Clarke, D.A., Norman, M.L., & Burns, J.O. 1989, ApJ, 342, 700.

Cohen, M.H., Cannon, W., Purcell, G.H., Shaffer, D.B., Broderick, J.J., Kellermann, K.I., & Jauncey, D.L. 1971, ApJ, 170, 207.

Colella, P., & Woodward, P.R. 1984, JCP, 54, 174.

Colgate, S.A., & Johnson, M.H. 1960, Phys. Rev. Lett., 5, 235.

Costa, E., *et al.* 1987, Nature, 387, 783.

Cox, J.P., & Giulli, R.T. 1968, in *Principles of Stellar Structure*, ed. Gordon & Breach, New York.

Curtis, H.D. 1918, *Publ. Lick Obs.*, 13, 9.

Daigne, F. 1999, Ph. D. Thesis, Universite de Paris Sud, U.F.R. Scientifique d'Orsay.

Daigne, F., & Moschkovitch, R. 1999, in Procedings of the Rome Conference *Gamma-Ray Bursts in the Afterglow Era*, astro-ph/9901343.

Daly, R.A. 1995, ApJ, 454, 580.

Daly, R.A., & Marscher, A.P., 1988, ApJ, 334, 539.

Davis, S.F. 1984, NASA Contractor Rep. 172373, ICASE Rep., No.84-20.

Dermer, C.D., & Mitman, K.E. 1999, ApJ, 513, 656.

De Young, D. 1993, ApJ, 405, L13.

Dezalay, J., Lestrade, J., Barat, C., Talon, R., Terenkhov, O., Sunyaev, R., & Kuznetsov, A. 1996, ApJ, 471, L27.

Djorgovski, S.G., Kulkarni, S.R., Bloom, J.S., Goddrich, R., Frail, D.A., Piro, L. and Palazzi, E. 1998, ApJ508, L17.

Donat, R., Font, J.A., Ibáñez, J.M$^{\underline{a}}$., & Marquina, A. 1998, *J. Comp. Phys.*, 146, 58.

Donat, R., & Marquina, A. 1996, JCP, 125, 42.

Duncan, G.C., & Hughes, P.A. 1994, ApJ, 436, L119.

Duncan, G.C., & Hughes, P.A., & Opperman, J., 1996, in *ASP Conf. 100, Energy Transport in Radio Galaxies and Quasars*, ed. P.E. Hardee, A.H. Bridle, & J.A. Zensus (San Francisco: ASP), p. 143.

Dubal, M.R., & Pantano, O. 1993, MNRAS, 261, 203.

Eichler, D., Livio, M., Piran, T. & Schramm, D.N., 1989, Nature, 340, 126.

Einfeldt, B. 1998,*SIAM J. Numer. Anal.*, 25, 294.

Elgroth, P.G. 1971, *Phys. Fluids*, 14, 2631.

Elgroth, P.G. 1972, *Phys. Fluids*, 15, 2140.

Eulderink, F., & G. Mellema, G. 1994, A&A, 284, 652.

Eulderink, F., & G. Mellema, G. 1995, A&AS, 110, 587.

Fanti, C., Fanti, R., Parma, P., Schilizzi, R.T., & van Breugel, W.J.M., 1985, *Astr. Ap.*, 143, 292.

Fanti, C., Fanti, R. 1986, in *Superluminal Radio Sources*, eds. J.A. Zensus & T.J. Pearson (Cambridge: Cambridge University Press), p. 174.

Fanti, C., Fanti, R., Schilizzi, R.T.,Spencer, R.E., Nanrendog, Parma, P., van Breugel, W.J.M., & Venturi, T. 1990, A&A, 231, 333.

Falle, S.A.E.G., & Komissarov, S.S. 1996, MNRAS, 278, 586.

Faranoff, B.L.,& Riley, J.M. 1974, MNRAS, 167, 31.

Fenimore, E., Epstein, R.I., & Ho, C.H. 1993, A&AS, 97, 59.

Fenimore, E., Madras, C., & Nayakshin, S. 1996, ApJ, 473, 998.

Fenimore, E., Ramirez, E., & Summer, M.C. 1998, in *Gamma-Ray Bursts, 4th Huntsville Symposium*, C. Meegan, R. Preece & T. Koshut, Eds. AIP Conf. Proc. 428 (New York: AIP).

Fishman, G. & Meegan, C., 1995, ARA&A, 33, 415.

Font, J.A., Ibáñez, J.Mª., Marquina, A., & Martí, & J.Mª. 1994, A&A, 282, 304.

Frail, D.A., *et al.* 1997, Nature, 389, 261.

Fryer, D.A., Wooslwey, S.E. 1998, ApJ, 502, L9.

Fryer, D.A., Wooslwey, S.E., Herant, M., & Colgate, S.A. 1999, ApJ, 520, 650.

Fruchter, A.S., *et al.* 1999, ApJ, 519, L13.

Galama, T.J., Vreeswijk, P.M., van Paradijs, J. Kouveliotou, C., Augusteijn, T., *et al.*. 1998, Nature395, 670.

Garrington, S.T., Leahy, J.P., Conway, R.G., & Laing, R.A. 1988, Nature, 331, 147.

Ghisellini, G., Padovani, P., Celotti, A., & Maraschi, L. 1993, ApJ, 407, 65.

Gómez, J.L. 1993, Ph. D. Thesis, Instituto de Astrofísica de Andalucía.

Gómez, J.L., Alberdi, A., & Marcaide, J.M. 1993, A&A, 274, 55.

Gómez, J.L., Alberdi, A., & Marcaide, J.M. 1994, A&A, 284, 51.

Gómez, J.L., Alberdi, A., Marcaide, J.M., Travis, J.P. 1994, A&A, 292, 33.

Gómez, J.L., Martí, J.Mª, Marscher, A.P., Ibáñez, J.Mª & Marcaide, J.M. 1995, ApJ, 449, L19.

Gómez, J.L., Martí, J.M$^{\underline{a}}$, Marscher, A.P., Ibáñez, J.M$^{\underline{a}}$., & Alberdi, A. 1997, ApJ, 482, L33.

Gómez, J.L., Marscher, A.P., Alberdi, A., Martí, J.M$^{\underline{a}}$, & Ibáñez, J.M$^{\underline{a}}$. 1998, ApJ, 499, 221.

Gómez, J.L., Marscher, A.P., Alberdi, A., & Gabuzda, D.C. 1999, ApJ, accepted, or astro-ph/9906199.

Gómez, J.L., Marscher, A.P., & Alberdi, A. 1999, ApJ, in press.

Goodman, J., 1986, ApJ, 308, L47.

Goodman, J., 1997, *New Astron.*, 5, 449.

Granot, J., Piran, T., & Sari, R. 1999, ApJ, 513, 679.

Grot, P.J., Piran, *et al.* 1998, ApJ, 502, L123.

Halpern, J.P, Kemp, J., Piran, T. and Bershady, M.A. 1999, ApJ, 517, 105 ; and astro-ph/9903418.

Hardee, P.E., & Norman, M.L. 1988, ApJ, 334, 70.

Hardee, P.E., Cooper, M.A., Norman, M.L., & Stone, J.M. 1992, ApJ, 399, 478.

Hardee, P.E., Clarke, D.A., Howell, D.A. 1995, ApJ, 441, 644.

Hardee, P.E. 1996, in *Energy transport in radio galaxies and quasars*, ASP Conference Series, Vol. 100, eds. P.E. Hardee, A.H. Bridle, J.A. Zensus, p. 273.

Hardee, P.E., & Rosen, A. 1999, ApJ*accepted*; and astro-ph/9906490.

Harten, A., Lax P.D., & van Leer, B. 1983,*SIAM Rev.*, 25, 35.

Harten, A. 1983, *J. Comp. Phys.*, 49, 357.

Harrison, F.A., *et al.* 1999, ApJ, submitted, or astro-ph/9905306.

Hartmann, D., 1996, A&AS, 120, 31.

Hawley, J.F., Smarr, L.L., & Wilson, J.R. 1984, ApJS, 55, 221.

Hooimeyer, J.R.A., Barthel, P.D., Schilizzi, R.T., & Miley, G.K. 1992, A&A, 261, 25.

Hughes, P.A., Aller, H.D., & Aller, M.F. 1985, ApJ, 298, 301.

Hughes, P.A., Aller, H.D., & Aller, M.F. 1989a, ApJ, 341, 54.

Hughes, P.A., Aller, H.D., & Aller, M.F. 1989b, ApJ, 341, 68.

Hummel, C.A., *et al.* 1992, A&A, 257, 489.

Ibáñez, J.Mª., & Martí, J.Mª. 1998, *J. Comp. Applied Math.*, in press.

Iwamoto, T.J., Mazzali, P.A., Nomoto, K., Umeda, H., Nakamura, T., *et al.* (1998), Nature, 395, 672.

Jenkins, E.B. 1997, IAU Symposia, vol. 188, E97.

Jenninson, R.C., & Das Gupta, M.K. 1953, Nature, 172, 996.

Johnson, M.H., & McKee, C.F. 1971, Phys. Rev. D, 3, 858.

Jones, T.W. 1988, in *Supermassive black holes*, Proc. of the Third George Mason Astrophysics Workshop, Fairfax, VA, (Cambridge: Cambridge University Press), p. 59.

Jones, T.W., & O'Dell, S.L. 1977a, ApJ, 214, 522.

Jones, T.W., & O'Dell, S.L. 1977b, ApJ, 215, 236.

Jones, T.W., Tregillis, I.L., & Dongsu Ryu, 1999, astro-ph/9908315.

Junor, W., & Bireta, J.A. 1995, ApJ, 109, 500.

Katz, J.I., 1994, ApJ, 432(2), L107.

Katz, J.I., 1997, ApJ, 490, 633.

Katz, J.I., & Canel, L.M. 1996, ApJ, 471, 915.

Katz, J.I., & Piran, T. 1997, ApJ, 490, 772.

Kembhavi, A.K., & Narlikar, J.V. 1999, *Quasars and Active Galactic Nuclei. An introduction* (Cambridge: Cambridge University Press).

Klebesadal, R.W., Strong, I.B., & Olsen, R.A. 1973, ApJ, 182, L85.

Krichbaum, T.P., Quirrenbach, A., & Witzel 1992, in Variability of Blazars, ed. E. Vataoja & M. Valtonen (Cambrige: Cambridge Univ. Press), 331.

Kobayashi, S., Piran, T. and Sari, R. 1999, ApJ, 513, 669.

Kössl, D., & Müller, E. 1988, A&A, 206, 204

Koide, S. 1997, ApJ, 478, 66

Koide, S., Nishikawa, K.-I., & Muttel, R.L. 1996, ApJ, 463, L71

Koide, S., David, L.M., Shibata, K. & Kudoh, T. 1999a, to appear in *Proceedings of the 19th Texas Symposium on Relativistic Astrophisics*, or astro-ph/9907434.

Koide, S., David, L.M., Shibata, K. & Kudoh, T. 1999b, ApJ, *submitted*, or astro-ph/9907435.

Komissarov, S.S. 1990, Sov. Astron. Lett. 16(4), 284

Komissarov, S.S., & Falle, S.A.E.G. 1996, in Energy Transport in Radio Galaxies and Quasars, eds. P.E. Hardee, A.H. Bridle, J.A. Zensus. ASP Conference Series, Vol. 100, p. 327

Komissarov, S.S., & Falle, S.A.E.G. 1997, MNRAS, 288, 833.

Komissarov, S.S., & Falle, S.A.E.G. 1998, MNRAS, 297, 1087.

Königl, A., 1980, *Phys. Fluids*, 23, 1083.

Königl, A., 1981, ApJ, 243, 700.

Kössl, D., Müller, E., & Hillebrandt, W. 1990, A&A, 229, 378.

Kouveliotou, C., Meegan, C., Fishmann, G., Bhat, N., Briggs, M., Koshut, T., Paciesas, W., & Pendleton, G. 1993, ApJ, 413, L101.

Krolik J.H., & Pier, E.A. 1991, ApJ, 373, 277.

Krolik J.H. 1999, in *Active Galactic Nuclei*, ed. Ostriker J.P., & Spergel D.N., Princenton University Press.

Kulkarni, S.R., Djorgovski, S.G., Ramaprakash, A.N., Goodrich, R., Bloom, J.S., *et al.* 1998a, Nature, 393, 35.

Kulkarni, S.R., Frail, D.A., Wieringa, M.H., Ekers, R.D., Sadler, E.M., Wark, R.M., Higdon, J.L., Phinney, E.S. and Bloom, J.S. 1998b, Nature, 395, 663.

Kulkarni, S.R., Djorgovski, S.G., Odewahn, S.C., Bloom, J.S., Gal, R.R., *et al.* 1999a, Nature, 398, 389.

Kulkarni, S.R., Frail, D.A., Sari, R., Moriarty-Schieven, G.H., Shepherd, D.S., Udomprasert, P., Readhead, A.C.S., Bloom, J.S., Feroci, M. and Costa, E. 1999b, preprint astro-ph/9903441.

Laing, R.A. 1988, Nature, 331, 149.

Laing, R.A. 1996, in Energy Transport in *Radio Galaxies and Quasars*, eds. P.E. Hardee, A.H. Bridle, J.A. Zensus. ASP Conference Series, Vol. 100, p. 241.

Lind, K.R., Payne, D.G., Meier, D.L., & Blandford, R.D. 1989, ApJ, 344, 89.

Lobanov, A.P., Krichbaum, T.P., Witzel, A., Kraus, A., Zensus, J.A., Britzen, S., Otterbein, K., Hummel, C.A., & Johnston, K. 1998, A&A, 340, L60.

Loken, C., Burns, J.O., Clarke, D.A. & Norman, M.L. 1992, ApJ, 392, 54.

Loken, C., Roettiger, K., Burns, J.O., & Norman, M.L. 1995, ApJ, 445, 80.

LeVeque, R.J. 1991, Numerical Methods for Conservation Laws (Birkhäuser).

MacFadyen, A. & Woosley, S.E. 1998, ApJ, submitted; and astro-ph/980102748.

Mao, S., Narayan, R., & Piran, T. 1994, ApJ, 420, 171.

Maraschi, L. 1992, in *Variability of Blazars*, ed. E. Valtaoja & M. Valtonen (Cambridge: Cambridge University Press), p. 205.

Marquina, A., Martí, J.Mª., Ibáñez, J.Mª., Miralles, J.A., & Donat, R. 1992, A&A, 258, 566.

Marquina, A. 1994, SIAM J. Scient. Comp., 15, 892.

Marscher, A.P. 1980, ApJ, 235, 386.

Marscher, A.P., & Gear, W.K. 1985, ApJ, 298, 114.

Marscher, A.P., Gear, W.K., & Travis, J.P. 1992, in *Variability of Blazars*, ed. E. Vataoja & M. Valtonen (Cambridge: Cambridge University Press).

Martí, J.Mª., Ibáñez, J.Mª., & Miralles, J.A. 1991, Phys. Rev. D, 43, 3794.

Martí, J.Mª., & Müller, E. 1994, J. Fluid Mech., 258, 317.

Martí, J.Mª., Müller, E., & Ibáñez, J.Mª. 1994, A&A, 281, L9.

Martí, J.Mª, Müller, E., Font, J.A., & Ibáñez, J.Mª 1995, ApJ, 448, L105.

Martí, J.Mª., & Müller, E. 1996, JCP, 123, 1.

Martí, J.Mª., Font, J.A., Ibáñez, J.Mª.& Müller, E. 1996, in Energy Transport in Radio Galaxies and Quasars, eds. P.E. Hardee, A.H. Bridle, J.A. Zensus. ASP Conference Series, Vol. 100, p. 149.

Martí, J.Mª., Müller, E., Font, J.A., Ibáñez, J.Mª. & Marquina, A. 1997, ApJ, 479, 151.

Martí, J.Mª. 1997a, in Relativistic Jets in AGNs, ed. by M. Ostrowski, M. Sikora, G. Madegski, M. Begelman (Astronomical Observatory of the Jagiellonian University, Cracovia), p. 90.

Martí, J. Mª. 1997b, in *Relativistic Gravitation and Gravitational Radiation*, ed. J-A. Marck and J-P. Lasota (Cambridge University Press, Cambridge, UK).

Martí, J.Mª., Müller, E. & Ibáñez, J.Mª. 1998, in *Astrophysical jets: Open problems*, eds. S. Massaglia & G. Bodo, Gordon and Breach, p.149.

Massaglia, S., Bodo, G., & Ferrari, A. 1996, A&A, 307, 997.

Metzger, M.R., Djorgovski, S.G., Kulkarni, S.R., Steidel, C.C., Adelberger, K.L., Frail, D.A., Costa, E. and Frontera, F. (1997), Nature, 387, 878.

Mészáros, P. 1995, in *Proc. of the 17th Texas Symp. on Relativistic Astrophysics and Cosmology*, H. Böhringer, G.E. Morfill, & J.E. Trümper (eds.), N. Y. Acad. Sci., p. 440.

Mészáros, P. 1999, in *Proc. of the 19th Texas Symp. on Relativistic Astrophysics & Cosmology*, Paris, Dec. 1998; and astro-ph/9904038.

Mézáros, P., & Rees, M.J. 1992, MNRAS, 257, 29.

Mézáros, P., Laguna, P. & Rees, M.J. 1993, ApJ, 415, 181.

Mézáros, P., & Rees, M.J. 1997, ApJ, 482, L29.

Mioduszewski, A.J., Hughes, P.A., & Duncan, G.C. 1997, ApJ, 476, 649.

Mirabel, I.F., & Rodriguez, L.F. 1994, Nature, 371, 46.

Mochkovitch, R., Hernanz, M., Isern, J. & Martin, X. 1993, Nature, 361, 236.

Mochkovitch, R., Hernanz, M., Isern, J. & Loiseau, S. 1995, A&A, 293, 803.

Muxlow, T.W.B., & Garrington, S.T. 1991, in *Beams and Jets in Astrophysics*, ed. P.A. Hughes (Cambridge: Cambridge Univ. Press), 52.

Muxlow, T.W.B., & Wilkinson, P.N. 1991, MNRAS, 251, 54.

Narayan, R., Paczyński, B., & Piran, T. 1992, ApJ, 395, L83.

Narayan, R., & Piran, T. 1999, in preparation.

Nishikawa, K.–I., Koide, S., Sakai, J., Christodoulou, D.M., Sol, H., & Mutel, R.L. 1997, ApJ, 483, L45.

Nishikawa, K.–I., Koide, S., Sakai, J., Christodoulou, D.M., Sol, H., & Mutel, R.L. 1998, ApJ, 498, 166.

Norman, M.L., Smarr, L., Winkler, K.-H.A., & Smith, M.D. 1982, A&A, 113, 285.

Norman, M.L., & Winkler, K.-H.A. 1986, in *Astrophysical Radiation Hydrodynamics*, ed. M.L. Norman, K.-H.A. Winkler. Reidel, Dordrecht, p. 227.

Norman, M.L., Burns, J.O., & Sulkanen, M.E. 1988, Nature, 335, 146.

Norman, M.L., & Hardee, P.E. 1988, ApJ, 334, 80.

Norman, M.L. 1996, in *Energy Transport in Radio Galaxies and Quasars*, eds. P.E. Hardee, A.H. Bridle, J.A. Zensus. ASP Conference Series, Vol. 100, p. 319.

Norris, J., Nemiroff, R., Bonell, J., Scargle, J., Kouveliotou, C., Paciesas, W., Meegan, C., & Fishmann, G. 1996, ApJ, 459, 393.

Noh, W.F. 1987, JCP, 72, 1.

Owen, F.N., & Rudnick, L. 1976, ApJ, 205, L1.

Pacholczyk, Q.G. 1970, *Radio Astrophysics*, Freeman, San Francisco.

Pacyński, B. 1986, ApJ, 308, L43.

Pacyński, B., & Rhoads, J.E. 1993, ApJ, 418, L5.

Pacyński, B., & Xu, G. 1994, ApJ, 427, 708.

Pacyński, B. 1998, ApJ, 494, L45.

Padman R., Lasenby A.N., & Green 1991, in *Beams and Jets in Astrophysics*, ed. P.A. Hughes (Cambridge: Cambridge Univ. Press), 484.

Panaitescu, A., Wen, L., Laguna, P. and Mészáros, P. 1997, ApJ, 482, 942.

Panaitescu, A., & Mészáros, P., 1998, ApJ, 492, 683.

Panaitescu, A. & Mészáros, P. 1999, ApJ, in press; and astro-ph/9810258.

Pen, U.-L. 1998, ApJS, 115, 19.

Pearson, T.J., Unwin, S.C., Cohen, M.H., Linfield, R.P., Readhead, A.C.S., Seielstad, G.A., Simon, R.S., & Walker, R.C. 1981, Nature, 290, 365.

Philips, R.B., & Mutel, R.L. 1980, ApJ, 236, 89.

Phinney E.S. 1987, in *Superluminal Radio Sources*, eds. J.A. Zensus & T.J. Pearson (Cambridge: Cambridge University Press), p. 301.

Pian, E., Fruchter, A.S., Bergeroni, L.E., Thorsett, S.E., Frontera, F., *et al.* 1998, ApJ492, L103.

Pian, E., Amati, L., Antonelli, L.A., Butler, R.C., Costa, E., *et al.* (1999), A&A, submitted; and astro-ph/9903113.

Piran, T., Shemi, A. & Narayan, R. 1993, MNRAS, 263, 861.

Piran, T. 1997, in *Unsolved Problems in Astrophysics*, J.N. Bahcall & J.P. Ostriker (eds.), Princeton Univ. Press, p. 343.

Piran, T. 1999, Physics Reports, in press; and astro-ph/9810256.

Pons J.A., Font J.A., Ibáñez, J.Mª., Martí, J.Mª., & Miralles, J.A. 1998, A&A, 339, 638.

Popham, R., Woosley, S.E. & Fryer, C. 1998, ApJ, submitted; and astro-ph/9807028.

Porter, D.H. & Woodward, P.R. 1994, ApJS, 93, 309.

Prilutskii, O.F. & Usov, V.V. 1975, Ap&SS, 34, 395.

Rawlings, S., & Saunders, R. 1991, Nature, 349, 138.

Rayburn, D.R., 1977, MNRAS, 179, 603.

Rees, M.J., & Mészáros, P. 1994, ApJ, 430, L93.

Rees, M.J. 1997, in *Relativistic Astrophysics*, ed. Jones, B.J.T., & Marković, Cambridge Univ. Press, 251.

Rhoads, J.E. (1999), ApJ, submitted; and astro-ph/9903399.

Roe, P.L. 1981, *J. Comput. Phys.*, 43, 357.

Rosen, A., Hughes, P. A., Duncan, G. C., & Hardee, P. E. 1999, ApJ, in press.

Ruderman, M. 1975, *Ann. N.Y. Acad. Sci.*, 262, 164.

Ruffert, M. & Janka, H.-T., Shäfer G. 1996, A&A, 319, 122.

Ruffert, M., Janka, H.-T., Takahashi, K. & Schäfer, G. 1997, A&A, 319, 122.

Ruffert, M. & Janka, H.-T. 1998, A&A, 338, 535.

Ruffert, M. & Janka, H.-T. 1999a, A&A, 344, 573.

Ruffert, M. & Janka, H.-T. 1999b, ApJ, *submitted*, or astro-ph/9908290.

Rybicki, G.B., Lightman, A.P. 1979, *Radiative Processes in Astrophysics.* Wiley, New York, p. 110.

Shakura, N.I., & Sunyaev, R.A. 1973, A&A, 24, 337.

Sari, R., & Piran, T. 1995, ApJ, 455, 143.

Sari, R., & Piran, T. 1997, ApJ, 485, 270.

Sari, R., Piran, T., & Halpern, J.P. 1999, ApJsubmitted; and astro-ph/9903339.

Sari, R., Piran, T., & Narayan, R. 1998, ApJ, 497, 17.

Scheuer, P.A.G. 1984, MNRAS, 166, 513.

Schneider, V., Katscher, V., Rischke, D.H., Waldhauser, B., Marhun, J.A., & Munz, C.-D. 1993, JCP, 105, 92.

Sedov, L.I. 1959, in *Similarity and Dimensional Methods in Mechanics*, London, Chapt. 4.

Seielstad, G.A., Cohen, M.H., Linfield, R.P., Moffet, A.T., Rommey, J.D., Schilizzi, R.T., & Shaffer, D.B. 1979, ApJ, 229, 53.

Shapiro, P.R. 1979, ApJ, 233, 831.

Shapiro, P.R. 1980, ApJ, 236, 958.

Shone, D.L., Porcas, R.W., & Zensus, J.A. 1985, Nature, 314, 603.

Shu, C.W., & Osher, S.J. 1989, JCP, 83, 32.

Soffitta, P., Feroci, M., Pior, L., In'tzand, J., Heise, J., DiCiolo, L., Muller, J.M., Palazzi, E. and Frontera, F. 1998, *IAU Circ.*, 6884.

Strang, G. 1968, SIAM J. Num. Anal., 5, 506.

Swain, M.R., Bridle, A.H., & Baum, S.A. 1998, ApJ, 507, L29.

Tabani, M. 1998, ApJ, 497, 21.

Tingay, S.J., *et al.* 1995, Nature, 374, 141.

Tinney, C., Stathakis, R. & Cannon, R. 1998, *IAU Circ.*, 6896.

Tutukov, A.V., & Yungelson, L.R. 1994, MNRAS, 268, 871.

Usov, V.V. 1994, MNRAS, 267, 1035.

van Leer, B. 1979, JCP, 32, 101.

van Paradijs, J., *et al.* 1997, Nature, 386, 686.

van Putten, M.H.P.M. 1993, ApJ, 408, L21.

van Putten, M.H.P.M. 1996, ApJ, 467, L57.

Vietri, M. 1997, ApJ, 488, L105.

Vitello, P., & Salvati, M. 1976, *Phys. Fluids*, 19, 1523.

Vreeswijk, P.M., *et al.* 1999, ApJ, *in press*, or astro-ph/9904286.

Witti, J., Janka, H.-T., & Takahashi, K. 1994, A&A, 286, 841.

Walker, R.C., Benson, J.M., & Unwin, S.C. 1987, ApJ, 316, 546.

Walker, R.C. 1997, ApJ, 488, 675.

Weynmann, R.J., Morris, S.L., Foltz, C.B. & Hewett, P.C. 1991, ApJ, 373, 23.

Wen, L., Panaitescu, A., & Laguna, P. 1997, ApJ, 486, 919.

Whitney, A.R., Shapiro, I.I., Rogers, A.E.E., Robertson, D.S., Knight, C.A., Clark, T.A., Goldstein, R.M., Marandino, G.E., & Vandenberg, N.R. 1971, *Science*, 173, 225.

Wijers, R.A.M., & Galama, T.J. 1988, ApJ, *in press*, or astro-ph/9805341.

Wilson, J.R. 1979, in *Sources of Gravitational Radiation*, ed. L.L. Smarr (Cambridge University Press).

Wilson, M.J. 1987, MNRAS, 216, 971.

Wilson, M.J., & Scheuer, P.A.G. 1983, MNRAS, 205, 449.

Woodward, P.R., & Colella, P. 1984, *J. Comput. Phys.*, 54, 115.

Woosley, S.E. 1993, ApJ, 405, 273.

Woosley, S.E., Eastman, R.G. and Schmidt, B.P. 1998, ApJ, submitted; and astro-ph/9806299.

Zel'dovich, Y.B., & Raizer, Y.P. 1966, in *Physics of Shock Waves and High-Temperature Phenomena* (New York: Academic Press), p. 101.

List of Figures